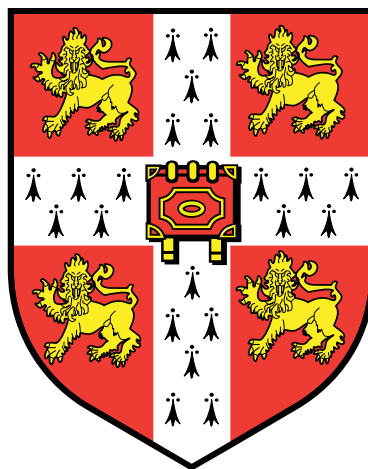


# Structural Properties of $\alpha$ -Synuclein in Functional and Pathological Contexts



**Giuliana Fusco**  
St John's College  
University of Cambridge

A dissertation submitted for the  
degree of Doctor of Philosophy

October 2016

*“Nothing in the world can take the place of persistence. Talent will not; nothing is more common than unsuccessful with talent. Genius will not; unrewarded genius is almost a proverb. Education will not; the world is full of educated derelicts. Persistence and determination alone are omnipotent.”*

*Calvin Coolidge*

*To Gabriel Francesco*

## **Preface**

This dissertation is a summary of research carried out under the supervision of Prof. C. M. Dobson in the Department of Chemistry of the University of Cambridge, between April 2012 and March 2016. It is my own work and contains nothing which is the outcome of work done in collaboration with others, except as specified in the text and acknowledgements. It has not, either in part, or as a whole, been submitted for a degree, diploma, or other qualification at any other university. The length of this dissertation is approximately 43000 words. This total is below the word limit of 60000 words. This revision was submitted in September 2016.

## **Acknowledgments**

I am grateful to many people who during these years have supported, guided and encouraged my work. I wish to thank my supervisor, Professor Christopher M. Dobson, for his inspirational expert guidance and encouragement. In particular for showing always his confidence in me and supporting my ideas and researches. I am also grateful to Dr. Alfonso De Simone for all his guidance and Professor Michele Vendruscolo for the fruitful and stimulating discussions. Their enthusiasm motivated me to improve myself as a scientist. I would like also to thank Professor Gianluigi Veglia for hosting me several times in his lab at University of Minnesota to produce key data for this thesis. I thank Dr. Tillman Pape for his collaboration to the acquisition of cryo-EM images and Dr. Pierre Mahou for his collaboration to the acquisition and analysis of STED images presented in Chapter IV. I am grateful to Dr. Philip Williamson for welcoming me during my visit in his lab and for his collaboration in some of the ssNMR measurements that are relevant to Chapter V. A special acknowledgment is for Ms Serene Chen for her sincere friendship during these years. I thank also for her invaluable help for producing the toxic oligomers and the collaboration to the acquisition of the biophysical data of Chapter V. In addition I thank Dr Liming Ying for contribute to work and collaboration in FRET and FCS measurements for Chapter V. I'd like also to thank Dr. Gabi Kaminski, Dr. Nunilo Cremades and Dr. Paolo Arosio for the stimulating discussions.

I am deeply grateful to the Parkinson's UK for funding my PhD and sponsoring the present research. I finally want to thank my family for believe in me but most of all because they have never tried to stop me in all my choices.

## Contents

<i>Declaration</i>	
<i>Abstract</i>	
<i>Preface</i>	<i>i</i>
<i>Acknowledgments</i>	<i>ii</i>
<i>Contents</i>	<i>iii</i>
<i>List of Figures</i>	<i>vii</i>
<i>List of Publications from the PhD studies</i>	<i>x</i>
<i>List of abbreviations</i>	<i>xi</i>
<b>Chapter I. Introduction</b>	<b>1</b>
1.1 Structural and biophysical properties of $\alpha$ S	1
1.2 Pathological relevance of $\alpha$ S in Parkinson's disease	3
1.2.1 Links between $\alpha$ S and Parkinson's disease	3
1.2.2 $\alpha$ S aggregation into amyloids	4
1.3 The physiological role of $\alpha$ S	7
1.4 Membrane interaction of $\alpha$ S in functional and pathological contexts	10
1.5 Overview of the PhD research	13
<b>Chapter II. Materials and Methods</b>	<b>16</b>
2.1 Purification of recombinant $\alpha$ S	16
2.2 Solution NMR of $\alpha$ S	17
2.2.1 The $^1\text{H}$ - $^{15}\text{N}$ -HSQC experiment	19
2.2.2 Assignment of the protein resonances	21
2.2.3 $^{13}\text{C}$ -detected solution NMR	23
2.2.4 Exploitation of CS to study the conformations of IDPs	24
2.2.5 Chemical Shift Saturation Transfer (CEST)	28
2.3 Biomolecular solid state NMR	31
2.3.1 Magic Angle Spinning	31
2.3.2 Cross Polarisation experiments	32

<b>Chapter III. The membrane-bound state of <math>\alpha</math>S: structure, topology and molecular determinants</b>	<b>34</b>
3.1 A hybrid of solution state and solid-state NMR approach to characterise $\alpha$ S-membrane interactions	34
3.2 Materials and Methods	36
3.2.1 $\alpha$ S purification	36
3.2.2 Preparation of SUVs for solid-state and solution NMR	36
3.2.3 Magic angle spinning measurements using ssNMR	36
3.2.4 Oriented ssNMR experiments	37
3.2.5 Solution NMR samples and CEST experiments	37
3.2.6 Paramagnetic relaxation enhancement at the magic angle spinning	38
3.2.7 Structural ensemble refinement by CS-restrained MD simulations	38
3.2.8 Restrained MD setup	39
3.2.9 Prediction of anisotropic $^{15}\text{N}$ CS in aligned samples	40
3.3 Three distinct regions of $\alpha$ S define its membrane-binding properties	42
3.4 Structure of the N-terminal region of $\alpha$ S in its membrane-bound state	50
3.5 Topology of the membrane anchor region of $\alpha$ S at the surface of SUVs	57
3.6 The central region of $\alpha$ S acts as a sensor to direct the membrane binding affinity	66
3.7 The C-terminal region of $\alpha$ S establishes transient interactions with the surface of synaptic-like vesicles	71
3.8 Discussion	72
<b>Chapter IV. Role of <math>\alpha</math>S in Synaptic Vesicle Trafficking. Function Solved?</b>	<b>76</b>
4.1 Role of $\alpha$ S in synaptic vesicle homeostasis	76
4.2 Materials and Methods	77
4.2.1 $\alpha$ S purification	77

4.2.2	Preparation of SUVs for solid-state and solution NMR	77
4.2.3	Purification of SVs from rat brain.	77
4.2.4	Magic angle spinning measurements using ssNMR	78
4.2.5	Solution NMR samples and CEST experiments	78
4.2.6	Cryo electron microscopy (Cryo-EM) measurements	78
4.2.7	Stimulated emission depletion (STED) microscopy	79
4.2.8	Analysis of STED images for vesicle size quantification	80
4.2.9	Direct stochastic optical reconstruction microscopy (dSTORM)	80
4.2.10	Modelling	81
4.2.11	Kinetics measurements of aggregation	81
4.2.12	Atomic force microscopy (AFM) measurements	82
4.2.13	Dynamic light scattering (DLS)	82
4.2.14	Fitting of the CD data.	82
4.3	Binding properties of pathological $\alpha$ S variants.	84
4.4	Mechanism of synaptic vesicle assembly induced by $\alpha$ S	92
4.5	The NAC region is fundamental for $\alpha$ S function and aggregation	97
4.6	Discussion	103
 <b>Chapter V. Structural Basis for the toxicity of <math>\alpha</math>S in Parkinson's Disease</b>		<b>106</b>
5.1	Identification of toxic and non-toxic $\alpha$ S oligomers	106
5.2	Materials and methods	114
5.2.1	$\alpha$ S purification	114
5.2.2	Preparation of <i>Type A*</i> and <i>Type B</i> $\alpha$ S oligomers	114
5.2.3	Preparation of fluorescently labelled $\alpha$ S for FRET	114
5.2.4	Magic angle spinning measurements using ssNMR	115
5.2.5	Solution NMR samples and CEST experiments	115
5.2.6	Foster resonance transfer (FRET) measurements	115
5.2.7	Sedimentation velocity experiments by analytical ultracentrifugation (AUC)	116
5.2.8	Fourier transform infra red spectroscopy (FT-IR)	116
5.3	Structural properties of toxic and non-toxic $\alpha$ S oligomers	118

5.4 The selective interaction with cellular membranes promotes the toxicity in type B $\alpha$ S oligomers	125
5.5 Discussion	131
<b><i>Chapter VI. Discussion</i></b>	<b>135</b>
6.1 Insight into the functional role of $\alpha$ S	135
6.2 Molecular role of $\alpha$ S in Parkinson's Disease	138
6.3 Challenges in $\alpha$ S research	140
<b><i>References</i></b>	<b>141</b>

## List of Figures

<i>Figure 1.1. Conformational heterogeneity of monomeric <math>\alpha</math>S in solution</i>	2
<i>Figure 1.2 Characteristic bodies in PD</i>	3
<i>Figure 1.3. Characterisations of the amyloid fibrillar state of <math>\alpha</math>S</i>	6
<i>Figure 1.4. Role of <math>\alpha</math>S in the regulation of the kinetics of synaptic vesicles exocytosis at the axon termini</i>	8
<i>Figure 1.5. Membrane interaction of <math>\alpha</math>S under physiological cellular conditions</i>	11
<i>Figure 1.6. Membrane interaction of <math>\alpha</math>S under pathological cellular conditions</i>	12
<i>Figure 2.1. Basic scheme for the pulse sequence of the <math>^1\text{H}</math>-<math>^{15}\text{N}</math>-HSQC</i>	19
<i>Figure 2.2. <math>^1\text{H}</math>-<math>^{15}\text{N}</math>-HSQC of monomeric <math>\alpha</math>S in water solution</i>	20
<i>Figure 2.3. From <math>^1\text{H}</math>-<math>^{15}\text{N}</math>-HSQC to 3D spectra to strips</i>	21
<i>Figure 2.4. Example of complementary strips in NMR backbone assignment</i>	22
<i>Figure 2.5. Advantage of using <math>^{13}\text{C}</math>-detected NMR experiments in <math>\alpha</math>S</i>	24
<i>Figure 2.6. Binding of <math>\alpha</math>S to small molecules</i>	25
<i>Figure 2.7. The CamShift method</i>	27
<i>Figure 2.8. The CEST experiment</i>	30
<i>Figure 2.9. Magic Angle Spinning</i>	32
<i>Figure 2.10. <math>^{13}\text{C}</math> cross polarisation experiment</i>	33
<i>Figure 3.1. CD analysis of <math>\alpha</math>S in the presence of different concentrations of SUVs</i>	43
<i>Figure 3.2. MAS ssNMR spectrum of <math>\alpha</math>S bound to DOPE:DOPS:DOPC SUVs</i>	44
<i>Figure 3.3. Carbonyl region of <math>^{13}\text{C}</math>-<math>^{13}\text{C}</math> DARR spectra of <math>\alpha</math>S bound to DOPE:DOPS:DOPC SUVs</i>	45
<i>Figure 3.4. Aliphatic region of <math>^{13}\text{C}</math>-<math>^{13}\text{C}</math> DARR spectra of <math>\alpha</math>S bound to DOPE:DOPS:DOPC SUVs</i>	46
<i>Figure 3.5. Heteronuclear DARR measurements of <math>\alpha</math>S bound to DOPE:DOPS:DOPC SUVs</i>	47
<i>Figure 3.6. Residue-specific <math>\alpha</math>-helix populations in the segment 5-26 of <math>\alpha</math>S bound to DOPE:DOPS:DOPC SUVs</i>	48
<i>Figure 3.7. Overlay of the ssNMR INEPT and solution NMR <math>^1\text{H}</math>-<math>^{13}\text{C}</math>-HSQC spectra</i>	49
<i>Figure 3.8. Convergence of the chemical shift restrained simulations of <math>\alpha</math>S<sub>1-30</sub></i>	51
<i>Figure 3.9 Validation of the CS-restrained simulations of <math>\alpha</math>S<sub>1-30</sub></i>	52
<i>Figure 3.10. Free energy surface (FES) of the membrane-bound state of <math>\alpha</math>S<sub>1-30</sub></i>	54
<i>Figure 3.11 Structural properties of the <math>\alpha</math>S<sub>1-30</sub> ensemble</i>	55
<i>Figure 3.12. Map of the occurrence of salt bridges in the main basin of the FES of <math>\alpha</math>S<sub>1-30</sub></i>	56
<i>Figure 3.13. Map of the contacts of the hydrophobic patches in the main basin of the FES of <math>\alpha</math>S<sub>1-30</sub></i>	56
<i>Figure 3.14. Interaction terms between <math>\alpha</math>S<sub>1-30</sub> and DOPE:DOPC:DOPS lipid bilayer</i>	59
<i>Figure 3.15. Orientation <math>\alpha</math>S<sub>1-30</sub> bound to lipid bilayers</i>	60

Figure 3.16. Estimation of the ranges of $^{15}\text{N}$ -ACS in aligned samples of membrane-bound $\alpha\text{S}$	61
Figure 3.17. Positions of residues of $\alpha\text{S}_{1-30}$ on the membrane normal	62
Figure 3.18. PRE of $\alpha\text{S}$ bound to DOPE:DOPS:DOPC SUVs doped using a paramagnetic spin label on the membrane surface	64
Figure 3.19. PRE of $\alpha\text{S}$ bound to DOPE:DOPS:DOPC SUVs doped using a paramagnetic label in the interior of the membrane	64
Figure 3.20. PRE of $\alpha\text{S}$ bound to DOPE:DOPS:DOPC SUVs doped using a paramagnetic label in positions 5 and 10 of the lipid tails	65
Figure 3.21. CEST experiments probing the membrane-sensor interactions of $\alpha\text{S}$	67
Figure 3.22. CEST experiments recorded using a RF value of 170Hz	68
Figure 3.23. Degree of CEST saturation along $\alpha\text{S}$ sequence	69
Figure 3.24. MAS ssNMR spectrum of $\alpha\text{S}$ bound to POPG SUV	70
Figure 3.25. Schematic illustration of the different roles of the three regions of $\alpha\text{S}$ in determining its interaction with lipid bilayers	75
Figure 4.1. CEST experiments probing the membrane interactions of $\alpha\text{S}_{\text{A30P}}$ and $\alpha\text{S}_{\text{E46K}}$	85
Figure 4.2. CEST experiments of $\alpha\text{S}_{\text{A30P}}$ and $\alpha\text{S}_{\text{E46K}}$ using a continuous wavelength of 170Hz	86
Figure 4.3. CEST differences between $\alpha\text{S}_{\text{WT}}$ and $\alpha\text{S}_{\text{A30P}}$ and $\alpha\text{S}_{\text{E46K}}$	87
Figure 4.4. MAS ssNMR spectra of $\alpha\text{S}_{\text{A30P}}$ and $\alpha\text{S}_{\text{E46K}}$ bound to SUVs	90
Figure 4.5. Paramagnetic relaxation experiments	91
Figure 4.6. Vesicle assembly induced by $\alpha\text{S}$	94
Figure 4.7. Differences in the structure, dynamics and binding affinity of $\alpha\text{S}_{\text{Sc}}$ and $\alpha\text{S}_{\text{WT}}$	95
Figure 4.8. Differences in CEST profiles of $\alpha\text{S}_{\text{Sc}}$ and $\alpha\text{S}_{\text{E46K}}$	96
Figure 4.9. Gallery of cryo-EM images of SUVs in the presence and absence of $\alpha\text{S}_{\text{WT}}$ and $\alpha\text{S}_{\text{Sc}}$	99
Figure 4.10. Fitting models employed in STED images	100
Figure 4.11. Average sizes of SUVs from DLS measurements	101
Figure 4.12. Clustering of synaptic vesicles promoted by $\alpha\text{S}$	102
Figure 4.13. SUV interactions and fusion promoted by $\alpha\text{S}$	105
Figure 5.1. Toxic and non-toxic $\alpha\text{S}$ oligomers	107
Figure 5.2. FRET efficiency in bulk measurements of Type A* and Type B $\alpha\text{S}$ oligomers	109
Figure 5.3. Sedimentation velocity analysis of the $\alpha\text{S}$ oligomeric samples	111
Figure 5.4 Toxicity of Type A* and Type B* $\alpha\text{S}$ oligomers	113
Figure 5.5. MAS ssNMR INEPT spectrum of $\alpha\text{S}$ oligomers Type A* and Type B*	120
Figure 5.6 Comparison of solution NMR $^1\text{H}$ - $^{13}\text{C}$ -HSQC and ssNMR INEPT	121

<i>Figure 5.7. <math>^{13}\text{C}</math>-<math>^{13}\text{C}</math> DARR spectrum of Type A* and Type B* <math>\alpha\text{S}</math> oligomers</i>	122
<i>Figure 5.8. Overlay of <math>^{13}\text{C}</math>-<math>^{13}\text{C}</math> DARR spectra of Type A* and Type B* <math>\alpha\text{S}</math> oligomers</i>	122
<i>Figure 5.9. FT-IR Type A* <math>\alpha\text{S}</math> oligomers</i>	123
<i>Figure 5.10. Identification of core-associated and solvent exposed dynamical regions in <math>\alpha\text{S}</math> oligomers using CEST</i>	124
<i>Figure 5.11. Fluorescence correlation spectroscopy of Type A* and Type B <math>\alpha\text{S}</math> oligomers at the surface of SUVs</i>	126
<i>Figure 5.12. PRE experiments of Type A* and Type B* <math>\alpha\text{S}</math> oligomers at the surface of SUVs</i>	127
<i>Figure 5.13. PRE experiments of Type A* and Type B* <math>\alpha\text{S}</math> oligomers in the interior of the lipid bilayers of SUVs</i>	128
<i>Figure 5.14. <math>^{13}\text{C}</math>-<math>^{13}\text{C}</math> DARR of Type A* and Type B* <math>\alpha\text{S}</math> oligomers at the surface of SUVs</i>	129
<i>Figure 5.15. Structural basis of membrane binding of <math>\alpha\text{S}</math> oligomers</i>	130
<i>Figure 5.16. Binding of EGCG to human Lysozyme</i>	132
<i>Figure 5.17. Binding of EGCG to human mAcP</i>	133

### ***List of Publications from the PhD studies***

- Fusco G, De Simone A, Gopinath T, Vostrikov V, Vendruscolo M, Dobson CM, Veglia G “Direct observation of the three regions in alpha-synuclein that determine its membrane-bound behaviour”, 2014, ***Nature Communications*** 5:3827. (*Chapter III*)
- Fusco G, De Simone A, Arosio P, Vendruscolo M, Veglia G, Dobson CM “Structural Ensembles of Membrane-bound  $\alpha$ -Synuclein Reveal the Molecular Determinants of Synaptic Vesicle Affinity” 2016, ***Scientific Reports***. 6:27125 (*Chapter III*)
- Fusco G, Pape T, Mahou P, Costa AR, Kaminski CF, Kaminski Schierle G, Vendruscolo M, Veglia G, Dobson CM, De Simone A “Structural basis of synaptic vesicle assembly induced by  $\alpha$ -synuclein”, 2016, ***Nature Communications***. 7:12563 (*Chapter IV*)
- Fusco G, Chen SW, Williamson PT, Cascella R, Perni M, Jarvis JA, Cecchi C, Vendruscolo M, Chiti F, Cremades N, Ying L, Dobson CM, De Simone A “Structural basis of membrane disruption and cellular toxicity by  $\alpha$ -synuclein oligomers”, 2016, *in preparation*. (*Chapter V*)
- Fusco G, Sanz-Hernandez M, Ruggeri FS, Vendruscolo M, Dobson CM, De Simone A “Molecular Determinants of the Interaction of EGCG with Ordered and Disordered Proteins”, 2016, *in preparation*. (*Chapter V*)
- Krieger JM, Fusco G, Leqitzky M, Simister P, Marchant J, Camilloni C, Feller SM, De Simone A “Conformational recognition of an intrinsically disordered protein”, 2014, ***Biophysical Journal*** 106(8):1771-1779 (Best of Biophys J 2014).

## List of Abbreviations

<b>ACS</b>	anisotropic chemical shifts
<b>AFM</b>	atomic force microscopy
<b><math>\alpha</math>S</b>	$\alpha$ -synuclein
<b><math>\alpha</math>S<sub>WT</sub></b>	$\alpha$ -synuclein wild type
<b><math>\alpha</math>S<sub>A30P</sub></b>	$\alpha$ -synuclein A30P mutant
<b><math>\alpha</math>S<sub>E46K</sub></b>	$\alpha$ -synuclein A30P mutant
<b><math>\alpha</math>S<sub>Sc</sub></b>	$\alpha$ -synuclein scrambled mutant E46K/K80E
<b>CEST</b>	chemical exchange saturation transfer
<b>CD</b>	circular dichroism
<b>CP</b>	cross polarization
<b>Cryo-EM</b>	cross polarization
<b>DARR</b>	dipolar assisted rotational resonance
<b>DLS</b>	dynamic light scattering
<b>DMPS</b>	2,3-Dimercapto-1-propanesulfonic acid
<b>DOPC</b>	1,2-dioleoyl-sn-glycero-3-phosphocholine
<b>DOPE</b>	1,2-dioleoyl-sn-glycero-3-phosphoethanolamine
<b>DOPS</b>	1,2-dioleoyl-sn-glycero-3-phospho-L-serine
<b>dSTORM</b>	direct stochastic optical reconstruction microscopy
<b>EGCG</b>	(-)-EpiGalloCatechin-3-Gallate
<b>EPR</b>	electron paramagnetic resonance
<b>ER</b>	endoplasmic reticulum
<b>FCS</b>	fluorescence correlation spectroscopy
<b>FES</b>	free energy surface
<b>FRET</b>	Forster resonance energy transfer
<b>FT-IR</b>	Fourier transform infrared spectroscopy
<b>HSQC</b>	heteronuclear single quantum coherence
<b>INEPT</b>	insensitive nuclei enhanced by polarization transfer
<b>MAS</b>	magic angle spinning
<b>MD</b>	molecular dynamics
<b><i>KD</i></b>	dissociation constant
<b>NAC</b>	non amyloid- $\beta$ component
<b>NMR</b>	nuclear magnetic resonance
<b>NOE</b>	nuclear overhauser effect
<b>NPT</b>	constant number of particles, pressure and temperature
<b>NVT</b>	constant number of particles, volume and temperature
<b>POPG</b>	1-hexadecanoyl-2-(9Z-octadecenoyl)-sn-glycero-3-phospho-(1'-rac-glycerol)
<b>PD</b>	Parkinson's Disease
<b>PE</b>	phospho-ethanolamine

<b>PE-DTPA</b>	1,2-dimyristoyl-sn-glycero-3-phosphoethanolamine-N-diethylenetriaminepentaacetic acid
<b>PRE</b>	paramagnetic relaxation enhancement
<b>RMSD</b>	root mean square deviation
<b>ROS</b>	reactive oxygen species
<b>SDS</b>	sodium dodecyl sulphate
<b>SLAS</b>	sodium lauroyl sarcosinate
<b>ssNMR</b>	solid state NMR
<b>SUVs</b>	small unilamellar vesicles
<b>STED</b>	stimulated emission depletion microscopy
<b>SVs</b>	synaptic vesicles
<b>WT</b>	wild type

# Chapter I

## *Introduction and Overview of the PhD work*

### **1.1 Structural and biophysical properties of $\alpha$ S.**

$\alpha$ -synuclein ( $\alpha$ S) is a 140-residue protein that is associated with a range of highly debilitating neurodegenerative conditions, of which the most common is Parkinson's disease (PD) (1-5). A hallmark of PD is indeed the formation of abnormal intracellular protein aggregates, known as Lewy bodies (6-9), which are largely composed of amyloid fibrils of  $\alpha$ S (10-14).

In its cytosolic form,  $\alpha$ S can be monomeric and intrinsically disordered (15-17) or associated with other proteins (3). Upon binding to lipid membranes,  $\alpha$ S undergoes a significant conformational transition with respect to its monomeric intrinsically disordered form, with some regions adopting a high level of  $\alpha$ -helical structure (18-21) (see section 1.4).

In its monomeric and disordered state,  $\alpha$ S does not adopt the conformational characteristics of a random coil polymer (15). NMR chemical shifts of this state of  $\alpha$ S are characteristics of a protein that is largely unfolded and lacking significant amount of secondary and tertiary structure, however, a consensus from NMR (22), EPR (23) and MD simulations (24) studies has formed on the relative compactness of this protein compared to a random coil peptide. Indeed, in a previous investigation based on paramagnetic relaxation enhancement at the solution NMR, prof. Dobson and co-workers showed that the distribution of  $\alpha$ S conformations in its monomeric state is significantly narrower than an idealised random-coil state (15). Moreover, structural refinement could reveal the native distribution of the radii of gyration ( $R_g$ ) in this protein (Figure 1.1 b). Despite its structural heterogeneity, the ensemble of conformations of  $\alpha$ S revealed a number of transient long-range interactions populated under physiological conditions (Figure 1.1 c), in particular between the region 120 to 140 and the segment 30 to 100 (15). As this contact involves the non amyloid- $\beta$  component (NAC) region, it was postulated that the proximity between NAC and the highly charged C-terminus could be evolutionary selected to prevent the aggregation of  $\alpha$ S under physiological conditions (15). Consistent results

with this observation were recently evidenced using *in vivo* NMR of  $\alpha$ S in mammalian cells (25). Recently it was also suggested that the actual physiological form of  $\alpha$ S was in a higher oligomeric state (trimer or tetramer) (26). The study, which was also corroborated by an NMR investigation (27), however, has raised a significant debate in literature (28), with a consensus forming that this assembly state might be a kinetically trapped intermediate, but not the actual predominant and active form of  $\alpha$ S *in vivo*.

Overall, investigations made using different approaches converge toward the scenario in which  $\alpha$ S is an intrinsically disordered proteins (IDPs) having unique sequence properties characterised by an overall hydrophobicity, low complexity and high net charge. In contrast to natively folded proteins, which can be characterised by relatively defined three-dimensional structures,  $\alpha$ S is expected to have its atom positions and backbone dihedral angles varying considerably in timescales ranging from nanoseconds to milliseconds with no major conformational minima dominating its monomeric state.

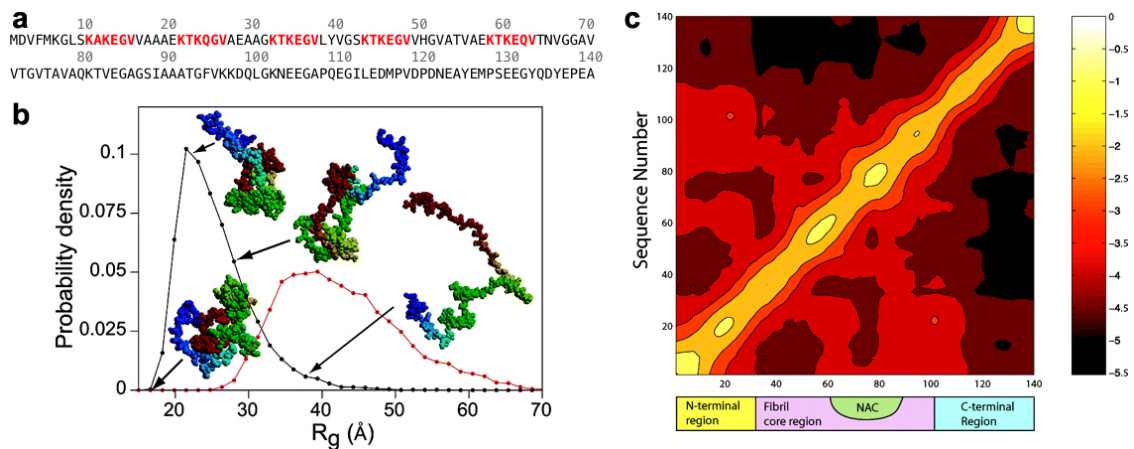


**Figure 1.1. Conformational heterogeneity of monomeric  $\alpha$ S in solution. a)**  $\alpha$ S Sequence, red marks indicate the imperfect KTKEGV repeats encoding for amphipathic helices. **b)** Gyration radii distribution from the PRE restrained simulations of  $\alpha$ S from Dedmon et al (15). Contact map from the same study indicating long range interaction (dark red) between residues 120-140 and 30-100. Figures adapted from (15).

## 1.2 Pathological relevance of $\alpha$ S in Parkinson's disease

### 1.2.1 Links between $\alpha$ S and Parkinson's disease.

$\alpha$ S was first identified as a neuronal protein that localises at the presynaptic terminals of axons as well as in the nucleus, which lead to the denomination of synuclein, however, the nuclear localisation has been debated through the years (29). Currently, the function of this protein is still obscure, although a general consensus is forming on its role in the homeostasis of synaptic vesicles (see Chapter III). In the context of PD  $\alpha$ -Synuclein has gained the interest of the scientific community in 1997 upon discovery of point mutations in the  $\alpha$ S gene that are strongly associated with early onset familial forms of PD (30, 31). The link between  $\alpha$ S and PD has been further corroborated by several experimental evidences (8, 13, 31-39).

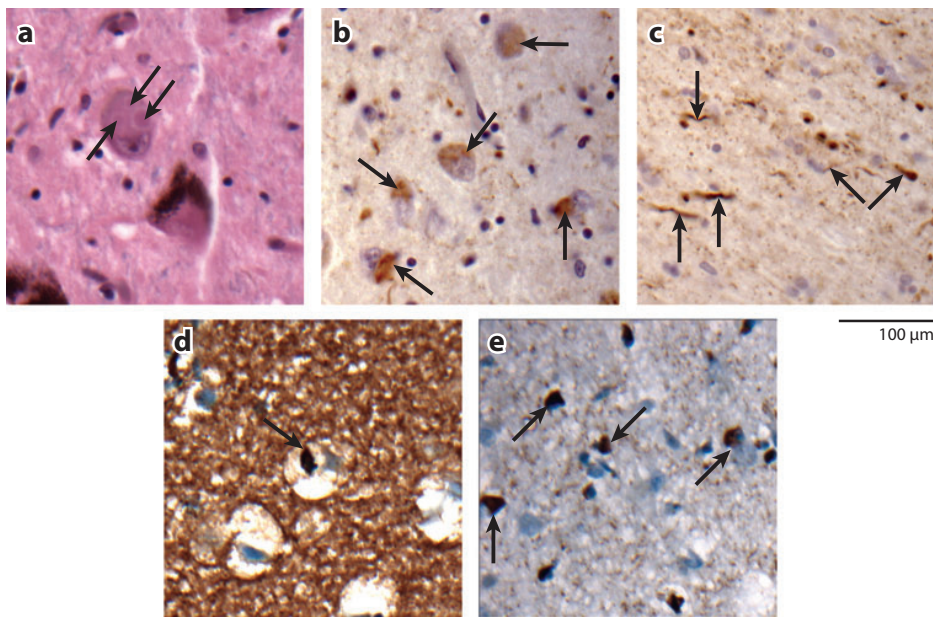


**Figure 1.2 Characteristic bodies in PD.** Figure adapted from (40).  $\alpha$ S fibrils are the major constituents of Lewy bodies and Lewy neuritis in PD, dementia with Lewy bodies, as well as of neuronal and glial cytoplasmic inclusions in multiple system atrophy. **a)** A section of the substantia nigra from a patient with PD showing three Lewy bodies (arrow) in the cytoplasm of a swollen dopaminergic neuron. **b,c)** Section of the amygdala from a patient with dementia with Lewy bodies. Arrows show cortical Lewy bodies in panel b and Lewy neuritis in panel c, which are labelled using antibodies targeting  $\alpha$ S. **d,e)** Section of the putamen from a patient with multiple system atrophy. Panel d shows a single neuronal cytoplasmic inclusion (arrow) whereas panel e reports several glial cytoplasmic inclusions (arrows) in severely degenerated areas of the putamen.

Among the main experimental indications of  $\alpha$ S involvement in PD we can include:

- Genetic traits:  $\alpha$ S point mutants A53T, A30P, E46K, H50Q and G51D have been linked to rare familial cases of Parkinson's Disease as well as duplications and triplications of the SNCA gene, encoding this protein (41).
- $\alpha$ S specific antibodies detect this protein in Lewy bodies and Lewy neuritis, which are distinctive lesions in the brain of PD patients (42).
- Overexpression of WT  $\alpha$ S or pathological mutants of the protein in transgenic mice or flies induces motor deficits and neuronal inclusions reminiscent of PD (32, 43).
- Locomotor defects were also found in *Caenorhabditis elegans* worms overexpressing WT or pathological mutants of  $\alpha$ S (44).
- Characteristic elements of PD were found in *Saccharomyces cerevisiae* overexpressing human  $\alpha$ S (45).

### 1.2.2 $\alpha$ S aggregation into amyloids.

The protein content of Lewy bodies is primarily composed of fibrils of  $\alpha$ S (Figure 1.2) (1, 8, 26, 34, 35, 40, 46-50). This has led to the hypothesis that the molecular mechanisms at the origin of PD are associated with the fibrilisation of  $\alpha$ S into amyloids. As a result, the amyloid formation by  $\alpha$ S has attracted a large interest from the scientific community (Figure 1.3). Recently, Eisenberg and coworkers have crystallised and solved the structure of some motifs of  $\alpha$ S in amyloid assembly (35) (Figure 1.3 b). These add to previous determinations of the atomic structure of cross- $\beta$  spines in  $\alpha$ S by X-ray crystallography (51) and by X-ray diffraction from both recombinant  $\alpha$ S fibrils or fibrils extracted from brain samples (52). Overall, a general consensus is forming that the fibrils of  $\alpha$ S are composed of several protofilaments based on the cross- $\beta$  structure. That is a pair of  $\beta$ -sheets facing each other with the side chains interdigitated to form a dry surface and the strands running orthogonal to the fibril axis. This steric zipper motif was identified for a large number of amyloids from different types of protein precursors (e.g. tau, the PrP, insulin, IAPP, lysozyme, and  $\beta$ 2-microglobulin (53)). Another key recent contribution in the study of the structural properties of toxic  $\alpha$ S fibrils was made by the Rienstra group

(54) showing a new type of structural topology running from residues 25 to 98 (Figure 1.3 c).

Studies from cryo-electron microscopy, atomic force microscopy, and solid state NMR and solution NMR also agree that  $\alpha$ S fibrils are characterised by distinctive levels of structural polymorphism, based on variations in the regions forming the steric zipper, packing of protofilaments, sidechains exposure and also the arrangement of the flanking disordered regions that decorate the spine of the fibrils (55). Indeed the properties of  $\alpha$ S fibrils can vary dramatically as a function of the production conditions, including buffer, pH temperature ionic strength, agitation, incubation time etc. Cryo-EM and ssNMR revealed that the morphology of  $\alpha$ S fibrils (including recombinant  $\alpha$ S<sub>30-110</sub> and fibrils and filaments extracted from PD patients) can be either straight or twisted fibrils (56, 57).

In the context of the aggregation mechanism of  $\alpha$ S, it is now clear that its fibrilisation is dominated by both primary and secondary nucleation. pH has been shown to be a determining factor in distinguishing between these two major mechanisms (58). In general  $\alpha$ S aggregation can follow multiple pathways, which are accordingly associated with different polymorphic aggregated forms as well as amorphous or fibrillar aggregates, that depend by environmental and intrinsic factors, such as pH, mutations, external factors (chaperones, antibodies) (59). A key element in the aggregation of  $\alpha$ S is the presence of surfaces (including lipid membranes and water-air surface), which is reviewed in section 1.4.

Another important element to consider in the aggregation of  $\alpha$ S is that the fibrillar states are currently considered the least harmful species and that the early oligomers, which are diffusible and highly interaction-prone, are generally acknowledged to be the most pernicious species in the ethiology of PD and in general in the mechanism of  $\alpha$ S toxicity (60), which is reviewed in detail in Chapter 5 of the present thesis.

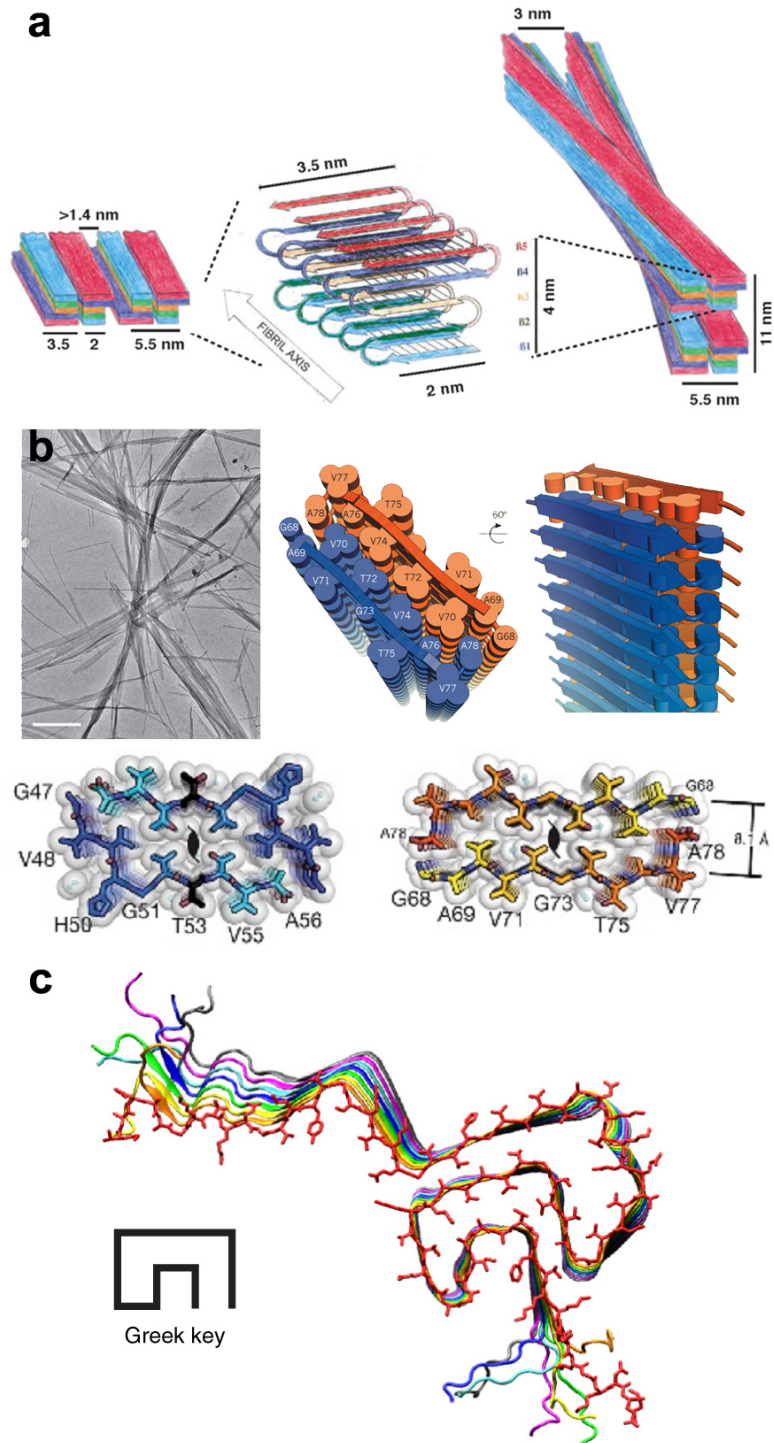


**Figure 1.3. Characterisations of the amyloid fibrillar state of  $\alpha$ S.** **a)** Solid state NMR investigation by Riek and co-workers of fibrils of  $\alpha$ S<sub>30-100</sub> showing that the core of these fibrils is rich in  $\beta$ -sheet structure with strand 1 (S1) interacting with S2, S2 with S3, S3 with S4 and S4 with S5. Figure adapted from (56). **b)** Recent crystallographic high-resolution structures of regions of  $\alpha$ S in its fibrillar state by Eisenberg and co-workers. Figures adapted from (61) and (35). **c)** Recent ssNMR high-resolution structure of  $\alpha$ S fibrils by Rienstra and co-workers. Figure adapted from (54).

### ***1.3 The physiological role of $\alpha$ S***

The large abundance of  $\alpha$ S in presynaptic terminals has strongly suggested that this protein can interplay with the biochemical mechanisms of neuronal function. Indeed  $\alpha$ S is found in both soluble and membrane-associated fractions of the brain, by composing ~1% of the total protein content in the soluble cytosolic fractions if in the brain (62). While the nuclear localisation of  $\alpha$ S is currently a matter of debate, its presynaptic localisation is well established. It is worth mentioning that, despite the general believe,  $\alpha$ S expression levels are not equal in all synaptic terminals, and its accumulation in neurodegenerative disorders is selective of some neuronal types (63), which explains the selective vulnerability of specific neuronal populations in PD. Moreover,  $\alpha$ S is not exclusive to nervous cells, as it has been shown to be highly abundant also in other cell types, primarily in red blood cells (64).

Despite the functional role of  $\alpha$ S is still obscure, including the interplay with the other two synuclein proteins ( $\beta$ -, and  $\gamma$ -), currently the scientific community seems converging toward a restricted number of possible function(s). These include the interplay with the homeostasis of synaptic vesicles (SV) release and trafficking, fatty acid binding and transport, the protection of dopaminergic neurons from oxidative stress and apoptosis (63). In the context of synaptic vesicle trafficking,  $\alpha$ S is believed to assist the formation of the SNARE complex, which is the machinery favouring the fusion of the SV with the synaptic membrane. It has been reported that  $\alpha$ S directly interacts with synaptobrevin-2 at the surface of SV via its C-terminal region (65). Interestingly,  $\alpha$ S has been shown to rescue the formation of SNARES in knockout mice of the CSP $\alpha$  chaperone (66). Similarly triple knockout mice of the three synucleins show a reduced SNARE formation with consequent neurophatological phenotypes (67). This role of  $\alpha$ S may become particularly important under stressful conditions and play a role for the long term functioning of neurons.

Another crucial role that has recently emerged for  $\alpha$ S involves the regulation of the kinetics of SV exocytosis (Figure 1.4) (40). Several data indicate that  $\alpha$ S has a key role in the regulation and/or maintenance of a distal pool of clustered SV that effectively regulates the availability of SV to be docked during neurotransmitter release (40). Indeed, mice lacking  $\alpha$ S show an inappropriate release of neurotransmitters upon stimulation, which evidences that the mechanisms that limit the number of vesicles to be fused at the

stimulus is somehow defective (68). These defects have been shown to correlate with the reduction of the distal reserve pool of SV at the axon terminals (69). In addition to knock out experiments, investigations have shown that the alteration of  $\alpha$ S expression levels or of its biophysical properties (i.e. by point mutations or oligomerisation) can interfere with the optimal trafficking of SV. Indeed, it was shown that hippocampal neurons exhibit deficits in the release of neurotransmitters when  $\alpha$ S is mildly overexpressed, which result in the increase of the distal reserve pool and consequent reduction in the number of docked SV (70).

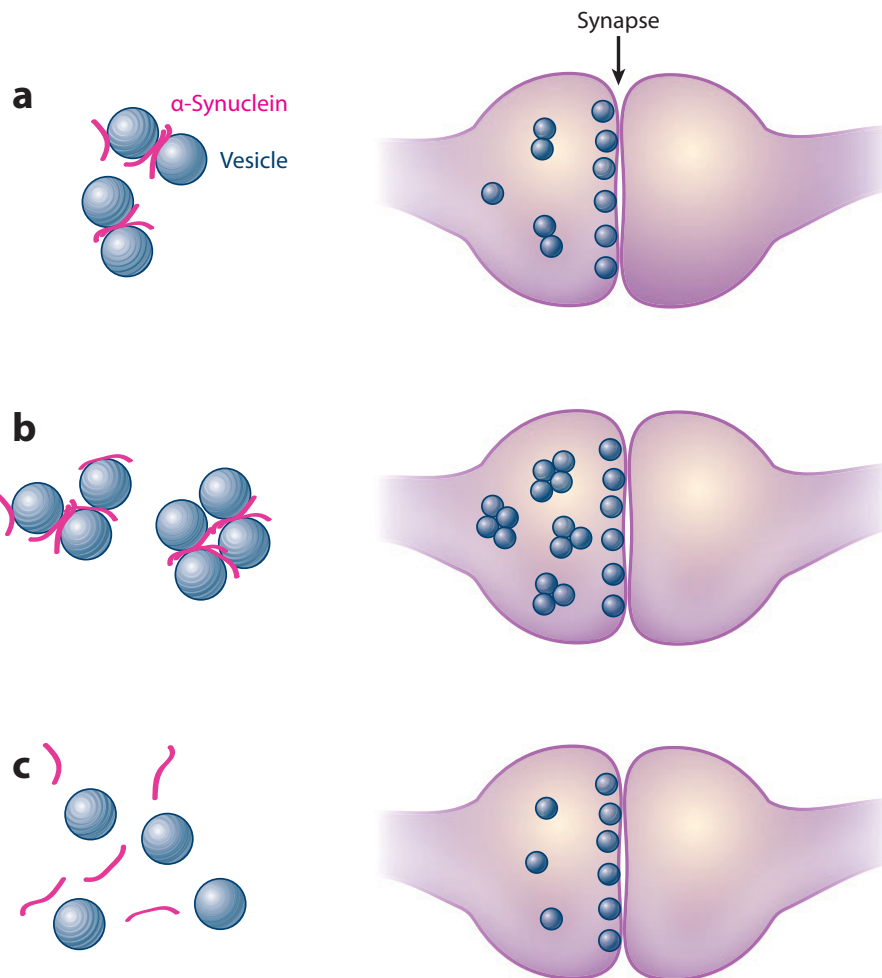


**Figure 1.4. Role of  $\alpha$ S in the regulation of the kinetics of synaptic vesicles exocytosis at the axon termini.** Image adapted from (40). **a)**  $\alpha$ S has been shown to participate in the formation and maintenance of a pool of synaptic vesicles distal to the synaptic membrane, which effectively regulates the amount of free vesicle to be docked by the SNARE complex during neurotransmitter release. **b, c)** Under conditions altering the properties of  $\alpha$ S, the vesicle clustering can be enhanced (b) or severely affected (c) and consequently alter the kinetics of exocytosis by changing the availability of vesicles at the termini of the axon during neurotransmitter release.

The interplay between  $\alpha$ S and vesicle trafficking is not only relevant in the processes of neurotransmitters release. In the ER-to-Golgi trafficking, for example, an overexpression of  $\alpha$ S in yeast has been shown to cause accumulation of vesicles that prevent their fusion with the Golgi membrane while keeping unaffected the bud from the ER (71). This disruption is contrasted somehow by control mechanisms in yeast such as proteins that can be employed to rescue of the vesicle accumulation induced by  $\alpha$ S. Among the strongest players in this context is the Rab GTPase Ypt1 (Rab1), which in yeast completely restores the ER-to-Golgi trafficking when intermediate levels of  $\alpha$ S play toxic effects in this process. Rab1 also restores  $\alpha$ S localisation at the plasma membrane.

Finally, many evidences have indicated that the fine tuning between  $\alpha$ S expression levels and vesicle trafficking is general to many other organisms, including worms, flies and mammals. Indeed in neuronal cultures of rat midbrain,  $\alpha$ S overexpression generated dopaminergic toxicity using a similar mechanism as in yeast, which eventually was reduced by human Rab1 overexpression (71). Thus, overexpression of  $\alpha$ S may result in toxicity arising from a gain of function.

Collectively, these results from yeast to *Homo sapiens* consistently evidence that  $\alpha$ S is key to maintain the optimal pool of synaptic vesicles and therefore regulate the SV ready for the release at the synapses.

#### ***1.4 Membrane interaction of $\alpha$ S in functional and pathological contexts***

While the exact function of  $\alpha$ S and its role in PD are still debated, it is now generally acknowledged that this protein adopt a biologically active form when interacting directly with lipids and membranes under both physiological and pathological contexts. Indeed in the synaptic termini  $\alpha$ S is partitioned between cytosolic and membrane-associated forms in an apparently strictly regulated fashion (72). Indeed this binding is probably the only common ground within all the proposed functions of  $\alpha$ S (see section 1.3) and has been shown to play a major role also in mechanisms triggering  $\alpha$ S aggregation, ultimately leading to the formation of Lewy bodies in PD (2, 4, 59, 73-76).

Indeed the sequence of  $\alpha$ S (Figure 1.1 a) can be divided in three regions, with the N-terminal 60 residues containing four imperfect repeats, each of 11 amino acid, that code for amphipathic  $\alpha$ -helices that elicit the membrane binding properties. These repeats share the motif KTKEGV. The second region, spanning residues 61 to 95, contains additional three KTKEGV repeats and hosts the non amyloid-b component (NAC), which is an hydrophobic amyloidogenic segment of the protein. Finally, the third region, spanning residue 96 to 140 is highly charged and enriched in acidic residues and prolines and has been shown to only transiently interacting with the membrane surface (see Chapter III).

Under functional conditions  $\alpha$ S can bind a variety of membranes (Figure 1.5).  $\alpha$ S has been reported to localise at the nucleus where the binding to the nuclear membrane enables this protein to interact with histones and DNA (77, 78). In other cellular compartments, a significant body of evidences have indicated that  $\alpha$ S may interact with mitochondrial membrane and have possibly two functions; the first being involved in reducing the oxidation stress by being converted in an oxidised form at it N-terminus (Met 1 and Met 5). Secondly,  $\alpha$ S has been shown to disfavour the fusion of mitochondria and favour their fission (79), a function that is also connected to cardiolipin concentration in the mitochondrial membrane. These membrane-associated functions add to those, previously reviewed, involving SV clustering and SNARE chaperoning.

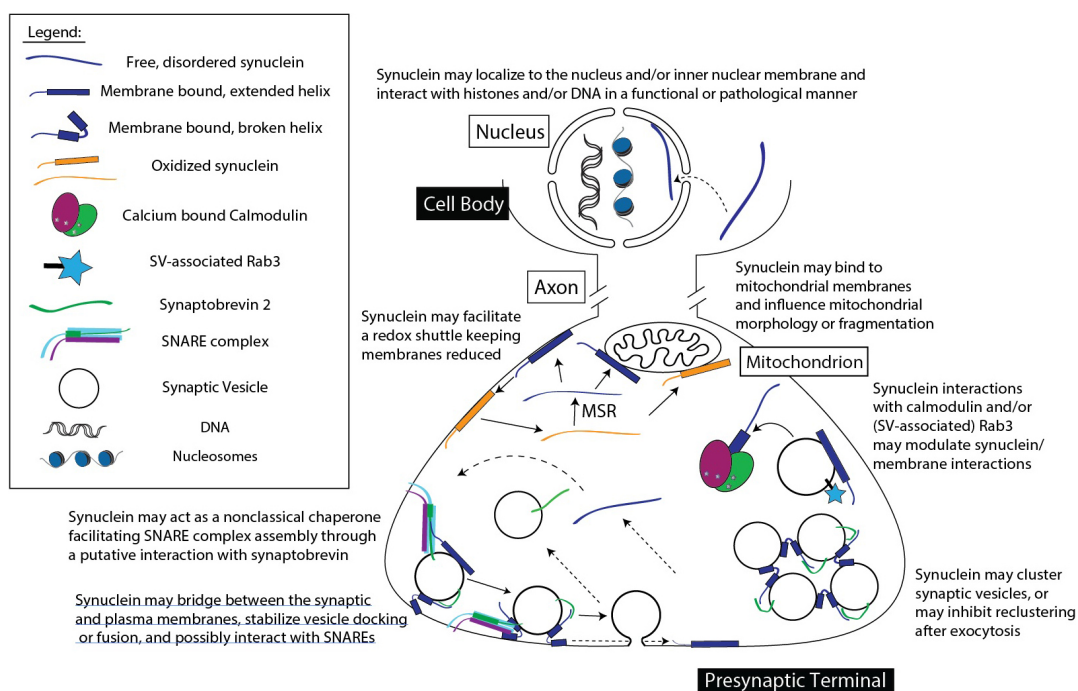


**Figure 1.5. Membrane interaction of  $\alpha$ S under physiological cellular conditions.** Figure adapted from (80). Cellular membranes are key for the targets and interactions that are potentially associated with the normal function of  $\alpha$ S.

Under pathological conditions, the interplay between  $\alpha$ S and membranes assumes a central role, as lipid bilayers have been shown to accelerate the fibrilisation of this protein of several orders of magnitude (81). It is worth stressing that the pathological conditions associated with  $\alpha$ S may not necessary be associated with aggregation. Indeed the mutation A30P can elicit toxicity in a loss-of-function manner, e.g. by impairing the optimal vesicle clustering by this protein (Figure 1.4). Similarly, in a non-aggregated state, but possibly with a milder increase of the expression levels,  $\alpha$ S has been shown to influence the mitochondrial morphology (Figure 1.6), inhibit the lysosomal glucocerebrosidase. As an aggregated state, oligomerisation of  $\alpha$ S can alter significantly the interaction with the membrane and generate toxic effects. The primary characteristic of toxic oligomers, in contrast to non-toxic aggregates, is indeed the ability to permeate and disrupt biological membranes. Experimental evidences have suggested that this process includes both the cellular and mitochondrial membranes. In this thesis, we focus specifically on this key step for the toxicity of  $\alpha$ S in Chapter V.

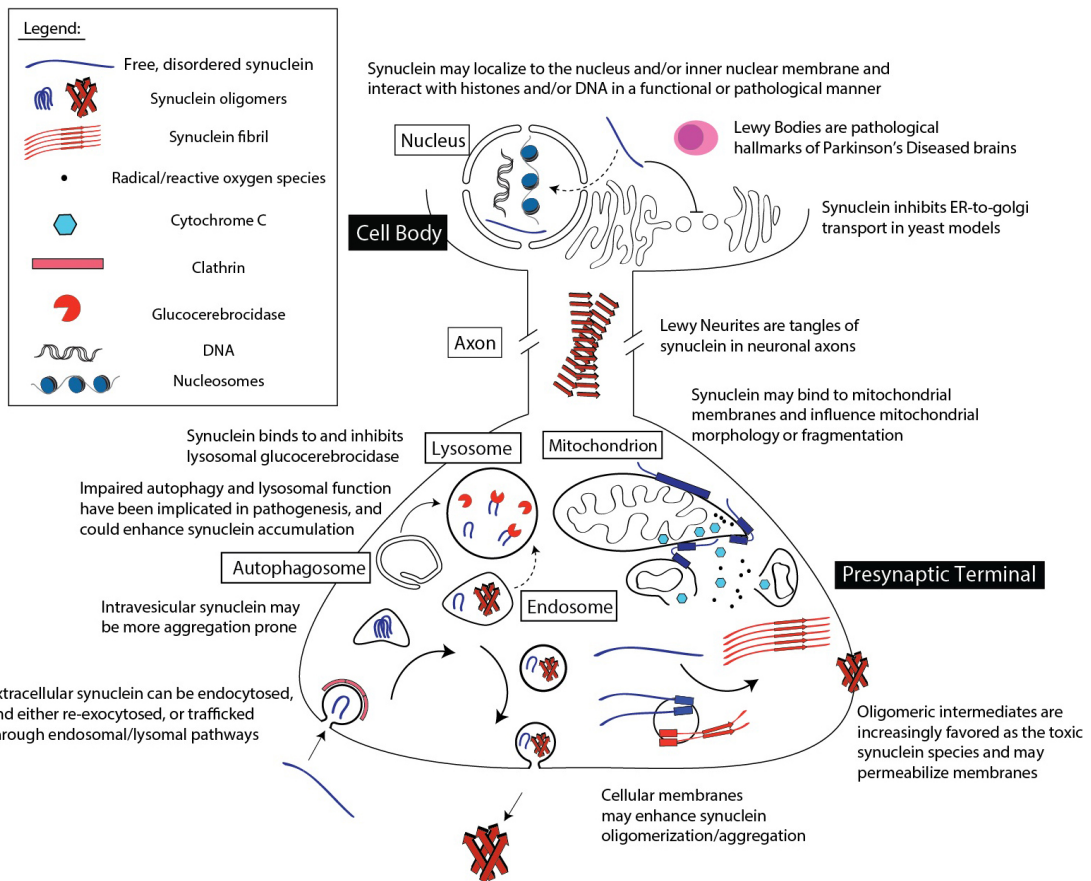


**Figure 1.6. Membrane interaction of  $\alpha S$  under pathological cellular conditions.** Figure adapted from (80). Cellular membranes are crucial in the processes that are potentially associated with the pathological role of  $\alpha S$ .

### ***1.5 Overview of the PhD research***

My PhD studies revolved around the characterisation of the molecular basis of the  $\alpha$ S binding to biological membranes. This process is central to determine the biological behaviour of  $\alpha$ S under both physiological and pathological conditions. Yet, the structural bases of this interaction are extremely difficult to characterise due to the intrinsic level of disorder of  $\alpha$ S, primarily in its unbound state but also when bound to membranes. The inspiration to focus on this key interaction came from the fact that previous studies show a number of biases that affect our understanding of the transient and dynamical binding of  $\alpha$ S to biological membranes. Indeed, it is not possible to approach this bound state using X-ray crystallography, as it is difficult to crystallise  $\alpha$ S bound to a lipid bilayer and also because of its dynamical nature, preventing any sensible electron density to be refined even in the presence of diffracting crystals. The small size and the conformational heterogeneity of membrane-bound  $\alpha$ S, on the other hand, prevent the application of a rapidly growing and powerful technique of structural biology, namely cryo-EM.

As a result of these factors, the primary experimental structural information on the membrane-bound state of  $\alpha$ S, available prior to my PhD, were obtained via solution NMR and EPR. In the first case, a significant bias was however associated with the employment of detergent micelles rather than lipid bilayers. Resonances from proteins bound to lipid bilayers, indeed, cannot be directly detected in solution NMR owing to the slow tumbling rate of these systems, resulting in extreme peak broadening. To overcome these problems, NMR investigations of  $\alpha$ S have been performed in the presence detergent micelles, which are small enough to enable the full recovery of the NMR signals of the bound state. The properties of detergent micelles are, however, significantly different from those of lipid bilayers, including a stronger curvature, which is a parameter that affects dramatically the binding affinity of  $\alpha$ S, and increased hydrophobicity, as they have more surface defects that result in the exposure of hydrophobic patches. As a result, the current micelle-bound structures of  $\alpha$ S are questionable models of the membrane-bound state of  $\alpha$ S. Indeed, in some cases it is appears evident from the shape of the structural models that  $\alpha$ S had “wrapped” around the micelle, which clearly is a non-physiological state. Moreover, by perturbing significantly the binding affinity, the micelle-bound structures fail to provide insights into the balance between structural order and disorder

in the bound state of  $\alpha$ S, which is the key to understand the biological activity of this protein at the surface of lipid membranes.

In the case of EPR, the protein is typically modified in its sequence (by mutating residues from the natural sequence into cysteine) and in its chemical nature (by using chemical ligation with hydrophobic probes). These procedures are also likely to significantly bias the conformational properties of the membrane-bound state of  $\alpha$ S.

As a result of the lack of a proper structural characterisation of the membrane-bound  $\alpha$ S, my PhD thesis has focused on the identification of an approach that could provide a non-invasive observation of the structural, dynamical and topological properties of  $\alpha$ S at the surface of synaptic-like vesicles. The research optimised a combination of solid-state NMR (i.e. to probe directly the NMR resonances of the bound state of  $\alpha$ S) and chemical exchange saturation transfer at the solution NMR (i.e. to accurately probe the nature of the fine-tuning between order and disorder at a residue-specific level in the bound state of  $\alpha$ S) as the optimal approach to characterise this crucial interaction under physiologically relevant conditions. This approach identified the key events in the binding to lipid vesicles that mimic synaptic vesicles for composition, charge and shape, and described structure, dynamics, topology and membrane-affinity along the  $\alpha$ S sequence in its bound state (Chapter III).

After successfully probing the interaction with synaptic-like vesicles, we focussed on two fundamental aspects of the biological activity of  $\alpha$ S under physiological and pathological condition. Firstly, our study evidenced a molecular mechanism by which  $\alpha$ S can induce the interaction between SV and therefore interplay with their homeostasis during neurotransmitter release (Chapter IV). Subsequently the mechanisms leading to  $\alpha$ S toxicity *in vivo* were studied by characterising the molecular basis of the toxicity of  $\alpha$ S oligomers in the context of their selective interaction with lipid membranes (Chapter V) and also in probing the effects of pathological mutations of  $\alpha$ S, associated with early onset PD, in its binding with synaptic vesicles (Chapter IV).

As a result, the major achievement of my PhD has been to develop and apply a multidisciplinary biophysical approach, revolving around solution and solid-state NMR but extending to a number of other biophysical techniques (FRET, FCS, FT-IR, AUC, Cryo-EM, CD, STED imaging), to elucidate in detail the order-disorder balance along the membrane

interaction of  $\alpha$ S and to apply this approach to understand the physiological and pathological relevance of this important biological molecule.

# Chapter II

## *Materials and Methods*

The present PhD investigation has been performed primarily by using recombinant  $\alpha$ -synuclein ( $\alpha$ S) in NMR experiments that could probe the interaction with lipid membranes. The experiments performed mainly exploit solution and solid-state nuclear magnetic resonance (NMR) for which this chapter will describe the essential elements. NMR is a spectroscopy that allows performing a large number of experiments and that can be used under very different experimental conditions (solution-state, solid-state, low- or high-temperature, proton-detected, carbon-detected etc.). As a result, the present chapter will focus on those essential elements for the primary techniques that I have extensively employed during my PhD work. Additional elements of biomolecular NMR are referred to external sources. As for other biophysical techniques employed in this PhD work (FRET, FCS, FT-IR, AUC, Cryo-EM, CD, STED imaging) brief introductions are made in the relevant chapters, however, for space limitations these are limited to materials and methods and brief descriptions of these methods.

### ***2.1 Purification of recombinant $\alpha$ S.***

Recombinant  $\alpha$ S for NMR experiments was purified in *E. coli* using plasmid pT7-7 encoding for the protein using an established protocol in the Dobson lab (82). Briefly, after transforming in BL21 (DE3)-gold (Agilent Technologies, Santa Clara, CA) cells, uniformly  $^{15}\text{N}$  and  $^{13}\text{C}$  labeled  $\alpha$ S was obtained by growing the bacteria in isotope-enriched M9 minimal media containing 1g/L of  $^{15}\text{N}$ - $\text{NH}_4\text{Cl}$  and 2g/L of  $^{13}\text{C}$ -glucose (Sigma-Aldrich, St Louis, USA). The cells were grown at 37 °C under constant shaking at 250 rpm in LB medium, supplemented with 100  $\mu\text{g}/\text{ml}$  ampicillin, to an OD600 of 0.6. Subsequently the expression of the protein was induced with 1mM IPTG at 37 °C for 4 h, and the cells were harvested by centrifugation at 6,200 g (Beckman Coulter, Brea, USA). The cell pellet was resuspended in lysis buffer (10mM Tris-HCl pH 8, 1mM EDTA and EDTA-free complete protease inhibitor cocktail tablets - Roche, Basel, Switzerland) and lysed by sonication. The cell lysate was centrifuged at 22,000 g for 30 min to remove cell debris. The

supernatant was then heated for 20 min at 70°C and centrifuged at 22,000 g in order to precipitate heat-sensitive proteins. Subsequently streptomycin sulfate was added to the supernatant to a final concentration of 10 mg/ml to stimulate DNA precipitation. The mixture was stirred for 15 min at 4°C followed by centrifugation at 22,000 g. Then, ammonium sulfate was added to the supernatant to a concentration of 360 mg/ml in order to precipitate the protein. The solution was stirred for 30 min at 4°C and centrifuged again at 22,000 g. The resulting pellet was resuspended in 25 mM Tris-HCl, pH 7.7 and dialyzed against the same buffer in order to remove salts. Dialyzed solutions were loaded onto an anion exchange column 26/10 Q sepharose high performance (GE Healthcare, Little Chalfont UK) and eluted with a 0–1 M NaCl step gradient, and then further purified by loading onto a size exclusion Column Hiload 26/60 Superdex 75 preparation grade (GE Healthcare, Little Chalfont UK). All the fractions containing the monomeric protein were pooled together and concentrated by using Vivaspin filter devices (Sartorius Stedim Biotech Gottingen, Germany). The purity of the aliquots after each step was analyzed by SDS-PAGE and the protein concentration was determined from the absorbance at 275 nm using an extinction coefficient of 5600 M<sup>-1</sup> cm<sup>-1</sup>.

## **2.2 Solution NMR of $\alpha$ S.**

In its cytosolic form,  $\alpha$ S is predominately monomeric and disordered. Intrinsically disordered proteins (IDPs) have gained only recently the interest of the biochemical community, as it is now clear that protein states that are entirely or partially disordered in their native conformations are relatively abundant in all organisms. It is indeed estimated that circa the 30% of the eukaryotic proteins possess a complete or significant level of structural disorder (83). These proteins have a distinctive functional repertoire from that of natively folded proteins and exert their biological role mainly through interactions. IDPs often assume a role of hubs in the protein-protein interaction network of an organism by showing the ability to select different partners in different biochemical contexts. As a result of this interaction promiscuity the most relevant information that structural biology can possibly obtain on these proteins revolves around their ability to select and bind the interaction partners (84). In this view, NMR is possibly the most relevant analytical technique. Firstly, solution NMR can probe IDPs by obtaining information at an atomic resolution. Secondly, solution NMR is ideal for high-throughput

experiments in discerning the interactions of IDPs. Finally, the significant dynamics of IDPs resolve the size limitations due to slow tumbling of folded proteins (setting an ideal limit between high-resolution and low-resolution NMR to  $\sim 40$ kDa). While the crowding of the peaks in the spectra remains a technical problem, which however could be resolved with multidimensional NMR or selective labelling, the size limitation is virtually removed in IDPs.

When studying IDPs, and the cytosolic and monomeric state of  $\alpha$ S, it is important to note that the NMR strategy must be different from that employed in the study of natively folded proteins. The traditional distance (from NOEs) + dihedral angle (from TALOS (85) or  $^3$ Jcouplings) approach cannot be effective by definition in the study of IDPs. Indeed these proteins are not associated with long-range NOEs, which are the important restraints in driving the conformational refinement in biomolecular NMR, and their accessibility to the Ramachandran space reflects the allowed space, which makes not useful the employment of fixed dihedral angles. As a result the optimal approach to study IDPs, and  $\alpha$ S, by solution NMR is to extract useful information from chemical shifts (CS) (86) and residual dipolar couplings (RDCs) (87, 88). Firstly these two NMR observables are fully accessible in the study of IDPs. Secondly, while being significantly averaged by the number of conformations composing the IDPs, CS and RDCs are able to provide information on the local propensity to secondary structure (89) as well as to long-range interactions within the sequence of the protein (84).

Additional NMR experiments that have been commonly employed in the study of IDPs are paramagnetic relaxation enhancement (PRE) (90), which however can significantly perturb the conformational space of IDPs due to mutations and the chemical ligation with hydrophobic probes, diffusion measurements, chemical shift saturation transfer (91) (CEST, see below) and the use of Jcouplings to access a highly detailed characterisation of the local conformational preferences in the residues composing the IDPs. In the present PhD work, we have studied the interaction between  $\alpha$ S and lipid membranes primarily by accessing the information provided by CS and CEST. This chapter, therefore, focuses primarily on the general introduction of these two measurements and defer the other techniques to reviews (92, 93) and textbooks (94).

### 2.2.1 the $^1\text{H}$ - $^{15}\text{N}$ -HSQC experiment.

In biomolecular NMR, the reference experiment is typically the proton-nitrogen heteronuclear single quantum coherence ( $^1\text{H}$ - $^{15}\text{N}$ -HSQC). This spectrum connects resonances of amide  $^1\text{H}$  with amide  $^{15}\text{N}$ , therefore identifying the backbone amides of 19 out of 20 of the natural residues (excluding proline) and groups from 4 side chains (Arg, Lys, Gln and Asn). Most of the 3D experiments as well as relaxation, H/D exchange, RDC and others, are based or analysed primarily through the  $^1\text{H}$ - $^{15}\text{N}$ -HSQC “fingerprint” of the protein spectrum.

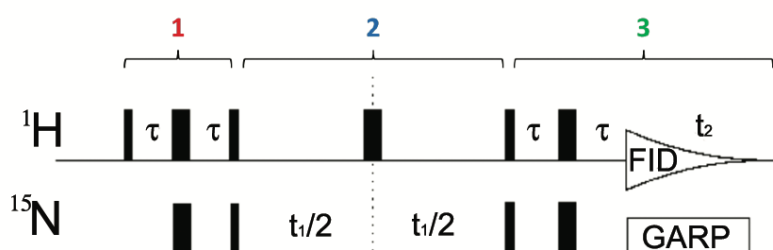


**Figure 2.1. Basic scheme for the pulse sequence of the  $^1\text{H}$ - $^{15}\text{N}$ -HSQC.** In its simplest version, an  $^1\text{H}$ - $^{15}\text{N}$ -HSQC pulse sequence is composed of three main phases. In the first phase, the magnetisation is induced on the  $^1\text{H}$  by means of a 90-degree pulse and subsequently transferred to the  $^{15}\text{N}$  via the INEPT scheme. The advantage of the INEPT scheme is that a more sensitive nucleus ( $^1\text{H}$ , which has the highest gyromagnetic ratio) can be excited and its coherence can be transferred efficiently to the less NMR-sensitive nucleus ( $^{15}\text{N}$ ). The INEPT is composed of an initial 90° hard pulse on the  $^1\text{H}$  channel in the x direction followed by a period  $\tau$ , which is equal to  $1/4J_{\text{N-H}}$  where  $J_{\text{N-H}}$  is the scalar coupling between proton and nitrogen in the amide. After this evolution period, two simultaneous 180° pulses are made on both  $^1\text{H}$  and  $^{15}\text{N}$  channels, both on the x direction, followed by another period  $\tau$  to refocus the spins evolutions at the end of it (spin echo). Finally two 90° pulses are made on the  $^1\text{H}$  and  $^{15}\text{N}$  channels, y and x axes respectively by creating an antiphase magnetisation on the  $^{15}\text{N}$ . In the second part of the  $^1\text{H}$ - $^{15}\text{N}$ -HSQC the antiphase magnetisation on the  $^{15}\text{N}$  that is created by the INEPT sequence is allowed to evolve during the time  $t_1$ , which defines the indirect dimension in the 2D spectrum. During  $t_1$ , a 180° is pulsed after  $t_1/2$  to refocus the  $^1\text{H}$  spins at the end of this evolution period and prepare them for the phase three of the  $^1\text{H}$ - $^{15}\text{N}$ -HSQC, which includes a retro-INEPT and a detection of the FID (direct dimension,  $t_2$ ) while a GARP sequence decouples the  $^1\text{H}$  and  $^{15}\text{N}$  in order to avoid splitting of the NMR peaks. This pulse sequence is typically enriched with additional features, such as for instance water suppression and phase cycling.

The  $^1\text{H}$ - $^{15}\text{N}$ -HSQC experiment is measured by 90° pulsing on the  $^1\text{H}$  channel and subsequently transferring the magnetisation to the  $^{15}\text{N}$  via INEPT transfer. Subsequently the coherence is let evolving on the  $^{15}\text{N}$  channel ( $t_1$ , representing the indirect dimension)

before the magnetisation is re-transferred with a retro-INEPT to the  $^1\text{H}$ , i.e. the atom with the highest gyromagnetic ratio (hence the most sensitive nucleus in biomolecular NMR), for detection while a decoupling is applied to avoid splitting of the peaks due to the scalar coupling between  $^1\text{H}$  and  $^{15}\text{N}$  (Figure 2.1). The  $^1\text{H}$ - $^{15}\text{N}$ -HSQC measured at 283K using pH 6.0 and phosphate buffer 20mM is shown in Figure 2.2.

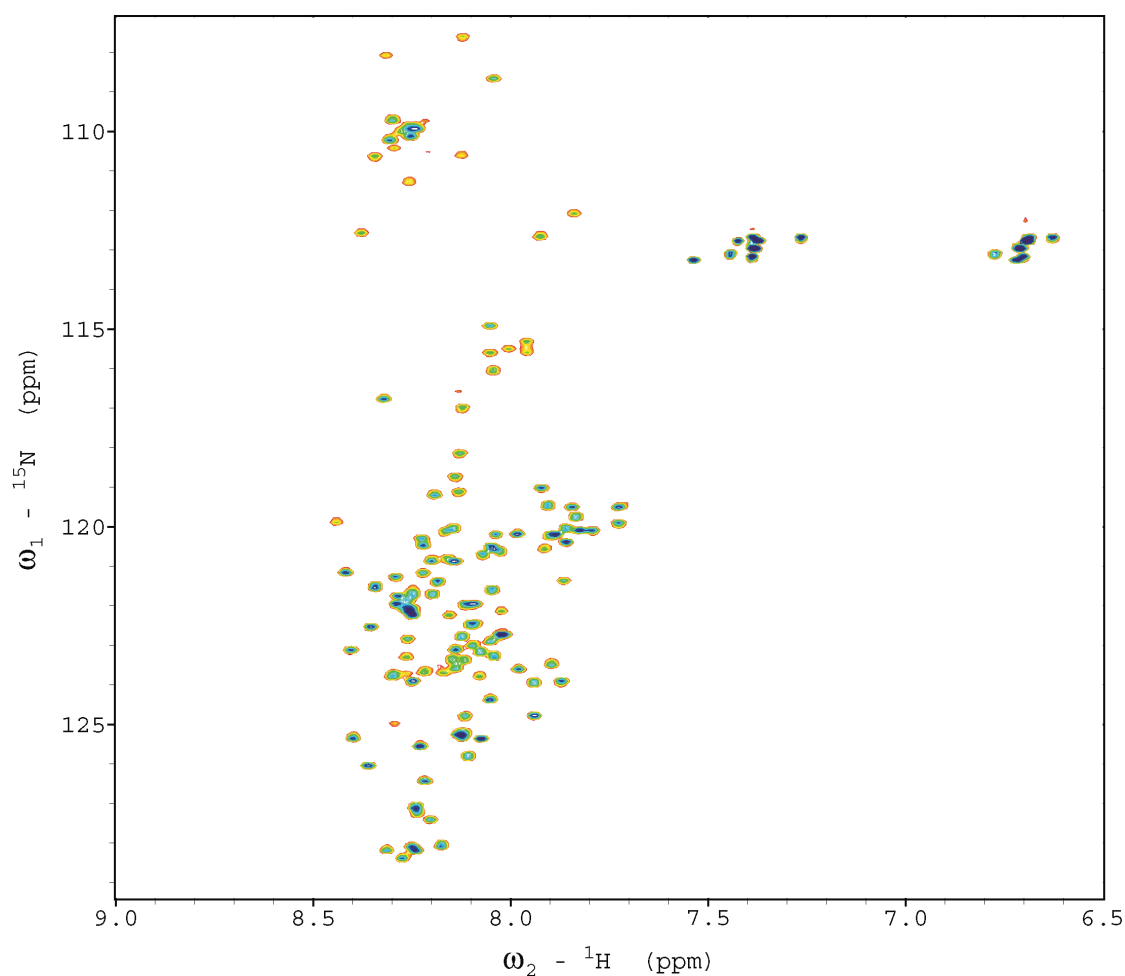


**Figure 2.2.**  $^1\text{H}$ - $^{15}\text{N}$ -HSQC of monomeric  $\alpha\text{S}$  in water solution. The spectrum was measured at a  $^1\text{H}$  frequency of 700 MHz, using an  $\alpha\text{S}$  concentration of 300  $\mu\text{M}$  in phosphate buffer 20mM at pH 6.  $^1\text{H}$ - $^{15}\text{N}$ -HSQC spectra recorded using a data matrix consisting of 2048 ( $t_2$ ,  $1\text{H}$ )  $\times$  440 ( $t_1$ ,  $^{15}\text{N}$ ) complex points. The spectrum was measured at 283K.

### 2.2.2 assignment of the protein resonances

The assignment of the backbone resonances can be approached using different combinations of NMR spectra. In protein NMR, when the isotopic enrichment of  $^{15}\text{N}$  and  $^{13}\text{C}$  atoms is feasible through the expression of the system in minimal medium complemented with  $^{15}\text{N-NH}_4\text{Cl}$  and 2g/l of  $^{13}\text{C}$ -glucose, the preferred approach is to assign the backbone resonances via a series of three-dimensional NMR spectra connecting the amide proton and nitrogen with carbon atoms in the backbone or sidechains. These atoms occupy the third dimension, which can be added by extending the 2D scheme (Figure 2.1) to a third evolution time ( $t_3$ ). As introduced above, the  $^1\text{H}$ - $^{15}\text{N}$ -HSQC is typically used as a fingerprint in all biomolecular experiments. For this reason the preferred approach to 3D NMR is to employ the  $^1\text{H}$ - $^{15}\text{N}$ -HSQC as the basic 2D spectrum and adding a third dimension, e.g. reporting the resonances of the chosen  $^{13}\text{C}$  atom, from this fingerprint. In this way, it is possible to visualise the 3D spectra as ‘strips’ along the third dimension taken from each peak in the  $^1\text{H}$ - $^{15}\text{N}$ -HSQC (Figure 2.3). Each strip will contain all  $^{13}\text{C}$  resonance(s) associated to the specific peak selected in the  $^1\text{H}$ - $^{15}\text{N}$ -HSQC.

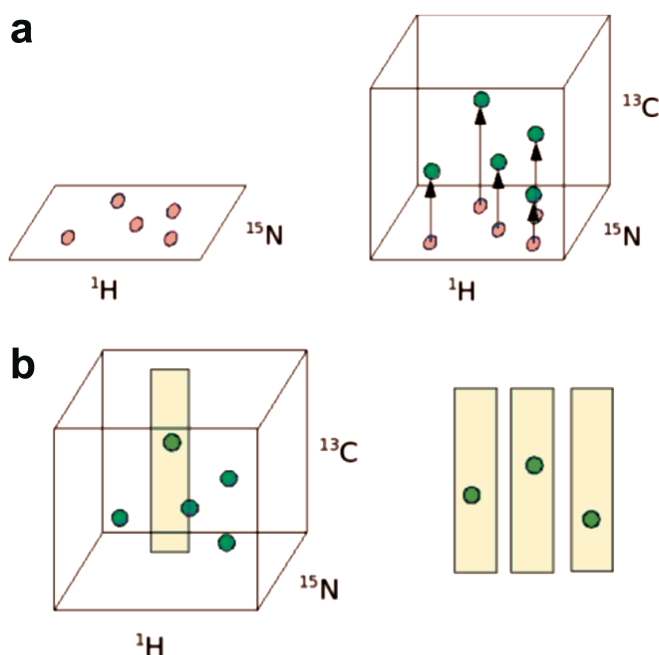


**Figure 2.3.** From  $^1\text{H}$ - $^{15}\text{N}$ -HSQC to 3D spectra to strips. **a)** The pulse sequence of the  $^1\text{H}$ - $^{15}\text{N}$ -HSQC can be extended by adding a new evolution time and allowing the magnetisation to pass from the  $^{15}\text{N}$  to a given  $^{13}\text{C}$  atom from the backbone or from the side chain of the residue “i-1” or simultaneously of residues “i-1” and “i”. **b)** From the peak  $^1\text{H}$ - $^{15}\text{N}$ -HSQC it is possible to extract a strip running on the  $^{13}\text{C}$  dimension and revealing the resonances of the third nucleus associated for a given peak in the  $^1\text{H}$ - $^{15}\text{N}$ -HSQC.

By combining strips reporting complementary  $^{13}\text{C}$  resonances of the residue “i-1”, where “i” is the residue corresponding to the given peak in the  $^1\text{H}$ - $^{15}\text{N}$ -HSQC, and those from “i-1” and “i”, it is possible to “walk” through the backbone resonances and assign the entire protein. The optimal approach is when different pairs of 3D spectra are combined. For example one of the most common pairs of complementary 3D spectra for protein assignment is composed of HNcoCACB and HNCACB, which provide strips for  $\text{C}\alpha$  and  $\text{C}\beta$  atoms of “i-1” and “i-1/i”, respectively (figure 2.4).

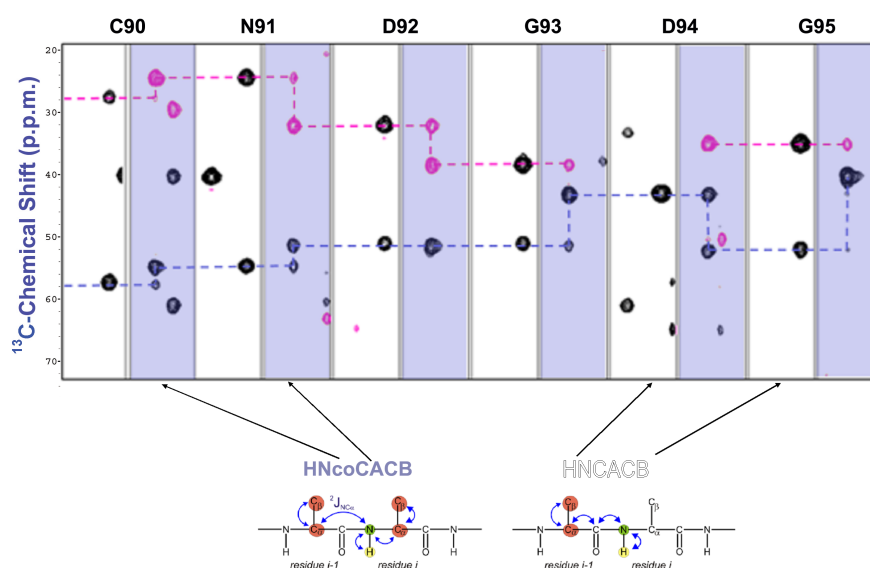


**Figure 2.4. Example of complementary strips in NMR backbone assignment.** The example of the HNcoCACB and HNCACB is reported. HNcoCACB (cyan strips) connects the resonances of the amide  $^1\text{H}$  and  $^{15}\text{N}$  spectrum of the residue “i” with the resonances of  $\text{C}\alpha$  and  $\text{C}\beta$  atoms of the residues “i-1” and “i”. This experiment has opposite phases for  $\text{C}\alpha$  and  $\text{C}\beta$  atoms. A similar experiment, but having the same phase for  $\text{C}\alpha$  and  $\text{C}\beta$  atoms, is the CBCAcoNH. HNCACB (white strips) connects the resonances of the amide  $^1\text{H}$  and  $^{15}\text{N}$  spectrum of the residue “i” with the resonances of  $\text{C}\alpha$  and  $\text{C}\beta$  atoms of the residue “i-1”. An example of backbone resonance “walk” is shown, with  $\text{C}\alpha$  atoms connected by blue dashed lines and  $\text{C}\beta$  atoms connected by pink dashed lines.

Additional pairs of 3D spectra can be used, including HNCA/HNcoCA and HNCO/HNcoCO. Once obtained the assignment of the  $^1\text{H}$ - $^{15}\text{N}$ -HSQC it is possible to complete the full assignment of all the resonances of a protein by using other 3D experiments, always based on the  $^1\text{H}$ - $^{15}\text{N}$ -HSQC. These include the HNHA spectrum, to provide the resonances of  $\text{H}\alpha$  atoms as well as the  $^3J_{\text{H}\alpha\text{HN}}$ , or TOCSY based 3D spectra to assign the resonances of the sidechains (hCcoNH-TOCSY and HcconH-TOCSY).

### 2.2.3 $^{13}\text{C}$ -detected solution NMR experiments.

The majority of solution NMR spectra are based on proton excitation and detection. For example, we have showed how in the most simple pulse sequence for a  $^1\text{H}$ - $^{15}\text{N}$ -HSQC the magnetisation is induced on the  $^1\text{H}$  via a 90-degree pulse, to be subsequently transferred to  $^{15}\text{N}$  to allow evolution to occur in  $t_1$  (the indirect dimension) and then transferred back to the  $^1\text{H}$  for detection. This is because the gyromagnetic ratio of  $^1\text{H}$  is *circa* 10 times higher than that of  $^{15}\text{N}$ . As a result, both the excitation and detections are more sensitive is made on the  $^1\text{H}$  channel. In some cases, however, it is more convenient to perform (at least) the detection on the  $^{13}\text{C}$ . Carbon-detected experiments are becoming more and more useful (95-101). The advantages of these experiments is that the  $^{13}\text{C}$  is less sensitive to the broadening of the peaks in the cases of conformational exchange in the millisecond timescale, because its gyromagnetic ratio of 4 times smaller than that of the proton. Also amides exchange chemically with the solvent, leading sometimes to the loss of signals under certain conditions of pH and temperature (especially in the case of IDPs, see example in figure 2.5). By using excitation and detection on heavy atoms that do not exchange with the solvent, for example the carbonyl and the nitrogen in the peptide bond,  $^{13}\text{C}$ -experiments are not affected by this problem. The example is clear in the case of  $\alpha\text{S}$ , where the  $^1\text{H}$ - $^{15}\text{N}$ -HSQC loses more than 70% of the peaks in going from 278K to 310K whereas  $^{13}\text{C}$ -experiments such as CON or CACO are unaffected (Figure 2.5). In the present PhD work we have used significantly the  $^{13}\text{C}$ -detected experiments as they allowed to study some protein-protein interactions at 310K leading to oligomeric species of  $\alpha\text{S}$ .

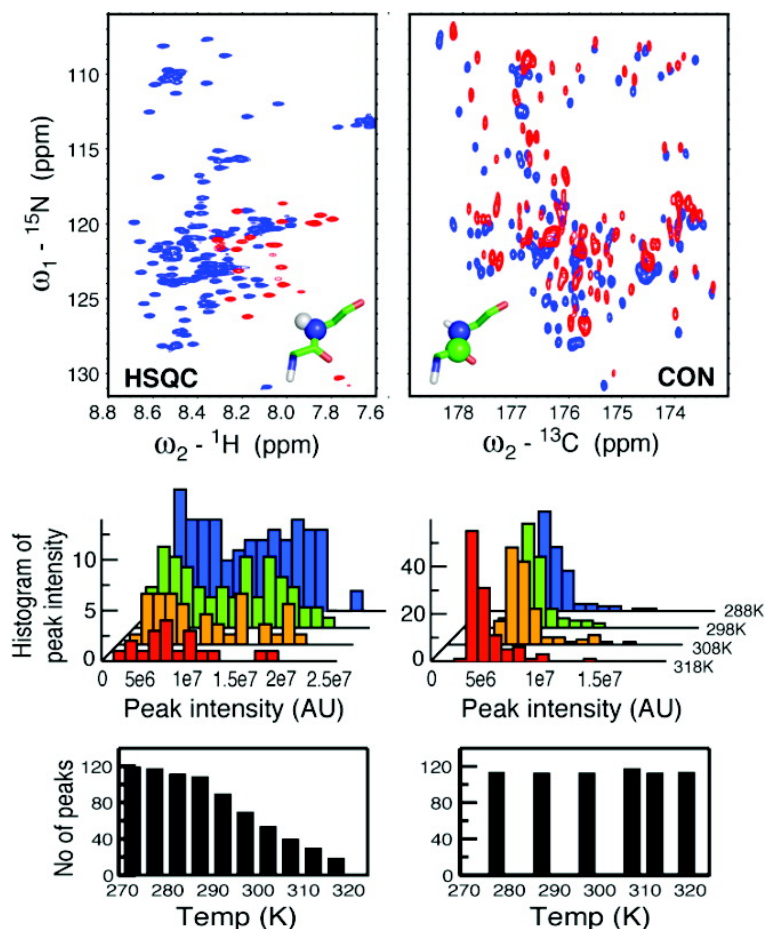


**Figure 2.5. Advantage of using  ${}^{13}\text{C}$ -detected NMR experiments in  $\alpha\text{S}$ .** Adapted from (102). The example reports a  ${}^1\text{H}$ - ${}^{15}\text{N}$ -HSQC of  $\alpha\text{S}$  at 288K (blue) and 318K (red) in comparison with a CON, a  ${}^{13}\text{C}$ -detected experiment connecting the carbonyl and the amide nitrogen in the peptide bond. At higher temperature the  ${}^1\text{H}$ - ${}^{15}\text{N}$ -HSQC loses more than 70% of the peaks due to the proton exchange with the solvent, whereas the CON maintains roughly all the peaks. Statistics of peak intensities and peak numbers at different temperatures are also reported.

#### 2.2.4 Exploitation of CS to study the conformations of IDPs

The significant advantage of biomolecular NMR in the study of IDPs, e.g. the solution state of  $\alpha\text{S}$ , is that this technique can provide experimental data for each residue of the protein without changing its sequence or chemical properties (for instance in the case of FRET). One of the most immediate results of this is the ability to study protein-protein interactions made by IDPs, including those that are transient and associated with a weak binding thermodynamic constant (84). For example, in Figure 2.6 it is reported the effect of two small molecules on the  $\alpha\text{S}$  at 283K. These small molecules, namely (-)-

EpiGalloCatechin-3-Gallate (EGCG) and miricetin (myr), establish transient interactions with  $\alpha$ S and prevent the fibrillar aggregation of this protein. It is clear from these plots that the simple measurement of CS enables an accurate understanding of the molecular details of these transient interactions. Such level of accuracy could not be achieved with any of the most resolved techniques of structural biology. Another type of information on the transient interactions of  $\alpha$ S is given by the broadening of the peaks. This information, which is again probed at a residue specific level and therefore highly resolved, has been exploited extensively in the present PhD work in the study of the interaction with the membrane and in particular using the chemical exchange saturation transfer (CEST) as introduced below.

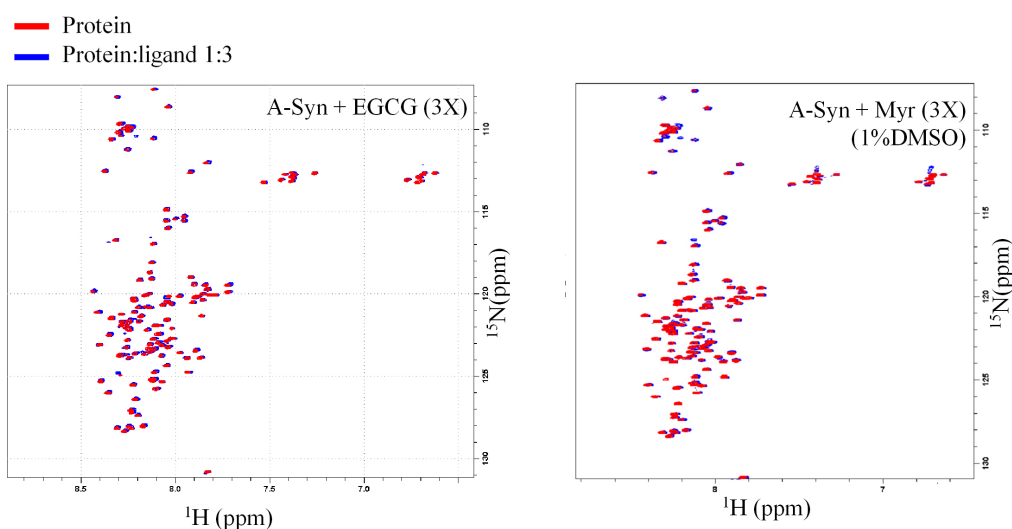


**Figure 2.6. Binding of  $\alpha$ S to small molecules.**  $^1\text{H}$ - $^{15}\text{N}$ -HSQC spectra of  $\alpha$ S isolated (red) and in the presence of 3 molar equivalents (blue) of the small molecules EGCG (left panel) and myricetin (Myr, right panel). The spectra were measured at the proton resonance of 700MHz, by using a BRUKER avance III spectrometer with cryoprobe TXI. The experiments have been recorded at 283K in 25mM Tris-HCl, 100mM NaCl buffer. The concentration of  $\alpha$ S is 300  $\mu\text{M}$ . EGCG is water soluble whereas myricetin requires at least 1% of DMSO. The effect of DMSO on the chemical shifts has been removed by double referencing.

In addition to direct probing the interactions of IDP, NMR can be used to infer on the extent of local secondary structure and even to refine structural ensembles for these heterogeneous proteins. Conventionally, NMR is employed to determine protein structures via the nuclear Overhauser effect (NOE) and dihedral angle restraints that are obtained via J couplings or via databases such as TALOS, which converts the local

information of chemical shifts into dihedral angles probability (85, 103, 104). Recently, new techniques have been introduced to employ NMR chemical shifts for protein structure determination (105, 106).

An even more effective use of NMR chemical shifts arises from the ability of these observables to probe secondary structures in proteins at an amino acid resolution. This information is derived from the analysis of the secondary chemical shifts, which represent the differences between measured chemical shifts and those corresponding to the random coil state of the same protein sequence (107). Many methods have been introduced in the past years, including the  $\delta 2D$  (89). The remarkable feature of  $\delta 2D$  is that, in addition to the accurate characterization of residue-specific populations of  $\alpha$ -helix, coil, and extended- $\beta$  structure, this statistical method provides a unique predictor of polyproline II (PPII), which has emerged as a key structural state for IDP (89). This structural element is employed in a variety of biological mechanisms and is key for molecular recognition and protein-protein interactions. The ability of retrieving accurate populations of relevant secondary structure elements *via* chemical shifts is particularly attractive, as these experimental data can be measured relatively quickly and even in cases when structural information is difficult to obtain otherwise (e.g. in the case of IDP). Another powerful approach to study the properties of biomacromolecules from chemical shifts is the “chemical shift index” (CSI) (108), which provides information on the local flexibility, in the form of order parameters  $S^2$ .

Finally, CS can be also used to refine structural ensembles. This is an emerging field and therefore has to be considered with precautions, however, in the case of folded proteins it has now reached a mature stage in which it has been shown that it is possible to characterise structural dynamics of proteins using the information contained in the sole CS. Some recent applications have also been used in the case of IDPs, as one side project to this thesis (84). These ensembles can be achieved via CS-restrained MD simulations, which in our implementation are introduced in the GROMCSA platform for molecular simulations (109). This package supports all the major force fields for MD simulations, implicit and explicit solvent as well as a variety of conformational sampling tools, including replica exchange, metadynamics and umbrella sampling. The general protocol for experimental restraints in MD simulations (eq. 2.1) is based on the definition of a

*pseudoenergy* potential term ( $V_{\Xi,j}$ ) which is added to the standard MD force field ( $V_{MM}$ ), eq. 2.2.

$$V_{TOT} = V_{MM} + \sum_j V_{\Xi,j} \quad (\text{eq. 2.1});$$

$$V_{\Xi,j} = \sum_l^{\Xi_{data}} \alpha_{\Xi,j} (\Xi_i^{\text{exp}} - \Xi_i^{\text{calc}})^2 \quad (\text{eq. 2.2});$$

where the force constant,  $\alpha_{\Xi,j}$ , weights the experimental restraint  $X_j$  over the total potential  $V_{TOT}$ . This general approach has proven effective in driving the conformational sampling towards accurate structures and populations of protein molecules (88, 110). In order to reproduce the time and ensemble averaging that is implicit in NMR measurements, several molecules (“replicas”) can be simulated simultaneously, so to restrain NMR parameters as average values over these copies.

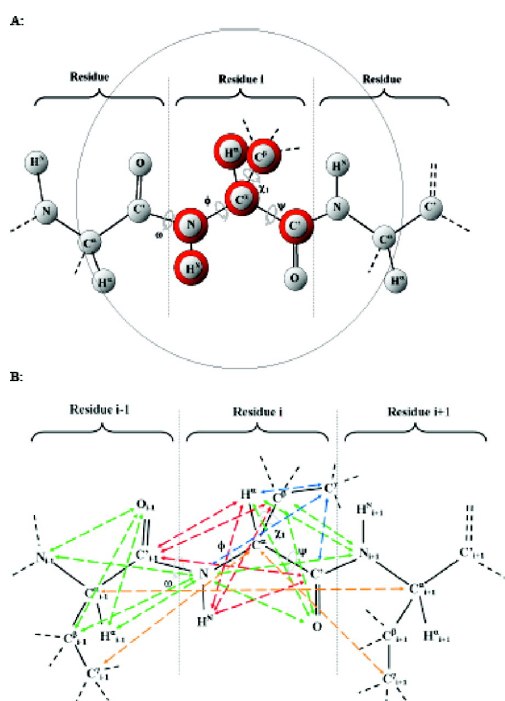


**Figure 2.7. The CamShift method.** From reference (111). **a)** Atoms for which the experimental chemical shifts are used as input data for the restrained simulations. **b)** Implementation of the CamShift as a linear combination of distances. Green, red and blue distances represent 1-4 interactions (i.e. atoms separated by three bonds). These have been divided for visual clearness into: distances involving exclusively H and C atoms (red), distances involving O and N atoms (green), distances involving sidechain atoms excluding C $\beta$  (blue). Long range distances are marked by orange dashed lines.

Chemical shift restraints can be imposed using Camshift (Figure 2.7) to calculate restraining forces in GROMCSA. Camshift models CS using a linear combination of interatomic distances (111). While it is not the most accurate predictor for CS, Camshift provides a unique opportunity to instantaneously calculate derivatives from protein coordinates, i.e. which is a direct way to calculate the forces in MD simulations to implement the restraint.

### 2.2.5 chemical exchange saturation transfer (CEST).

Despite the general believe that NMR has limitations when studying large biomolecules, its ability to characterise structure, dynamics and interactions of increasingly large biological macromolecules in solution has expanded dramatically by enabling a highly detailed mechanistic understanding of protein functions. Although the study of large macromolecules (i.e. > 70 kDa) is prevented to methods for high-resolution structural and dynamic characterisation of proteins, many opportunities are still available in the study of large systems. Among these, NMR provides a unique the ability to characterise kinetics, thermodynamics and structure within a dynamic equilibrium between a “visible” state (which is observable in standard solution NMR techniques) and an “invisible” state (for example an extremely large system). In this context, chemical shift saturation transfer (CEST) (91), denominated also dark-state exchange saturation transfer (DEST) (112), is a very powerful technique to probe at a residue specific resolution the exchange between bound and unbound states, such for example the equilibrium between monomeric and membrane-bound states of  $\alpha$ S.

More specifically, when the protein is in exchange with a bound state to a species of > MDa, the limited tumbling rate of the complex results in a significant increase in transverse relaxation with peak resonances broadening beyond detection. The significant differences in  $R_2$  between unbound (visible) and bound (invisible) states offer an opportunity to study the interaction by using  $^{15}\text{N}$ -CEST. In particular, as the bound state features extremely broad resonances, i.e. close to a powder pattern, the corresponding peaks can be saturated over a large range of radiofrequency (RF) bands, including those centred at very large offsets that are far from the range of chemical shifts of the unbound (visible) state. As a result, by applying a saturation band that has a large offset (i.e. up to 30 kHz), it is possible to selectively target and saturate the bound (invisible) state while

leaving unperturbed the unbound (visible) state. This saturation of the bound state resonances is eventually transferred to the unbound (visible) state by chemical exchange, thereby resulting in selective attenuation of the visible resonances of the unbound state. The attenuation that is transferred to the unbound state is a fine probe of the thermodynamics and kinetics of the binding process. In this thesis we have optimised the use of  $^{15}\text{N}$ -CEST spectroscopy to probe the exchange of and large lipid assemblies. As previously estimated (19) this exchange is in the timescales of 200ms, which is perfectly suitable for the timescale range of  $^{15}\text{N}$ -CEST sensitivity (i.e.  $\approx 10$  ms to  $\approx 1$  s). The advantage of  $^{15}\text{N}$ -CEST is that it covers a timewindow of interactions that is in between those covered by relaxation dispersion (sub-milliseconds) and H/D exchange experiments (seconds and beyond). The other advantage of  $^{15}\text{N}$ -CEST compared to other saturation transfer experiments, e.g. transferred NOE or STD, is that the saturation is performed on an heteronuclear channel ( $^{15}\text{N}$  in our application), thus avoiding unwanted dipolar-assisted magnetisation transfer phenomena such as spin diffusion, which occur when  $^1\text{H}$  saturation is applied.

In the study of membrane interaction of  $\alpha\text{S}$  we used  $^{15}\text{N}$ -CEST to gain a deeper understanding of the equilibrium between membrane unbound and membrane bound states. In the study of  $\alpha\text{S}$ -SUV interactions,  $^{15}\text{N}$ -CEST shows enhanced characteristics compared to standard heteronuclear correlation spectroscopy, including a significantly higher sensitivity at low lipid/protein ratios, conditions under which protein or lipid aggregation can be minimised, and a NMR signal that probes exclusively the interaction between  $\alpha\text{S}$  and the membrane surface without interference from additional factors that may influence the transverse relaxation rates of the protein resonances (91, 112, 113). In the  $^{15}\text{N}$ -CEST experiments employed here, a continuous weak radiofrequency field (either 350 Hz or 170 Hz) is applied off-resonance (up to 28 kHz) in the  $^{15}\text{N}$  channel, thereby saturating the broad spectroscopic transitions in the bound (undetectable) state but leaving the resonances of the free (detectable) state virtually unperturbed (91, 112, 113). The saturation of the bound state was then transferred to the free state *via* chemical exchange, resulting in the attenuation of the intensities of the observable resonances in the visible unbound state. By carrying out a series of experiments at various offsets, it

was possible to obtain a map of the strength of interactions between the low and high molecular weight species at a residue specific resolution.

Solution state NMR experiments were carried out at 10 °C on Bruker spectrometers operating at  $^1\text{H}$  frequencies of 700 MHz equipped with triple resonance HCN cryo-probes.  $^{15}\text{N}$ -CEST experiments were based on  $^1\text{H}$ - $^{15}\text{N}$  HSQC experiments by applying constant wave saturation in the  $^{15}\text{N}$  channel. Since we are probing the exchange between monomeric  $\alpha\text{S}$  (having sharp resonances) and  $\alpha\text{S}$  bound to SUVs (having significantly broad resonances), a series of large offsets was employed (-28, -21, -14, -9, -5, -3, -1.5, 0, 1.5, 3, 5, 9, 14, 21 and 28 kHz), resulting in  $^{15}\text{N}$ -CEST profiles of symmetrical shapes (112, 114). An additional spectrum, saturated at -100 kHz, was recorded as a reference.  $^{15}\text{N}$ -CEST experiments were performed using two continuous wave radio frequencies (170Hz and 350Hz) to saturate  $^1\text{H}$ - $^{15}\text{N}$ -HSQC spectra recorded using a data matrix consisting of 2048 ( $t_2$ ,  $^1\text{H}$ )  $\times$  220 ( $t_1$ ,  $^{15}\text{N}$ ) complex points. An example of  $^{15}\text{N}$ -CEST application is provided in figure 2.8.

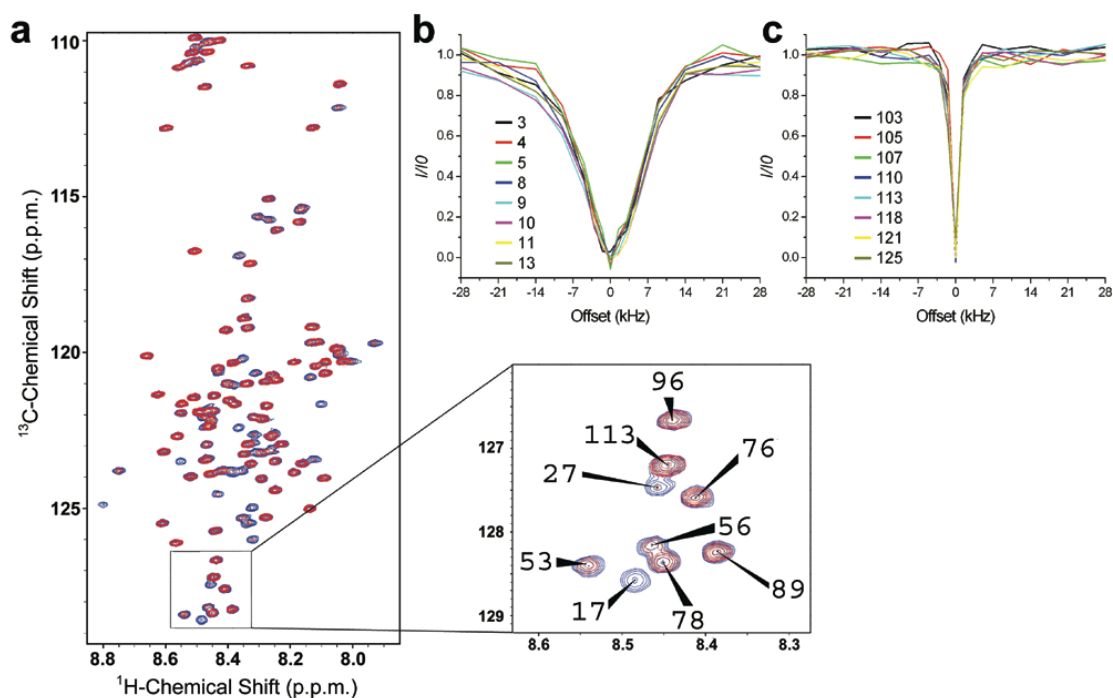


**Figure 2.8. The CEST experiment.** (a) Two representative CEST spectra based  $^1\text{H}$ - $^{15}\text{N}$ -HSQC of  $\alpha\text{S}_{\text{WT}}$ . Blue and red spectra represent CEST  $^1\text{H}$ - $^{15}\text{N}$ -HSQC measured using a 350 Hz continuous wave length at offsets of 100 kHz (reference) and 1.5 kHz, respectively. (b-c) Individual CEST profiles for residues at the N- and C-termini are shown in panels b and c, respectively.

### ***2.3 Biomolecular solid-state NMR.***

One of the key energy terms in the transitions occurring in NMR spectroscopy includes strong dipolar interactions between nuclei. In addition to these dipolar couplings (DC), chemical shift anisotropy (CSA) and quadrupolar interactions (QI) can affect the energy levels in the transitions sampled in NMR. In large molecules, such as proteins, every nucleus that is sensitive to the spectroscopic transitions sampled in NMR is surrounded by a vast number of nuclei, giving rise to many DC. CSA and QI are also strong in large molecules. Many of these anisotropic interactions follow a law that depends on  $\cos^2(\theta)$ , where  $\theta$  is the angle between the anisotropic spin interaction and the magnetic field solution NMR. As a result, in solution the fast tumbling of the molecules results in a complete averaging of these interactions. On the contrary, with the increasing size of the molecule, the tumbling becomes too slow for a complete averaging of the anisotropic interactions, which results in fast transverse relaxation and consequent broadening of the peaks. In the upper limit of molecules assuming large proportions, the tumbling is so slow to prevent any sensitivity to the NMR peaks.

In contrast to solution NMR, solid state NMR (ssNMR) enables to study molecules even when they are prevented from fast tumbling, i.e. such as in solids. Most of the techniques in ssNMR are based on the mechanical cancellation of the anisotropic interaction terms due to spinning around the magic angle (see below) (115, 116). Other approaches on the other hand are tailored to measure the anisotropic interactions, as these can be fine probes of the structure and dynamics of biomacromolecules (114).

#### ***2.3.1 Magic angle spinning***

The magic angle spinning (MAS) technique exploits the mechanical rotation of the sample at the magic angle ( $54.7^\circ$ ), which enables the cancellation of the anisotropic interactions in solid samples, most of which depending from  $\cos^2(\theta)$  (117). If the spinning is faster than the frequency corresponding to the transition of the interaction, the specific anisotropic interaction is averaged to zero. This is the case for instance of the  $^{15}\text{N}$  CSA. As this anisotropic interaction is typically lower than 100 p.p.m., in a 700 MHz spectrometer, by using MAS rates significantly larger than 7 kHz, the  $^{15}\text{N}$  CSA can be completely averaged to zero. The resulting spectra can therefore reach the limit of solution NMR. When the MAS rate is similar or lower than the frequency of the anisotropic interaction, a

series of “spinning side bands”, which are spaced at intervals that correspond to the spinning rate, do appear (Figure 2.9). The ratio of intensities between the side band families can be used to characterize the nature of the anisotropic interaction. This is becoming a very powerful method to measure DC and CSA in unaligned samples at the magic angle spinning.

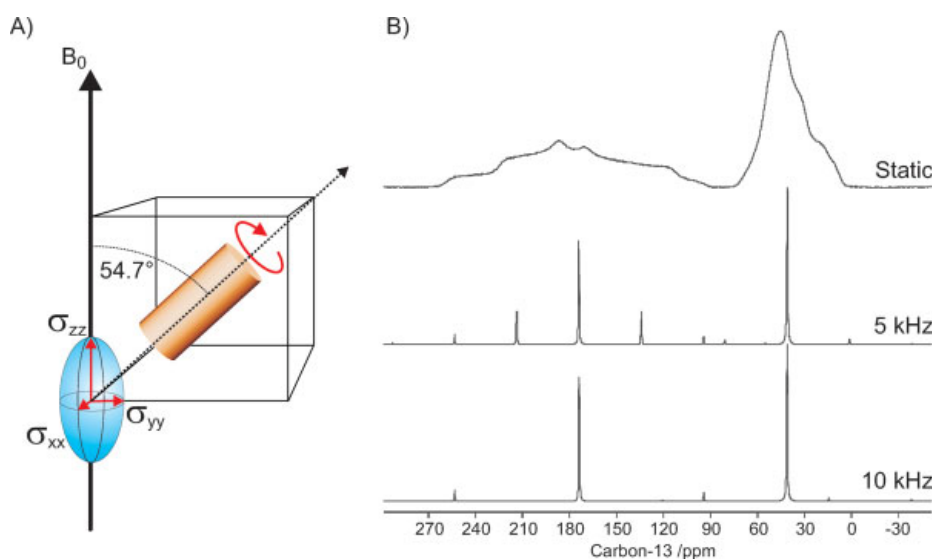


**Figure 2.9. Magic Angle Spinning.** Figure adapted from (117). (a) Scheme of the rotation of solid-state samples at the magic angle. (b) Removal of the anisotropic interactions in MAS and appearance of the spinning side bands.

### 2.3.2 Cross polarisation

Despite the mechanical averaging in MAS is able to remove most of the anisotropic interactions, the impossibility to fully delete DC between  $^1\text{H}$  atoms prevents its employment for spectra detection. As a result, the most sensitive atom cannot be employed and instead nuclei with low gyromagnetic ratio, such as  $^{13}\text{C}$ ,  $^{15}\text{N}$ , or  $^2\text{H}$ , must be utilised for detection. The drawbacks of using such nuclei include low sensitivity (low gyromagnetic ratio), unfavourable relaxation rates (long acquisition times) and low natural abundance (i.e. that can be overcome with isotopic enrichment). In order to compensate with these negative points, cross polarization (CP) has been introduced to exploit the higher equilibrium polarization and favorable relaxation properties of protons. In particular, CP enables to enhance the sensitivity of low gamma nuclei by a factor that is proportional to the ratio between their gyromagnetic ratios a those of the proton, leading

to a theoretical increase in sensitivity of 4 in the case of  $^{13}\text{C}$  and up to a factor of 10 for  $^{15}\text{N}$ . In addition to the sensitivity enhancement, as the cross polarization is based on the excitation of the protons, the delay employed between subsequent pulses is now depending on the speed by which protons return to their equilibrium positions ( $t_1$ ). As the relaxation properties of protons are faster to those of  $^{13}\text{C}$  or  $^{15}\text{N}$ , the delay between experiments is significantly reduced, leading to faster acquisition in general.

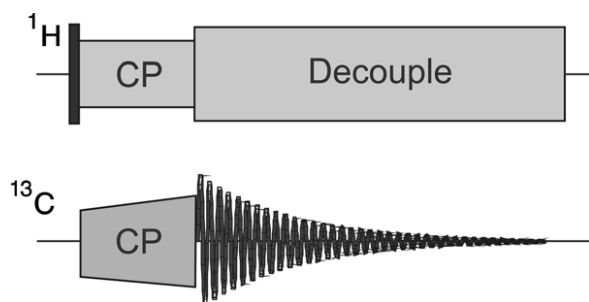


**Figure 2.10.**  $^{13}\text{C}$  cross polarisation experiment. Figure adapted from (117). Scheme for a basic CP to detect  $^{13}\text{C}$  NMR resonances at the ssNMR. After an initial  $90^\circ$  pulse on the  $^1\text{H}$  channel, two simultaneous radiofrequencies satisfying the Hartmann-Hahn condition are applied on the  $^1\text{H}$  and  $^{13}\text{C}$  in such a way to enable the transfer of the polarisation from the proton to the  $^{13}\text{C}$ . Under optimal conditions, this transfer leads to a sensitivity enhancement corresponding to  $\gamma_I/\gamma_S$ , which in the case of  $^1\text{H}$  and  $^{13}\text{C}$  is circa 4.

Differently from solution NMR, where the transfer between proton and heteronuclei is Jcoupling mediated, in CP the transfer of polarisation is obtained via heteronuclei DC. Thus, the typical CP is used to transfer polarisation to a nucleus at low gyromagnetic ratio after applying a 90-degrees pulse to the proton and by simultaneously irradiating with radiofrequencies protons and the coupled nucleus (Figure 2.10). The optimal transfer is achieved by tuning the radiofrequencies for matching the Hartmann-Hahn condition,  $|\gamma_I B_{1I}| = |\gamma_S B_{1S}|$ , where  $B_{1I}$  and  $B_{1S}$  are the radiofrequencies employed for the nucleus I and S, respectively. In the case of MAS becomes the Hartmann-Hahn condition becomes  $|\gamma_I B_{1I}| = |\gamma_S B_{1S} \pm n\omega_r|$  (where  $n = 1, 2$ ). The transfer efficiency depends on matching these conditions whose width depends on the strength of the dipolar coupling between the protons and the low-gamma nuclei.

The CP block is therefore an extremely useful tool to enhance sensitivity and time accessibility of ssNMR experiments in biomolecular NMR. This block can be used in various multidimensional spectra, in a similar spirit of the INEPT block introduced before.

## Chapter III

### *The membrane-bound state of $\alpha$ S: structure, topology and molecular determinants*

#### *3.1 A hybrid approach of solution state and solid-state NMR to characterise the nature of the $\alpha$ S-membrane interaction*

Understanding the structure and dynamics of the membrane-bound state of  $\alpha$ S is a central task in biochemistry, as the membrane interaction is central for both function and aggregation of  $\alpha$ S (Chapter I). The dynamic nature of  $\alpha$ S in both its cytosolic and membrane-bound states has, however, limited the application of standard methods of structural biology, including X-ray crystallography and solution-state NMR spectroscopy.

In its cytosolic form,  $\alpha$ S can be monomeric and intrinsically disordered (15-17) or associated with other proteins (3). Upon binding to lipid membranes,  $\alpha$ S undergoes a significant conformational transition with respect to its monomeric intrinsically disordered form, with some regions adopting a high level of  $\alpha$ -helical structure (18, 19, 21, 118). This ordering process is driven by specific amino acid patterns in the  $\alpha$ S sequence, in particular those coding for amphipathic class A2 lipid-binding  $\alpha$ -helical segments in the region of the molecule spanning residues from 1 to 90 (21). The modular organization of such  $\alpha$ -helical fragments promotes  $\alpha$ S binding to a wide variety of lipid assemblies, from micelles and lipid vesicles to cellular membranes (19, 20, 118, 119). As a consequence of its metamorphic character,  $\alpha$ S is able to sense membrane curvature and defects, and respond to the presence of specific features such as lipid rafts, adopting a range of structural architectures, such as a pair of anti-parallel curved  $\alpha$ -helices (residues 3-37 and 45-92) (20, 118) or a single curved  $\alpha$ -helix, encompassing essentially the entire N-terminal region (119-121). Indeed, NMR studies involving lipids that mimic key features of synaptic vesicles, such as composition and curvature, have revealed that  $\alpha$ S binds to lipid bilayers via a multiplicity of distinct binding modes (19).

Taken together these studies are providing a general view about the structural plasticity and the dynamical nature (122-124) of the membrane-bound state of  $\alpha$ S, whose structural properties can sometimes be perturbed even by relatively minor external factors. Indeed NMR studies of  $\alpha$ S bound to detergent in micelle assembly have shown that the protein can adapt its structure to the shape of the micelle, in some cases by 'wrapping' around the detergents (120). It is therefore clear that these structures, while technically correct, are representative of a detergent-bound state of  $\alpha$ S that is not physiologically relevant. Similarly, in studies involving electron paramagnetic relaxation (EPR),  $\alpha$ S was chemically modified using hydrophobic spin-labelled molecules attached to cysteine residues that were introduced *ad hoc* by mutagenesis. Again, while these structures are technically correct (20, 118, 120), they are severely affected by the chemical modifications of  $\alpha$ S, with the increased local hydrophobicity likely affecting the binding properties of this highly dynamical state. Indeed, it is known that single-point pathological mutations of the protein can have severe effects on the lipid affinity and structure of the membrane-bound state of  $\alpha$ S (73). It is therefore of fundamental importance to introduce an approach that can study the interactions of  $\alpha$ S with lipids under conditions that reproduce as closely as possible the physical properties of presynaptic membranes. In this challenge, small unilamellar vesicles (SUVs) with appropriate lipid mixtures of DOPE, DOPC and DOPS can provide excellent models for studying the binding of  $\alpha$ S to synaptic vesicles, however, their slow tumbling rates prevent the detection of most of the signals from the bound state of the protein in conventional solution-state NMR methods (19). Under these experimental conditions, only resonances from the disordered C-terminus, the region of the protein having low membrane affinity, can be detected, while the segment of the protein containing residues that can interact strongly with membranes is essentially undetectable for solution-state NMR.

In the present PhD work, we show that it is possible to describe the conformational properties of the elusive membrane-bound state of  $\alpha$ S by using a combination of solid-state NMR (ssNMR) spectroscopy and chemical exchange saturation transfer (CEST) measurements in solution NMR (91, 112, 113). This approach proved to be highly effective in enabling the fine tuning between structural order and disorder in the

membrane-bound state of  $\alpha$ S to be probed directly without requiring any chemical modification of the protein or changes to its amino acid sequence (114).

## **3.2 Materials and Methods**

### 3.2.1 $\alpha$ S purification.

$\alpha$ S was purified in *E. coli* using plasmid pT7-7 encoding for the protein as previously described (82). See Chapter II for further details.

### 3.2.2 Preparation of SUVs for solid-state and solution NMR.

Small unilamellar vesicles (SUVs) containing a molar ratio of 5:3:2 of DOPE:DOPS:DOPC (Avanti Polar Lipids Inc. Alabaster) were prepared from chloroform solution of the lipid. The lipid mixture was evaporated under a stream of nitrogen gas and then dried thoroughly under vacuum, to yield a thin lipid film. Then the dried thin film was re-hydrated adding an aqueous buffer (20 mM sodium phosphate, pH 6.0) and subjected to vortex mixing. Several cycles of freeze-thawing cycles and sonication were carried out until the mixture become clear. In the case of CEST experiments, after sonication, SUVs were mixed with  $\alpha$ S samples with a concentration of 0.06% (0.6 mg/ml). In the case of ssNMR, after sonication,  $\alpha$ S was then added to the SUVs mixture up to a molar ratio of 1:65 protein:lipid. Then the mixture was pelleted at 75k (22,000 g) for 30 min and 4°C (Beckman Coulter Optima TLX Inc. Brea, USA) by using a rotor TLA 100.3. Subsequently the SUV- $\alpha$ S sample was transferred to 3.2 mm Zirconia XC thin-walled MAS rotor for the SSNMR experiments. POPG SUV- $\alpha$ S samples were prepared using the same protocol but a 50 mM potassium phosphate buffer and 100 mM NaCl at pH 7.4 was used. (120)

### 3.2.3 Magic angle spinning measurements using ssNMR.

MAS experiments in this chapter were carried out using two spectrometers at the University of Minnesota (14.09T or a 16.85T VNMRS Spectrometer with a 3.2 mm BioMASTM probe, Agilent Technologies) or using a 14.09T Bruker Ascend magnet with Avance III HD console and equipped with a 3.2 mm E<sup>Free</sup> probe at Imperial College London. Dipolar assisted rotational resonance (DARR) experiments (125) in this chapter were performed on a MAS rate of 10 kHz using different contact time (20, 50, 100, 200 and

500 ms). DARR were acquired at -19 °C and 4 °C (the latter is for control experiments only) by using a 1 ms contact time and a DARR mixing times ranging from 20ms to 500ms. Insensitive nuclei enhanced by polarization transfer (INEPT) were carried out at 4 °C using a MAS rate of 10 kHz. Pulse widths were 2.5  $\mu$ s for  $^1\text{H}$  and 5.5  $\mu$ s for  $^{13}\text{C}$  and proton TPPM decoupling was applied at  $\omega_{\text{RF}}/(2\pi) = 71.4\text{-}100$  kHz.

#### 3.2.4 Oriented ssNMR experiments.

Oriented ssNMR experiments were performed at the University of Minnesota on a 16.85T VNMRs spectrometer at a temperature of 25°C using a low-*E* bicelle probe built by the RF Team at the National High Magnetic Field Laboratory (NHMFL) in Florida (126). To prepare the oriented samples, recombinant  $\alpha\text{S}$  was dialysed into 20mM phosphate buffer at pH 6.0 and mixed with a solution containing 6.7 mg of short chain DOPC and 31 mg of long chain lipid (DMPC/POPG 4/1 w/w) suspended in  $\text{H}_2\text{O}$  to give a final lipid concentration of 25% (w/v). Bicelles with a q-ratio (long-chain lipid/short-chain lipid ratio) of  $\sim 3.2$  were formed after several freeze–thaw–vortex cycles. To prepare *flipped* bicelles (i.e., with the membrane normal parallel with the direction of the static field),  $\text{YbCl}_3$  was added to give a final concentration of 5 mM. These bicelles show an order parameter of 0.8 (127). Cross polarization times of 1 ms with  $^1\text{H}$  RF field strengths corresponding 50.0 kHz were used. FSLG decoupling was obtained by ramping the phase of the  $^1\text{H}$  RF with an effective field strength of 50.0 kHz. An acquisition time of 5 ms was used in the direct dimension with 50.0 kHz SPINAL decoupling (128) on the proton channel and a recycle delay of 4 s was used.

#### 3.2.5 Solution NMR samples and CEST experiments.

Solution NMR experiments were carried out at 10 °C on two Bruker spectrometers (at the Universities of Minnesota and Cambridge) operating at  $^1\text{H}$  frequencies of 700 MHz equipped with triple resonance HCN cryo-probes. CEST experiments were based on  $^1\text{H}$ - $^{15}\text{N}$  HSQC experiments by applying constant wave saturation in the  $^{15}\text{N}$  channel. As the exchange is probed between monomeric  $\alpha\text{S}$  (having sharp resonances) and the slow tumbling SUVs-bound state (having significantly broad resonances), a series of large offsets was employed (-28, -21, -14, -9, -5, -3, -1.5, 0, 1.5, 3, 5, 9, 14, 21 and 28 kHz) resulting in CEST profiles of symmetric shape (Figure 2.8). An additional spectrum,

saturated at -100 kHz was recorded as reference. CEST experiments were performed using two continuous wave radio frequencies (170Hz and 350Hz) to saturate  $^1\text{H}$ - $^{15}\text{N}$ -HSQC spectra recorded using a data matrix consisting of 2048 ( $t_2, ^1\text{H}$ )  $\times$  440 ( $t_1, ^{15}\text{N}$ ) complex points. Assignments of the spectra resonances for  $^1\text{H}$ - $^{15}\text{N}$ -HSQC spectra in solution NMR were obtained from previous works of the lab (15, 19, 73).

### 3.2.6 Paramagnetic relaxation enhancement at the magic angle spinning.

PRE data were measured with magic angle spinning using a 14.09T Bruker Ascend magnet with Avance III HD console and equipped with a 3.2 mm  $E^{\text{Free}}$  probe (Imperial College) or using an Agilent 16.85T VNMRS Spectrometer with a 3.2 mm BioMASTM probe (University of Minnesota). Dipolar assisted rotational resonance (DARR) experiments (125) were performed at a MAS rate of 10.0 kHz at -19 °C and 4 °C (the latter is for control experiments only), using a 1 ms contact time and 20 ms mixing time in  $^{13}\text{C}$ - $^{13}\text{C}$  cross polarization. PRE data were measured by using unlabelled membranes to measure a reference spectrum and then spectra were obtained by using paramagnetic labeled membranes doped with 2% of paramagnetic labeled lipid molecules, carrying the unpaired electron on the head group or on carbons 5, 10 or 16 of the lipid chain.

### 3.2.7 Structural ensemble refinement by chemical shift restrained MD.

Chemical shifts were employed in restrained molecular dynamics simulations using the CamShift method (111) to refine accurate structural ensembles of the anchor region of  $\alpha\text{S}$ . These methods have been largely described in literature. A brief description is provided in the supplementary materials.

CS restrained simulations were run with a modified version of the GROMCSA package (109) that allows restraining the simulations using the CamShift program (111). Briefly, the restraints were imposed by adding a pseudo-energy term ( $E^{\text{CS}}$ ) to a standard molecular mechanics force field ( $E^{\text{FF}}$ ):

$$E^{\text{Tot}} = E^{\text{FF}} + E^{\text{CS}} \quad (3.1)$$

The resulting force field ( $E^{\text{Tot}}$ ) was employed in molecular dynamics simulations, where the pseudo-energy term is given by

$$E^{CS} = \alpha \sum_i (\delta_i^{Exp} - \delta_i^{Calc})^2 \quad (3.2)$$

where the  $i$  sum runs over all the chemical shifts employed in the refinement,  $\alpha$  is the weight of the restraint term, and  $\delta^{exp}$  and  $\delta^{calc}$  are the experimental and calculated chemical shifts, respectively. We employed the replica-averaged scheme which implies that a given chemical shift is calculated by

$$\delta^{Calc} = \frac{1}{m} \sum_m^4 \delta_m^{Calc} \quad (3.3)$$

where  $m$  runs over four replicas and  $\delta_m^{Calc}$  is the chemical shift of replica  $m$ .

### 3.2.8 Restrained MD setup.

Restrained molecular dynamics simulations were performed by averaging chemical shift restraints over four replicas, as previously described (84). The calculations were made using our implementation of the GROMCSA package (109) that allows restraining the simulations using the CamShift program (111). Each of the four replicas was equilibrated separately by starting from random conformations accommodated in a dodecahedron box of 276 nm<sup>3</sup> in volume. The box was filled with explicit waters and energy minimized. For each replica, the system was thermalised during a NVT simulation of 250 ps in which the temperature was increased from 10K to 278K. Subsequently the pressure was equilibrated at 1 Atm for a 200 ps MD simulation. Finally, the individual replicas were equilibrated for 1 ns long simulations.

The replica-averaged restrained molecular dynamics simulations were carried out using the following protocol. The four replicas evolved through a series of annealing cycles between 278K and 350K, each cycle being composed of 100ps of simulation carried at 278K followed by 100ps of simulations in which the temperature of the system was increased up to 350K and 100ps of simulation carried at a constant temperature of 350K. The final part of the cycle allowed cooling slowly the system in 300ps from 350K to 278K. During these cycles the experimental restraints were imposed as averages over the four replicas according to equations 1-3. The total amount of sampling in each system simulated was 1  $\mu$ s (250.2 ns *per* replica equivalent to 417 cycles). The first refinement of the structural ensemble of the anchor region of  $\alpha$ S was performed by starting from four

random conformations generated by a single 100 ns all atom simulation (NPT ensemble carried out at 500K) starting from a linearised protein with the sequence of  $\alpha$ S. The second ensemble, involving the interaction with the membrane, was started by equilibrating the representative minimum in the FES generated with the first ensemble in the presence of a pre-equilibrated membrane bilayer composed of DOPE:DOPS:DOPC lipids in a ratio 5:3:2.

The simulations were carried out using the AMBER99sb-ILDN force field (129) and the Tip4pEW (130) water model. In the case of simulations performed in the presence of the lipid bilayer, we employed the parameters of the all-atom force field defined for phosphatidylcholine lipids (131). The protonation states of pH-sensitive residues were as follows: Arg and Lys were positively charged, Asp and Glu were negatively charged, and His was neutral and the net charge of the system was neutralized by the addition of  $\text{Na}^+$  and  $\text{Cl}^-$  ions. A time step of 2 fs was used together with LINCS constraints (132). The van der Waals and electrostatic interactions were cut off at 0.9 nm, and long-range electrostatic effects were treated with the particle mesh Ewald method (133). All the simulations were carried out in the canonical ensemble by keeping the volume fixed and by setting the system temperature with the V-rescale thermostat (134). The final samplings were collected from the 278K portions of the replica simulations after discarding the initial 50ns in each replica, which represented the equilibration phases of the ensemble. The total conformations collected in each sampling amounted to 13320 and convergence was tested using four different structural parameters (Figure 3.8).

### 3.2.9 Prediction of the anisotropic $^{15}\text{N}$ CSA in aligned samples.

Analysing the ranges of  $^{15}\text{N}$  anisotropic chemical shifts (CSA) in oriented ssNMR can provide accurate information on the orientation of helices in membrane proteins. This is illustrated for  $\alpha$ S by back-calculating (see next section) the  $^{15}\text{N}$  CSA of the membrane anchor region of  $\alpha$ S in an ideal helical conformation that is oriented at tilt angles ranging from  $0^\circ$  to  $90^\circ$  (Figure 3.16). This calculation can be further refined by including the effects of both internal protein dynamics, as accounted by the ensemble of structures of  $\alpha\text{S}_{1-30}$  discussed in this study, and the intrinsic dispersion in the orientations of the alignment media in oriented ssNMR experiments, which in the case of *flipped* bicelles is

associated with an order parameter of 0.8 (135). These two factors result in a scaling of the calculated  $^{15}\text{N}$  CSA towards more isotropic values (120 ppm, Figure 3.16 b).

### 3.2.10 Back-calculation of anisotropic $^{15}\text{N}$ CS values from structural ensembles.

For the anisotropic chemical shifts, we used the following formula:

$$\delta_{^{15}\text{N}} = \delta_{11} \cdot \sin^2(\alpha - 17) \cdot \sin^2(\beta) + \delta_{22} \cdot \cos^2(\beta) + \delta_{33} \cdot \cos^2(\alpha - 17) \cdot \sin^2(\beta) \quad (3.4)$$

where  $\delta_{11}$ ,  $\delta_{22}$  and  $\delta_{33}$  are the experimentally determined components (in ppm) of the  $^{15}\text{N}$  amide chemical shift tensor in the principal axis frame (PAF), and  $\alpha$  and  $\beta$  are the experimentally determined Euler angles (in degrees) used to transform from the laboratory frame to the PAF (136). We employed constant values of the chemical shift tensor using standard parameters ( $\delta_{11} = 64.0$ ,  $\delta_{22} = 76.0$ ,  $\delta_{33} = 216.9$  for non-glycine residues and  $\delta_{11} = 46.5$ ,  $\delta_{22} = 66.3$ ,  $\delta_{33} = 211.6$  for glycine residues). Using fixed values of the tensor may introduce a minor source of errors as *ab initio* studies have shown that CSA tensors may be subject to variation due to different factors (137), however, these errors are negligible for the scopes of our back calculation.

### ***3.3 Three distinct regions of $\alpha$ S define its membrane-binding properties***

Using a hybrid approach of solution and solid-state ssNMR we probed the structural properties of  $\alpha$ S bound to SUVs that mimic the native composition and curvature of synaptic vesicles (19). The SUVs utilised in our study are acidic and consist of mixtures of 1,2-dioleoyl-sn-glycero-3-phosphoethanolamine (DOPE), 1,2-dioleoyl-sn-glycero-3-phospho-L-serine (DOPS), and 1,2-dioleoyl-sn-glycero-3-phosphocholine (DOPC) in 5:3:2 molar ratios (19). To characterise the conformational preferences of the  $\alpha$ S bound state to these vesicles, we used a series of magic angle spinning (MAS) ssNMR techniques in conjunction with isotope labeling of the protein, an approach that has been shown to be a powerful means of studying interactions between proteins and membranes (138-143). A solution of  $^{13}\text{C}$ - $^{15}\text{N}$  labeled  $\alpha$ S was mixed with DOPE:DOPS:DOPC SUVs, as described previously (19) and in Chapter II. The resulting vesicles incorporating the labeled  $\alpha$ S were subsequently packed into a 3.2 mm MAS rotor (Supplementary Material). Using circular dichroism, we selected a protein:lipid ratio of 1:65 by monitoring the transition of the protein signal from the disordered state to one with a high degree of  $\alpha$ -helical structure, consequent upon addition of lipids (Figure 3.1). With this protein-lipid ratio, the first 97 residues of  $\alpha$ S are effectively invisible for solution NMR techniques because the association of  $\alpha$ S with the SUVs broadens dramatically the protein resonances as a result of the slow tumbling of the complex in the absence of a very high degree of internal dynamics, such as that observed in the C-terminal region (19).

To investigate this elusive state, we carried out a series of ssNMR experiments involving  $^{13}\text{C}$ - $^{13}\text{C}$  dipolar assisted rotational resonance (DARR)(125). These spectra correlate both main-chain and side-chain  $^{13}\text{C}$  labeled resonances of the protein, as a result of cross-polarization (CP) effects, and hence are able to detect rigid moieties of biomacromolecules even in the absence of rapid overall tumbling of the molecule. Indeed, in the study of interactions between proteins and membranes, DARR experiments have been shown to be particularly effective for detecting the resonances of residues that become highly rigid upon interaction with the lipid bilayer, such as for example transmembrane  $\alpha$ -helices (141, 144). Using a DARR contact time of 20 ms, we were able to detect homonuclear correlations between directly bonded carbon atoms in regions that are tightly bound to the membrane (Figure 3.2 a,b). The highest signal intensities in the spectra of the samples studied here were obtained by performing the measurements

at -19 °C, i.e. under conditions where the lipids adopt a gel phase (145); other than having increased signal-to-noise ratios, however, these spectra are fully consistent with those measured at 4 °C. Moreover, no variations in the number of observed resonances or the values of their chemical shifts were observed when the protein:lipid ratios were varied from 1:30 to 1:200.

DARR experiments performed at a range of different contact times (50, 100, 200 and 500 ms, Figures 2.3 and 2.4) revealed an intense network of dipolar interactions, indicating that the  $^{13}\text{C}$ - $^{13}\text{C}$  DARR resonances belong to a well-defined structural segment of consecutive residues. The relatively low signal-to-noise ratios did not enable the acquisition of three-dimensional spectra, but we were nevertheless able to measure  $^{15}\text{N}$ - $^{13}\text{C}$  cross polarization correlations (Figure 3.5) that have provided additional connectivities to those obtained from the  $^{13}\text{C}$ - $^{13}\text{C}$  DARR spectra.

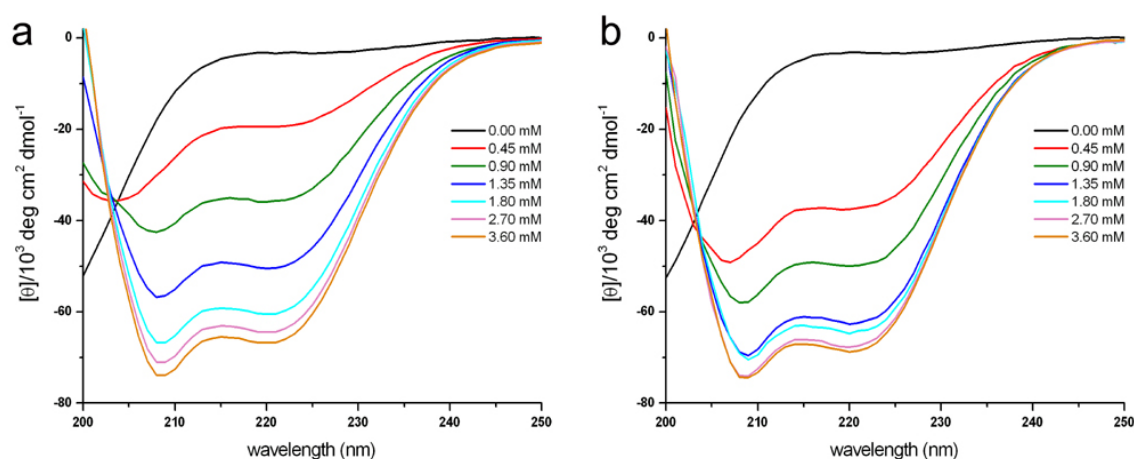


**Figure 3.1. CD analysis of  $\alpha\text{S}$  in the presence of different concentrations of SUVs.** In all measurements, the concentration of  $\alpha\text{S}$  was kept constant at 20  $\mu\text{M}$ . **a)**  $\alpha\text{S}$  binding to DOPE:DOPS:DOPC SUVs. The buffer conditions and SUV preparation were chosen according to Bodner et al (19). **b)**  $\alpha\text{S}$  binding to POPG SUVs. POPG SUVs were prepared under conditions reported by Lokappa and Ulmer(120). Using the values of the ellipticity at 222 nm we estimated an apparent dissociation constant  $K_D$  of  $93 \pm 15 \mu\text{M}$  for POPG SUVs and  $261 \pm 21 \mu\text{M}$  for DOPE:DOPS:DOPC SUVs under the conditions employed in the present study.

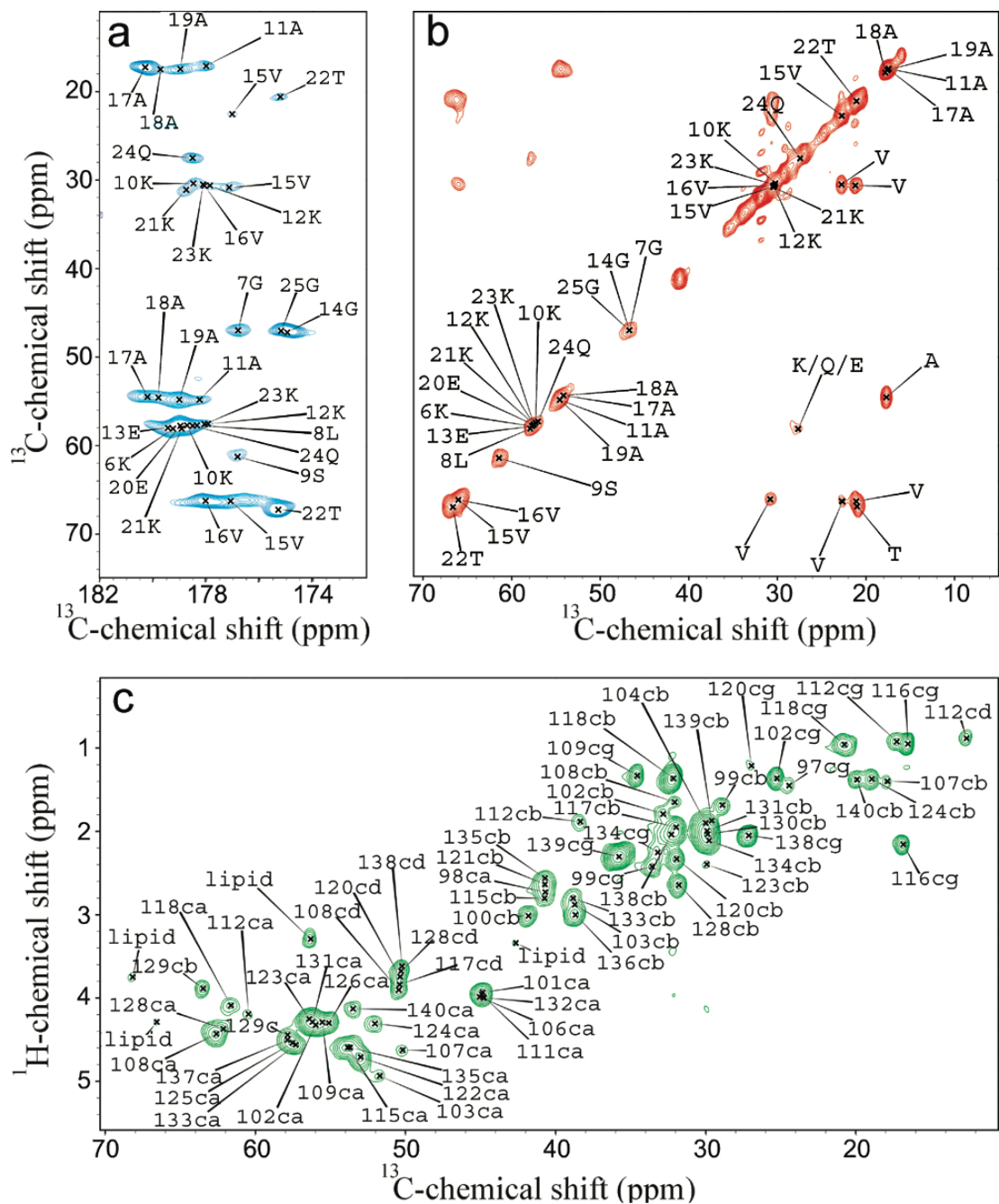


**Figure 3.2. MAS ssNMR spectrum of  $\alpha$ S bound to DOPE:DOPS:DOPC SUVs.**  $^{13}\text{C}$ - $^{13}\text{C}$  DARR correlation spectrum recorded at  $-19^\circ\text{C}$  using a 20 ms contact time at a MAS rate of 10 kHz. Carbonyl and aliphatic regions are showed in panels a and b, respectively. Residue names are reported using the single letter convention. **c)**  $^1\text{H}$ - $^{13}\text{C}$  correlation via INEPT transfer recorded at  $4^\circ\text{C}$  at a MAS rate of 10 kHz. The experiments were performed at  $^1\text{H}$  frequencies of 600 and 700 MHz using a  $^1\text{H}/^{13}\text{C}$  3.2-mm probe and a spinning speed of 10.0 kHz. Atom names ca, cb, cg, cd are used for  $\text{C}^\alpha$ ,  $\text{C}^\beta$ ,  $\text{C}^\gamma$  and  $\text{C}^\delta$  atoms, respectively.

The high redundancy in the  $\alpha$ S primary sequence, which includes a series of conserved KTKEGV segments that are repeated imperfectly throughout the N-terminal region, poses a significant challenge for residue-specific assignments. Nonetheless, we were able to assign individual spin systems using  $^{13}\text{C}$ - $^{13}\text{C}$  DARR spectra recorded at different contact times, in conjunction with heteronuclear correlation experiments (Figure 3.5) and information from the analysis of the chemical exchange saturation transfer (CEST) experiments (see below). As a consistency check, the chemical shifts of the assigned resonances were compared to those obtained by solution NMR experiments of  $\alpha$ S in SDS and SLAS micelles (20, 146). Overall, we have been able to obtain the sequential assignments for the segment  $\text{K}_6\text{GLSKAKEGVVAAAETKQG}_{25}$ . The ability to observe and assign the resonances of this stretch of the sequence revealed that the N-terminal segment of  $\alpha$ S was sufficiently strongly anchored to the membrane to be visible using CP experiments. The measured chemical shifts values indicate that this  $\alpha$ S segment was in a continuous  $\alpha$ -helical conformation when bound to SUVs and, using the d2D method (89), we estimated that the population of  $\alpha$ -helical structure in this segment was on average  $86 \pm 11\%$  (Figure 3.6).

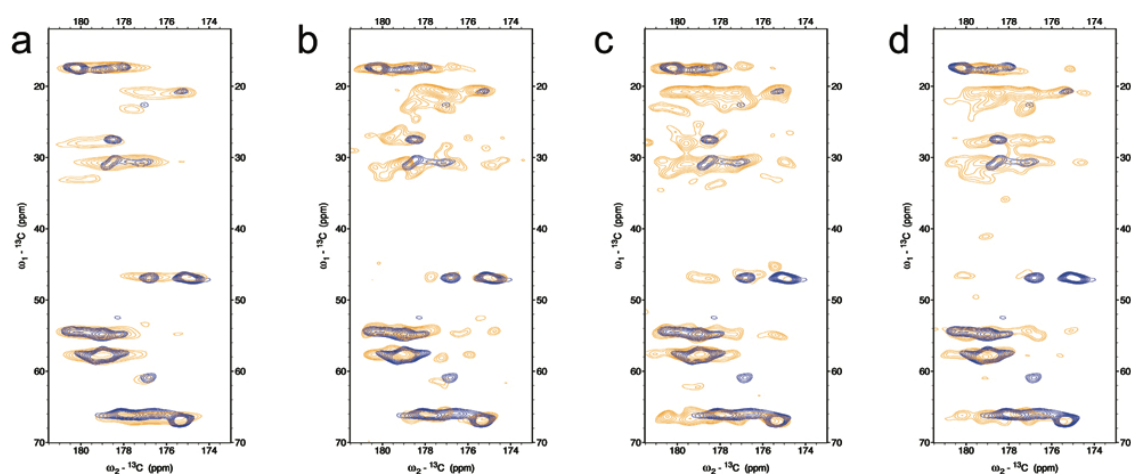


**Figure 3.3. Carbonyl region of  $^{13}\text{C}$ - $^{13}\text{C}$  DARR spectra of  $\alpha$ S bound to DOPE:DOPS:POPC SUVs.**  $^{13}\text{C}$ - $^{13}\text{C}$  DARR correlation spectrum recorded using (a) 50 ms, (b) 100 ms, (c) 200 ms and (d) 500 ms of DARR contact time are shown in orange. For comparison a  $^{13}\text{C}$ - $^{13}\text{C}$  DARR correlation spectrum recorded using 20 ms of contact time is shown in blue for all the panels.

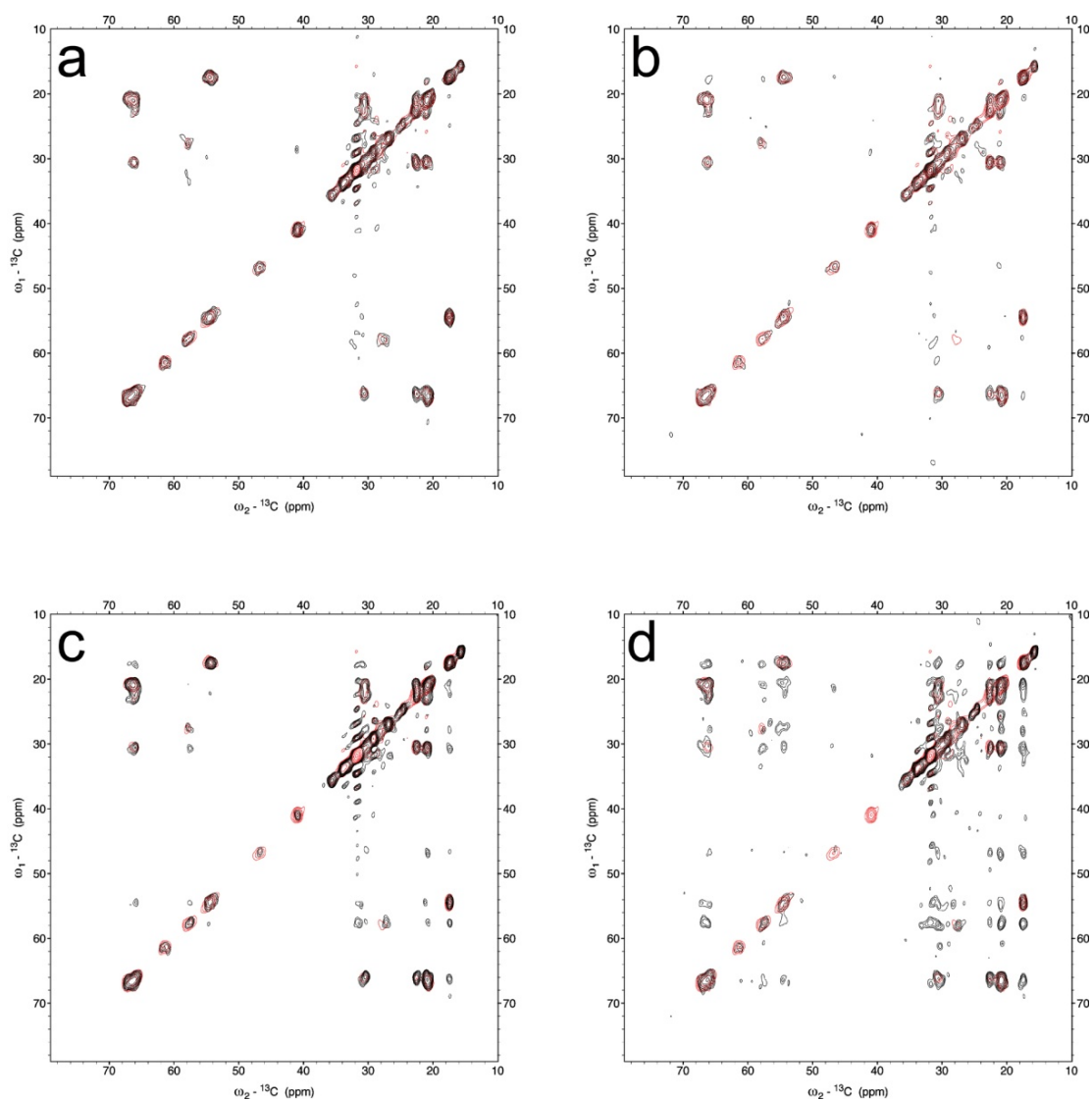


**Figure 3.4. Aliphatic region of  $^{13}\text{C}$ - $^{13}\text{C}$  DARR spectra of  $\alpha\text{S}$  bound to DOPE:DOPS:DOPC SUVs.**  $^{13}\text{C}$ - $^{13}\text{C}$  DARR spectra recorded using (a) 50 ms, (b) 100 ms, (c) 200 ms and (d) 500 ms are shown in black. For comparison,  $^{13}\text{C}$ - $^{13}\text{C}$  DARR spectrum recorded using 20 ms is shown in red for all the panels.

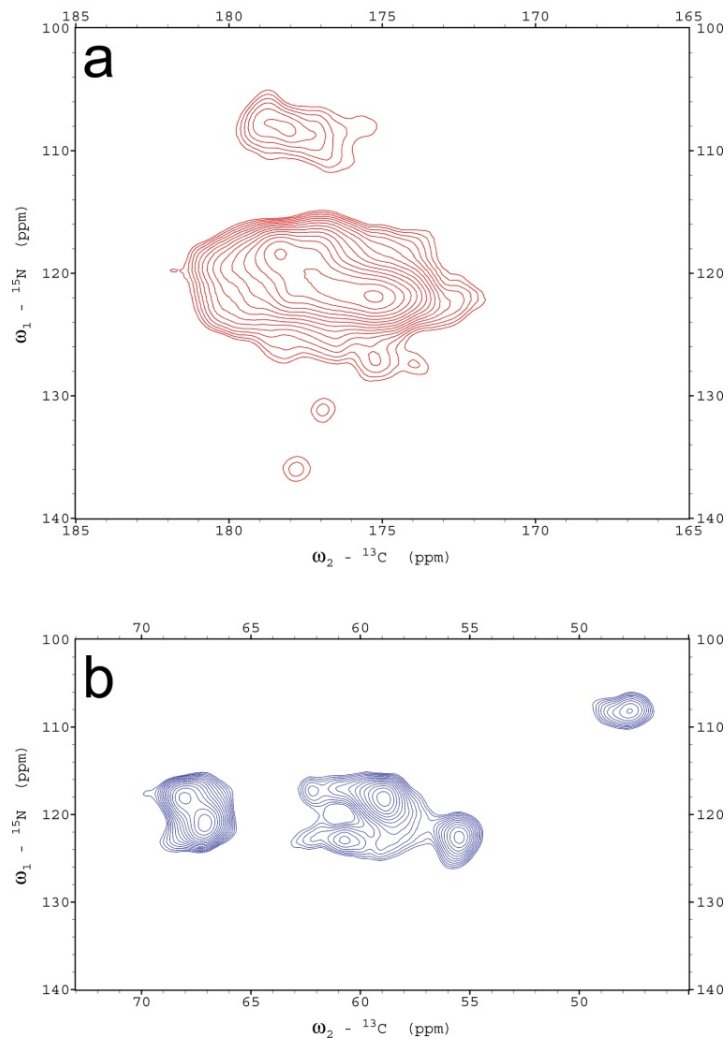


**Figure 3.5. Heteronuclear DARR measurements of  $\alpha\text{S}$  bound to DOPE:DOPS:DOPC SUVs.** Heteronuclear MAS experiments were carried out on a 16.85T VNMRS Spectrometer with a 3.2 mm BioMASTM probe (Agilent Technologies). DARR measurements (125) were performed on a MAS rate of 10 kHz at  $-19^\circ\text{C}$ . Panel **a** reports the correlation between backbone  ${}^{15}\text{N}$  amide atoms and  ${}^{13}\text{C}$  of the carbonyl groups recorded using an NCO experiment. Panel **b** reports the correlation between backbone  ${}^{15}\text{N}$  amide and  ${}^{13}\text{C}$ -alpha atoms recorded using an NCA experiment.

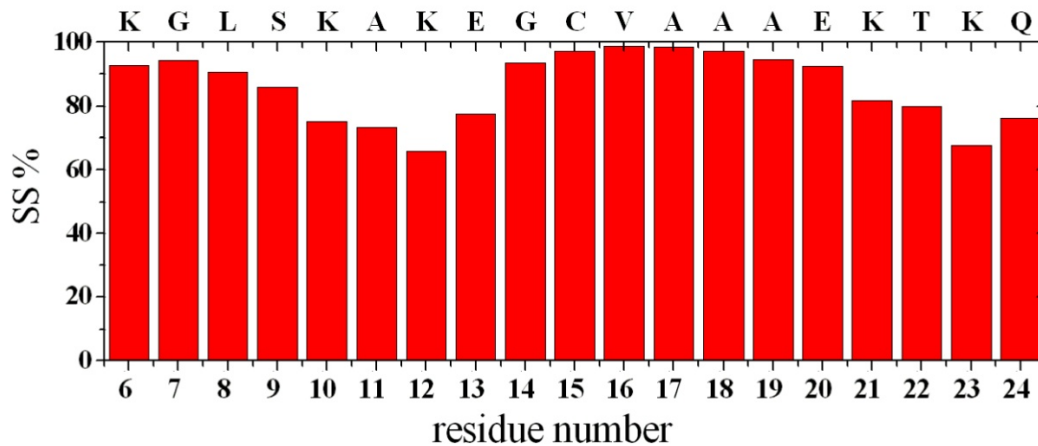


**Figure 3.6. Residue-specific  $\alpha$ -helix populations in the segment 5-26 of  $\alpha$ S bound to DOPE:DOPS:DOPC SUVs.** The populations of  $\alpha$ -helix (SS%) have been derived by using the chemical shifts from the DARR spectra as input for the  $\delta$ 2D program(89).

In addition to the DARR experiments, which provided direct evidence of the regions of  $\alpha$ S that are tightly bound to the membranes, insensitive nuclei enhanced by polarization transfer (INEPT) MAS measurements (147) were used to monitor  $^1\text{H}$ - $^{13}\text{C}$  correlations of the most dynamic parts of the protein in the bound state (Figure 3.2c). Such experiments have been shown to be highly effective probes of regions such as loops in cytoplasmic domains that possess extensive conformational fluctuations relative to those of the more rigid segments of membrane proteins. INEPT spectra of  $\alpha$ S bound to DOPE:DOPS:DOPC SUVs showed a significant number of resonances that closely overlap with those observed in solution NMR  $^1\text{H}$ - $^{13}\text{C}$  HSQC spectra of  $\alpha$ S in the presence of an excess of SUVs (Figure 3.7). As the solution state  $^1\text{H}$ - $^{13}\text{C}$  HSQC spectra have been assigned (15, 19), the overlap of the spectra readily enabled the assignments of the MAS INEPT resonances to be defined (Figure 1c). The resulting assignments correspond to the region 97-140 and indicate that this fragment adopts unstructured conformations in the membrane-bound state. Overall the MAS measurements evidence three regions in the  $\alpha$ S sequence, including a highly rigid N-terminal fragment adopting  $\alpha$ -helical conformation, denoted as “membrane-anchor”, an unstructured C-terminal fragment and a central region, residues 26-96, that adopts an intermediate dynamical regime.

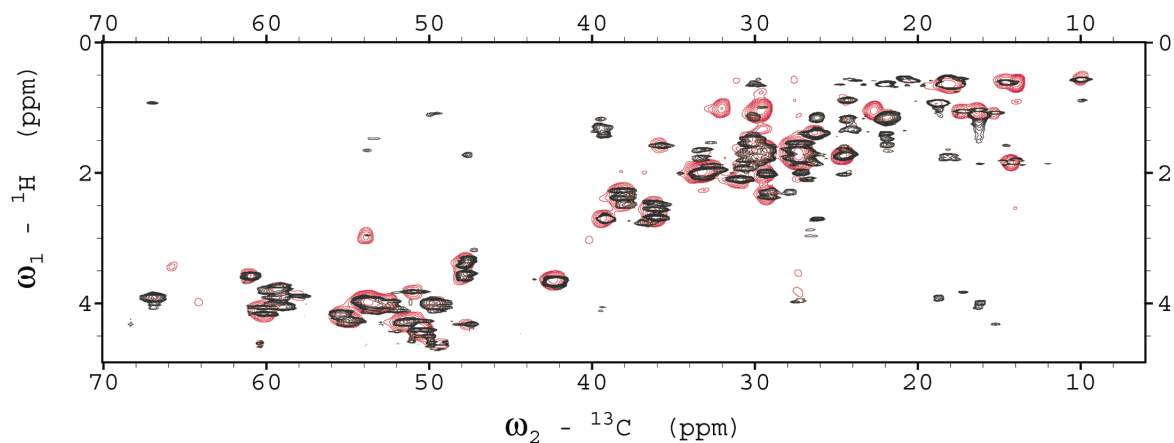


**Figure 3.7. Overlay of the ssNMR INEPT (red) and solution NMR  $^1\text{H}$ - $^{13}\text{C}$ -HSQC (black) spectra.** Both spectra have been measured for  $\alpha\text{S}$  bound to DOPE:DOPS:DOPC SUVs. In the case of the solution NMR,  $^1\text{H}$ - $^{13}\text{C}$ -HSQC spectrum of  $\alpha\text{S}$  has been measured under the sample conditions described by Bodner et al.(19) and by using an excess of lipids (4 mg/ml). Under these conditions the resonances of the initial ca 97 residues are broadened beyond detection in solution state NMR.

### **3.4 Structure of the N-terminal region of $\alpha$ S in its membrane-bound state**

Having directly detected the chemical shifts (CS) of the regions of  $\alpha$ S that are tightly bound to the membrane, we employed these experimental data to generate atomic resolution structural ensembles of this key protein bound to synaptic-like vesicles. In particular, by using experimental ssNMR data of the full length protein bound to SUVs, we characterised the atomic detailed structures of the segment spanning residues 1 to 30 of  $\alpha$ S, denoted as  $\alpha$ S<sub>1-30</sub>, which includes the membrane-anchor region that initiates the adhesion to the vesicle surface (114). The structural refinement of this region of the protein has been obtained by using experimental chemical shifts from ssNMR as restraints in ensemble averaged molecular dynamics simulations (111, 148), using an established protocol based on four replicas (84) that evolve simultaneously starting from random conformations. Samplings were carried out for 1  $\mu$ s until convergence were observed for four parameters, namely the root mean square deviations (RMSDs) in the C <sup>$\alpha$</sup>  Cartesian coordinates and in the backbone dihedral angles, the radius of gyration and the solvent accessible surface area (Figure 3.8). The resulting structural ensemble showed good agreement between the experimental chemical shifts and those calculated using an highly accurate predictor, SPARTA+(149), which is based on a fundamentally different approach to that of the CamShift method(111) used in our structural refinement procedure (Figure 3.9). The back calculations indicate that the refined ensemble matches the experimental data with standard deviations that are within the statistical errors of SPARTA+ (Figure 3.9), providing evidence of its validity.

We then projected the ensemble of  $\alpha$ S<sub>1-30</sub> onto two coordinates, the C <sup>$\alpha$</sup> -RMSD deviation from an ideal helical conformation and the dipole moment of the structure, to obtain a free energy surface (FES) for this region of  $\alpha$ S (Figure 3.10). Overall the FES shows that the conformational heterogeneity of this region of  $\alpha$ S is very significantly reduced when the protein is bound to lipid membranes, with this segment of the protein adopting a stable  $\alpha$ -helical conformation characterised by a single free energy basin centred at a C <sup>$\alpha$</sup> -RMSD of 1.0 Å from an ideal helix and a dipolar moment of 1.3 e $\cdot$ nm. In addition to the main basin, the FES also reveals a low-population conformation centred on an RMSD value greater than 3.0 Å from an ideal helix and a dipolar moment of *ca* 0.9 e $\cdot$ nm.

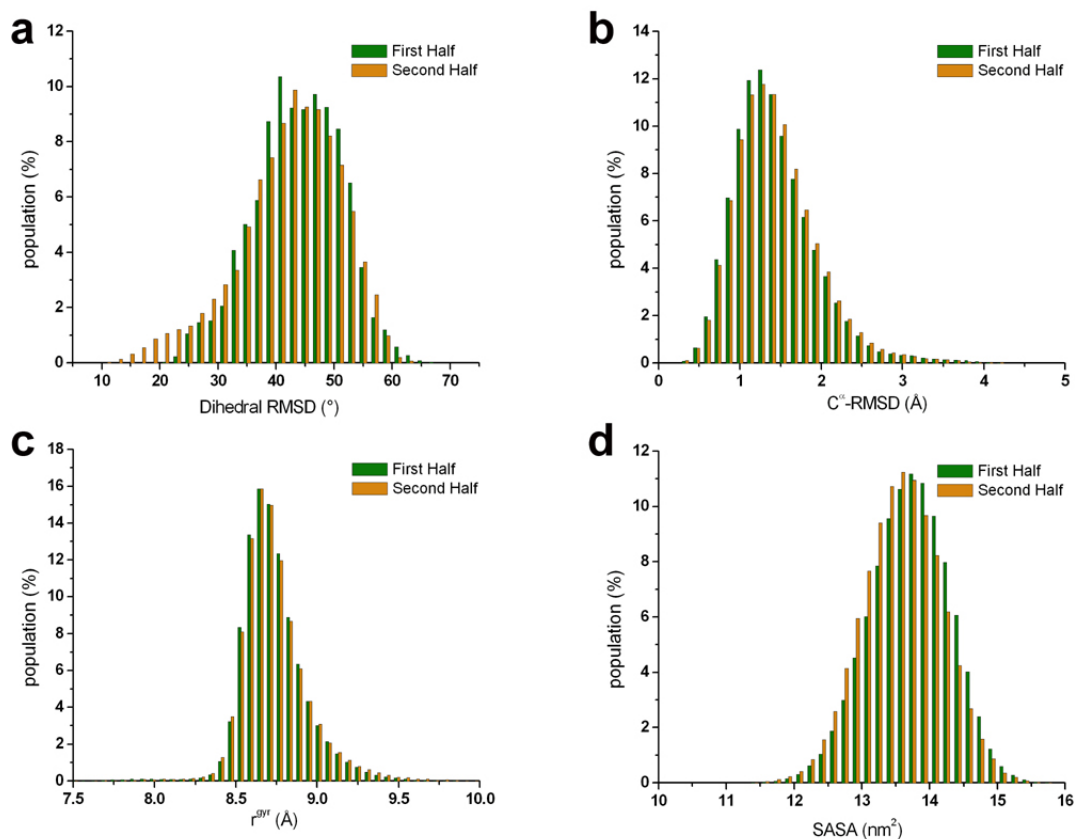


**Figure 3.8. Convergence of the chemical shift restrained simulations of  $\alpha S_{1-30}$ .** To check the convergence of the simulations, the resulting ensemble was divided in two parts, with the first half (green histograms) being composed of the 50 ns to 150 ns segment of each of the four replicas of the sampling, and the second half (orange histograms) being composed of the 150 ns to 250 ns segment. The segment 0 ns to 50 ns was discarded from this analysis as it represents the equilibration phase. Comparison of the distributions of the values of dihedral RMSDs ( $\phi$  and  $\psi$  angles), C <sup>$\alpha$</sup> -RMSDs, radii of gyration and surface accessibility areas are shown in panels a, b, c, and d, respectively.

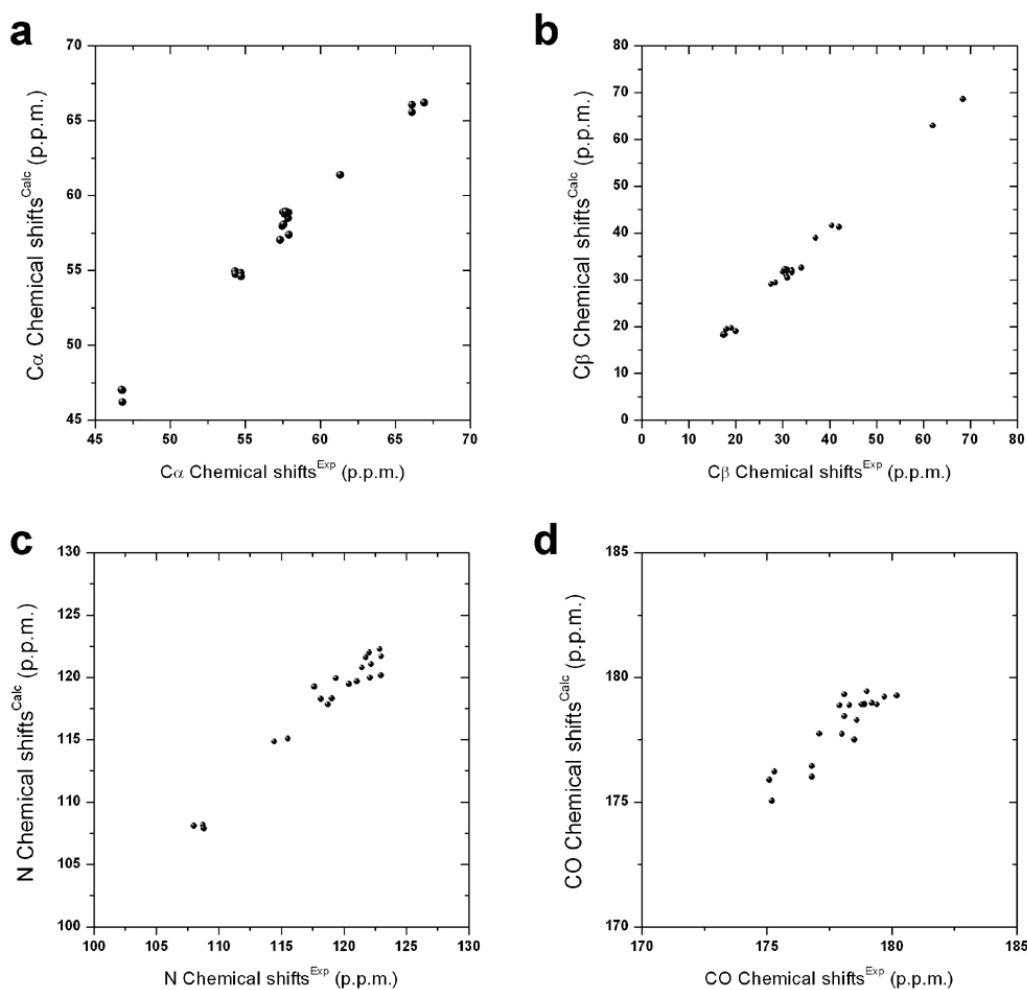


**Figure 3.9 Validation of the CS-restrained simulations of  $\alpha S_{1-30}$ .** Validation of the structural ensemble of  $\alpha S_{1-30}$  was made by comparing the experimental chemical shifts and those back calculated from the structures by using the SPARTA+ (149). As SPARTA+ (149) is based on principles that are different from those of CamShift (111), as employed in the present study to restrain the MD simulations, the high level of agreement provides an independent validation of the quality of the ensembles. The standard deviations are within the statistical errors of SPARTA+ for all the atoms, giving an indication of the high quality of the structural ensembles. Validation for resonances corresponding to C $\alpha$ , C $\beta$ , N, and CO atoms is shown in panels a, b, c and d, respectively.

The fact that the ensemble of structures of  $\alpha S_{1-30}$  in the membrane-bound state has a significant  $\alpha$ -helical content is in agreement with independent estimates of the helical population calculated from an algorithm using statistical mechanics of the CS data ( $\delta 2D(89)$ , Figure 3.11 a). Moreover, the major fluctuations in the structural ensemble of this segment involve the five N-terminal residues and the region spanning residues 26 to 30 (Figure 3.11 b), in line with previous findings that the most rigid helical region in the membrane-bound state of this segment of  $\alpha S$  spans residues 6 to 25 (114). Indeed, residues 6 to 25 show sufficient rigidity to enable number of cross-peaks in multidimensional ssNMR cross polarisation (CP) experiments to be observed, allowing assignment of its backbone resonances (114). In contrast with the present structural ensemble, the solution NMR structures of the micelle-bound state of  $\alpha S$  (PDB codes 1qx8 and 2kkw) occupy a region of our FES that is indicative of conformations that are very close to the ideal  $\alpha$ -helix. The reduced structural variability amongst the 1qx8 and 2kkw structures, as compared with the present CS-restrained ensemble, is possibly due to the strong interactions that  $\alpha S$  establishes with detergent micelles, which result in very significant stabilisation of the helical conformation.

The FES defined in the present work indicates the nature of the key interactions that stabilise the optimal conformation of  $\alpha S$  for membrane binding. In particular, a fundamental element of conformational stabilisation is a network of salt bridges with probabilities ranging from 30% to 70% (Figure 3.11 c). These salt bridges, which are not described in the NMR structures of the micelle-bound state of  $\alpha S$  (PDB codes 1qx8 and 2kkw), include those formed between the pairs of residues K6/D2, K10/E13, K21/E28 and K23/E20, although, that formed between K21 and E28 is not present in the conformations within the major basin of the FES (Figure 3.12). Another key element in the stabilisation of the amphipathic helical conformation of  $\alpha S_{1-30}$  is indicated by the FES in an extended network of highly populated exposed hydrophobic patches (Figure 3.11 d and 2.13). Such hydrophobic patches are likely to stabilise the helical structure in the presence of extended hydrophobic surfaces such as those of lipid bilayers (18, 19, 73, 114, 150), detergent assemblies (20) and water/air interfaces (151).

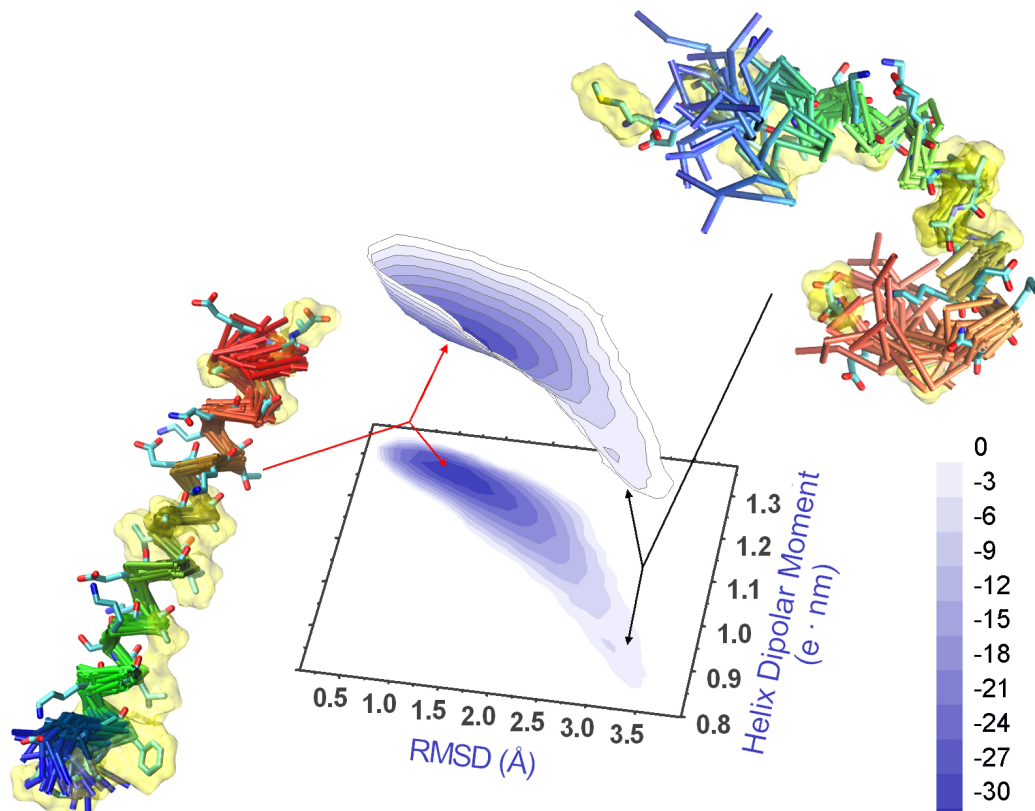


**Figure 3.10. Free energy surface (FES) of the membrane-bound state of  $\alpha S_{1-30}$ .** The ensemble was generated by means of molecular dynamics simulations restrained using ssNMR chemical shifts measured on the SUVs-bound state of the full-length  $\alpha S$ . The conformations are projected on to two reaction coordinates to define a two-dimensional free energy landscape. The coordinates employed are the  $C^\alpha$  root mean square deviation (RMSD) from an ideal helix and the dipolar moment of  $\alpha S_{1-30}$ . The surfaces are generated by means of contour levels reproducing isosurfaces of free energy from 0.0 (white) to -30.0 (darkest blue) kJ/mol. Two representative structural bundles from the FES are shown.

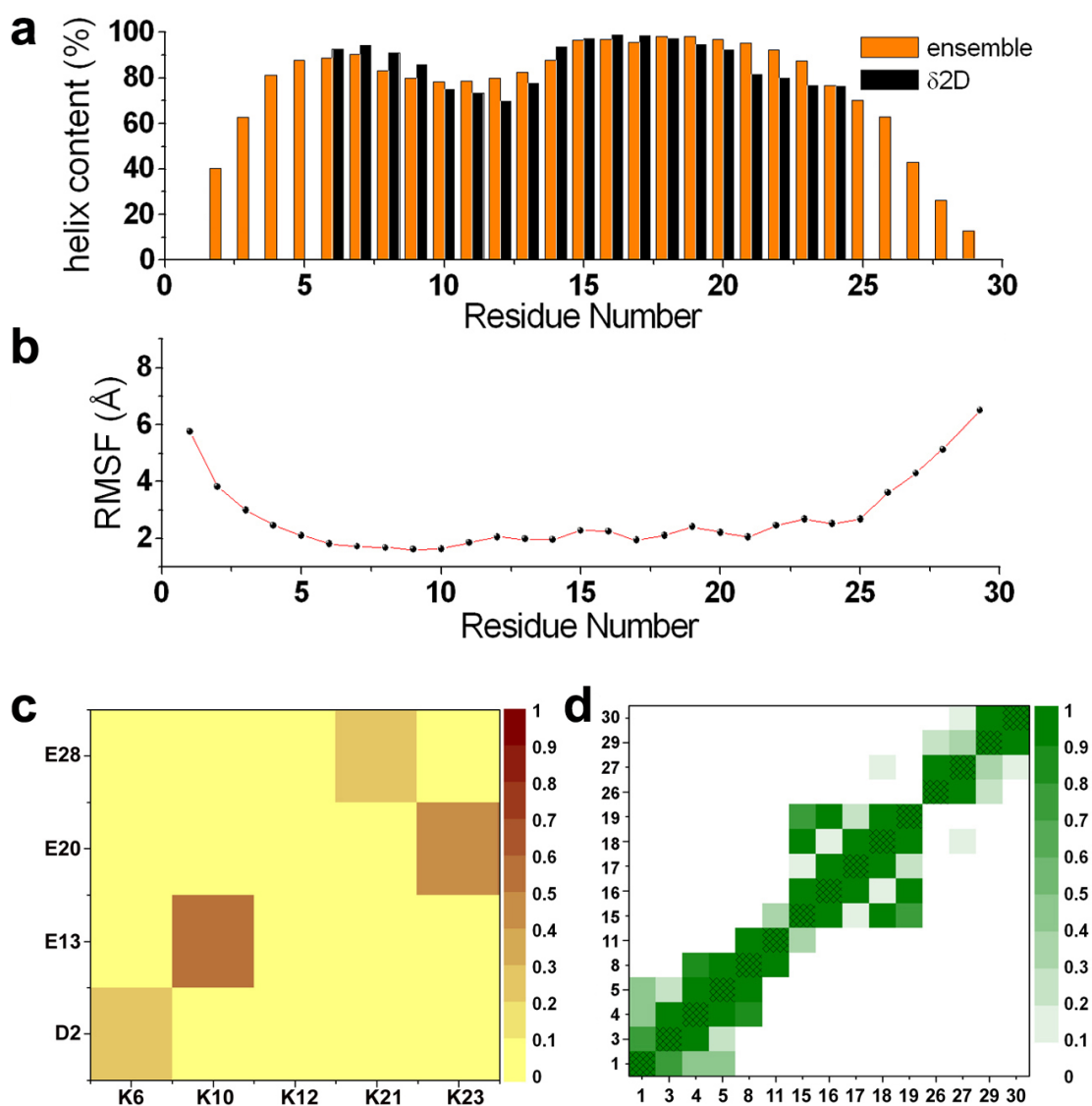


**Figure 3.11 Structural properties of the  $\alpha S_{1-30}$  ensemble. a)** Comparison between the  $\alpha$ -population of  $\alpha$ -helix along the sequence of  $\alpha S_{1-30}$  in the structural ensemble, which was calculated by using the DSSP (152), and as estimated from the analysis of chemical shifts by means of  $\delta 2D$  (89), which estimates the populations of secondary structure elements using a statistical mechanics approach to the CS. **b)** Root mean square fluctuations (RMSF), reporting the standard deviations of the position of  $C^\alpha$  atoms in the ensemble. **c)** Identification of salt bridges in the ensemble, calculated using a cutoff of  $5.0 \text{ \AA}$  between the centres of masses of the charged groups of the sidechains. The occurrence of the salt bridges in the ensemble is color coded from 0 (yellow) to 1 (brown). **d)** Identification of hydrophobic contacts, calculated using a cutoff of  $5.0 \text{ \AA}$  between the centres of masses of the hydrophobic sidechains. The axes indicate residue numbers. The occurrence of hydrophobic contacts in the ensemble is color coded from 0 (white) to 1 (dark green).

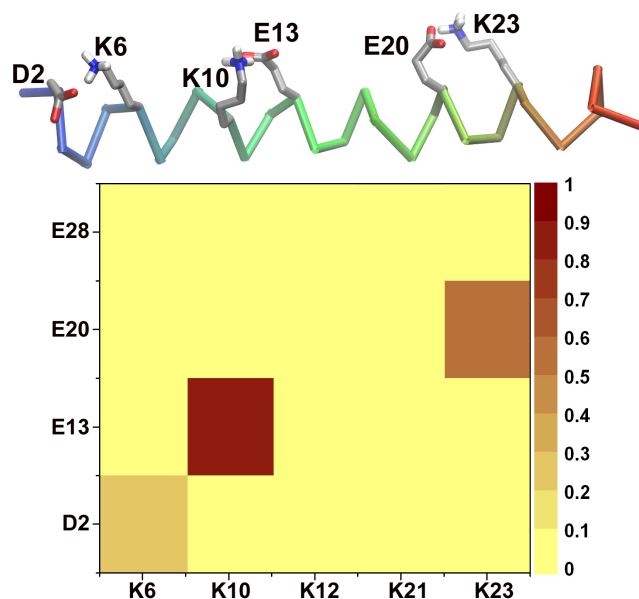


**Figure 3.12. Map of the occurrence of salt bridges in the main basin of the FES of  $\alpha S_{1-30}$ .** Salt bridges are identified using a cutoff of 5.0 Å between the centres of masses of the charged groups of the sidechains. The populations of each salt bridges in the ensemble are color coded from 0 (yellow) to 1 (brown). The structure above is the representative conformation of the main basin of the FES (Fig. 1).

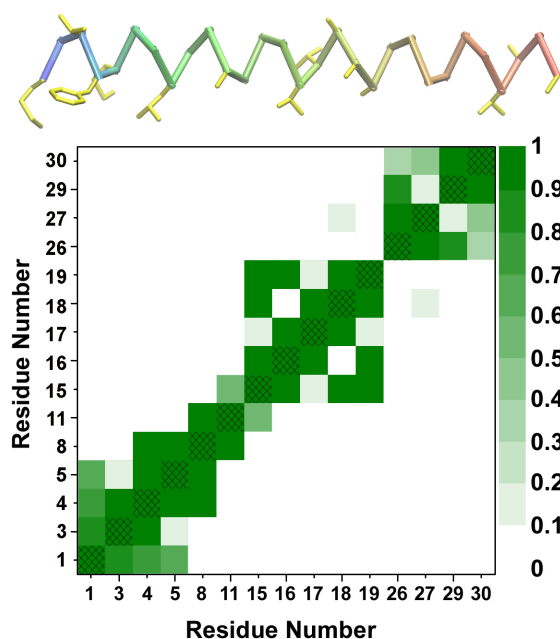


**Figure 3.13. Map of the contacts of the hydrophobic patches in the main basin of the FES of  $\alpha S_{1-30}$ .** Hydrophobic contacts are identified using a cutoff of 5.0 Å between the centres of masses of the hydrophobic sidechains. The populations of each hydrophobic contact in the ensemble are color coded from 0 (white) to 1 (green). The structure above is the representative conformation of the main basin of the FES (Fig. 1).

### **3.5 Topology of the membrane-anchor region of $\alpha$ S at the surface of SUVs**

A detailed characterisation of the topological properties of the membrane-anchor region of  $\alpha$ S at the surface of SUVs is crucial for elucidating the biological behavior of the protein. In order to characterise this fundamental aspect of the membrane bound state of  $\alpha$ S, we performed CS-restrained MD simulations of  $\alpha$ S<sub>1-30</sub> in explicit DOPE:DOPS:DOPC bilayers and explicit waters, using simulation procedures that we have described previously(153). The simulations, totalling 1  $\mu$ s in length, were restrained using experimental data measured from full length  $\alpha$ S bound to SUVs.

The restrained simulations provide a detailed description of the energy terms of interaction between  $\alpha$ S<sub>1-30</sub> and hydrophilic/hydrophobic regions of the DOPE:DOPS:DOPC bilayers (Figure 3.14). In particular, this indicates the presence of strong stabilising van der Waals' interactions between the side chains of residues M1, V3, F4, L8 and hydrophobic groups of the lipid tails (Figure 3.14 b), which result from a number of intermolecular contacts between these residues and the lipid chains (Figure 3.14 d). Electrostatic interactions between M1, K6, K10 and K12 and charged groups of the lipids are also observed, evidencing a stabilising factor for the membrane binding by the N-terminal region of  $\alpha$ S<sub>1-30</sub> (Figure 3.14 c), which represents a consistent key factor within different membrane binding systems (154-156). Overall these data indicate that the initial 12 residues of the protein sequence enable  $\alpha$ S to establish tight interactions with the membrane, including the internal hydrophobic region of the lipid bilayer. These interactions were found to be associated with a tilt angle ( $\theta$ ) of 12° (Figure 3.15 a) between  $\alpha$ S<sub>1-30</sub> and the membrane surface suggesting a degree of partial insertion in the membrane.

To gain further evidence for the topological orientation of membrane-anchored regions of  $\alpha$ S at the surface of acidic lipid bilayers, we utilised oriented ssNMR experiments to measure the <sup>15</sup>N chemical shift anisotropy (<sup>15</sup>N-CSA) of residues from regions of the protein that are tightly associated with the membrane. Indeed, <sup>15</sup>N-CSA data are sensitive probes of the tilt ( $\theta$ ) angles of  $\alpha$ -helices in membrane proteins (157, 158) and their overall dynamical behaviour (144, 159-161). By using cross-polarisation (CP) experiments, we therefore measured the <sup>15</sup>N spectrum of the full-length  $\alpha$ S bound to magnetically-aligned *flipped* bicelles (127, 162), which enable orienting the lipid bilayer

orthogonally to the static magnetic field at 25 °C (see methods). Previous CP measurements of  $\alpha$ S bound to SUVs at the magic angle spinning ssNMR could enable the assignment of the resonances of residues 6 to 25 of the membrane-anchor region by showing a significant increase in sensitivity when reducing the temperature from 4 °C to -19 °C (114). As the optimal condition for magnetic alignment of bicelle samples requires a temperature of 25 °C, oriented ssNMR measurements of membrane-bound  $\alpha$ S are extremely challenging, however, in this study we compensated the partial loss of signal to noise associated with this temperature with a lipid mixture that includes the negatively charged 1-hexadecanoyl-2-[9Z-octadecenoyl]-sn-glycero-3-phospho-[1'-rac-glycerol] (POPG), which has been shown to enhance the affinity for membrane binding of  $\alpha$ S by preserving the structural and dynamical properties of its membrane-anchor region (114). The resulting  $^{15}\text{N}$  CP of the full-length  $\alpha$ S bound to aligned bicelles showed peaks in both the isotropic ( $\sim$ 120 p.p.m.) and the anisotropic (ranging from 60 to 110 p.p.m.) regions of the spectrum. The isotropic component of the CP spectrum is attributed to those regions of  $\alpha$ S that are still highly disordered in its membrane-bound state, whereas the anisotropic peaks are associated with structured residues belonging to the membrane-anchor region, as previously detected in CP experiments at the magic angle spinning (114). The signal to noise in these  $^{15}\text{N}$  CP was not sufficient to perform multidimensional NMR spectra to enable peak assignment, however, indications on the orientation of  $\alpha$ S with respect to the membrane were obtained by analysing the range of  $^{15}\text{N}$ -CSA (see methods and figure 3.16). This analysis indicated that the membrane-anchored residues of  $\alpha$ S adopt a tilt angle of *ca* 15° with respect to the lipid bilayer (Figure 3.15 b), in striking agreement with the CS-restrained MD simulations.

The evidenced tilt angle of *ca* 15° of the N-terminal region of  $\alpha$ S with respect to the lipid bilayer requires a partial insertion of the N-terminal residues in the hydrophobic region of the membrane. In order to obtain a detailed characterisation of this topological aspect, we calculated the average positions of the amino acid residues in our simulations of  $\alpha\text{S}_{1-30}$  with respect to the membrane normal (Figure 3.17). This analysis evidenced that those residues in the region 1-12 are up to 8 Å more inserted in the lipid bilayer than the rest of the membrane-anchor region. This is exemplified with F4 and A18, both orienting their side chains on the same side of the amphipathic helical conformation of  $\alpha$ S, that show average positions on the membrane normal of 8.9 Å and 16.9 Å from the centre of

the lipid bilayer, respectively (Figure 3.17 b). This analysis also evidenced that the five N-terminal residues of  $\alpha S$ , which establish key electrostatic and van der Waals interactions with the membrane (Figure 3.14), are associated with a higher degree of variability along the membrane normal than the following region 6-25. This finding suggests that the local conformational heterogeneity of the region 1 to 5 is responsible for peak broadening that prevents the assignment of its resonances in  $^{13}\text{C}$ - $^{13}\text{C}$ -DARR spectra (114).

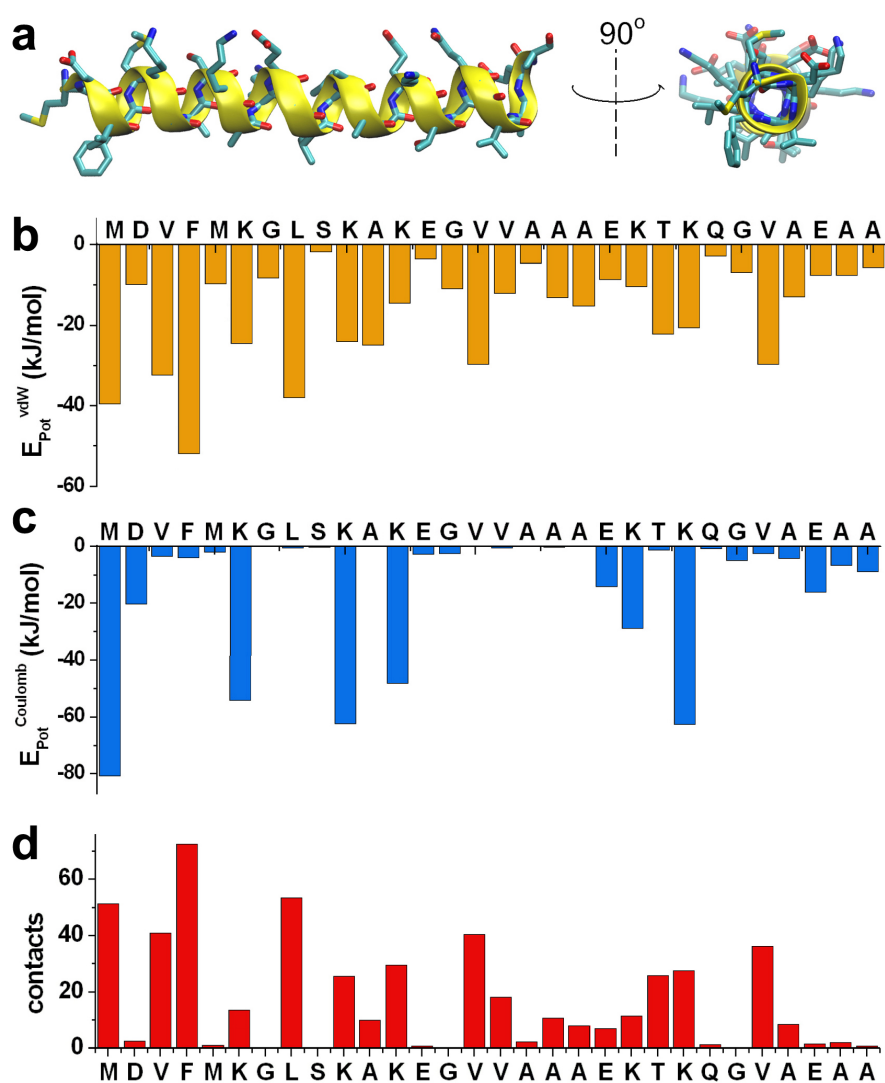


**Figure 3.14. Interaction terms between  $\alpha S_{1-30}$  and DOPE:DOPC:DOPS lipid bilayer. a)** Ribbon representation of a representative conformation from the main basin in the FES of  $\alpha S_{1-30}$  (Fig. 2.10). Sidechains are represented by sticks. **b-d)** Coulomb (**b**) and van der Waals (**c**) energies (kJ/mol) for the sidechain-lipid interactions in CS-restrained simulations (see Methods). **(d)** Average number of sidechain-lipid contacts in the ensemble. Contacts are identified using a cutoff of 5.0 Å between the heavy atoms of the sidechains and the lipids.

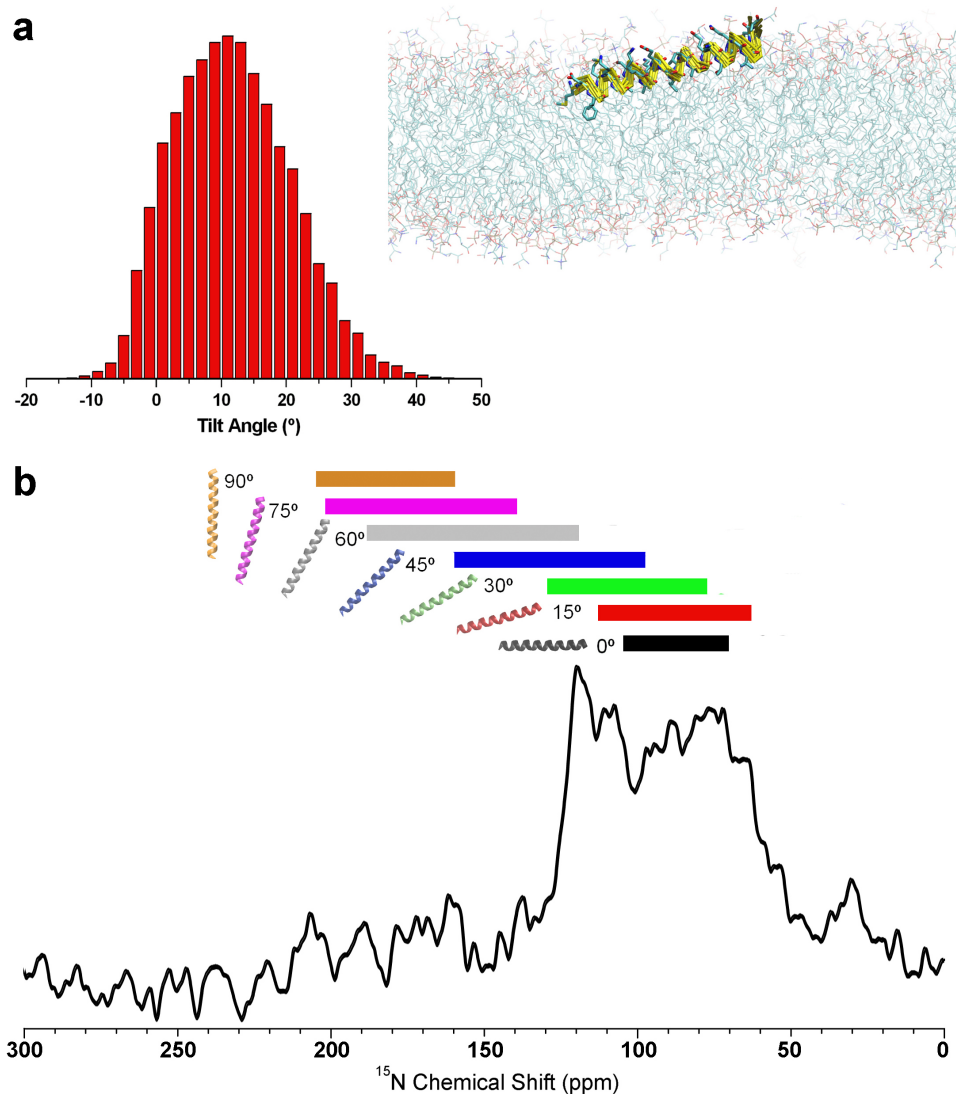


**Figure 3.15. Orientation  $\alpha S_{1-30}$  bound to lipid bilayers. a)** Orientations of  $\alpha S_{1-30}$  with respect to the membrane surface in the structural ensemble generated by using CS-restrained simulations. The angle is calculated as that between the axis of the helix and the local surface plane of the membrane. The latter is interpolated across the phosphorus atoms of the head groups of the lipid molecules that are positioned within 10 Å of any of the protein atoms. **b)**  $^{15}\text{N}$  chemical shifts of  $\alpha S$  at the surface of magnetically aligned bicelles obtained by CP measurements in oriented ssNMR. The plot shows the estimated ranges (see methods and figure 3.16) of  $^{15}\text{N}$ -CPA as a function of the orientation of  $\alpha S_{1-30}$  with respect to the lipid bilayer. The analysis evidences that the experimental  $^{15}\text{N}$ -CPA occupy a region of the  $^{15}\text{N}$  CP spectrum (60-110 ppm) that corresponds to the calculated range obtained by orienting the  $\alpha S_{1-30}$  ensemble at 15° with respect to the lipid bilayer (marked in red).

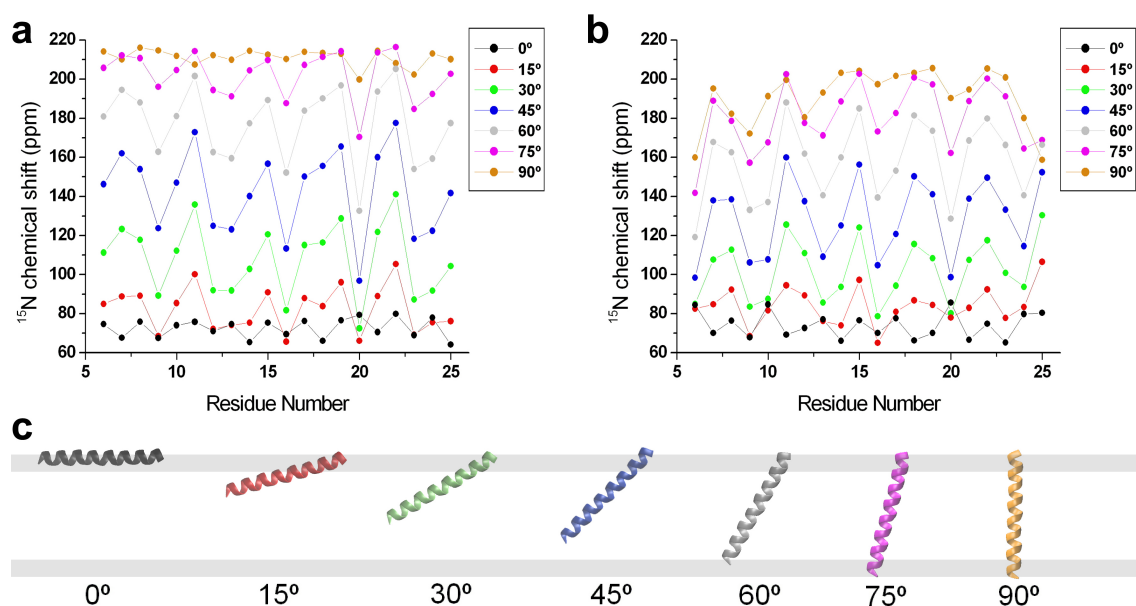


**Figure 3.16. Estimation of the ranges of  $^{15}\text{N}$ -CSA in aligned samples of membrane-bound  $\alpha\text{S}$ .** **a)** Simulated  $^{15}\text{N}$ -CSA for the region spanning residues 6 to 25 of  $\alpha\text{S}$  structured in an ideal  $\alpha$ -helical conformation that is oriented at tilt angles ranging from 0 to 90 degrees with respect to the membrane surface. The lipid bilayer is assumed to adopt an orthogonal orientation with respect to the external magnetic field, as in the case of flipped bicelles employed in this work. The calculation has been restricted to region spanning residues 6 to 25 of  $\alpha\text{S}$ , which could be assigned in CP experiments at the magic angle spinning<sup>25</sup>. **b)** Calculated  $^{15}\text{N}$ -CSA as in panel **a**, but using the structural ensemble of  $\alpha\text{S}_{1-30}$  instead of a single conformation and overall parameter of 0.8 to account of the effect of the orientational dispersion of the employed bicelles (127). **c)** Illustration of the different tilt angles employed for panels **a-b**.

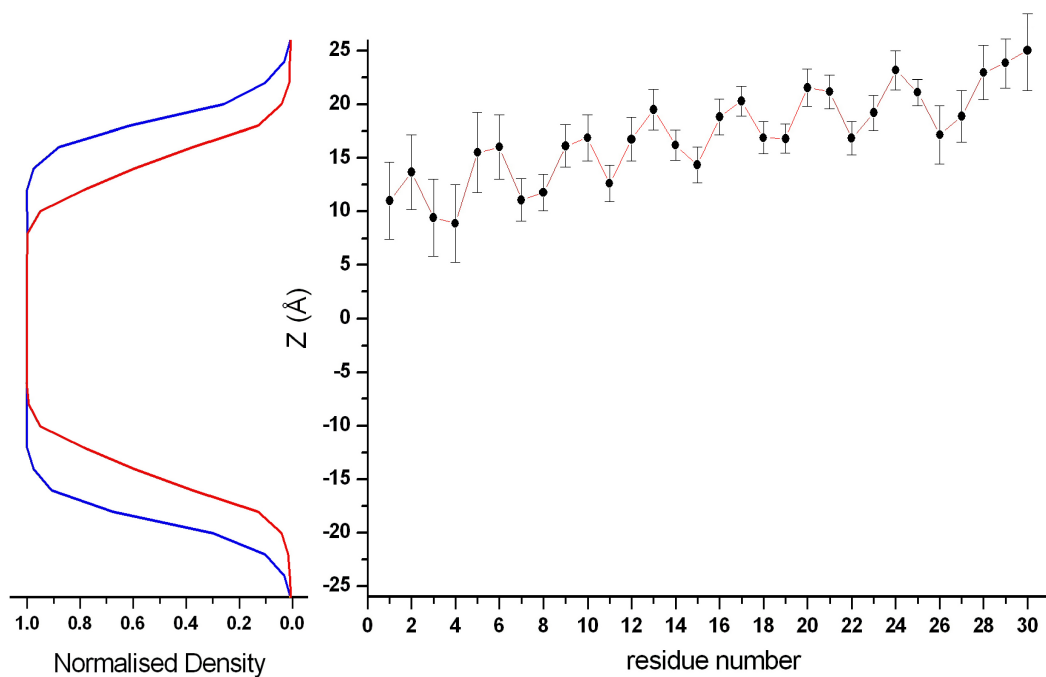


**Figure 3.17. Positions of residues of  $\alpha S_{1-30}$  on the membrane normal. a)** Normalised density of atoms from the lipid molecules in the direction of the membrane normal (blue). Red curve includes atoms from hydrophobic groups of the lipids only. **b)** Average positions of the centre of mass of each residue of the  $\alpha S_{1-30}$  projected on the membrane normal. The plot is referenced in the frame of the membrane, such that the centre of the lipid bilayer assumes a value of 0 on the membrane normal.

In order to look for further experimental evidence for or against the partial insertion of  $\alpha$ S into the lipid bilayer, we employed paramagnetic relaxation enhancement (PRE)(141) experiments to probe if transient contacts occur between  $\alpha$ S and the interior of the lipid bilayer. Initial PRE data were obtained in the presence of paramagnetic labels placed in the hydrophilic head groups, using the gadolinium salt of 1,2-dimyristoyl-sn-glycero-3-phosphoethanolamine-N-diethylenetriaminepentaacetic acid (Figure 3.18 a), and at the position of carbon 16 of the lipid tail, using 1-palmitoyl-2-stearoyl-[16-doxyl]-sn-glycero-3-phosphocholine (Figure 3.19 a). These two PRE experiments generated markedly different spectra, with only that performed by placing the spin label in the head group of the lipid resulting in selective peak broadening in  $^{13}\text{C}$ - $^{13}\text{C}$ -DARR. Based on the CS-restrained simulations, indicating that the first twelve residues of  $\alpha$ S can be partially inserted into the lipid bilayer upon binding, we extended the PRE using labelled lipids with unpaired electrons at the positions of carbons 5 and 10 of the lipid tail (Figure 3.20). In the first case,  $^{13}\text{C}$ - $^{13}\text{C}$ -DARR spectrum (Figure 3.20 a) showed a selective broadening of cross peaks corresponding to side chain groups of Valine ( $\text{C}^{\alpha}$ - $\text{C}^{\beta}$  and  $\text{C}^{\alpha}$ - $\text{C}^{\delta}$  cross correlations) and Lysine residues ( $\text{C}^{\alpha}$ - $\text{C}^{\beta}$  cross correlations). This result suggests that these groups of the protein are spatially close to the unpaired electron at the position of the carbon 5 of the lipid tail. The paramagnetic broadening of the resonances in the  $^{13}\text{C}$ - $^{13}\text{C}$ -DARR, however, is almost completely disappeared when the PRE experiments are performed by using spin labelled lipids with unpaired electrons at the position of the carbon 10 of the lipid tail (Figure 3.20 b), indicating that the insertion is limited to the upper part of the hydrophobic region of the membrane.

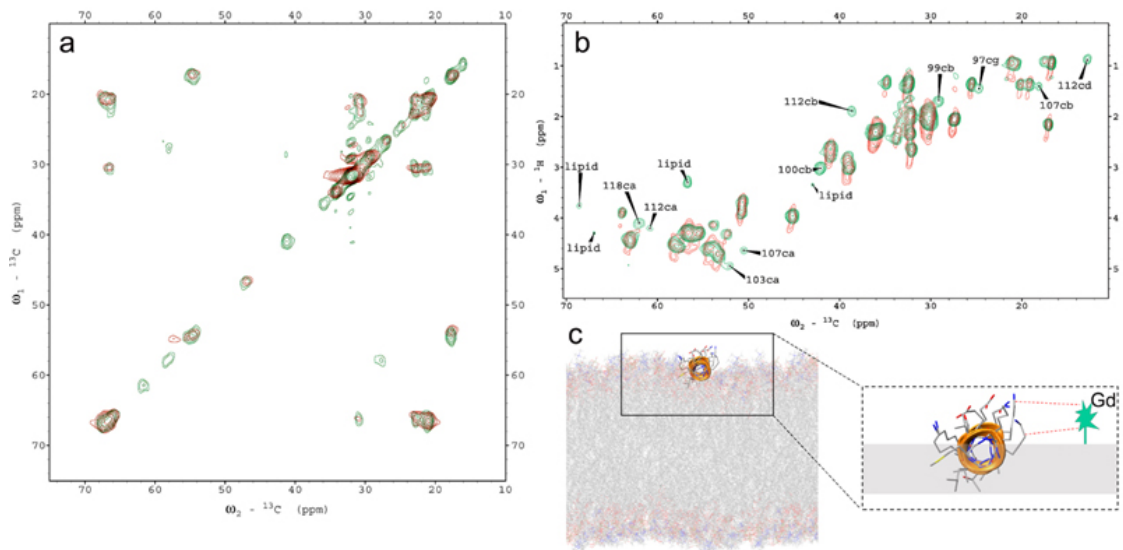


**Figure 3.18. Paramagnetic relaxation experiments of  $\alpha S$  bound to DOPE:DOPS:DOPC SUVs doped using a paramagnetic spin label on the membrane surface.** The DOPE:DOPS:DOPC mixture was doped with 2% of (1,2-dimyristoyl-sn-glycero-3-phosphoethanolamine-N-DTPA (gadolinium salt). Comparison between DARR and INEPT spectra with (red) and without (green) the spin label are shown in panels **a** and **b**, respectively. **c**) Schematic description of the PRE measurements using SUVs doped with PE-DTPA (Gd) lipids.

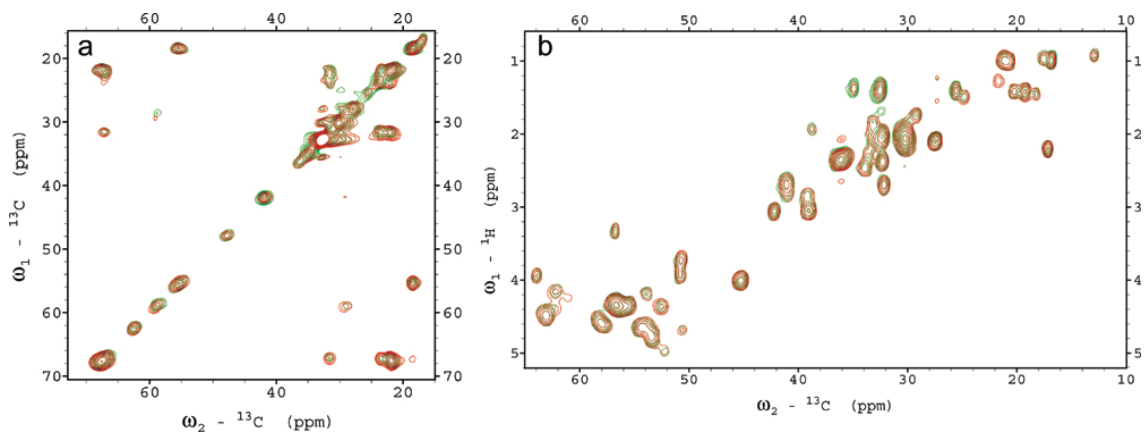


**Figure 3.19. Paramagnetic relaxation experiments of  $\alpha S$  bound to DOPE:DOPS:DOPC SUVs doped using a paramagnetic label in the interior of the membrane.** The DOPE:DOPS:DOPC mixture has been doped with 2% of [16 Doxyl PC] 1-palmitoyl-2-stearoyl-(16-doxyl)-sn-glycero-3-phosphocholine. Comparison between DARR and INEPT spectra with (red) and without (green) the paramagnetic label are shown in panels **a** and **b**, respectively.

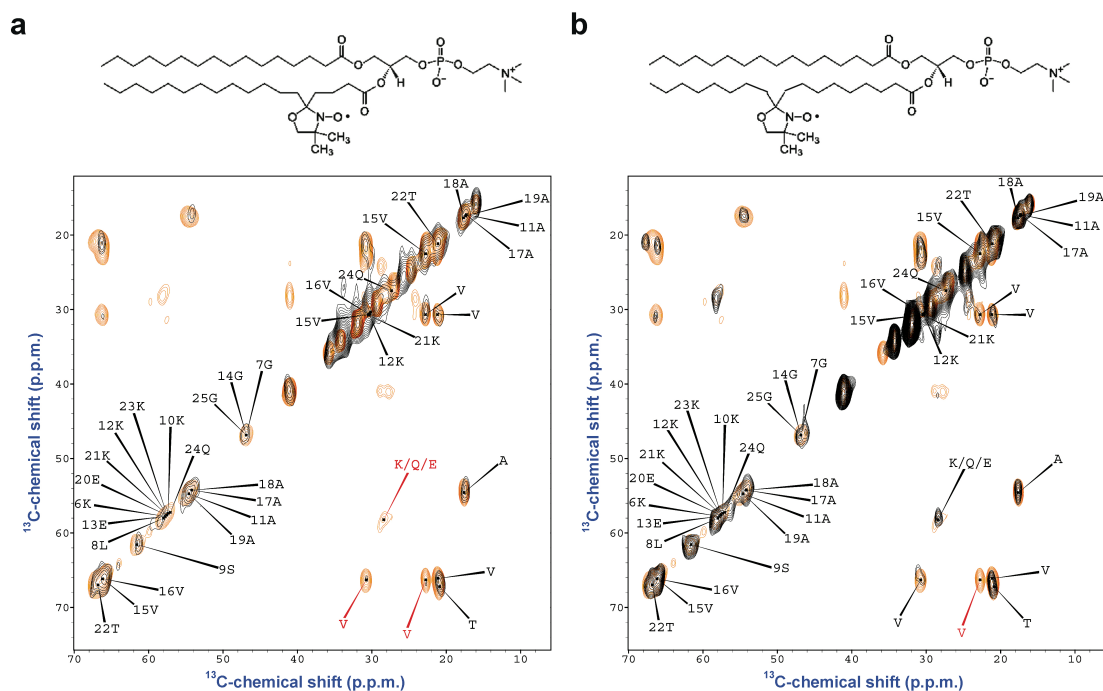


**Figure 3.20. Paramagnetic relaxation experiments of  $\alpha$ S bound to DOPE:DOPS:DOPC SUVs doped using a paramagnetic label in positions 5 and 10 of the lipid tails. a)** PRE of full length  $\alpha$ S bound to DOPE:DOPS:DOPC SUVs doped with 2% of 1-palmitoyl-2-stearoyl-[5-doxyl]-sn-glycero-3-phosphocholine, which carries an unpaired electron at the position of the carbon 5 of the lipid tail. The chemical structure of the paramagnetic labelled lipid is shown on the top of the figure. The bottom view shows the  $^{13}\text{C}$ - $^{13}\text{C}$ -DARR spectra the membrane-bound  $\alpha$ S measured as described previously (114) at mixing and contact times of 50 ms and 1 ms, respectively, and in the presence (black) and absence (orange) of paramagnetic labelled lipids. Under the conditions employed in this study, the  $^{13}\text{C}$ - $^{13}\text{C}$ -DARR spectra can detect the region spanning residues 6 to 25 of the membrane-bound  $\alpha$ S. Red labels evidence the pattern of selective peak attenuations, indicating a spatial proximity to the paramagnetic probe. **b)** PRE experiments performed using 1-palmitoyl-2-stearoyl-[10-doxyl]-sn-glycero-3-phosphocholine, which carries an unpaired electron at the position of the carbon 10 of the lipid tail.

### ***3.6 The central region of $\alpha$ S acts as a sensor to direct the membrane binding affinity***

We next carried out a series of chemical exchange saturation transfer (CEST) experiments (91, 112, 113) to gain a deeper understanding of the equilibrium between the unbound and bound states of  $\alpha$ S. The CEST approach is an ideal method for probing equilibria between NMR visible (detectable) and invisible (undetectable) states of proteins, including low molecular weight species that are transiently bound to slow-tumbling high-molecular-weight complexes, which indeed cannot be observed directly in solution NMR experiments as a result of excessive line broadening. In the CEST experiments, a continuous weak radiofrequency field is applied off-resonance (by up to 28 kHz) in the  $^{15}\text{N}$  channel, thereby saturating the broad spectroscopic transitions in the bound (undetectable) state but leaving the resonances of the free (detectable) state virtually unperturbed (91, 112, 113). The saturation of the bound state can then be transferred to the free state *via* chemical exchange, attenuating the intensities of the observable resonances of the latter. By carrying out a series of experiments at various offsets, it is possible to obtain a map of the strength of interactions between the low and high molecular weight species at a residue specific resolution.

In the presence of a small quantity of SUVs (0.06% of lipid mixture, 0.6 mg/ml) all of the  $\alpha$ S resonances are detectable in the  $^1\text{H}$ - $^{15}\text{N}$  HSQC spectra, and only marginal changes in the peak intensities are observed. By contrast, substantial differences are observed in CEST experiments (Figure 3.21 a), which in the presence of SUVs evidenced specific resonances from the protein sequence that exhibit strong saturation effects over a broad range of offsets resulting in symmetric CEST profiles (Figure 3.21 b). In probing the interactions between  $\alpha$ S and DOPC:DOPE:DOPS SUVs, these experiments show clearly that the strongest saturation effects are observed for residues in the N-terminal region of the protein, indicating that this segment has a tighter association with the SUVs than any other region of the protein (Figure 3.21 b). The saturation effects decrease gradually for residues 26-97 with a sharp transition in the vicinity of residue 98, where the peak intensities of the resonances coincide with those observed in the absence of lipids (Figure 3.23). These experiments therefore provide a residue-specific measure of the magnitude of the interactions between  $\alpha$ S and DOPC:DOPE:DOPS SUVs, and these results are fully

consistent with the conclusions of the ssNMR experiments discussed above. Together these findings reveal that the N-terminal region of  $\alpha$ S bound to SUVs forms a stable helix that interacts strongly with the surface of the lipid bilayer while the C-terminal region of the protein is highly dynamic and motionally independent of the SUVs.

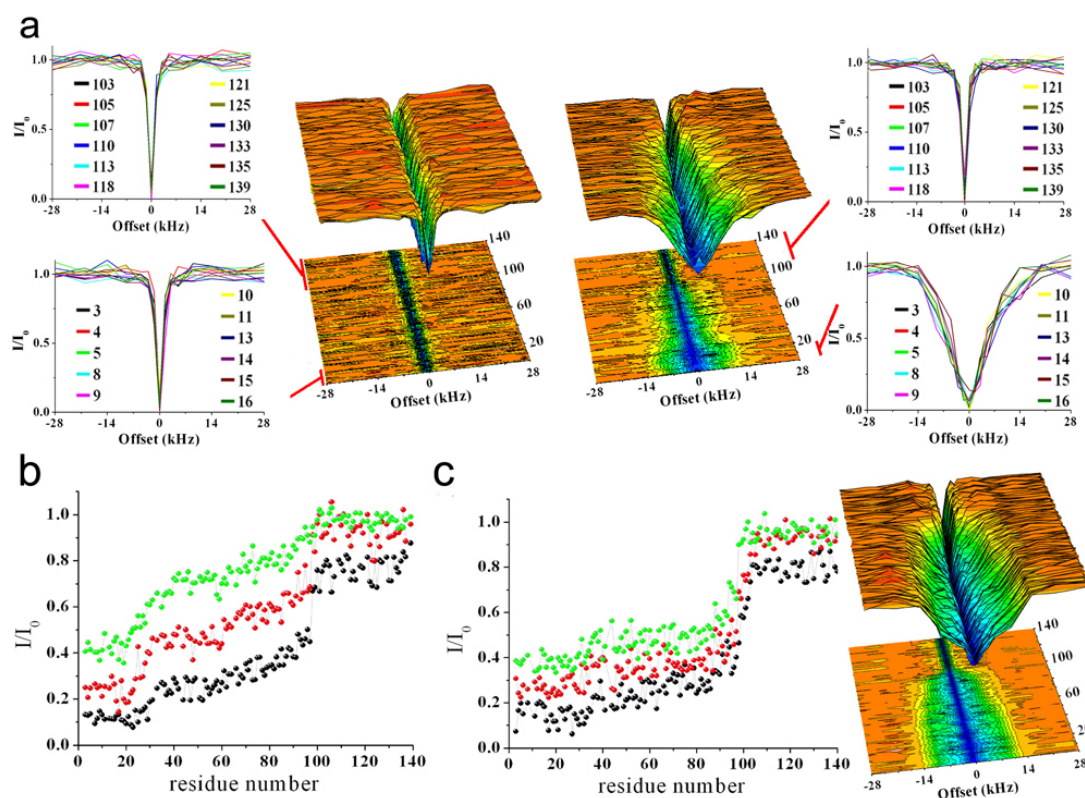


**Figure 3.21. CEST experiments probing the membrane-sensor interactions of  $\alpha$ S.** CEST experiments were recorded at a  $^1\text{H}$  frequency of 700 MHz (see Methods), using a protein concentration of 300  $\mu\text{M}$  and 0.06% (0.6  $\text{mg ml}^{-1}$ ) of DOPE:DOPS:DOPC lipids in a ratio of 5:3:2 and assembled in SUVs.  $^1\text{H}$ - $^{15}\text{N}$ -HSQC spectra were recorded by using a continuous wave saturation (170 Hz or 350 Hz) on the  $^{15}\text{N}$  channel at a range of offsets: -28, -21, -14, -9, -5, -3, -1.5, 0, 1.5, 3, 5, 9, 14, 21 and 28 kHz. An additional spectrum, saturated at -100 kHz was recorded as a reference. Data recorded using 350 Hz are shown (data measured using 170 Hz are reported in Figure 3.22 a). **a)** CEST surface for unbound (left) and bound (right)  $\alpha$ S; the upper and lower inserts report individual CEST profiles for residues at the N- and C-termini, respectively. **b)** CEST saturation along the  $\alpha$ S sequence. Black lines refer to the averaged CEST profiles measured using offsets at  $\pm 1.5$  kHz. Similarly, profiles for  $\pm 3$  kHz and  $\pm 5$  kHz are shown in red and green, respectively. **c)** The interactions between  $\alpha$ S and POPG SUVs probed by CEST. Labels as in panel b. The data were measured using 350 Hz, (see Figure 3.22 b for data acquired using 170 Hz).

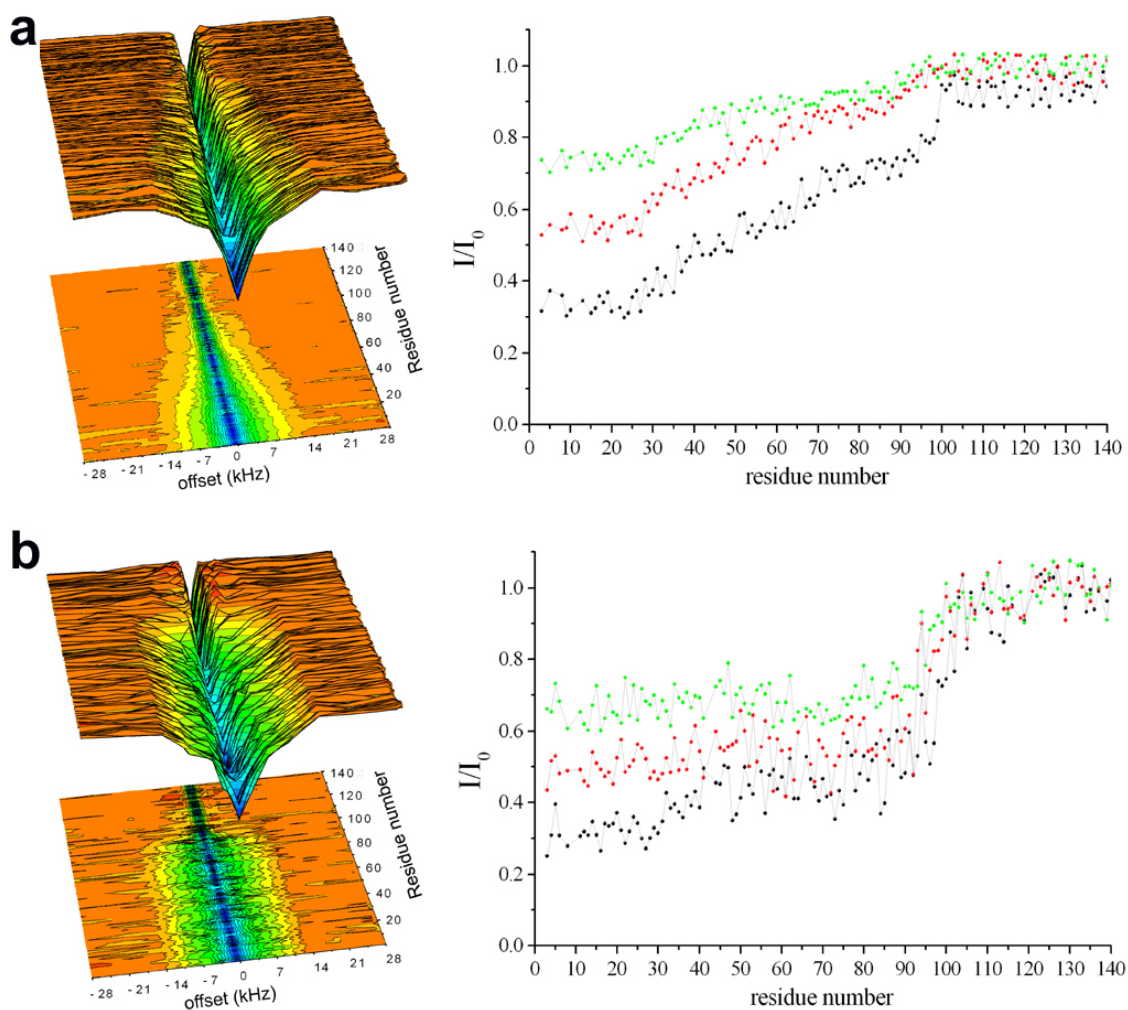


**Figure 3.22. CEST experiments recorded using a RF value of 170 Hz.** **a)** Experiments were performed on a 700 MHz Bruker Avance III NMR spectrometer, with a TCI cryoprobe, using a protein concentration of 300  $\mu$ M and 0.06% of DOPE:DOPS:DOPC SUV in a ratio of 5:3:2. Continuous wave saturation was carried out in the  $^{15}\text{N}$  channel and applied on  $^1\text{H}$ - $^{15}\text{N}$  HSQC spectra. Saturation was performed at different offsets of -28, -21, -14, -9, -5, -3, -1.5, 0, 1.5, 3, 5, 9, 14, 21 and 28 kHz. An additional spectrum, saturated at -100 kHz was recorded as reference. The left panel reports the CEST surface. The right panel reports individual CEST saturations along  $\alpha$ S sequence. The black lines refer to the averaged CEST profiles measured using offsets at  $\pm 1.5$  kHz. Similarly, profiles for  $\pm 3.0$  kHz and  $\pm 5.0$  kHz are reported in red and green, respectively. **b)** Experiment performed with the same setting of panel a, but by using POPG SUV.

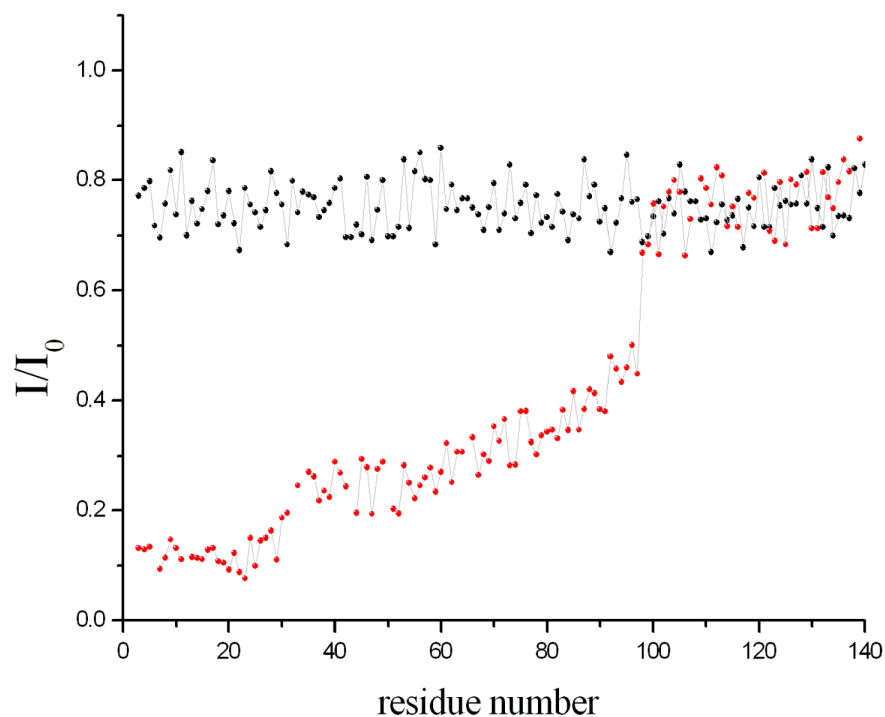


**Figure 3.23. Degree of CEST saturation along  $\alpha$ S sequence.** Profiles are averaged between CEST measured using offsets at  $\pm 1.5$  kHz. The ratio of the intensity with saturation ( $I$ ) and without saturation ( $I_0$ ) is reported as a function of the residue number. The black line and red lines refer to  $\alpha$ S unbound and bound to SUVs, respectively.

In order to probe the effects of lipid composition on the affinity of  $\alpha$ S for membranes, we studied the interactions of  $\alpha$ S with SUVs consisting of 1-hexadecanoyl-2-(9Z-octadecenoyl)-sn-glycero-3-phospho-(1'-rac-glycerol) (POPG) lipids.  $\alpha$ S has been shown to bind strongly to such lipid vesicles(163) and with an affinity that is approximately three fold higher than that found for DOPE:DOPS:DOPC SUVs (120). This finding is in good agreement with our CD measurements which enabled apparent dissociation constants to be calculated and give values for  $K_d$  of  $93 \pm 15 \mu\text{M}$  for POPG and  $261 \pm 21 \mu\text{M}$  for DOPE:DOPS:DOPC SUVs under the conditions employed in the present study. Despite the different binding affinities, however, no significant differences were observed between the DARR spectra of  $\alpha$ S bound to POPG (Figure 3.24) and those of  $\alpha$ S bound to DOPE:DOPS:DOPC vesicles (Figure 3.2 a), indicating that the regions of the protein that are rigid in the membrane bound state are essentially identical for the two types of SUVs.

When CEST experiments were repeated with SUVs prepared with POPS lipids (163) (Figures 3.20 c and 3.24), the saturation profiles obtained under these conditions are generally similar to those obtained with DOPC:DOPE:DOPS SUVs, where resonances of residues of the membrane-associated N-terminus are strongly affected by off-resonance saturation, while those of the residues of the C-terminus are essentially unchanged in intensity. A significant difference in the saturation profiles is, however, found for the central region of the sequence (residues 26-97) which shows remarkably stronger levels of saturation when bound to SUVs composed of POPS lipids (Figure 3.20 c) compared to those observed in the presence of DOPE:DOPC:DOPS SUVs (Figure 3.20 a,b). These data suggest that different regions of  $\alpha$ S have distinct roles in the process of association with lipid membranes, such that the N-terminal  $\alpha$ -helix (residues 6-25) acts to anchor  $\alpha$ S strongly to the membrane, and is only marginally affected by lipid composition, while the region 26-97 appear to act as a membrane ‘sensor’, modulating the strength of the interactions in a lipid-specific manner.

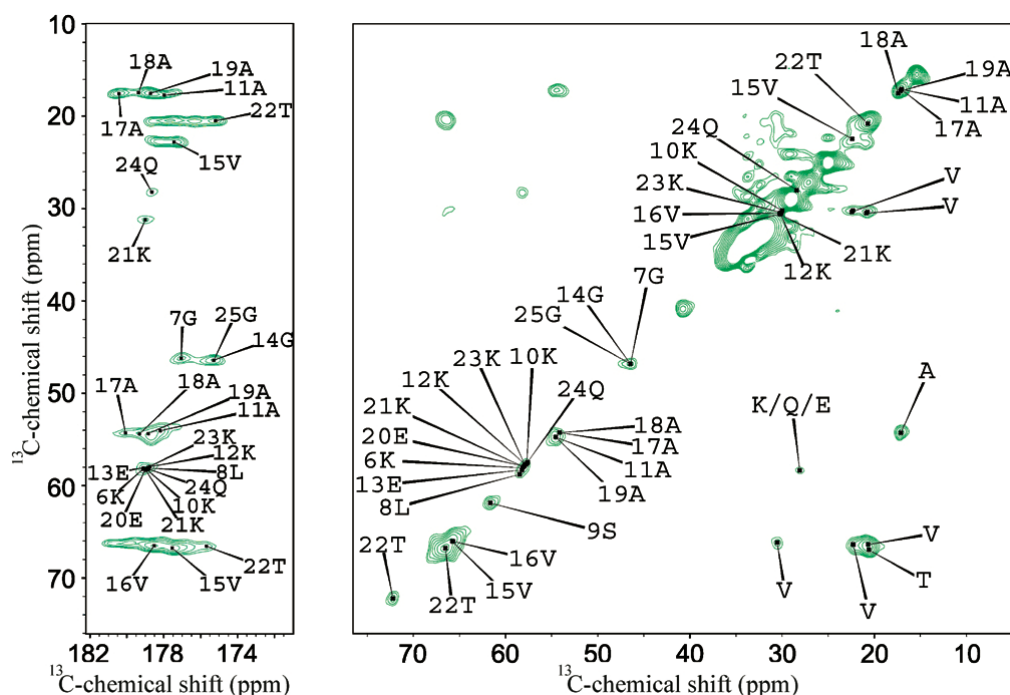


**Figure 3.24. MAS ssNMR spectrum of  $\alpha$ S bound to POPS SUV.** The carbonyl region (left panel) and the aliphatic region (right panel) are shown in a  $^{13}\text{C}$ - $^{13}\text{C}$  DARR correlation spectrum of a sample of  $\alpha$ S bound to POPS SUV recorded using a contact time of 100 ms at a temperature of  $-19^\circ\text{C}$  at a MAS rate of 10 kHz. Residue names are reported using the single letter convention.

### ***3.7 The C-terminal region of $\alpha$ S establishes transient interactions with the surface of synaptic-like vesicles***

The solution NMR measurements of CEST and ssNMR indicate that the regions of  $\alpha$ S that interact significantly with the lipid surfaces are the N-terminal “membrane-anchor” and the central “sensor” regions. The C-terminal acidic region of the protein (residues 98-140) is mainly unstructured and maintains the same pattern of random-coiled chemical shifts in solution NMR  $^1\text{H}$ - $^{13}\text{C}$ -HSQC and ssNMR  $^1\text{H}$ - $^{13}\text{C}$  INEPT spectra (Figure 3.7). Moreover CEST experiments show that the saturation profiles of this region are the same in the presence and in the absence of SUVs (Figure 3.23). These data suggest that the C-terminal region of  $\alpha$ S has negligible affinity for acidic lipid bilayers and remains essentially detached from the membrane surface in the bound state of the protein. We further investigate on the nature of the interactions of the C-terminal region with the SUVs surface by using PRE. Indeed PRE are sensitive to even transient interactions, which might not be probed by chemical shift changes. In the analysis of PRE measured by labelling the surface of SUVs with 2% of gadolinium salt of 1,2-dimyristoyl-sn-glycero-3-phosphoethanolamine-N-diethylenetriaminepentaacetic acid, we observed non-negligible attenuations of some of the signals in the  $^1\text{H}$ - $^{13}\text{C}$  INEPT spectrum of  $\alpha$ S (Figure 3.18 b), including the positively charged K97 and 102, the uncharged polar residues Q99 and N103, and the hydrophobic residues L100, A107, P108, I12, I113, P117, V118, P120. No attenuations of the peaks in the  $^1\text{H}$ - $^{13}\text{C}$  INEPT spectrum of  $\alpha$ S were however found when the PRE were measured by labelling the lipids at the position of the carbon 16 (Figure 3.19 b). These findings indicate that the C-terminal region of  $\alpha$ S interacts weakly and transiently with the membrane surface when bound to SUVs. This property might have a very significant importance in driving the biological properties of  $\alpha$ S at the surface of synaptic vesicles. Indeed the C-terminal region of the protein has been shown to be of fundamental importance in the interaction of  $\alpha$ S with synaptobrevin-2, which likely is a fundamental factor interplaying with the chaperone role of  $\alpha$ S in assisting the formation of the SNARE complex during SV exocytosis.

### **3.8 Discussion**

Although it is now generally recognized that the formation of fibrillar aggregates by  $\alpha$ S is a hallmark of Parkinson's disease, much remains to be understood about the physiological role of this protein (4).  $\alpha$ S possesses an eclectic character and the ability to adopt different conformations resulting in a variety of cytosolic, membrane-bound and aggregated states. In aqueous solutions (15) as well as in cellular milieu (16),  $\alpha$ S has been shown to behave as an intrinsically disordered protein, although there has been evidence for and against the possible existence of more highly structured forms of soluble  $\alpha$ S in some environments and in complexes (26, 27). Considerable attention has also been focused on the membrane-associated state of  $\alpha$ S, which has been suggested to be of great significance in both physiological and pathological contexts. It is indeed evident that  $\alpha$ S exists *in vivo* in an equilibrium between cytosolic and membrane-bound states, with membrane partitioning being tightly regulated (3, 164).

A particularly intriguing issue in this context is the mechanism by which the affinity of  $\alpha$ S to lipid membranes is modulated. There is strong evidence that the population of the bound state is regulated by the intrinsic structural properties of  $\alpha$ S and on the composition and the physical properties of the membrane bilayer, such as curvature, charge, packing defects and surface hydrophobicity (20, 118, 119, 146, 165).

We explored this fundamental issue by probing the structure and conformational dynamics of  $\alpha$ S bound to membranes in its physiological, non-aggregated state. This membrane-bound state is effectively intractable to current X-ray crystallography techniques but the success of solution state NMR spectroscopy in describing the disordered soluble protein (15, 16, 18-21, 118, 146, 166, 167) and of solid state NMR studies in defining the structural properties of the polymorphic forms of the aggregated state of  $\alpha$ S (57, 168-170) has prompted us to explore the use of a combination of these techniques to define the structures and dynamics of  $\alpha$ S bound in its non-aggregated state to lipid membranes.

Our approach could directly probe the interaction with lipid mixtures that mimic those of synaptic vesicles without requiring alterations of the protein sequence or any chemical modification. We have found that, in line with the metamorphic nature of  $\alpha$ S (171), three distinct regions of this protein, namely the N-terminal, central, and C-terminal segments (Figure 3.25) interact in very different ways with lipid bilayers as a

result of their different structural and dynamical properties. The N-terminal 25 residues, which we denote as the membrane anchor region, adopt a well-defined and highly motionally restricted  $\alpha$ -helical conformation that appears to be largely independent of lipid composition. The finding that the resonances of this segment of  $\alpha$ S are detectable in cross polarisation spectra measured at the magic angle indicates that this region of  $\alpha$ S associates with the lipid bilayer with significantly high affinity, despite being in rapid equilibrium between its bound and unbound states (exchange constant of *ca* 200 ms(19)).

In order to define in detail the characteristics of this lipid-binding region, we generated an atomic resolution structural ensemble of the N-terminal 30 residues of  $\alpha$ S region bound to the lipid bilayers of DOPE:DOPS:DOPC SUVs by using MD simulations restrained with experimental chemical shifts. The resulting FES provided the structural determinants that stabilise the interaction with the membrane in this fundamental region for  $\alpha$ S binding to SUVs. In addition, we have probed the local topology of this region of the protein with respect to the lipid bilayer by using both simulations and experiments of oriented ssNMR and PRE. These studies indicate that  $\alpha$ S<sub>1-30</sub> adopts a topology in its membrane bound state that involves a partial insertion of the initial 12 residues in the lipid bilayer. This insertion is likely to contribute significantly to the overall ability of  $\alpha$ S to bind tightly to the vesicles, however, by remaining largely on the surface of the vesicles in a amphipathic helical conformation, the membrane-anchor region enables  $\alpha$ S to exist in rapid equilibrium between membrane-bound and membrane-detached states.

By contrast to the N-terminal membrane-anchor, the central segment of the protein (residues 26-97), which can be described as a membrane-sensor region, has intermediate dynamical properties. This region is indeed too flexible to be detected by cross-polarization experiments but too rigid to be seen by INEPT-type transfer experiments. It is legitimate to assume, based on EPR measurements (119, 121) and transferred NOE data (19), that this membrane-sensor region adopts  $\alpha$ -helical structure when transiently bound to a lipid membrane surface. The present results indicate that the NAC sequence, which has been shown to play a role in the mechanisms of  $\alpha$ S aggregation (4, 172-174), being included in the membrane-sensor region is also likely to have functional relevance, specifically in defining the affinity of  $\alpha$ S for lipid membranes and therefore to modulate the partitioning between membrane-bound and membrane-free states in the synaptic termini. Finally, we have found from PRE experiments that the C-terminal domain

(residues 99-140), which has been reported to be highly unstructured and extremely flexible, experiences weak and transient interactions with the membrane surface.

Taken together the data presented in this chapter characterise a series of key structural features of the membrane-bound state of  $\alpha$ S. Using a combination of solution and solid-state NMR techniques we could identify the nature of the interactions that  $\alpha$ S established with lipid assemblies (SUVs) that mimic synaptic-like lipid membranes. These data suggested a model to describe the interactions of  $\alpha$ S with membranes (Figure 3.25), which reconciles the results of a range of previous studies (18-21, 118-121, 146) and also sheds new light on the molecular determinants of binding affinity that are likely to be associated with the physiological role of  $\alpha$ S. The membrane interactions in the processes of  $\alpha$ S aggregation underscores the importance of the interplay between different functional states of  $\alpha$ S and its aggregation mechanism leading to Parkinson's disease.

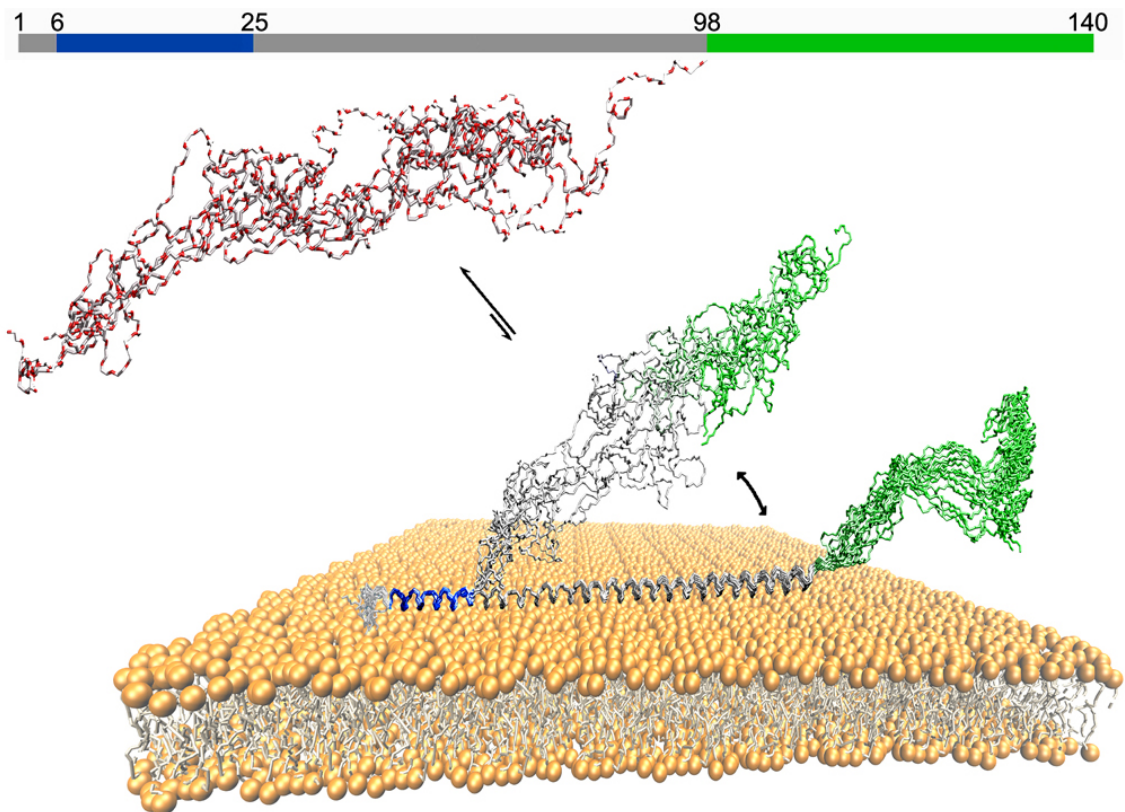


**Figure 3.25. Schematic illustration of the different roles of the three regions in of  $\alpha S$  in determining its interaction with lipid bilayers.** We identified three different regimes of protein dynamics and membrane affinity by using a combination of solution and solid state NMR spectroscopy. The N-terminal region (blue) is visible in DARR experiments, indicating that it is rigidly bound and anchored to the membrane. The central region (grey), showing intermediate dynamics and therefore being invisible in both CP and INEPT experiments, is suggested to play a key role in modulating the affinity of  $\alpha S$  for membranes. Finally a C-terminal fragment (green) maintains its unstructured nature and remains essentially uncorrelated with the membrane surface, despite showing weak and transient contacts in PRE experiments.

## Chapter IV

### ***Role of $\alpha$ S in Synaptic Vesicle Trafficking. Function Solved?***

#### ***4.1 Role of $\alpha$ S in synaptic vesicles homeostasis***

Despite the general consensus on its pathological relevance, the physiological role of  $\alpha$ S remains widely debated. In this context, a view is emerging in which  $\alpha$ S is involved in the dynamics of synaptic vesicle (SV) trafficking by regulating a distal reserve pool of SVs that controls the amount of vesicles docked at the synapses during neurotransmitter release(40, 175). This biological role is directly associated with the ability of  $\alpha$ S to bind to synaptic vesicles and induce their interaction and assembly *in vitro* and *in vivo*(19, 176-178). Indeed, in dopaminergic neurons  $\alpha$ S exists in a tightly regulated equilibrium(164) between a cytosolic monomeric form, which is predominantly disordered(17, 25, 100), and a membrane-bound state, which is rich in  $\alpha$ -helix structure in the region spanning residue 1 to 90 of the protein sequence(18, 19, 118, 150, 167, 179, 180).

We describe in this chapter a detailed characterisation of the dynamical and structural properties at the surface of synaptic-like vesicles of two familial  $\alpha$ S mutations that have opposite effects on its affinity for membrane binding (73, 181). On the basis of these studies, we characterised the details of the underlying mechanism by which a single molecule of  $\alpha$ S binds two different vesicles and promotes their interaction and assembly. This mechanism, which involves a double-anchoring step enabling  $\alpha$ S to form a dynamic link between two vesicles, was strongly supported by an experiment in which a variant of  $\alpha$ S was engineered to adopt structural properties in its membrane bound state that result in enhanced  $\alpha$ S-mediated interactions between vesicles while maintaining the same amino-acid composition, charge and membrane binding affinity of the wild type protein. The mechanism provides evidence that the exact level of affinity for membrane binding of the non amyloid-b component (NAC) region of  $\alpha$ S is a fundamental functional property enabling this protein to mediate the interaction between vesicles.

## **4.2 Materials and Methods**

### 4.2.1 $\alpha$ S purification.

$\alpha$ S was purified in *E. coli* using plasmid pT7-7 encoding for the protein as previously described(82). See Chapter II for further details.

### 4.2.2 Preparation of SUVs for solid-state and solution NMR.

Small unilamellar vesicles (SUVs) containing a molar ratio of 5:3:2 of DOPE:DOPS:DOPC (Avanti Polar Lipids Inc. Alabaster) were prepared from chloroform solution of the lipid. See Chapter III for further details. For ssNMR studies  $\alpha$ S was added to the SUV mixtures up to a molar ratio of 1:65 protein:lipid. The mixtures were then pelleted at 300,000 g for 30 min at 4°C (Beckman Coulter Optima TLX Inc. Brea, USA) by using a TLA 100.3 rotor. Subsequently the SUV- $\alpha$ S samples were transferred into 3.2 mm Zirconia XC thin-walled MAS rotors for ssNMR experiments. For STED, cryo-EM imaging experiments and DLS measurements, DOPE:DOPS:DOPC SUVs were prepared by extrusion through membranes with a 50 nm pore diameter (Avanti Polar Lipids, Inc) after re-hydration in 20 mM sodium phosphate (pH 6.0) at a concentration of 1.0 mg.ml<sup>-1</sup> (0.1%).

### 4.2.3 Purification of SVs from rat brain.

SVs composed of phospholipid molecules (amounting to 30% of their composition), proteins (58%) and cholesterol (12%)<sup>44,45</sup> were purified from brains of rat provided by Charles River Laboratories (Animal work was approved by the Named Animal Care & Welfare Officer (NACWO) and the Ethics Review Committee of the University of Cambridge). Rat brains were homogenised in 4mM HEPES and 320 mM sucrose buffer using protease inhibitors *via* ten strokes at 900 r.p.m. in a glass-Teflon homogenizer (Wheaton, Millville, USA) (182, 183). All steps were carried out at 4°C or in ice. The homogenates were centrifuged at 1000g for 10 min and the supernatants were collected and further centrifuged at 15000g for 15 min. The supernatants from the second centrifugation (Sup-2) were stored at 4°C. The pellets from the second centrifugation, which contained the synaptosomes, were lysed using ice-cold water by applying three strokes at 2000 r.p.m. Subsequently, HEPES buffer solutions containing protease inhibitors were added to the lysates and the resulting solutions were centrifuged at 17,000 g for 15 min, and the supernatant was combined with the Sup-2 supernatants. The

resulting mixtures were centrifuged at 48000g for 25 min and the supernatants were loaded onto a 0.7 M sucrose cushion and centrifuged at 133,000 g for 1 h. The bottom half of the sucrose cushion was pooled and centrifuged at 300,000 g for 2 h. The pellets were resuspended in buffer (100 mM Tris-HCl, pH 7.4, 100 mM KCl) and loaded onto a Sephacryl S-1000 size-exclusion chromatography column (100 × 1 cm) resulting in a distinctive peak of the SVs(182, 183). The SVs were then stained against specific SV antibodies, including synaptotagmin 1, synaptobrevin 2, by western blot(182, 183). In order to perform dSTORM analyses, the SVs were incubated with a primary antibody (dilution 1:1000) that specifically recognizes synaptotagmin 1 (105103, Synaptic Systems, Göttingen, Germany) and a secondary antibody (dilution 1:100) fluorescently labeled with Atto 647N (40839, Sigma-Aldrich, St Louis, USA).

#### 4.2.4 Magic angle spinning measurements using ssNMR.

MAS experiments in this chapter were carried out using a 16.85T Bruker Spectrometer with a 3.2 mm E<sup>Free</sup> probe (University of Minnesota) or using a 14.09T Bruker Ascend magnet with Avance III HD console and equipped with a 3.2 mm E<sup>Free</sup> probe (Imperial College London). See Chapter III for further details on MAS experiments.

#### 4.2.5 Solution NMR samples and CEST experiments.

Solution NMR experiments in this chapter were carried out at 10 °C on two Bruker spectrometers (at the Universities of Minnesota and Cambridge) operating at <sup>1</sup>H frequencies of 700 MHz equipped with triple resonance HCN cryo-probes. See Chapter III for further details on CEST experiments.

#### 4.2.6 Cryo-electron microscopy (cryo-EM) measurements.

All samples used in cryo-EM measurements were incubated, with or without αS (200 μM), for 12h at 298K using fresh preparations of DOPE:DOPS:DOPC SUVs at a concentration of 0.05%. After incubation cryo-EM grids were prepared by vitrifying the sample solutions using aliquots of 2 μL and a Vitrobot Mark IV (FEI, Hillsboro, USA) at a relative humidity of 100%. The samples were loaded on a glow-discharged Quantifoil Copper 300 mesh R2/2 grids (Quantifoil Micro Tools GmbH, Germany) and blotted with filter paper for 2.5 s to leave a thin film of solution. The blotted samples were immediately plunged into liquid ethane and stored under liquid nitrogen prior to imaging. Samples were examined using a

Philips CM200 FEG electron microscope operating at 200 kV (FEI, Hillsboro, USA), using a Gatan 626 cryo-holder (Gatan, Pleasantos, USA) cooled with liquid nitrogen to temperatures below  $-180\text{ }^{\circ}\text{C}$ . Digital images were acquired on a TVIPS FC415 CCD camera using the EMMENU 4 software package (TVIPS, Munich, Germany).

#### 4.2.7 Stimulated emission depletion (STED) microscopy.

STED imaging (184, 185) was carried out by fluorescently labelling the DOPE:DOPS:DOPC SUVs with 2% of fluorescently labelled DOPE (ATTO 647N DOPE, ATTO-TECH, USA). STED microscopy allows the diffraction limit in optical microscopy ( $\sim 200\text{nm}$ ) to be overcome (186) and imaging was performed on a home-built pulsed STED microscope (186) using a single titanium-sapphire oscillator centered at  $\lambda_{\text{STED}} = 765\text{ nm}$  (Ti:S, Mai Tai HP, Spectra-physics, Santa Clara, USA) to generate the STED beam, which was subsequently split into two using a half-plate and a polarisation beam splitter. Of these two beams, the one transmitted was focused onto a photonic crystal fiber (FemtoWhite, NKT Photonics, Cologne, Germany) to produce white light radiation. From this light, an excitation beam, centered at  $\lambda_{\text{Exc}} = 640\text{ nm}$ , was extracted using a bandpass filter (637/7 BrightLine HC, Semrock, New York, USA) and coupled into a 30 m long polarization maintaining single-mode fiber (PM630-HP, Thorlabs, Newton, UK). The reflected STED beam was passed through a 50 cm long glass block of SF66 and a 100 m long polarization maintaining single-mode fiber (PM-S630-HP, Thorlabs, Newton, UK) to stretch the pulse duration to approximately 100-200 ps. Additionally the STED beam was converted into a so called donut beam by a spatial light modulator (X10468-02, Hamamatsu Photonics, Hamamatsu City, Japan). The excitation and STED beams were recombined with a dichroic mirror (T735spxr, Chroma, Bellow Falls, USA) and detected using a commercial point-scanning microscope (Abberior Instruments, Göttingen, Germany) comprising of a microscope frame (IX83, Olympus, Shinjiuku, Japan), a set of galvanometer mirrors (Quad scanner, Abberior Instruments, Göttingen, Germany) and a detection unit. The beams were focused onto the sample by a 100x/1.4 NA oil immersion objective lens (UPLSAPO 100XO, Olympus, Göttingen, Germany) and images were acquired by raster scanning the beams across the sample using the Inspector software (Andreas Schönle, Max Planck Institute for Biophysical Chemistry, Göttingen, Germany). We used a field of view of  $30 \times 30\text{ }\mu\text{m}^2$  with a pixel size of  $15 \times 15\text{ nm}^2$  and a pixel dwell time of 20  $\mu\text{s}$ . Fluorescence photons

emerging from the sample were collected by the microscope objective lens, de-scanned by the galvanometer mirrors, focused onto a pinhole and detected using an avalanche photodiode (SPCM-AQRH, Excelitas Technologies, Waltham, USA). The laser powers, measured at the objective back aperture, were ca. 20  $\mu$ W and 150 mW for the excitation beam and for the STED beam, respectively.

#### 4.2.8 Analysis of STED images for vesicle size measurement.

Vesicle sizes were estimated from STED images by using in-house Matlab scripts. First, images of isolated vesicles were identified and analysed using a fitting based on a 2D Gaussian function, by convolving the images with a Gaussian filter whose dimensions match the extension of the expected STED point spread function. The centres of the vesicles were identified by finding local maxima of the convolved images, excluding the local maxima corresponding to fused vesicles by means of a threshold applied on the peak intensities. A different fitting procedure was optimised in the case of assembled vesicles that appear as hollow shapes in the STED images, as for a vesicle larger than the lateral resolution of the STED microscope the number of dye molecules probed increases on the edge of the shell. To estimate the size of the clusters and their relative number compared to the non-fused vesicles, all the vesicles appearing as fused were fitted by annular functions having a Gaussian radial profile (amplitude, position, radius and offset) using a nonlinear least squares approach.

#### 4.2.9 Direct stochastic optical reconstruction microscopy (dSTORM).

Super-resolution imaging was performed using dSTORM microscopy with a Nikon Eclipse TE 300 inverted wide-field microscope using a 100 X, 1.49-N.A total internal reflection fluorescence (TIRF)(187) objective lens (Nikon Ltd, Kingston upon Thames, UK.). The vesicle and  $\alpha$ S samples were adhered to a glass coverslip coated in poly-L-lysine (P4707, Sigma Aldrich, St Louis, USA) before photoswitching buffer solution was added, consisting of 100 mM mercaptoethylamine (MEA) in phosphate buffered saline (PBS, pH 8.2). For imaging, a laser emitting at a wavelength of 640 nm was used (Toptica Photonics AG, Graefelfing, Germany) for excitation of the Atto 647N dye. A 405 nm laser (Mitsubishi S3 Electronics Corp., Tokyo, Japan) was used as the reactivation source, which was only turned on when the number of active fluorophores in the field of view was visibly reduced. Imaging was performed under TIRF illumination conditions, ensuring that the

exact centre of the field of view, FOV, was illuminated. The FOV covered  $1997 \times 1997$  camera pixels, corresponding to an area on the sample of  $\sim 20 \times 20 \mu\text{m}^2$ . 10,000 fluorescence frames were recorded, each corresponding to an exposure time of 10 ms; the latter was matched to be in the range of the average “on” time of the fluorescent dyes. The fluorescence light in the detection path was filtered and imaged with an Ixon DV887 ECS-BV EM-CCD camera (Andor, Belfast UK). The image analysis was performed using frames 1,000 to 10,000 in each sequence. From each image stack, a reconstructed dSTORM image was generated using the open-source rapidSTORM software developed in house using MATLAB (The MathWorks, Inc.).

#### 4.2.10 Modelling.

Schematic representations of  $\alpha\text{S}$  bound to SUVs were obtained by using molecular dynamics (MD) simulations in implicit solvent. The structure of  $\alpha\text{S}$  in the double-anchoring mechanism (see below) were obtained by starting from the model of membrane-bound conformation  $\alpha\text{S}$  characterised by an elongated helix (residues 1 to 97) with a disordered C-terminal region (residues 98 to 140) which was part of the ensemble characterised previously (114). Atomic coordinates (Cartesian space) of the N-terminal anchor were harmonically restrained to maintain a fixed position whereas the region spanning residues 65 to 97 was restrained in the alpha-helical. A constant force in the Z dimension was applied to this region to extend it toward the upper vesicle. The remainder of the protein (residues 26 to 59 and 98 to 140) was allowed to relax under the Newtonian laws of motions during the MD simulation. Curved vesicle surfaces were generated by starting from atomic models of DOPE:DOPS:DOPC bilayers and by generating roto-translations that imposed a spherical symmetry with a radius of 25 nm.

#### 4.2.11 Kinetics measurements of aggregation.

$\alpha\text{S}$  solutions in the absence and in the presence of DMPS SUV were prepared in 20 mM phosphate buffer at pH 6.0. 35  $\mu\text{M}$  and 50  $\mu\text{M}$  protein solutions were supplemented with 560  $\mu\text{M}$  and 500  $\mu\text{M}$  DMPS SUV, respectively. Aggregation kinetic assays were initiated by incubating the samples in 96-well plate at 37 °C under quiescent conditions in a plate reader (Fluostar Omega, Fluostar Optima or Fluostar Galaxy, BMGLabtech, Offenburg, Germany) in the presence of 50  $\mu\text{M}$  Thioflavin T (ThT) (Sigma). The ThT fluorescence was measured through the bottom of the plate every 10 min with a 440 nm excitation filter

and a 480 nm emission filter. The ThT fluorescence was followed for three repeats of each sample, and the whole setup was repeated twice in separate plates.

#### 4.2.12 Atomic force microscopy (AFM) imaging.

20  $\mu$ l aliquots were sampled after 11h of incubation under the conditions employed in the kinetic assays were diluted to 5  $\mu$ M and deposited on cleaved mica surfaces (Agar Scientific, Stansted, UK). The surfaces were left to dry in air for 60 min while being shielded from dust particles. Topographic data were then acquired using a Nanowizard II atomic force microscope (JPK Instruments, Waterbeach, UK) in intermittent contact mode in air, using NSC 36 cantilevers (Mikromasch, Tallinn, Estonia) with resonant frequencies between 70 kHz and 150 kHz.

#### 4.2.13 Dynamic Light Scattering (DLS).

DLS measurements of vesicle size distributions were performed using a Zetasizer Nano ZSP instrument (Malvern Instruments, Malvern, UK) with backscatter detection at a scattering angle of 173°. The viscosity (0.8882 cP) and the refractive index (1.330) of water were used as parameters for the buffer solution, and the material properties of the analyte were set to those of the lipids (absorption coefficient of 0.001 and refractive index of 1.440). SUVs were used at a concentration of 0.05% in these measurements and the experiments were performed at 25 °C. The acquisition time for the collection of each dataset was 10 sec and accumulation of the correlation curves was obtained using 10 repetitions. Each measurement was repeated 10 times to estimate standard deviations and average values of the centres of the size distributions.

#### 4.2.14 Fitting of the CD data.

Assuming a single site binding (eq. 4.1), the dissociation constant,  $K_D$ , is given by eq. 2:

$$PL = P + SUVs \tag{4.1}$$

$$K_D = [P][Suv]/[PSuv] \tag{4.2}$$

Where [P], [L] and [PL] are the equilibrium concentrations of protein, SUVs and protein-ligand complex, respectively.

For each measurement, the observed CD value,  $F_{obs}$ , is by the population-weighted combination of the CD values in the unbound and bound protein states

$$F_{obs} = P_b F_b + P_u F_u = P_b (F_b - F_u) + F_u \quad (4.3)$$

Where  $P_u$  and  $P_b$  are the populations of the unbound and bound states, respectively, and  $F_u$  and  $F_b$  are the intrinsic values of CD signal at 222nm for bound and unbound protein states. Note that  $P_u + P_b = 1$ .  $P_b$  can be expressed in terms of [P], [L], [PL] and  $K_D$  according to:

$$P_b = \frac{[PSuv]}{[P] + [PSuv]} = \frac{[P][Suv]}{K_D \left( [P] + \frac{[P][Suv]}{K_D} \right)} \quad (4.4)$$

The fitting formula here employed is the combination of eq.s 3 and 4:

$$\Delta F = F_{obs} - F_u = \frac{[P][Suv]}{K_D \left( [P] + \frac{[P][Suv]}{K_D} \right)} (F_b - F_u) \quad (4.5)$$

### **4.3 Binding properties of pathological $\alpha$ S variants.**

Using solution-state and solid-state NMR spectroscopy in combination with cryo-electron microscopy (cryo-EM) and stimulated emission depletion (STED) imaging, we characterised the structural properties at the surface of synaptic-like vesicles of the familial  $\alpha$ S mutants A30P (188) ( $\alpha$ S<sub>A30P</sub>) and E46K (189) ( $\alpha$ S<sub>E46K</sub>) and compared their behaviour with that of the wild type protein ( $\alpha$ S<sub>WT</sub>) (114). In particular, as in the study of  $\alpha$ S<sub>WT</sub> (see Chapter III), we studied the interactions of  $\alpha$ S<sub>A30P</sub> and  $\alpha$ S<sub>E46K</sub> with small unilamellar vesicles (SUVs) composed of a mixture of 1,2-dioleoyl-sn-glycero-3-phosphoethanolamine (DOPE), 1,2-dioleoyl-sn-glycero-3-phospho-L-serine (DOPS), and 1,2-dioleoyl-sn-glycero-3-phosphocholine (DOPC) in 5:3:2 molar ratios (73), as such SUVs have been reported to be good mimics of synaptic vesicles for composition and curvature (19). The employed combination of magic angle spinning (MAS (115, 116)) measurements in solid-state NMR (ssNMR(190)) and chemical exchange saturation transfer (CEST (91, 112-114, 191), Figure 2.10) experiments in solution-state NMR has proved to be highly effective in probing interactions between  $\alpha$ S and SUVs, enabling the degree of order and disorder in the membrane-bound state of  $\alpha$ S<sub>WT</sub> to be characterised (Chapter III) (114).

In the analysis of the interaction between  $\alpha$ S<sub>A30P</sub> and SUVs, CEST profiles (Figures 2.10, 4.1 and 4.2) provided detailed information concerning the effects of the A30P mutation, which was shown to reduce very substantially the binding affinity of  $\alpha$ S for SUVs (19). In  $\alpha$ S<sub>A30P</sub>, indeed, the binding of the N-terminal anchor region was found to involve a smaller number of residues than in the case of  $\alpha$ S<sub>WT</sub> (residues 6-20 compared with residues 6-25 in  $\alpha$ S<sub>WT</sub>) with generally a lower degree of CEST saturation than in the case of  $\alpha$ S<sub>WT</sub>. The major differences between  $\alpha$ S<sub>A30P</sub> and  $\alpha$ S<sub>WT</sub> were evident in this membrane-anchor N-terminal region, while the remainder of the protein sequence showed very limited variations in the CEST profiles of these two proteins. The opposite behaviour was observed for the  $\alpha$ S<sub>E46K</sub> variant, which binds SUVs with higher affinity than  $\alpha$ S<sub>WT</sub> (19). Indeed, the CEST data indicate a significantly stronger interaction with the membrane for the N-terminal anchor region of  $\alpha$ S<sub>E46K</sub>, which in this case extends up to residue 42 with a generally higher degree of saturation than in the case of  $\alpha$ S<sub>WT</sub>. As with  $\alpha$ S<sub>A30P</sub>, minor variations in the CEST profiles were also observed in other regions of the

sequence of  $\alpha S_{E46K}$ . The differences in the CEST saturation profiles of the two mutants compared to  $\alpha S_{WT}$  (Figure 4.3) evidenced more specifically that the major changes in the modes of binding to SUVs of these mutational variants are associated primarily with the N-terminal region of the protein.

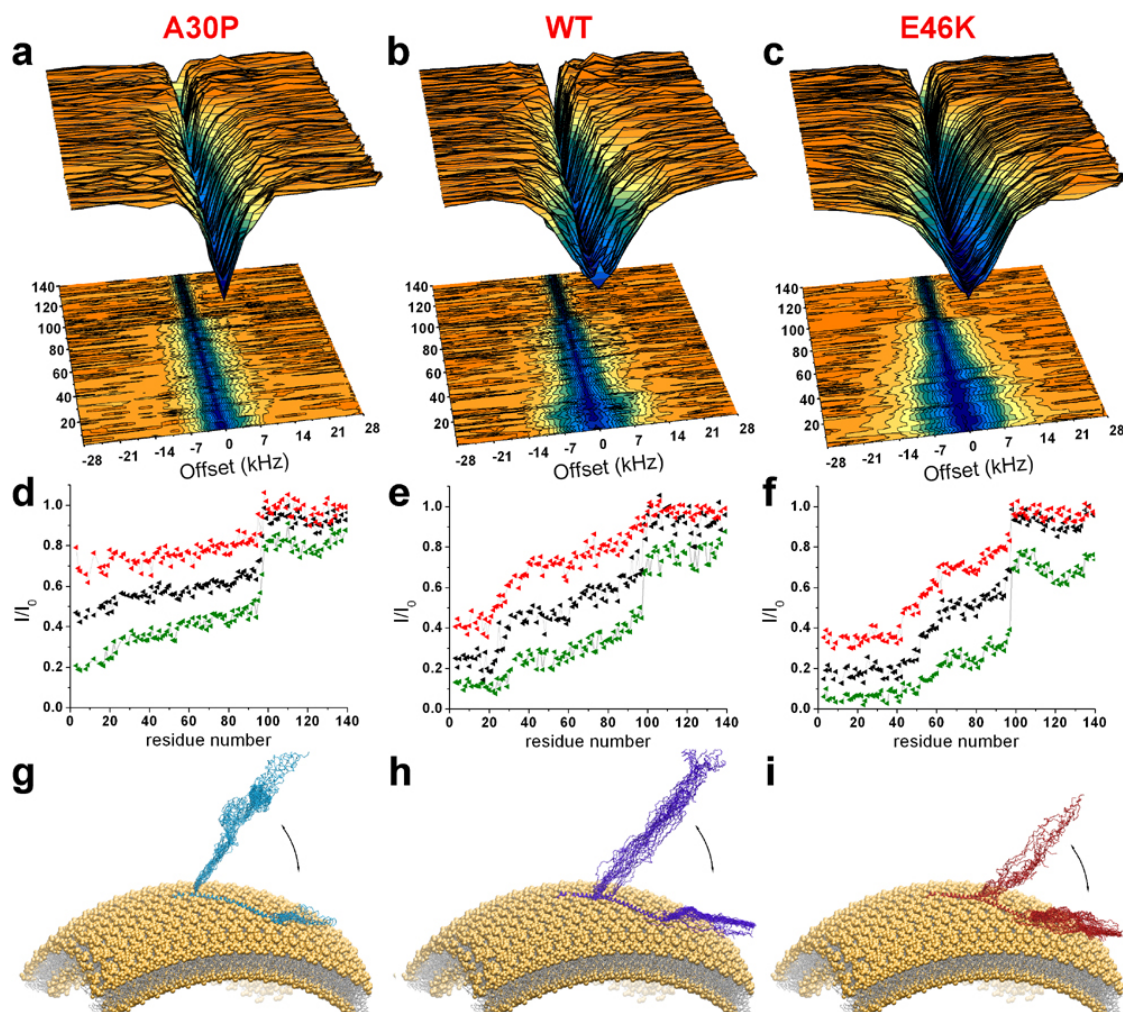


**Figure 4.1. CEST experiments probing the membrane interactions of  $\alpha S_{A30P}$  and  $\alpha S_{E46K}$ .** CEST experiments were recorded at a  $^1H$  frequency of 700 MHz (see Materials and Methods), using protein concentrations of 300 mM and 0.06% ( $0.6 \text{ mg ml}^{-1}$ ) of DOPE:DOPS:DOPC lipids in a ratio of 5:3:2 and assembled into SUVs.  $^1H$ - $^{15}N$  HSQC spectra were recorded by using continuous wave saturation (170 Hz or 350 Hz) in the  $^{15}N$  channel at offsets ranging between -28 kHz and +28 kHz; an additional spectrum, saturated at -100 kHz, was recorded as a reference. Data recorded using a saturation bandwidth of 350 Hz are shown here (the data measured using a saturation bandwidth of 170 Hz are shown in Figure 4.2). For comparison, the plots in panels **b** and **e** are drawn using  $\alpha S_{WT}$  data from our previous investigation(114). (**a-c**) CEST surfaces for  $\alpha S_{A30P}$  (**a**)  $\alpha S_{WT}$ (114) (**b**) and  $\alpha S_{E46K}$  (**c**). (**d-f**) CEST saturation along the sequences of  $\alpha S_{A30P}$  (**d**),  $\alpha S_{WT}$ (114) (**e**) and  $\alpha S_{E46K}$  (**f**). The green lines refer to the averaged CEST profiles measured using offsets at  $\pm 1.5$  kHz,

and the profiles for  $\pm 3$  kHz and  $\pm 5$  kHz are shown in black and red, respectively. (g-i) Schematic illustration (see Materials and Methods) of the equilibrium between surface attached/detached local conformations in the membrane-bound states  $\alpha S_{A30P}$  (g)  $\alpha S_{WT(114)}$  (h) and  $\alpha S_{E46K}$  (i). The major differences in the data of  $\alpha S_{A30P}$ ,  $\alpha S_{WT}$  and  $\alpha S_{E46K}$  are located in the anchor region. Overall, these three variants of  $\alpha S$  maintain the same topological properties at the surfaces of synaptic-like SUVs.

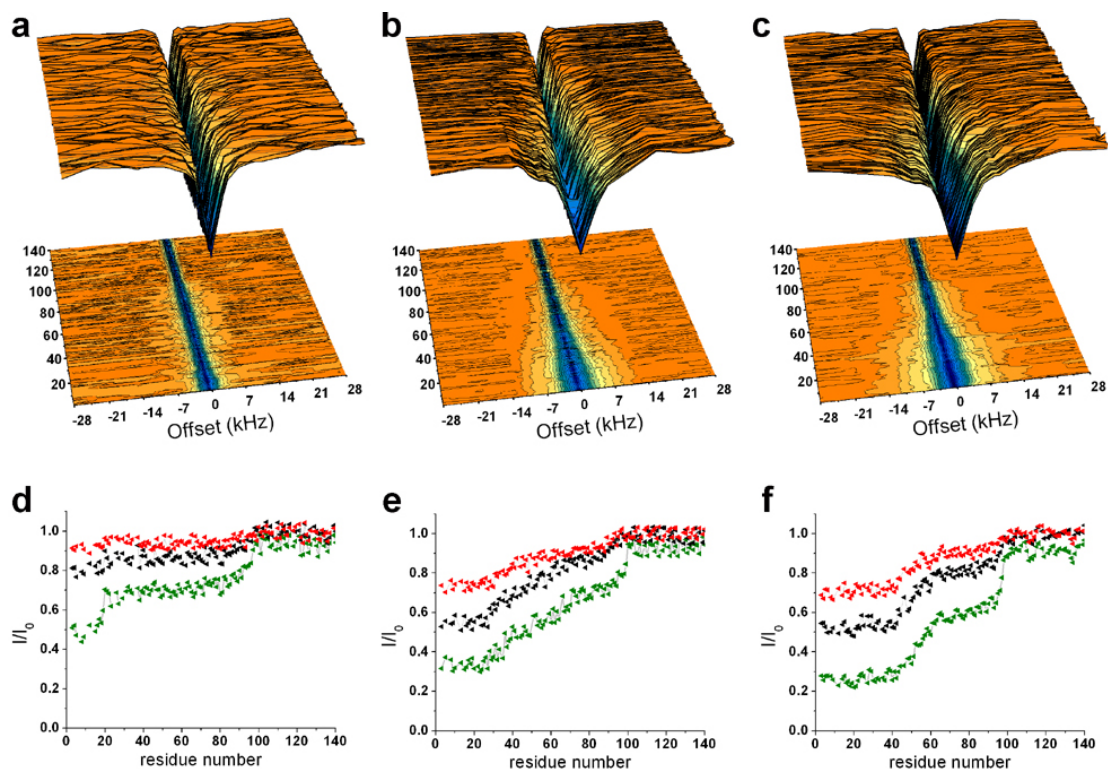


**Figure 4.2. CEST experiments of  $\alpha S_{A30P}$  and  $\alpha S_{E46K}$  using a continuous wavelength of 170 Hz.**  $^1H$ - $^{15}N$  HSQC spectra recorded by using a continuous wave saturation of 170 Hz in the  $^{15}N$  channel at offsets ranging between -28 kHz and +28 kHz. An additional spectrum, saturated at -100 kHz was recorded as a reference. For the sake of comparison, plots in panels b and e are drawn using  $\alpha S_{WT}$  data from our previous investigation(114). (a-c) CEST surfaces for  $\alpha S_{A30P}$  (a)  $\alpha S_{WT(114)}$  (b) and  $\alpha S_{E46K}$  (c). (d-f) CEST saturation along the sequences of  $\alpha S_{A30P}$  (d)  $\alpha S_{WT(114)}$  (e) and  $\alpha S_{E46K}$  (f). Green lines refer to the averaged CEST profiles measured using offsets at  $\pm 1.5$  kHz. Similarly, profiles for  $\pm 3$  kHz and  $\pm 5$  kHz are shown in black and red, respectively.

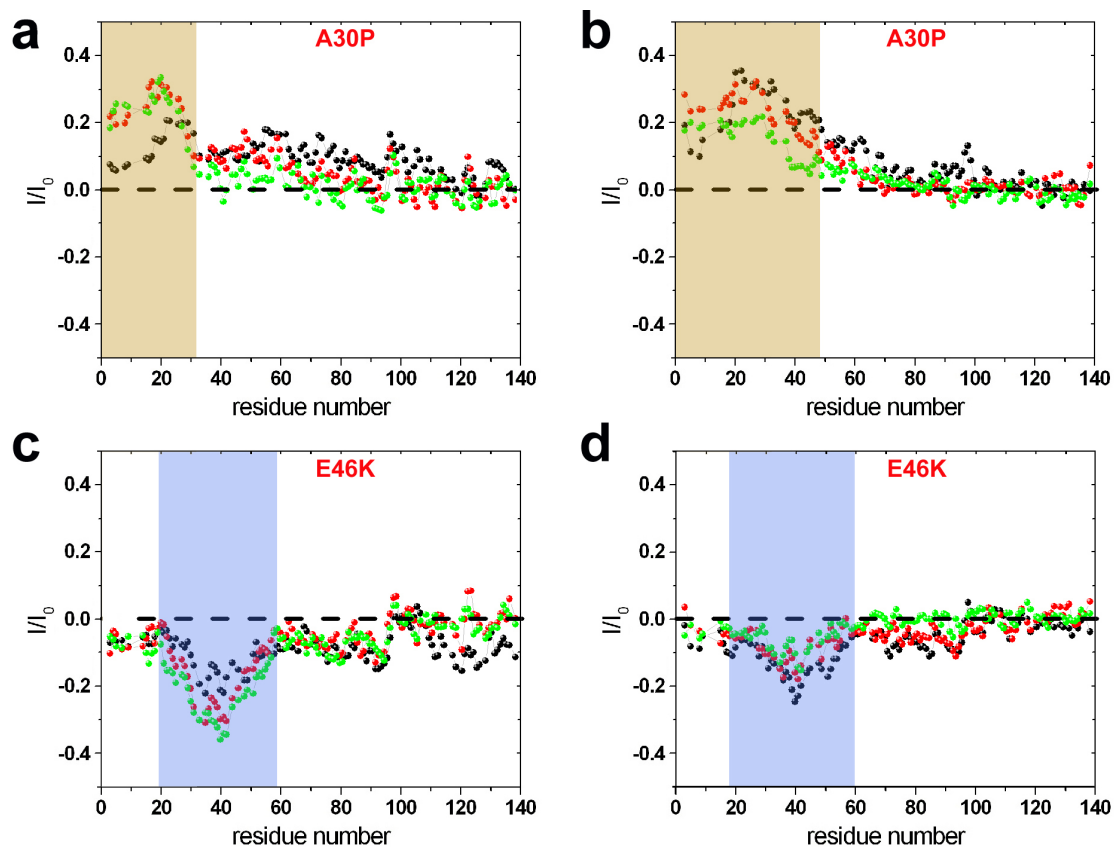


**Figure 4.3. CEST differences between  $\alpha S_{WT}$  and  $\alpha S_{A30P}$  and  $\alpha S_{E46K}$ .** CEST profiles of the  $\alpha S_{WT}$  variants have been subtracted from those of  $\alpha S_{A30P}$  and  $\alpha S_{E46K}$ . Green, red and black lines are used for offsets of  $\pm 1.5$  kHz,  $\pm 3.0$  kHz and  $\pm 5.0$  kHz, respectively. **(a-b)** Difference in CEST profiles of  $\alpha S_{A30P}$  and  $\alpha S_{WT}$ , measured with bandwidths of 350Hz **(a)** and 170Hz **(b)**. The three offsets show a peak of positive differences in the regions indicated in yellow, showing that in this region the saturation is weaker for  $\alpha S_{A30P}$  than for  $\alpha S_{WT}$ . **(c-d)** Difference in CEST profiles of  $\alpha S_{E46K}$  and  $\alpha S_{WT}$ , measured with bandwidths of 350Hz **(c)** and 170Hz **(d)**. Green, red and black lines are used for offsets of  $\pm 1.5$  kHz,  $\pm 3.0$  kHz and  $\pm 5.0$  kHz, respectively. The three offsets show a peak of negative differences in the regions indicated in blue, showing that in this region the saturation is stronger for  $\alpha S_{E46K}$  than for  $\alpha S_{WT}$ .

In order to obtain detailed information on the topology of  $\alpha S_{A30P}$  and  $\alpha S_{E46K}$  when bound to the surface of SUVs, we employed again MAS ssNMR experiments.  $^{13}\text{C}$ - $^{15}\text{N}$  labelled  $\alpha S$  samples were mixed with SUVs, as described in chapter III in the case of  $\alpha S_{WT}$  (19, 114) to reach a protein/lipid ratio of 1:65 (114). Under these conditions we could observe directly the resonances of both rigid and dynamical regions of the membrane-bound  $\alpha S$  molecule by using cross polarisation (CP) and insensitive nuclei enhanced by polarization transfer (INEPT) experiments (147), respectively (Chapter III). In the CP regime, we performed  $^{13}\text{C}$ - $^{13}\text{C}$  dipolar assisted rotational resonance (DARR)(125) measurements to detect homonuclear correlations between carbon atoms of residues strongly anchored to the membrane (Figure 4.4). In our previous study of  $\alpha S_{WT}$  (114), the  $^{13}\text{C}$ - $^{13}\text{C}$ -DARR spectra identified resonances of residues 6-25 of the anchor region, showing that this region folds into a highly rigid  $\alpha$ -helix lying essentially parallel to the membrane surface (114). The  $^{13}\text{C}$ - $^{13}\text{C}$ -DARR spectra of the membrane bound states of  $\alpha S_{A30P}$  and  $\alpha S_{E46K}$  are, however, substantially different from those of  $\alpha S_{WT}$ , indicating that the dynamical and structural properties of the anchor region vary considerably between the wild type and variant forms of  $\alpha S$ .

In the case of  $\alpha S_{A30P}$ , the  $^{13}\text{C}$ - $^{13}\text{C}$ -DARR spectrum showed a very limited signal-to-noise ratio and almost a complete absence of cross peaks, suggesting that the anchor region of this variant is significantly more dynamic than the same region of the wild type protein. In contrast, the  $^{13}\text{C}$ - $^{13}\text{C}$  DARR spectrum of  $\alpha S_{E46K}$  showed a higher signal-to-noise ratio and a significantly larger number of intense cross peaks, indicating an elongated anchor region in this mutational variant that binds more strongly to SUVs. Using the dipolar connectivities from  $^{15}\text{N}$ - $^{13}\text{C}$  CP-based experiments, along with our previous assignment of  $\alpha S_{WT}$  and  $^{13}\text{C}$ - $^{13}\text{C}$  DARR spectra acquired at different mixing times, we were able to assign individual spin systems in the  $^{13}\text{C}$ - $^{13}\text{C}$  DARR spectra of  $\alpha S_{A30P}$  and  $\alpha S_{E46K}$  (Figure 4.4 a). The chemical shifts were then compared to those obtained from solution state NMR studies of  $\alpha S_{WT}$  in SDS and SLAS micelles (118, 146), and indicated that, despite the differences in dynamics and in the binding strength relative to lipid membranes, all the variants analysed here adopt a helical conformation at the N-terminal anchor when bound to membranes. This finding is particularly relevant in the case of the A30P mutation because it shows that, as the other variants,  $\alpha S_{A30P}$  is able to bind the lipid

bilayer *via* an amphipathic  $\alpha$ -helix at the N-terminus rather than a disordered state tethered onto the lipid surface.

The highly dynamical regions of  $\alpha S_{A30P}$  and  $\alpha S_{E46K}$  bound to SUVs were then probed directly by INEPT measurements acquired using MAS ssNMR experiments (147) and revealed  $^1\text{H}$ - $^{13}\text{C}$  correlations for resonances of the disordered C-terminal region of  $\alpha S$  (Figure 4.4 b), which is only weakly associated with the membrane (114). In contrast to the results obtained from the DARR spectra, no significant differences were found between  $\alpha S_{A30P}$  and  $\alpha S_{E46K}$  in the INEPT spectra, indicating that the disordered C-terminal regions (residues 98-140) of the membrane-bound states of these variants have similar structural and dynamical properties to those of  $\alpha S_{WT}$ . To gain further insights into the topological nature of mobile regions in the membrane-bound  $\alpha S_{A30P}$  and  $\alpha S_{E46K}$  variant, we used paramagnetic relaxation enhancement (PREs) experiments(114). By doping the SUVs with low levels (2%) of a lipid carrying an unpaired electron on the head group, namely the gadolinium salt of 1,2-dimyristoyl-sn-glycero-3-phosphoethanolamine-N-diethylenetriaminepentaacetic acid, PE-DTPA, we could observe selective line broadening of individual resonances in the INEPT spectrum (Figure 4.5), revealing those residues that interact transiently with the membrane surface. The resulting broadening patterns of hydrophobic (including L100, A107, P108, I12, I113, P117, V118, P120) and positively charged (K97 and K102) residues were found to be similar to those observed in  $\alpha S_{WT}$ .

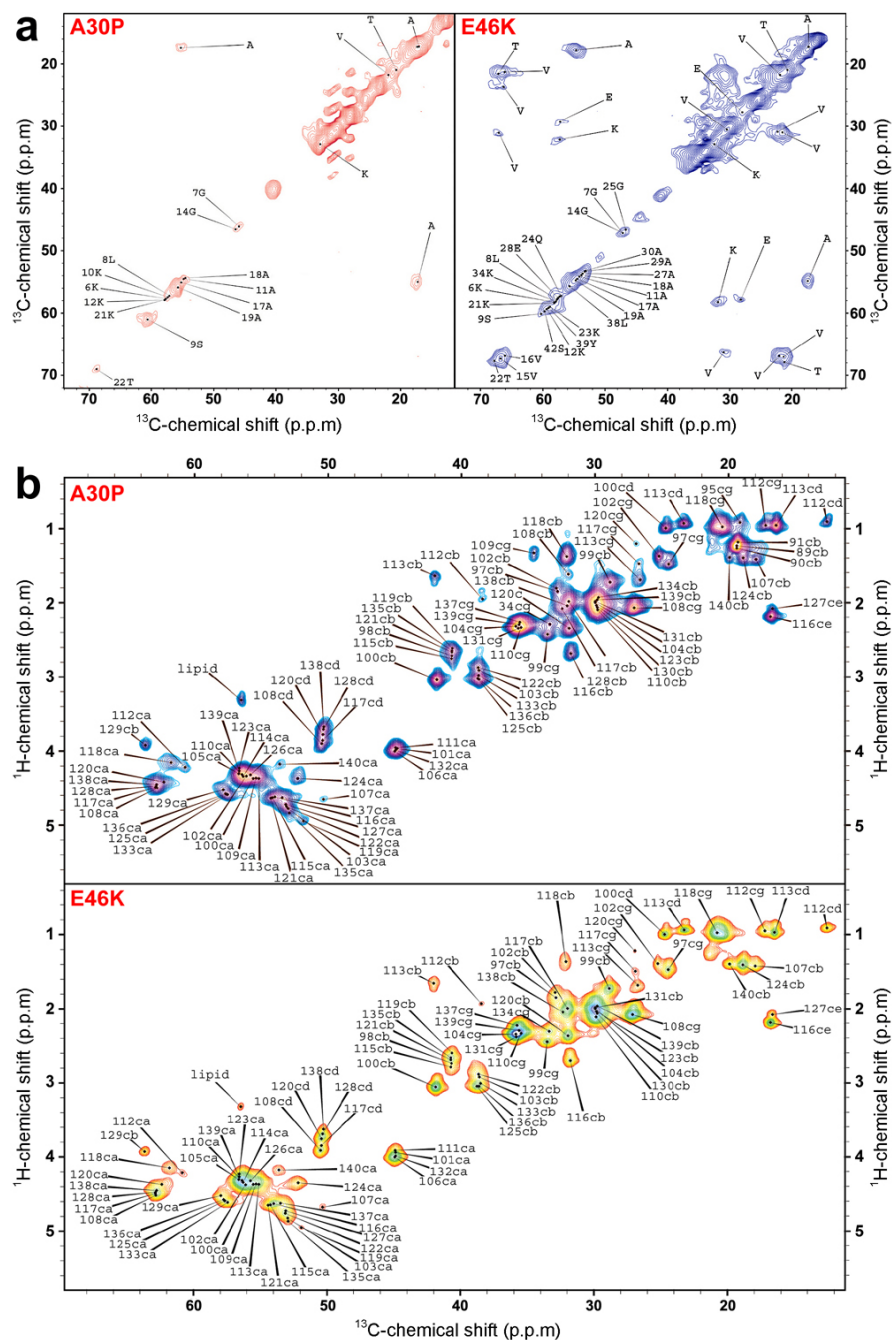


**Figure 4.4. MAS ssNMR spectra of  $\alpha S_{A30P}$  and  $\alpha S_{E46K}$  bound to SUVs.** (a)  $^{13}\text{C}$ - $^{13}\text{C}$  DARR correlation spectra (aliphatic regions) recorded at  $-19^\circ\text{C}$  using a 50 ms mixing time at a MAS rate of 10 kHz. We used a 1:65 protein:lipid ratio in both cases, and spectra of  $\alpha S_{A30P}$  and  $\alpha S_{E46K}$  are shown in the left and right panels, respectively. Residues are indicated using the single letter convention. The highest signal intensities in the spectra of the samples studied here were obtained by performing the measurements at  $-19^\circ\text{C}$ . Under these conditions the lipid mixtures used here are in the gel phase (145), enabling  $^{13}\text{C}$ - $^{13}\text{C}$  DARR spectra to be measured with significantly increased signal-to-noise ratios but without affecting the pattern of chemical shifts; the latter are consistent with those measured at  $4^\circ\text{C}$  (114). No variations in the number of observed resonances or in the chemical shifts were observed using protein:lipid ratios ranging from 1:30 to 1:200 (114).

(b)  $^1\text{H}$ - $^{13}\text{C}$  correlation via INEPT transfer recorded at 4 °C at a MAS rate of 10 kHz. The experiments were performed at a  $^1\text{H}$  frequency of 700 MHz using a  $^1\text{H}/^{13}\text{C}$  3.2 mm  $E^{\text{Free}}$  probe. Atom names ca, cb, cg, cd and ce are used for  $\text{C}^\alpha$ ,  $\text{C}^\beta$ ,  $\text{C}^\gamma$ ,  $\text{C}^\delta$  and Ce atoms, respectively.

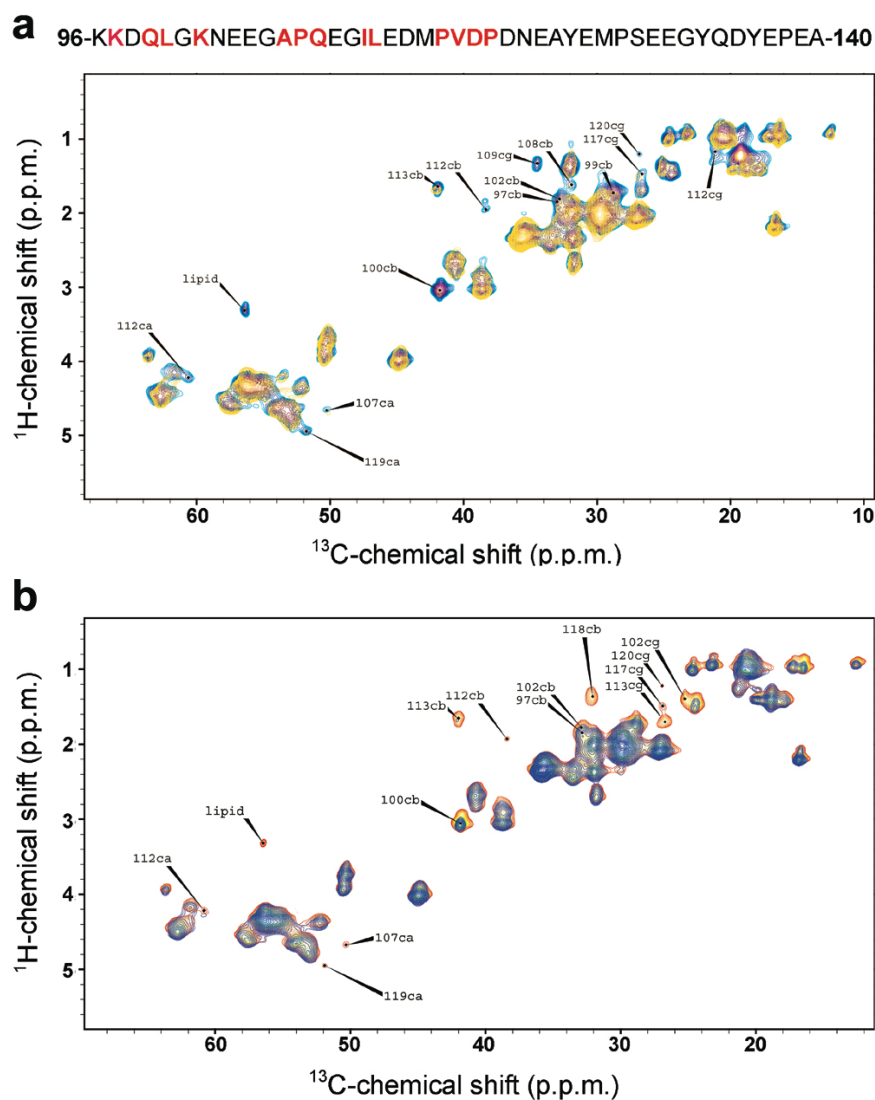


**Figure 4.5. Paramagnetic relaxation experiments.**  $\alpha\text{S}_{\text{A30P}}$  and  $\alpha\text{S}_{\text{E46K}}$  PRE data with paramagnetic SUVs are shown in panels a and b, respectively. To obtain paramagnetic vesicles, the DOPE:DOPS:DOPC mixture was doped with 2% of (1,2-dimyristoyl-sn-glycero-3-phosphoethanolamine-N-DTPA, gadolinium salt). (a) Comparison between INEPT spectra of  $\alpha\text{S}_{\text{A30P}}$  with (yellow) and without (blue) the spin label. (b) Comparison between INEPT spectra of  $\alpha\text{S}_{\text{E46K}}$  with (blue) and without (yellow) the spin label. The two variants show similar patterns of enhanced relaxation, which indicated intermolecular contacts due to the spatial proximity of the atoms of  $\alpha\text{S}$  and the unpaired spins on the surfaces of the SUVs. Residues that showed PRE effects with the membrane are found to be mainly hydrophobic and have been indicated in red in the sequence of the disordered C-terminal tail (top of panel a).

#### **4.4 Mechanism of synaptic vesicle assembly induced by $\alpha$ S**

The solution-state and solid-state NMR measurements described in Chapters III and IV reveal a striking degree of independence between the membrane binding properties of the N-terminal membrane-anchor region of  $\alpha$ S, which is significantly affected by the A30P and E46K mutations, and of the region spanning residues 65 to 97, which instead shows negligible differences as a result of these mutations (Figure 4.3). These independent membrane-binding modes suggest that, in addition to interacting with the membrane surface of the same SUV, these two regions are sufficiently independent to bind simultaneously two different SUVs. Indeed our modelling studies show that a single  $\alpha$ S molecule could bind and bridge two vesicles that are even 150 Å apart (Figure 4.6 a), with both the N-terminal anchor region (initial 25 residues) and the central region (residues 65 to 97) adopting the conformations of amphipathic  $\alpha$ -helices. These data therefore provide the structural basis of the mechanism by which  $\alpha$ S promotes the interaction between vesicles that has been observed experimentally both *in vitro* (19, 177) and *in vivo* (176, 178).

To obtain further evidence of this 'double-anchor' mechanism (Figure 4.6 a), we used our findings to design a further variant of  $\alpha$ S having structural properties that we anticipated should enhance the probability of  $\alpha$ S to bind simultaneously to two different vesicles in such a way to mediate their interaction. In particular, to favour the double-anchor mechanism (Figure 4.6 a), this variant was designed to enhance the detachment of the region 65 to 97 from the membrane surface when  $\alpha$ S is bound to the SUVs *via* its N-terminal anchor region. We identified for this purpose a scrambled sequence ( $\alpha$ S<sub>Sc</sub>) incorporating the E46K and K80E mutations. In particular, by replacing the lysine at position 80 with a glutamic acid (K80E), the local binding to negatively charged vesicles is disfavoured, hence shifting the conformational equilibrium of the fragment 65 to 97 towards a state where this region is less strongly bound to the SUV surface. By contrast, while K80E is designed to reduce the overall membrane affinity of  $\alpha$ S, a second mutation in which the glutamic acid at position 46 is replaced by a lysine (E46K) was selected to increase the interaction between the N-terminal anchor region and the SUV surface, as probed in  $\alpha$ S<sub>E46K</sub> (Figure 4.1 and 4.4), thereby restoring an overall  $K_D$  comparable to that of the wild type protein.

We tested experimentally whether or not  $\alpha S_{Sc}$  possessed the anticipated structural and thermodynamical properties characteristic of its membrane-bound state. In agreement with our design, we found the binding affinity of  $\alpha S_{Sc}$  for SUVs, measured by circular dichroism (CD) (114), to be similar to that of  $\alpha S_{WT}$  (Figure 4.7 a-c). By contrast the structural properties of the  $\alpha S_{Sc}$  variant, as probed by CEST (Figure 4.7 d-f), showed a significant reduction in the membrane interaction of the central region (residues 65 to 97) of the variant than in  $\alpha S_{WT}$ . These data indicate that  $\alpha S_{Sc}$  binds SUVs with essentially the same affinity as  $\alpha S_{WT}$  but with different structural dynamical properties that increase exposure of the residues 65 to 97 in its membrane-bound state. CEST also confirmed the stronger interaction of the anchor region of  $\alpha S_{Sc}$  compared to that of  $\alpha S_{WT}$ , which in the designed variant is extended to residue 42 as a consequence of the E46K mutation (Figure 4.7 e). As  $\alpha S_{Sc}$  and  $\alpha S_{E46K}$  have the same sequence except at position 80, we plotted the differences in the CEST profiles of these two variants; this comparison reveals clearly that the binding properties of these two variants to the SUVs are overall indistinguishable except in the region 65 to 97 (Figure 4.8) thereby providing additional evidence for the independence of the membrane-binding properties of the N-terminal and central regions in  $\alpha S$ .

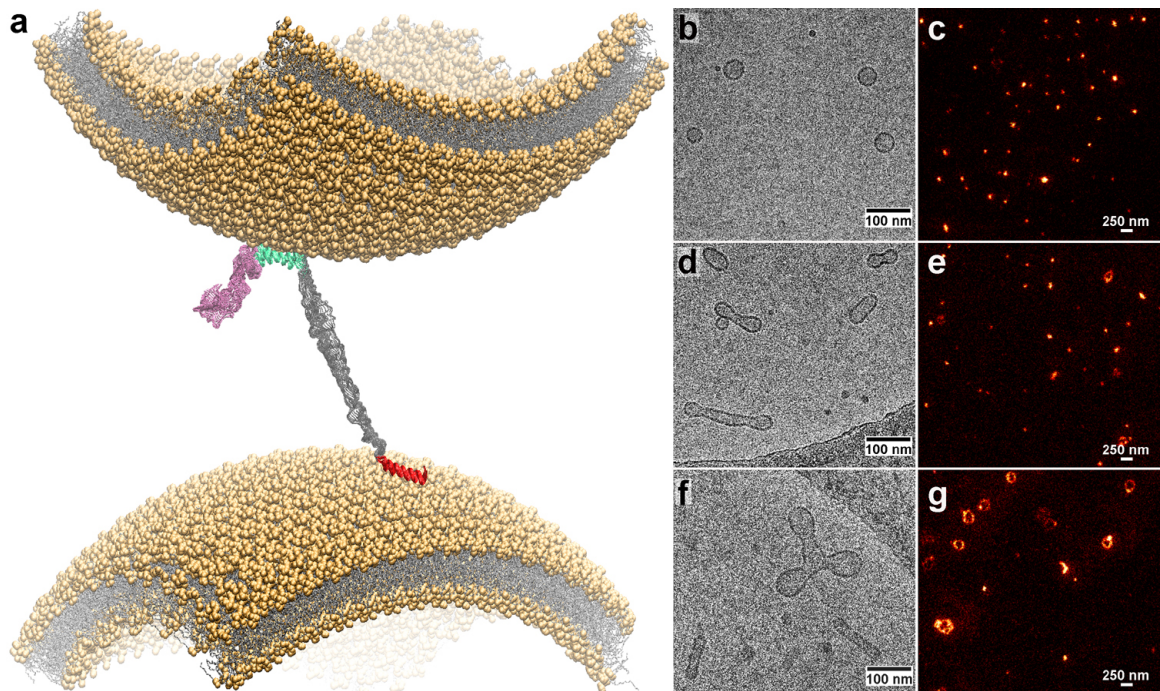


**Figure 4.6. Vesicle assembly induced by  $\alpha$ S.** (a) Molecular details of the double-anchor mechanism described in this work. SUVs of 50 nm in diameter were modelled to mimic as closely as possible the experimental conditions in this study (see Materials and Methods).  $\alpha$ S was modelled with the N-terminal anchor in an amphipathic  $\alpha$ -helical conformation (red) and bound to the lower vesicle. The region 65 to 97 (cyan) of  $\alpha$ S was modelled in an amphipathic  $\alpha$ -helical conformation bound to the upper vesicle. The C-terminal fragment (residues 98 to 140) and the linker region 26 to 59 are shown in pink and grey colours, respectively. With this topology the modelling reveals that a single  $\alpha$ S molecule could simultaneously bind two vesicles that are up to 150 Å apart. (b-c) Cryo-EM (b) and STED (c) images acquired on SUVs at a concentration of 0.6 mg/ml. (d-e) Cryo-EM (d) and STED (e) images measured on SUVs following a 12 h incubation with 200 mM  $\alpha$ S<sub>WT</sub>. (f-g) Cryo-EM (f) and STED (g) images acquired on SUVs following 12 h incubation with 200 mM  $\alpha$ S<sub>SC</sub>.

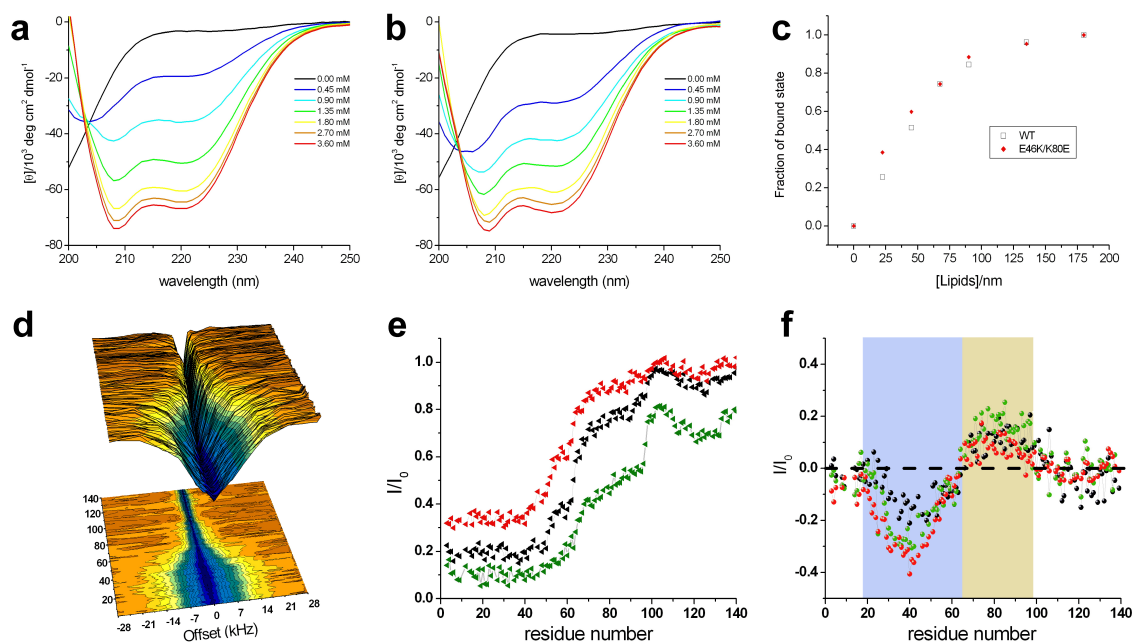


**Figure 4.7. Differences in the structure, dynamics and binding affinity of  $\alpha S_{Sc}$  and  $\alpha S_{WT}$ .** (a-b) CD analysis of  $\alpha S_{WT}$  (a) and  $\alpha S_{Sc}$  (b) in the presence of different concentrations of SUVs. In all measurements, the concentration of  $\alpha S$  was kept constant at  $20 \mu M$ . (c) Using the values of the ellipticity at 222 nm we estimated an apparent dissociation constant  $K_D$  of  $207 \pm 17 \mu M$  for  $\alpha S_{Sc}$  and  $261 \pm 21 \mu M$  for  $\alpha S_{WT}$  under the conditions employed in the present study. See fitting procedure in the materials and methods. (d) CEST surface of  $\alpha S_{Sc}$ .  $^1H$ - $^{15}N$  HSQC spectra were recorded by using a continuous wave saturation (350 Hz) on the  $^{15}N$  channel at offsets ranging between -28 kHz and +28 kHz. An additional spectrum, saturated at -100 kHz was recorded as a reference. (e) CEST saturation along the sequences of  $\alpha S_{Sc}$ . Green lines refer to the averaged CEST profiles measured using offsets of  $\pm 1.5$  kHz. Similarly, profiles for  $\pm 3$  kHz and  $\pm 5$  kHz are shown in black and red, respectively. (f) CEST difference between  $\alpha S_{WT}$  and  $\alpha S_{Sc}$ . Green, black and red lines are used for offsets of  $\pm 1.5$  kHz,  $\pm 3$  kHz and  $\pm 5$  kHz, respectively.

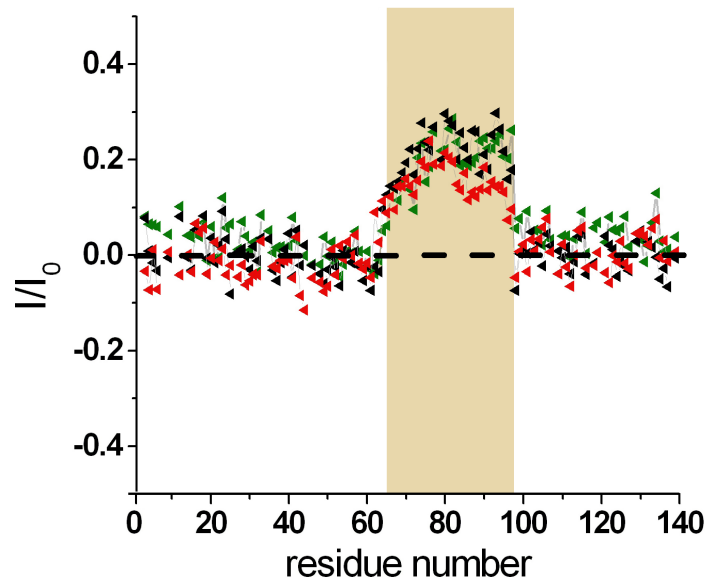


**Figure 4.8. Differences in CEST profiles of  $\alpha S_{Sc}$  and  $\alpha S_{E46K}$ .** CEST profiles (with a bandwidth of 350Hz) of the  $\alpha S_{E46K}$  variants have been subtracted from those of  $\alpha S_{Sc}$ . Green, black and red lines are used for offsets of  $\pm 1.5$  kHz,  $\pm 3$  kHz and  $\pm 5$  kHz, respectively. The three offsets show a peak of positive difference in the regions indicated in yellow, showing that in this region saturation of  $\alpha S_{Sc}$  weaker than that of  $\alpha S_{E46K}$ .

#### **4.5 The NAC region is fundamental for $\alpha$ S function and aggregation**

We compared the efficiency with which  $\alpha$ S<sub>Sc</sub> and  $\alpha$ S<sub>WT</sub> promote the interaction and assembly of vesicles by monitoring, using cryo-EM, the ability of the two variants to promote coalescence and fusion of synaptic-like vesicles *in vitro*<sup>16</sup>. As a control, cryo-EM images of 0.05% DOPE:DOPS:DOPC SUVs incubated for 12 h in the absence of  $\alpha$ S showed spherical vesicles of diameters ranging between 30 nm and 60 nm, with negligible evidence of vesicle fusion over the period of incubation (Figure 4.6 b and 4.9 a), showing that in the absence of  $\alpha$ S the spontaneous fusion of SUVs occurs with extremely slow kinetics. In the presence of  $\alpha$ S, however, the SUVs experience a considerable number of fusion events with cryo-EM images revealing the presence of elongated fused vesicles having long axes of up to 200 nm under the conditions used in this study (Figure 4.6 d and 4.9 b). Incubating SUVs with  $\alpha$ S<sub>Sc</sub>, however, resulted in a very significant increase in the extent of vesicle fusion, with cryo-EM images clearly indicating that this variant is significantly more active in promoting the interaction of SUVs ultimately leading to very large vesicle assemblies (Figure 4.6 f and 4.9 c).

To generate a quantitative analysis of the sizes of the SUVs in the presence and absence of the  $\alpha$ S variants, we used STED microscopy imaging, which enabled us to sample rapidly the sizes of thousands of vesicles to achieve statistically significant differences in the distributions. STED imaging was carried out by fluorescently labelling the DOPE:DOPS:DOPC SUVs with 2% of DOPE labelled with the ATTO 647N fluorophore. Images of isolated vesicles resulted in a size distribution centred at  $55 \pm 11$  nm (Figure 4.6 c and 4.10 a-b), within the range anticipated from the preparation protocol(114). However, STED images of vesicles incubated with  $\alpha$ S<sub>WT</sub> clearly revealed the presence of numerous clusters of fused lipids, whose sizes were quantified by using an algorithm that fits annular shapes to the vesicles, rather than the 2D Gaussian fitting used in the case of isolated vesicles (Methods and Figure 4.10). The resulting distributions indicate that SUVs incubated with  $\alpha$ S<sub>WT</sub> give rise to two populations of vesicles, a species with properties similar to those of vesicles imaged in the absence of  $\alpha$ S and another species attributable to fused vesicles, with a distribution centred at  $115 \pm 30$  nm (Figure 4.6 e and 4.10 c-d).

Following incubation with  $\alpha$ S<sub>Sc</sub>, however, both the sizes and relative populations of the fused vesicles increased dramatically, with the size distribution of fused vesicles now

centred at  $181 \pm 48$  nm (Figure 4.6 g and 4.10 e-f). Similar conclusions to those obtained from STED analysis were obtained from measurements of dynamic light scattering (DLS), which showed that the average size of the SUVs increases in the presence of  $\alpha$ S and that this effect is considerably greater with  $\alpha$ S<sub>Sc</sub> than with  $\alpha$ S<sub>WT</sub> (Figure 4.11). Overall, the cryo-EM, STED and DLS data show that the engineered  $\alpha$ S<sub>Sc</sub> variant has a very significantly enhanced activity in promoting the interactions between SUVs. As  $\alpha$ S<sub>Sc</sub> and  $\alpha$ S<sub>WT</sub> have the same amino acid composition and net charge, and bind SUVs with similar thermodynamic affinity, the enhanced interaction between vesicles upon incubation with  $\alpha$ S<sub>Sc</sub> can be attributed to the higher population of conformations with an enhanced exposure of the region 65 to 97 from the membrane surface, which increases the probability to associate with a different vesicle and to mediate the vesicle assembly *via* a double-anchor mechanism (Figure 4.6 a).

In order to assess the role of the double-anchor mechanism in the clustering of synaptic vesicles (SVs) induced by  $\alpha$ S, we incubated SVs purified from rat brain (182, 183) for 48 h at 37 °C in the presence or absence of  $\alpha$ S samples ( $\alpha$ S<sub>WT</sub> or  $\alpha$ S<sub>Sc</sub>). The distribution of the sizes of the clusters of SVs upon incubation were quantified using direct stochastic optical reconstruction microscopy (*d*STORM) (187) to acquire images on poly-L-lysine-coated glass plates. In order to visualise SVs, we used a primary antibody that is specific for the synaptic protein synaptotagmin 1 and therefore binds selectively to SVs, and a secondary antibody fluorescently labelled with ATTO 647N. The resulting *d*STORM images (Figure 4.12 a-c) were analysed by identifying the centres of mass of each of the SVs and then by applying a clustering approach (192) to identify groups of SVs that, according to a distance cutoff of 60 nm, belong to the same cluster. The resulting distribution of sizes of SV clusters (Figure 4.12 d) showed that 93% of the vesicles remain isolated after incubation for 48h at 37 °C in the absence of  $\alpha$ S, with the remaining 6% and 1% assembled in clusters consisting of two and three SVs, respectively. After incubation under the same conditions but in the presence of 85  $\mu$ M of  $\alpha$ S<sub>WT</sub>, up to 17% of the vesicles were clustered, some including assemblies composed up to 5 SVs (1%). In the presence of  $\alpha$ S<sub>Sc</sub>, however, over 29% of the vesicles were observed to be clustered up to 6 SVs (2%). Cryo-EM images of the assembled structures (Figure 4.12 d) revealed that the

surfaces of the SVs composing the clusters are separated by distances that extend up to 15 nm, in agreement with the double-anchor mechanism (Figure 4.6 a).

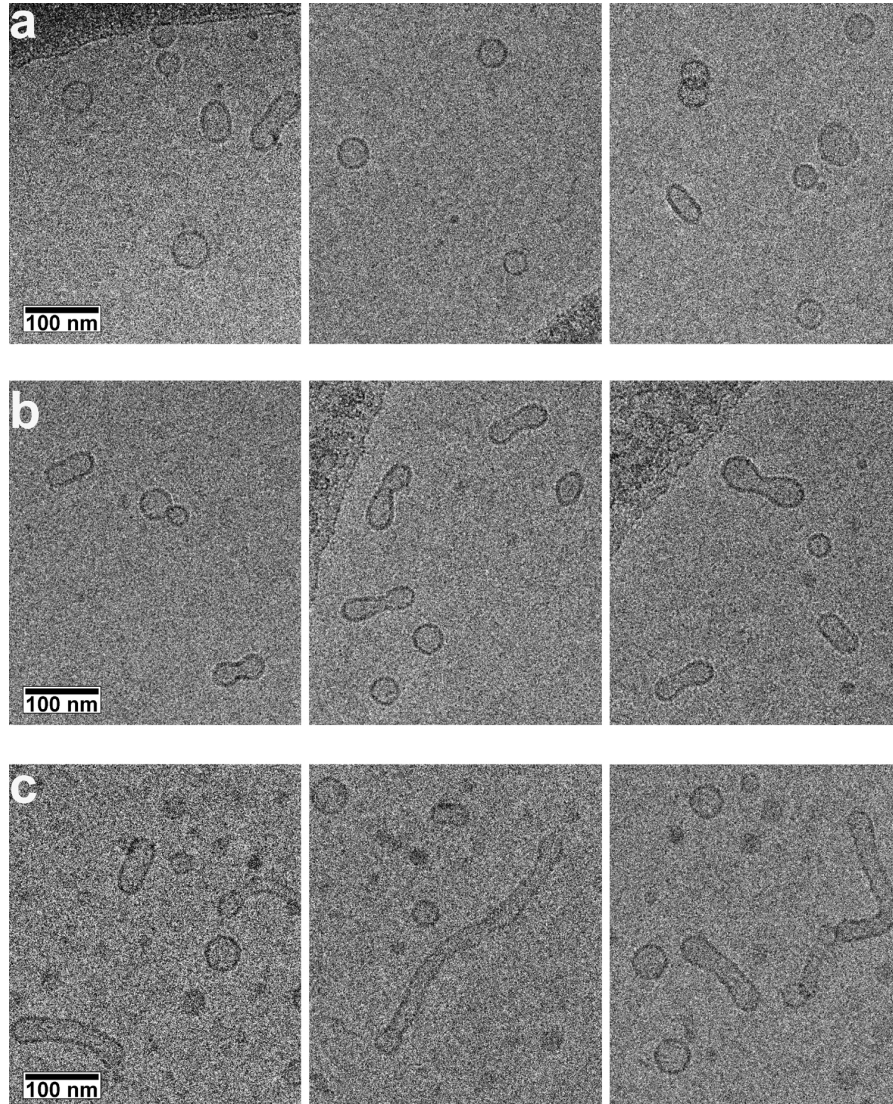


**Figure 4.9. Gallery of cryo-EM images of SUVs in the presence and absence of  $\alpha S_{WT}$  and  $\alpha S_{Sc}$ .** (a) isolated SUV, (b) vesicles incubated with  $\alpha S_{WT}$ , (c) vesicles incubated with  $\alpha S_{Sc}$ . Samples used in cryo-EM measurements were incubated, with or without  $\alpha S$  molecules (wild type and scrambled variants) at 200  $\mu M$  concentration, for 12 h at 298 K using freshly prepared samples of 0.05% DOPE:DOPS:DOPC SUVs. After incubation, cryo-EM grids were prepared by vitrifying the sample solutions into liquid ethane and stored under liquid nitrogen prior to imaging. Samples were examined using a Philips CM200 FEG electron microscope operating at 200 kV (Philips, Amsterdam, NL), using a Gatan 626 cryo-holder (Gatan, Pleasanton, USA) cooled with liquid nitrogen to temperatures below  $-180$  °C. Digital images were acquired on a TVIPS FC415 CCD camera with the EMMENU 4 software package (TVIPS, Munich, Germany).

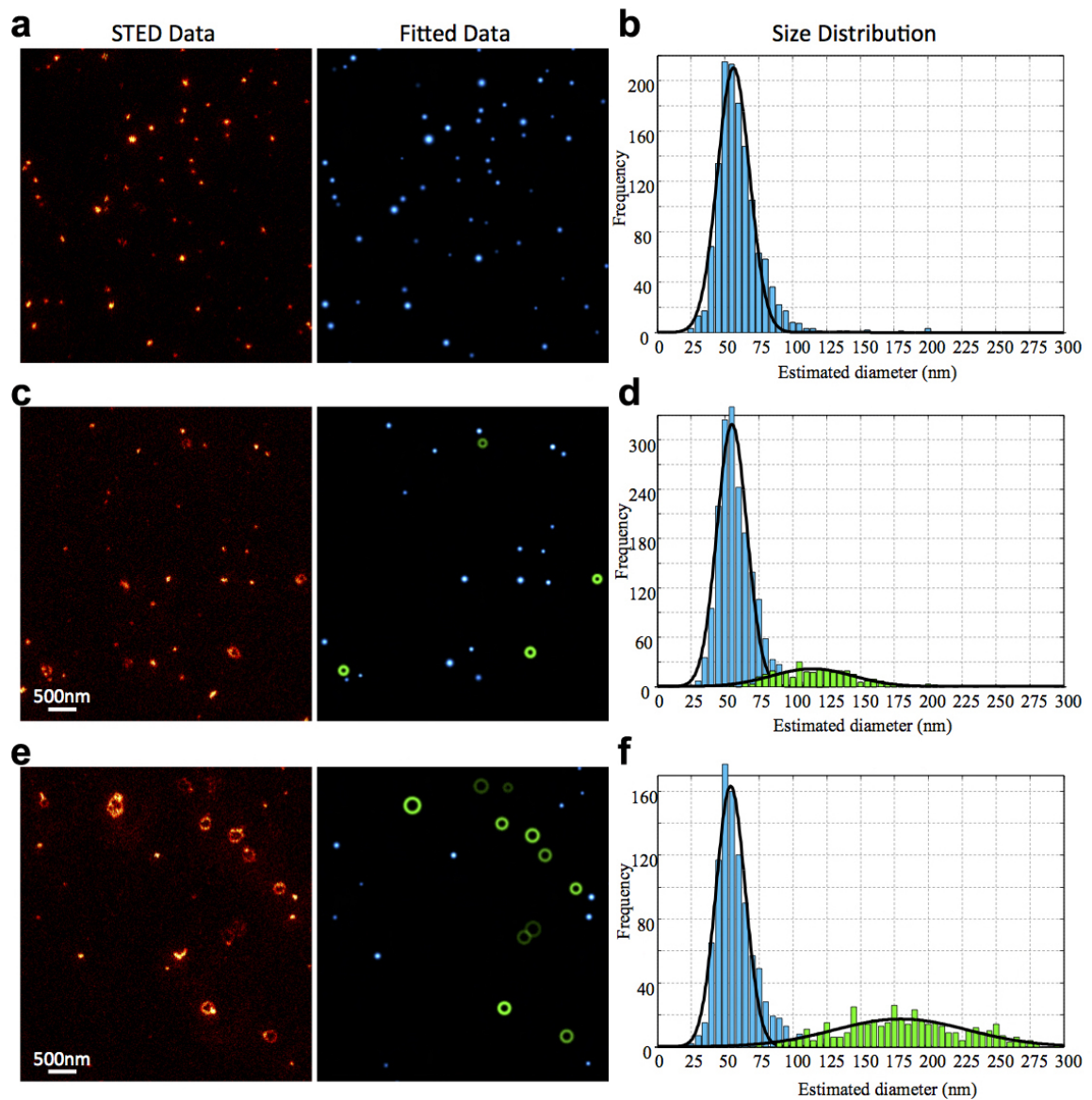


**Figure 4.10. Fitting models employed in STED images.** (a) STED image and (b) size distribution of ATTO labelled SUVs as isolated. 2D Gaussian fitting was employed to fit isolated vesicles (blue beads). (c) STED image and (d) size distributions of SUVs upon incubation with  $\alpha_{S_{WT}}$ . 2D Gaussian fitting (blue beads) and annular fitting (green rings) were employed to fit isolated and fused vesicles, respectively. (e) STED image and (f) size distributions of SUVs upon incubation with  $\alpha_{S_c}$ .

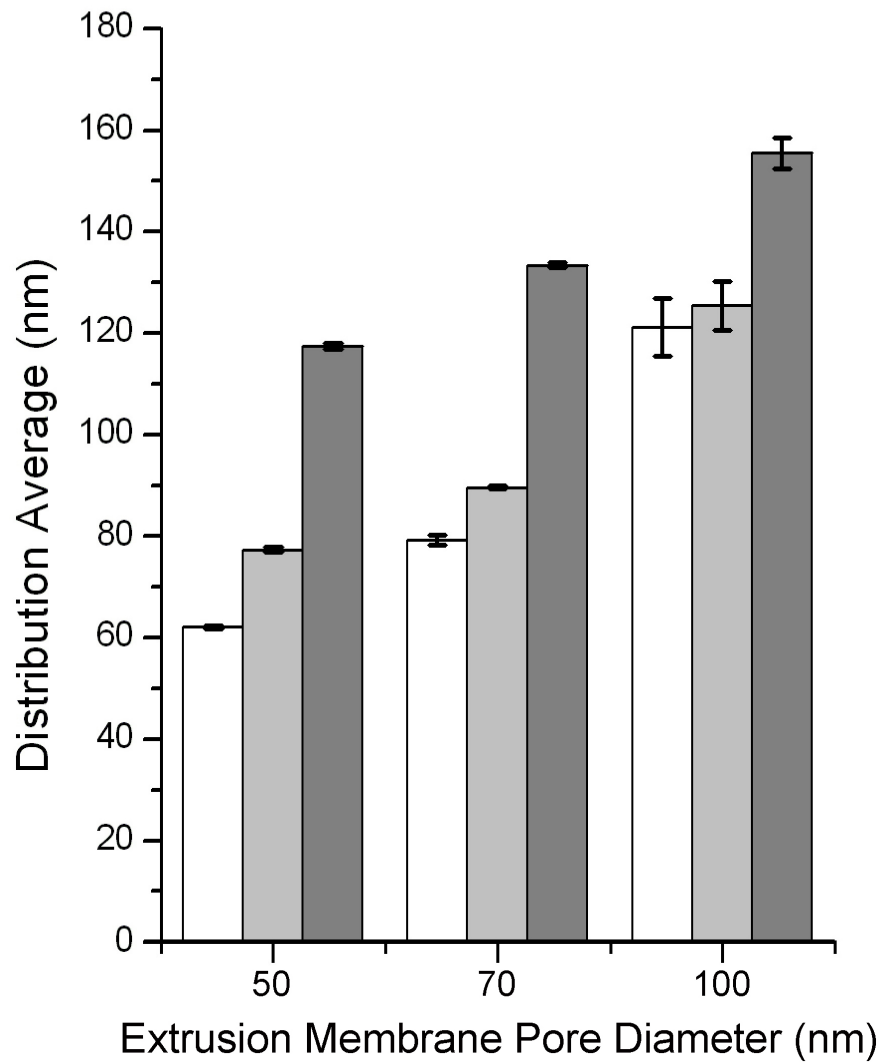


**Figure 4.11. Average sizes of SUVs from DLS measurements.** Measurements were made with a Zetasizer Nano ZSP instrument (Malvern Instruments, Malvern, UK). White bars represent the initial SUVs, whereas light gray and dark grey bars represent SUVs incubated with  $\alpha S_{WT}$  and  $\alpha S_{Sc}$ , respectively. Three different sizes were obtained by extrusion of the vesicles through membranes with different pore diameters. Error bars were calculated as standard deviations from 10 repetitions of each experiment. Regardless of the initial size, the incubation of the vesicles with  $\alpha S_{WT}$  induces an increase of the average size of the DLS distribution. A stronger effect, however, is measured upon incubation with  $\alpha S_{Sc}$ . In the latter case, the measurements were associated with larger standard deviations; this finding is probably associated with the bias of DLS arising from the enhanced scattering properties of large particles. Despite these biases, the measurements consistently showed an increase in size in the  $\alpha S_{Sc}$ -incubated samples. Thus, while the enhanced scattering properties of large particles affect the average values of the distributions, the DLS measurements conclusively show an enhanced ability of  $\alpha S_{Sc}$  to favour interaction and fusion of synaptic-like vesicles, which is in agreement with STED and cryo-EM measurements.

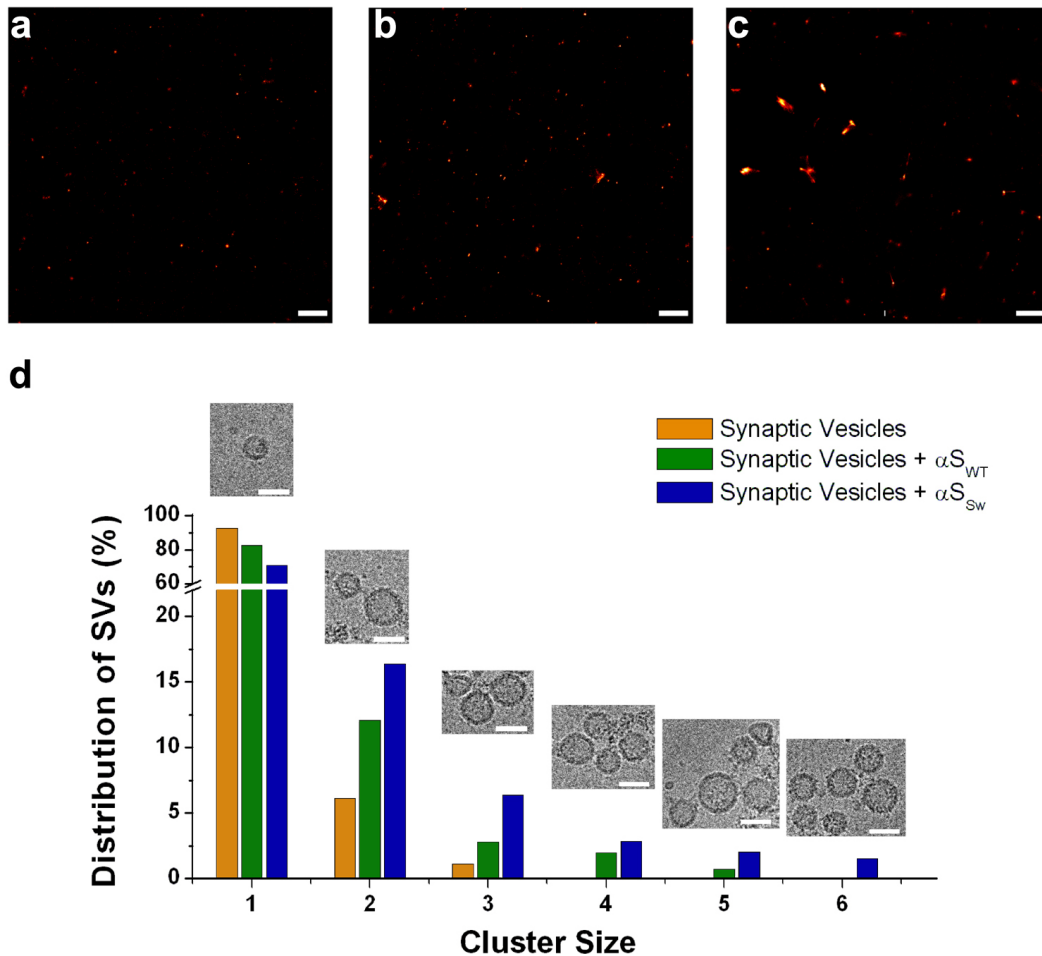


**Figure 4.12. Clustering of synaptic vesicles promoted by  $\alpha S$ .** SVs purified from rat brain were incubated for 48h at 37°C. The concentrations during the incubation were 0.5 mg/ml and 85  $\mu M$  for the SVs and the  $\alpha S$  variants, respectively. (a-c) dSTORM imaging of SVs alone (a) and SVs incubated with  $\alpha S_{WT}$  (b) and with  $\alpha S_{Sc}$  (c). The images were collected using a previously described protocol(187). Scale bars indicate 1  $\mu m$ . In order to generate fluorescent SVs, we used a primary antibody that is specific for synaptotagmin 1 and a secondary antibody that is covalently linked to an ATTO 647N dye. 10,000 fluorescence frames with an exposure time of 10 ms were recorded. The field of view imaged covered  $1997 \times 1997$  camera pixels, corresponding to an area on the sample of  $\sim 20 \times 20 \mu m^2$ . (d) To assess the level of clustering of the SVs, we adapted an approach that has previously been successfully employed to analyse protein self-assembly. For each dSTORM image, clusters of SVs were identified on the basis of the distances between the centers of mass of the SVs. In particular two or more vesicles were associated with a specific cluster if their distances apart are less than 60 nm. The distribution of SVs in clusters of different sizes is reported using orange, green and blue histograms for SVs, SVs in the presence of  $\alpha S_{WT}$  and SVs in the presence of  $\alpha S_{Sc}$ , respectively. Cryo-EM images (scale bar of 50 nm) show representative clusters of different size.

## 4.6 Discussion

It is widely recognised that the physiological activity of  $\alpha$ S is associated with its ability to bind to a variety of lipid membranes, including synaptic vesicles (80). A number of studies support an emerging view that a key biological role of  $\alpha$ S is to mediate interactions and assembly of vesicles (177, 178). Vesicle clustering by  $\alpha$ S has been shown to be a vital step in many functional processes, including the ER-to-Golgi vesicle trafficking (71, 176) and SVs recycling within the mechanisms of neuronal communication (40). In the present study we have examined the structural mechanism underlying the  $\alpha$ S-induced SUVs interactions and assembly by characterising the membrane binding properties of two mutational variants of  $\alpha$ S linked with familial Parkinson's disease. This analysis evidenced that two key regions of the protein, namely the N-terminal membrane-anchor (initial 25 residues) and the central region of the sequence (residues 65 to 97), have independent membrane binding properties and therefore are not only able to interact with a single SUV, but can also simultaneously bind to two different vesicles (Figure 4.6 a) thereby promoting their interaction and assembly as shown *in vitro* and *in vivo* (19, 177, 178). The resulting double-anchor mechanism explains the evidence that either the deletion of the hydrophobic residues in the NAC or the impairment of the membrane affinity at the N-terminal region reduces significantly the ability of  $\alpha$ S to induce vesicular clustering *in vivo* (178).

We tested this molecular mechanism by engineering a mutational variant of  $\alpha$ S, called  $\alpha$ S<sub>sc</sub> ( $\alpha$ S scrambled), which was designed to enhance the probability of  $\alpha$ S to bind simultaneously two different vesicles. Our studies of this variant have provided strong evidence in support of the proposed mechanism by showing that enhanced exposure of the central region, spanning residues 65 to 97 in the membrane-bound state of  $\alpha$ S, promotes more strongly the clustering of SVs purified from rat brain (Figure 4.12) and the assembly and fusion of DOPE:DOPS:DOPC SUVs (Figure 4.6). It has previously been suggested that a broken  $\alpha$ -helix structural topology of  $\alpha$ S (118, 193), which is a conformation that  $\alpha$ S adopts upon binding to detergent micelles, could play a role in vesicle-vesicle interactions stimulated by  $\alpha$ S (80, 194). The present study, however, shows experimentally that the underlying mechanism by which  $\alpha$ S mediates the interactions between lipid vesicles relies on the balance between ordered (membrane-bound) and

disordered (membrane-detached) conformational states of the region spanning residues 65 to 97 of the protein. Perturbing this balance, as we have done rationally with  $\alpha S_{Sc}$ , or upon alteration of the expression levels of  $\alpha S$ , can dramatically affect its ability to promote the physiological vesicle assembly *in vivo* leading to defects in the regulation of vesicle trafficking (40, 68-71, 176, 195, 196).

Other studies also suggest that  $\alpha S$  could act as a molecular chaperone for the formation of SNARE complexes, which appears to result from the direct interaction between  $\alpha S$  and synaptobrevin-2 at the surface of SVs (65, 177). Such an interaction was shown to be independent of the NAC region, suggesting that this region has no direct functional role in this particular process (197). The present data, however, show that the NAC region is not only involved in  $\alpha S$  aggregation, as extensive evidence has indicated (4, 35, 173), but also has a specific role in a key molecular mechanism associated with the normal function of  $\alpha S$ . This study provides evidence that the membrane affinity of the NAC region of  $\alpha S$  is finely tuned to ensure an optimal degree of local detachment from the membrane surface to enable binding to occur between different vesicles. The conformations that, in the membrane-bound state of  $\alpha S$ , feature an exposed region 65 to 97 are shown to be the active states for mediating vesicle interactions *via* the double-anchor mechanism. We also note a possible aberrant behaviour associated with this functional mechanism, as by increasing the accessibility of the amyloidogenic NAC region, these states can also be vulnerable to self-association leading to  $\alpha S$  aggregation at membrane surfaces (40, 75, 198-200).

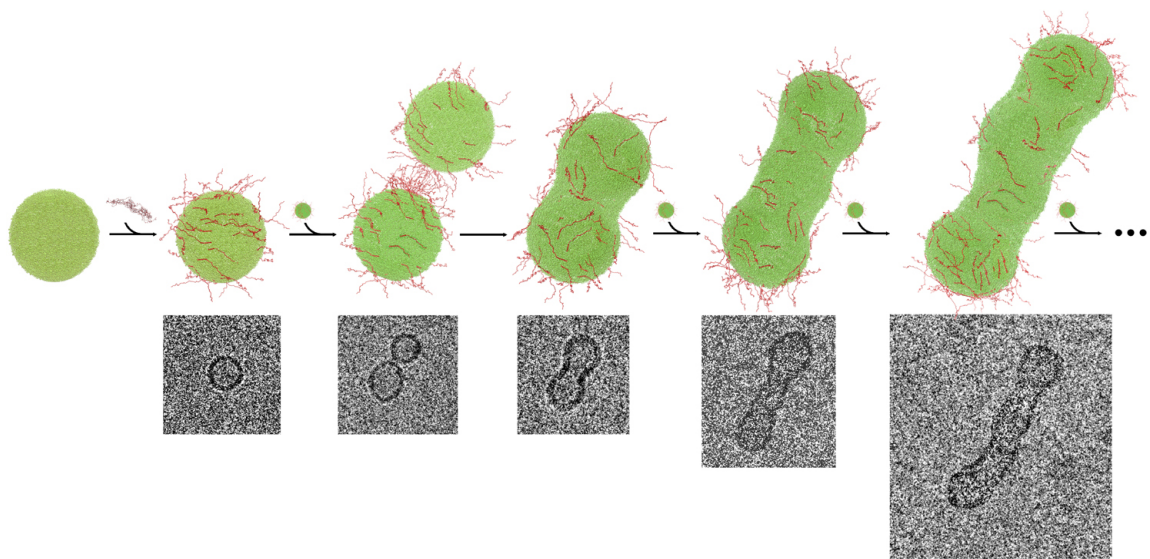


**Figure 4.13. Stepwise representation of SUV interactions and fusion promoted by  $\alpha$ S.** The scheme shows the stepwise mechanism of vesicles assembly as probed from images obtained *in vitro* by cryo-EM, which are also shown. Disordered cytoplasmatic  $\alpha$ S (red) binds dynamically to the surface of SUVs (green), as described in this study. SUVs coated with  $\alpha$ S assemble with fast kinetics as a consequence of the double-anchor mechanism promoted by the  $\alpha$ S molecules decorating their surfaces. The tethered SUVs, which are initially assembled together in dimeric, trimeric, tetrameric and higher order states, eventually fuse to form larger vesicles. With the increasing size of the fused vesicle, we could observe preferential fusion events at the termini of the aggregated vesicles. This observation can be explained by the higher affinity of  $\alpha$ S for significantly curved membrane surfaces<sup>19</sup>, which increases the concentration of bound  $\alpha$ S at the termini of the elongated vesicles thereby promoting a stronger double-anchor mechanism in these loci.

# Chapter V

## ***Structural Basis for the toxicity of $\alpha$ S in Parkinson's Disease***

### ***5.1 Identification of toxic and non-toxic $\alpha$ S oligomers***

The aggregation of  $\alpha$ S into aberrant fibrillar aggregates is strongly associated with Parkinson's disease (PD) and a range of debilitating neurodegenerative disorders, including Parkinson's disease with dementia (PDD), dementia with Lewy bodies (DLB) and multiple system amyotrophy (MSA). Medical conditions associated with protein aggregation are becoming increasingly prevalent in Western societies. Alzheimer's disease, for instance, which affects over 465,000 people in the UK alone and is estimated to steadily grow over the next three to four decades, is recognised as one of the greatest medical challenges of our time. PD, the second most common debilitating disease, afflicts about 2% of the global population over 65 years of age and its prevalence is also likely to increase significantly as our population ages. Although the social and economical impact of these diseases is increasingly recognised, substantial gaps are present in our knowledge about their molecular determinants, including the mechanisms determining neuronal toxicity and death in PD.

Several lines of evidence indicate that specific interactions of  $\alpha$ S oligomers with biological membranes, resulting in the loss of cellular integrity, are crucial elements that promote the neuronal toxicity these  $\alpha$ S aggregates (202, 203). Neither the underlying molecular mechanisms of these interactions nor the structural properties of the oligomers formed by  $\alpha$ S under pathological conditions are, however, currently understood in any detail. Describing such features has proved to be extremely challenging, primarily because of the difficulties in characterizing the structural nature of these often short-lived and highly heterogeneous protein assemblies. This target is, however, crucial in the quest to define the underlying molecular origins of these neurodegenerative conditions.

The key open questions include:

- What are the relevant structural properties eliciting the toxicity of  $\alpha$ S oligomers?

- What are the key membrane properties governing the selective interactions with  $\alpha$ S oligomers?
- How do pathological  $\alpha$ S mutations affect these mechanisms?

In this chapter we aimed at the ambitious goal of unveiling the molecular bases of the cellular toxicity of  $\alpha$ S oligomers by characterising and comparing the structural properties of two types of pre-fibrillar oligomers having similar morphologies but significantly different toxicity levels (60, 204). By using solution and solid-state nuclear magnetic resonance (NMR) spectroscopy in combination with FRET, AUC, FT-IR, FCS, we have determined the structural properties of these  $\alpha$ S oligomers and investigated the origins of their selective interaction with biological lipid membranes.

To achieve this major goal, we used unique and robust protocols to isolate non-toxic and toxic  $\alpha$ S oligomers (Figure 5.1 a) (60, 204), which enabled us to investigate in detail the relationship between their structure and toxicity. Firstly, in contrast to other types protein oligomers where model systems have been employed (202, 205), these  $\alpha$ S oligomers have well-characterised biological relevance. Indeed, when added to healthy neuronal cultures, oligomers of the toxic type reproduce most of the pathophysiological effects observed in PD model neurons, which were obtained by inducing pluripotent stem cells-derived neurons from a patient with triplication of the  $\alpha$ S gene (206-208).

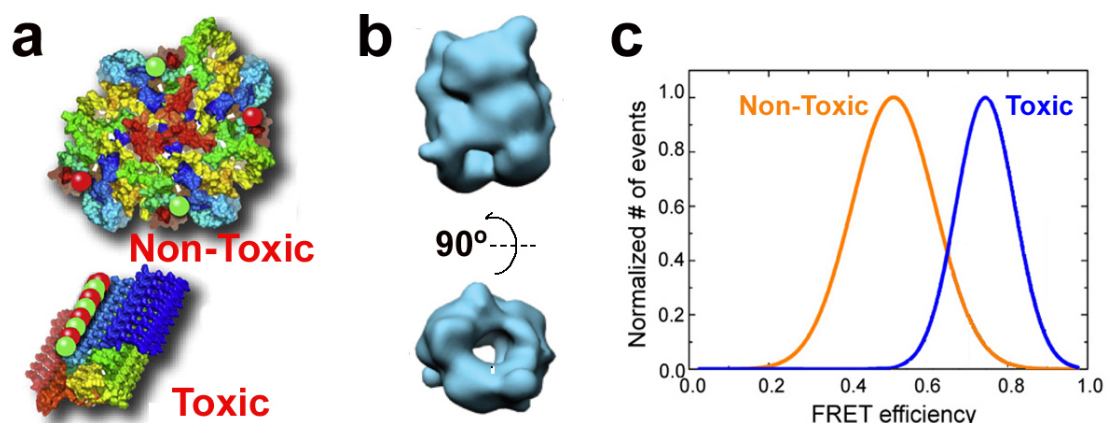


**Figure 5.1. Toxic and non-toxic  $\alpha$ S oligomers.** **a)** Scheme of toxic and non-toxic  $\alpha$ S oligomers from reference (60). **b)** CryoEM surface reconstruction of toxic oligomers from (204). **c)** FRET efficiency in toxic and non-toxic oligomers from reference (60).

Secondly, while being similar in composition, shape, size and morphology, the two oligomer types exhibit different toxicity, as showed by different cytoplasmatic ROS production (60), with only one type being harmful to cell cultures. Furthermore, differences in protease sensitivity and FRET efficiency (more details in reference (60), Figure 5.1 c) indicate inherent structural differences that, if defined at high resolution, can unveil the molecular origins of  $\alpha$ S toxicity in PD. Finally, these  $\alpha$ S oligomers show ideal properties for our goals, including significant stability, homogeneity (e.g. for example suitable to cryoEM investigations, Figure 5.1 b (60, 204), narrow size distributions (Figure 5.3), reproducibility and relatively elevated production yields.

The original literature description identified two types of  $\alpha$ S oligomers as A and B (60, 204). In this study we used a protocol developed by Chen et al (204) to isolate oligomers very similar to the toxic species *Type B*, and with sufficient yield to enable biophysical and spectroscopic investigations (denominated throughout this thesis as *Type B\**). By contrast, the non-toxic *Type A*  $\alpha$ S oligomers cannot be isolated in full, as these species are on-pathway for the most pernicious *Type B*. To overcome this problem, I tested the opportunity to use  $\alpha$ S oligomers formed upon incubation of the protein with the natural molecule (-)-Epigallocatechin-3-gallate (EGCG), which is known to induce the formation of oligomers that are off-pathway for the fibril assembly of  $\alpha$ S and that have very limited toxicity (209).

We first checked if the EGCG-induced  $\alpha$ S oligomers (denominated throughout this thesis as *Type A\**) had similar structural properties of the original *Type A* oligomers identified via single-molecule FRET (60, 204). To reproduce these FRET experiments, we produced two types of fluorescently labelled  $\alpha$ S molecules. As first we mutated the Alanine 90 with a Cysteine residue. Subsequently, the A90C mutant variant of  $\alpha$ S, which was purified as in the case of the wild type protein, was labeled with either maleimide-modified AF488 or AF647 dyes (Invitrogen, Carlsbad, CA, USA) via the cysteine thiol using a fairly standard reaction protocol (see methods).

Using equimolar mixtures of AF488 and AF647 we generated the two types of oligomers (i.e. by following the protocol of Chen *et al* in the case *Type B\** (204) and by incubating  $\alpha$ S with 10 molar equivalents of EGCG at 37 °C for 48h to produce *Type A\** oligomers, see Methods) for intermolecular fluorescence resonance energy transfer (FRET) measurements. The samples were irradiated using a blue laser alone that excites only

AF488-labeled molecules. In the aggregated species, AF647 dyes were excited indirectly by FRET from adjacent AF488 fluorophores within the oligomers, generating coincident fluorescence events in both the AF488 and AF647 channels. This coincident fluorescence is not observed in the case of monomers as a monomeric sample gives rise only to bursts of fluorescence in the AF488 emission channel. This approach was employed by Cremades *et al* (60) to quantify the ratio of  $\alpha$ S oligomers and monomers in their samples and identify Type A and Type B oligomers based on the differences in their FRET efficiency that rely to differences in the oligomer structure.

The present experiments of FRET were performed in bulk and not at a single molecule level as previously performed by Cremades *et al* (60). The main reason for this choice is that the single-molecule FRET instrument employed by Cremades *et al* has been discontinued at the University of Cambridge. Single-molecule FRET instruments are mainly home made and therefore trying to reassemble the same instrument was judged too costly and unnecessary. Indeed, in collaboration with the Liming Lab at the Imperial College, we could obtain the same FRET results in the bulk mode, which allows also obtaining large statistics in a relatively small time of experiment sampling.

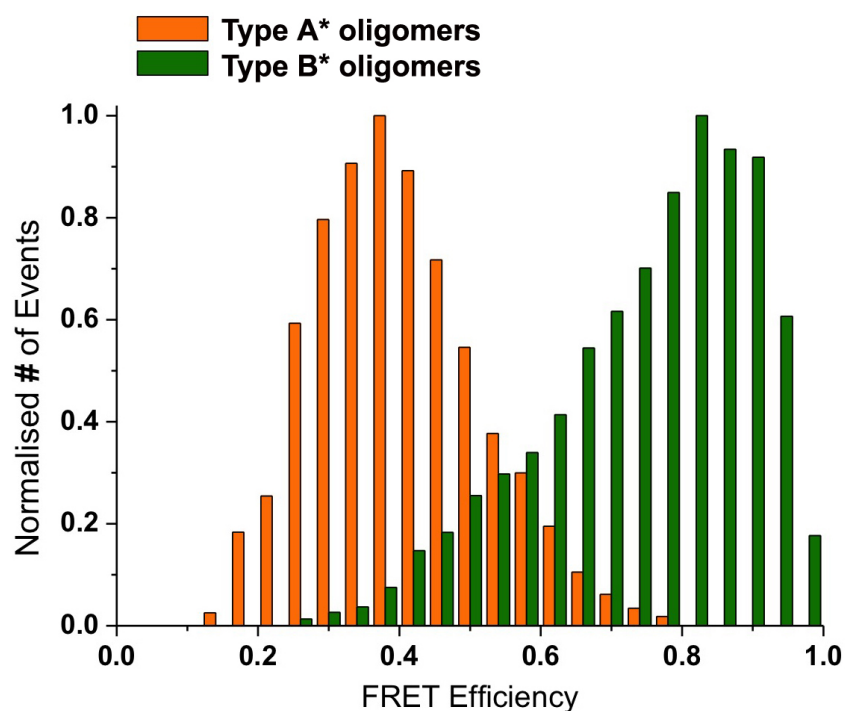


**Figure 5.2. FRET efficiency in bulk measurements of Type A\* and Type B\*  $\alpha$ S oligomers.**

When comparing the distribution of FRET efficiencies (see Methods) measured in bulk experiments using the *Type B\** oligomers (Figure 5.2) and those measured in single molecule experiments by Cremades *et al* (Figure 5.1 c), we obtained a striking coincidence of the results. These findings provide two fundamental insights to our targets. The first is that the Type B  $\alpha$ S oligomers formed under the conditions of Cremades *et al* (very diluted solutions for single molecule experiments) have the same structural properties of the *Type B\** oligomers isolated through the protocol identified subsequently by Chen *et al* (204), which has a significant advantage of enabling for large quantities (milligrams) of oligomers to be isolated, an essential requirement for our plans of using ssNMR experiments. The second outcome of this experiment is that the bulk measurements can be used in an effective manner to reproduce in fractions of hours the statistics that arise from several weeks of sampling in single molecule mode. Encouraged by these results, we then analysed the FRET efficiency of *Type A\**  $\alpha$ S oligomers. The resulting FRET efficiency was distributed around a value of 0.38, which is much smaller than the efficiency of *Type B\** oligomers (0.82). This data indicates that, as in the original study (Figure 5.1 c), the structural properties of *Type A\** and *Type B\** have significantly different structural properties, with the toxic oligomers having donor and acceptor fluorophores very close in space and in an ordered environment (note that these are chemically bound to residue 90 of the protein that is close to the NAC region) and the *Type A\** having the fluorophores far apart and possibly in a more disordered state. When comparing the FRET efficiencies of *Type A* and *Type A\**  $\alpha$ S oligomers (respectively,  $\sim 0.4$  and  $\sim 0.5$ , Figures 5.1 c and 5.2) it is found that the *Type A\** are even more destructured and dynamic than *Type A*. It is possible, however, that in Cremades *et al* the simultaneous characterisation of *Type A* and *Type B*, i.e. the first being on-pathway for the second, could have enriched the FRET efficiency of *Type A* with that of *Type B*, thereby overestimating the FRET efficiency of the first. Besides this possibility, the present result is highly encouraging for showing that *Type A\** has comparable structural properties to those of *Type A* and, most importantly, very different features from those of *Type B\**.

We then compared the size distribution of the *Type A\** and *Type B\** using analytical ultracentrifugation (AUC). The distributions of the two types of oligomers resulted similar (Figure 5.3), with the sedimentation coefficient identifying an initial peak for monomers and a distribution of species up to 20S. In the oligomers of *Type B\**  $\alpha$ S oligomers a dual

distribution of sizes was identified, with peaks at 10S and 16S. In Chen *et al* (204) my colleagues showed that by treating the oligomers with urea, it is possible to isolate a more homogenous species around the 10S peak (Figure 5.3, red). When analysing *Type A\**  $\alpha$ S oligomers we found a more continuous distribution of states ranging from the monomer to a peak centred at 13S and extending up to 26S (Figure 5.3, green). On the contrary, the *Type B\** show a phase separation between the oligomers and the monomers with no significant distribution of species between 1S and 6S. This is due to the fact that the *Type B\** are fibrillar oligomers and therefore require a certain number of copies to form a critical  $\beta$ -sheeted steric zipper nucleus for being stable (204). On the other hand, *Type A\**  $\alpha$ S oligomers, by having putatively a more disordered and amorphous core, can be formed also at intermediate species in between 1S and 6S.

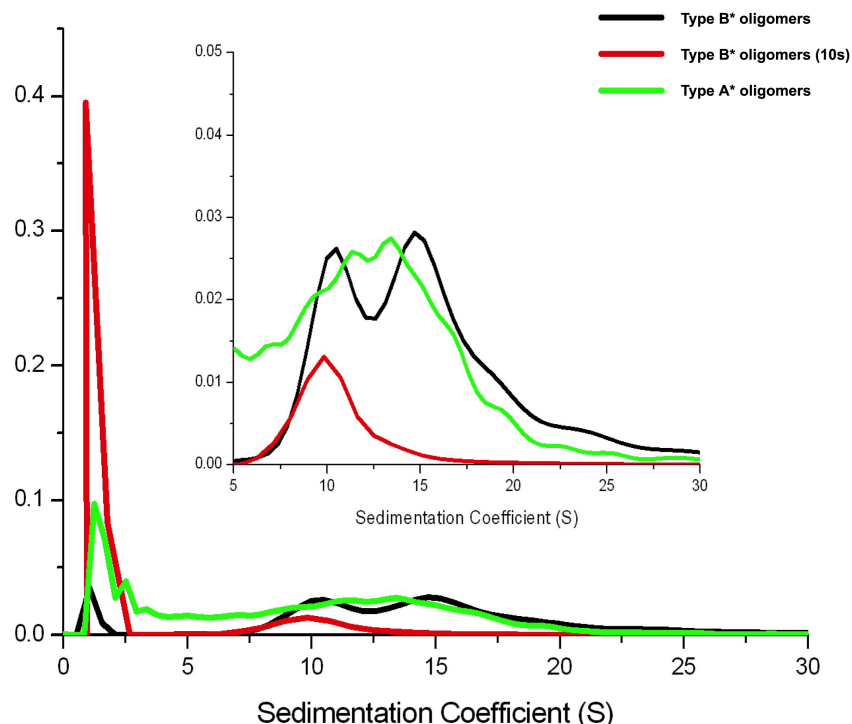


**Figure 5.3. Sedimentation velocity analysis of the  $\alpha$ S oligomeric samples.** The plots report the size distribution of sedimenting species obtained by  $c(s)$  analysis (See Methods). Black, red and green lines correspond to *Type B\**, *Type B\** 10S (i.e. obtained using 4.5M of urea Chen *et al* (204), and *Type A\**.

Despite having similar sizes and morphologies, the two types of  $\alpha$ S oligomers exhibit very different abilities to disrupt lipid bilayers, as shown by the induction of calcein release upon incubation with calcein-loaded small unilamellar vesicles (SUVs) composed of the acidic 1-palmitoyl-2-oleoyl-sn-glycero-3-phospho-L-serine (POPS) *in vitro* (204). In particular, when incubated with SUVs, *Type A\** oligomers induce only a marginal release of calcein, with the extent of membrane disruption being comparable to that induced by monomers and mature fibrils of  $\alpha$ S (Fig. 5.4a). By contrast, *Type B\** oligomers induce a very significant level of release of calcein from the vesicles (~14 times the values measured for *Type A\** oligomers), indicating that these oligomers are able to generate significant disruption of lipid bilayers (Fig. 5.4a). We also verified that the two types of  $\alpha$ S oligomers employed in this investigation (*Type A\** and *Type B\**) present very significantly different levels of cellular toxicity. This test has been performed by our collaborators in the lab of Prof. Fabrizio Chiti in Florence (IT). Upon incubation with human neuroblastoma SH-SY5Y cells and with primary cortical neurons from rats, the *Type B\**  $\alpha$ S oligomers induce similar loss of membrane integrity to the cells as that observed with POPS vesicles *in vitro*. In particular, the incubation with both cell types resulted in the level of intracellular calcein-derived fluorescence being reduced to ~30 % of that of untreated cells (Fig. 5.4b). By contrast, only marginal disruption of the cellular membranes was observed in both cell types upon incubation with *Type A\** oligomers, monomers and mature fibrils of  $\alpha$ S, resulting in more than 90% of the calcein-induced fluorescence relative to that measured in untreated cells (Fig. 5.4b). The significant disruption of synthetic and cellular membranes by *Type B\**  $\alpha$ S oligomers, in contrast to the negligible effects of *Type A\** species, have been found to be strongly correlated with the different levels of cellular toxicity induced by these types of oligomers. In particular, *Type B\** oligomers were found to reduce significantly the mitochondrial activity of neuroblastoma cells and primary cortical neurons, as probed by the reduction of 3-(4,5-dimethylthiazol-2-yl)-2,5-diphenyltetrazolium bromide (MTT, Fig. 5.4c). By contrast, only very small effects on the mitochondrial activity were observed upon incubation of SH-SY5Y cells or primary cortical neurons with *type-A\** oligomers or with monomers of  $\alpha$ S, while mature  $\alpha$ S fibrils (30) generated an intermediate level of mitochondrial damage. The incubation of SH-SY5Y cells with *Type B\**  $\alpha$ S oligomers was also found to induce a very significant increase (nearly 4 fold relative to untreated cells)

of intracellular reactive oxygen species (ROS, Fig. 5.4d), whereas *Type A\** oligomers, monomers and fibrils of  $\alpha$ S induced only marginal levels of intracellular ROS in these experiments.

Overall, the initial investigation presented in this paragraph suggest that we have identified two oligomers (*Type A\** and *Type B\**) showing remarkably different FRET efficiencies (Figure 5.2), which are compatible with those identified by Cremades *et al* (60), having similar size distributions (Figure 5.3) and very different toxicity to cellular cultures (Figure 5.4). Based on this initial study, this Chapter has the ambitious goal to achieve a highly detailed characterisation of the structural properties of these oligomers, particularly in view of the mechanisms that enable *Type B\** to have a selective interaction with lipid membranes that enable this oligomers type to generate cellular toxicity.

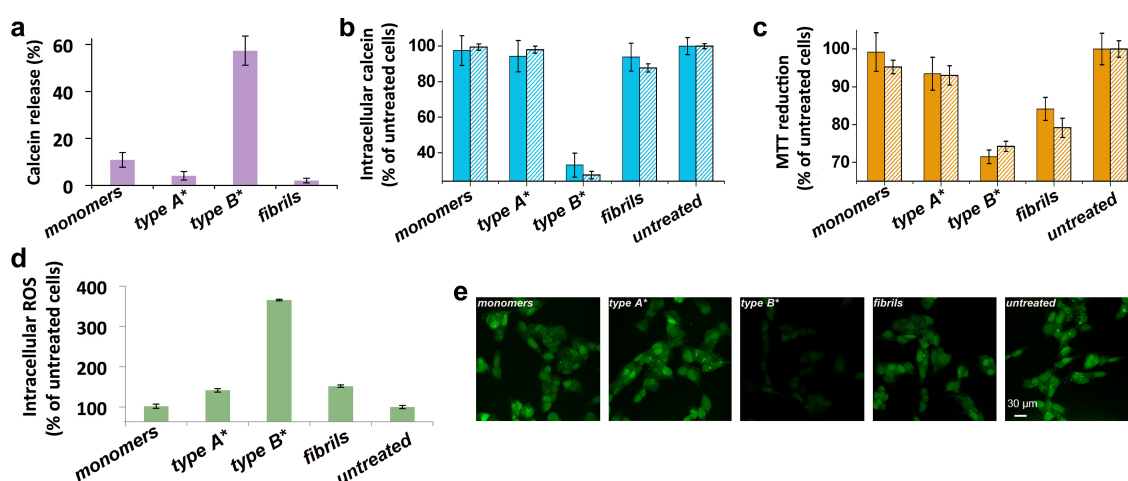


**Figure 5.4 Toxicity of Type A\* and Type B\*  $\alpha$ S oligomers.** **a)** *In vitro* calcein release assay from POPS SUVs incubated for 2h with monomers, Type A\* and Type B\* oligomers and mature fibrils of  $\alpha$ S at a ratio of 1:100 protein:lipid molecules. The signal obtained when the detergent Triton X-100 was added to the SUVs was taken as 100% release. **b-c)** Intracellular calcein-induced fluorescence (b) and mitochondrial activity monitored by the reduction of MTT (c) measured on human neuroblastoma SH-SY5Y cells (filled bars) and rat primary cortical neurons (striped bars) upon incubation with the various  $\alpha$ S species. **d)** Measurement of the intracellular ROS in SH-SY5Y cells induced upon 1h incubation with monomers, Type A\* and Type B\* oligomers and mature fibrils of  $\alpha$ S. **e)** Representative confocal scanning microscopy images of SH-SY5Y cells (scale bar 30  $\mu$ m) showing the different levels of intracellular calcein-induced fluorescence. Cellular experiment were performed by the lab of Prof. Fabrizio Chiti, using oligomers produced by me (Type A\*) and Ms. Serene Chen (Type B\*).

## **5.2 Materials and Methods**

### 5.2.1 $\alpha$ S purification.

$\alpha$ S was purified in *E. coli* using plasmid pT7-7 encoding for the protein as previously described(82). See Chapter II for further details.

### 5.2.2 Preparation of Type A\* and Type B\* $\alpha$ S oligomers.

Type B\*  $\alpha$ S oligomeric samples were prepared as previously described (204). Briefly, 6 mg of lyophilised protein was resuspended in PBS buffer using a pH of 7.4 and at a concentration of 12 mg/mL. The solution was filtered using a 0.22- $\mu$ m cutoff filter and subsequently incubated at 37 °C for 24 h in stationary mode and without any source of shearing to avoiding the acceleration of the fibril formation (204). Despite this precaution, a small number of fibrillar species are typically formed during this incubation and require removal by ultracentrifugation for 1 h at 90,000 rpm (using a TLA-120.2 Beckman rotor; 288,000  $\times$  g). The excess of monomers and small oligomers are also removed by means of several filtration steps using 100-kDa cutoff membranes, which result in the enrichment of the sample in pure oligomeric species of  $\alpha$ S. *Type B\** oligomeric samples prepared in this way have been found to remain stable for many days, although we have used them within the first two days after their production. To estimate the concentrations of the final oligomers we monitored the absorbance at 275 nm by using a molar extinction coefficient of 5,600 M<sup>-1</sup>·cm<sup>-1</sup> (i.e. same as for the monomeric protein).

*Type A\** oligomers are prepared by incubating at 37°C for 48h  $\alpha$ S samples at a concentration of 3mg/mL with 10 molar equivalents of EGCG in PBS buffer at a pH of 7.4. After incubation, monomers of  $\alpha$ S are removed with multiple steps of filtering using 100-kDa cutoff membranes, which is done typically before performing any measurement on these oligomers.

### 5.2.3 Preparation of fluorescently labelled $\alpha$ S for FRET.

The A90C mutant variant of  $\alpha$ S was purified as a monomeric fraction from *E.Coli* as described above. Labelling with fluorescent molecules was performed via maleimide reaction using either maleimide-modified AF488 or AF647 dyes (Invitrogen, Carlsbad, CA, USA). These fluorescent molecules were allowed to react with the thiol moiety of Cys 90 using a well-established reaction protocol (Thirunavukkuarasu et al., 2008). The labeled

proteins were purified from the excess of free dye by a P10 desalting column with Sephadex G25 matrix (GE Healthcare, Waukesha, WI, USA) and concentrated (Amicon Ultra Centricons Millipore, Billerica, MA, USA) before being aliquoted and flash frozen. Stocks were stored at  $-80^{\circ}\text{C}$ .

#### 5.2.4 Magic angle spinning measurements using ssNMR.

MAS experiments in this chapter were carried out using a 14.09T Bruker Ascend<sup>TM</sup> Spectrometer powered by Avance III HD console and mounting a 3.2 mm E<sup>Free</sup> probe (Imperial College London) or using a 14.09T Varian (University of Southampton). See Chapter III for further details on MAS experiments.

#### 5.2.5 Solution NMR samples and CEST experiments.

Solution NMR experiments in this chapter were carried out at  $10^{\circ}\text{C}$  on a Bruker spectrometer (University of Cambridge) operating at  $^1\text{H}$  frequencies of 700 MHz equipped with triple resonance HCN cryo-probes. CEST experiments were based on  $^1\text{H}$ - $^{15}\text{N}$  HSQC experiments by applying constant wave saturation in the  $^{15}\text{N}$  channel. As the exchange is probed between monomeric  $\alpha\text{S}$  (having sharp resonances) and the slow tumbling oligomeric states (having significantly broad resonances), a series of relatively large offsets was employed (-9, -8, -7, -6, -5, -4, -3, -1.5, 0, 1.5, 3, 4, 5, 6, 7, 8 and 9 kHz) resulting in CEST profiles of symmetric shape (Figure 3a). An additional spectrum, saturated at -100 kHz was recorded as reference. CEST experiments were performed using one continuous wave radio frequency of 400Hz to saturate  $^1\text{H}$ - $^{15}\text{N}$ -HSQC spectra recorded using a data matrix consisting of 2048 ( $t_2, ^1\text{H}$ )  $\times$  440 ( $t_1, ^{15}\text{N}$ ) complex points. Assignments of the spectra resonances in for  $^1\text{H}$ - $^{15}\text{N}$ -HSQC spectra in solution NMR were obtained from previous works of the lab(15, 19, 73).

#### 5.2.6 Foster Resonance Transfer (FRET) measurements.

Bulk FRET experiments were performed in the Ying lab at the Imperial College London. Excitation was made by via a 488 nm laser using a total laser power of 47.5 mW. Photon counts were collected using two avalanche photodiode detectors with 2 ms bin times over 8,000 channels on two MCS cards PC-implemented (MCS-PCS, Ortec). Background noise was removed by setting an optimised threshold value for each channel (20 photon/ms bin for the donor channel and a 10 photon/ms bin for the acceptor

channel). We analyzed the event data to derive the distributions of oligomer sizes and FRET values. Analysis assumed a 50/50 balance of donors and acceptors in the oligomers, as previously verified (60). FRET efficiency in each oligomer sample was calculated as

$$E_{FRET} = \frac{I_A}{\gamma I_{DA} + I_A}. \quad (\text{eq. 5.1})$$

Where  $I_A$  and  $I_{DA}$  are the fluorescence intensity of the acceptor and donor in the presence of acceptor, respectively, and  $\gamma$  is the correction coefficient to account of the different quantum yields and detection efficiencies of the donor and acceptor ( $\gamma = 0.26$ ).

#### 5.2.7 Sedimentation Velocity Experiments by Analytical Ultracentrifugation (AUC).

Sedimentation velocity measurements were carried out at 20 °C for Type A\* oligomers only (AUC on Type B\* was previously performed in Chen et al (204)), with spinning at 38,000 to 43,000 rpm (106,750 to 136,680 × g) by using a Beckman-Coulter Optima XL-I analytical ultracentrifuge. The measurements of Type A\* were performed using an An50Ti rotor and the detection mode based on the changes in the refractive index (Rayleigh Interference Optics). This is because the presence of EGCG prevents the employment of standard detection based on UV-visible absorbance. Type A\* protein samples (40–80 μM) were incubated in their respective buffers for 48 h before the start of the sedimentation velocity experiments. The sedimentation coefficient distributions, corrected to standard conditions by using the SEDNTERP program (210), were calculated via least-squares boundary modeling of sedimentation velocity data using the c(s) and lsg\*(s) methods, as implemented in the SEDFIT program ([www.analyticalultracentrifugation.com](http://www.analyticalultracentrifugation.com)).

#### 5.2.8 Fourier Transform InfraRed (FT-IR) spectroscopy.

FT-IR: FT-IR spectra of monomeric αS and Type A\* oligomers were performed on solutions of 100 μM and 400 μM, respectively, in PBS at pH 7.4 using a Bruker BioATRCell II and a Bruker Equinox 55 FT-IR spectrophotometer (Bruker Optics Limited, UK) equipped with a liquid nitrogen cooled mercury cadmium telluride (MCT) detector and a silicon internal reflection element (IRE). For each spectrum, we collected 256 interferograms and co-added at 2 cm<sup>-1</sup> resolution. Buffer contribution to the signal (i.e. PBS buffer and EGCG)

was independently measured and subtracted during data analysis of each protein spectrum and before curve fitting of the amide I region (1720-1580  $\text{cm}^{-1}$ ). The analysis of the data was performed with the Opus software package (Bruker Optics Limited, UK) and included these steps: atmospheric compensation, baseline subtraction, second derivative analysis, and deconvolution with Gaussian/Lorentzian curves using a Levenberg-Marquardt algorithm. Data presented are a result of the fitting of 3 independent FTIR spectra for each protein sample. For comparison all absorbance spectra were normalized.

### **5.3 Structural properties of toxic and non-toxic $\alpha$ S oligomers**

In order to identify the major structural differences between *Type A\** and *Type B\**  $\alpha$ S oligomers, we employed ssNMR experiments to probe both rigid (CP regime) and disordered regions (INEPT regime) of the oligomers. Both types of oligomers could be pelleted into a MAS rotor by ultracentrifugation of 4 h at 90,000 rpm (using a TLA-120.2 Beckman rotor; 288,000  $\times$  g). Experiments were performed using a 1.6mm MAS rotor, which requires minimal amount of material (only 8  $\mu$ L of pellet) at the University of Southampton. MAS experiments were performed at 5  $^{\circ}$ C and by spinning the sample at 12.5 kHz. We first analysed the disordered regions of both *Type A\** and *Type B\**  $\alpha$ S oligomers (Figure 5.5) by using INEPT experiments to probe the C-H cross-peaks of highly mobile regions in the sample. INEPT experiments are extremely sensitive in the analysis of the structural differences of these two types of oligomers as they rely on disordered regions likely exposed on the surface of the oligomers and therefore promoting macromolecular interactions by these aggregates. Interestingly, the INEPT spectra of the two types of oligomers indicate the two assemblies expose some different segments of the protein. As expected, both INEPT spectra can be completely overlapped the  $^1\text{H}$ - $^{13}\text{C}$ -HSQC of the monomeric and disordered  $\alpha$ S in solution NMR (Figure 5.6). This data confirm that the highly mobile regions of the oligomers maintain the disordered nature of the monomeric  $\alpha$ S precursor molecules. The correspondence with the solution NMR  $^1\text{H}$ - $^{13}\text{C}$ -HSQC enables a rapid assignment of the resonances of the INEPT spectrum of the two oligomers. Overall, the assignment suggests that the C-terminal region of the protein is exposed in both the oligomers (Figure 5.6 c). The major difference in the two is that toxic *Type B\** oligomers expose also resonances belonging to residues at the N-terminus. Another major difference is that the non-toxic *Type A\** species feature the exposure of peaks from the central region of the protein, including the NAC region, whereas no peaks belonging to the NAC are identified in the INEPT spectra of *Type B*, suggesting that this fragment represent a part of the core of the oligomer. This indication is also in line with the FRET data (Figure 5.2).

We also recorded the  $^{13}\text{C}$ - $^{13}\text{C}$ -DARR spectra on these oligomeric samples to provide structural information of the rigid core regions of the oligomers. The comparison of the DARR spectra of *Type A\** and *Type B\** oligomers suggests that the two cores are fundamentally different in their structure (Figure 5.7). In particular, it is clear that the

shifts in the cross peaks in the DARR spectra of these two oligomers indicate that the *Type B\** primarily features a shift of its resonances toward the beta sheet structures compared to the *Type A\**, the latter showing chemical shifts that approach the random coil ranges (Figure 5.8). As a result the MAS experiments in cross polarisation regime indicate that the core of *Type A\**  $\alpha$ S oligomers lacks specific secondary structure conformations whereas that of *Type B\**  $\alpha$ S oligomers feature beta-sheet conformations. This indication is in agreement with FT-IR experiments on these oligomers compared to fibrillar species (Figure 5.9). In particular, FT-IR of *Type A\**  $\alpha$ S oligomers shows a peak in the  $1654\text{ cm}^{-1}$ , which is overlappable with the peak of the random coil  $\alpha$ S monomers. The FT-IR data of *Type A\** are, therefore, in agreement with the ssNMR measurements that indicate that both core ( $^{13}\text{C}$ - $^{13}\text{C}$ -DARR, Figure 5.7 a) and surficial regions ( $^1\text{H}$ - $^{13}\text{C}$ -INEPT, Figure 5.5) of these oligomers lack specific elements of secondary structure. Similarly FT-IR data of *Type B\** oligomers show the presence of antiparallel  $\beta$ -sheet structures in the assembly, which is in agreement with the chemical shifts in the  $^{13}\text{C}$ - $^{13}\text{C}$ -DARR spectrum indicating  $\beta$ -sheet structure in the core of the oligomers (Figure 5.7 b). FT-IR also shows random-coil peak in *Type B\** oligomers, which is in line with  $^1\text{H}$ - $^{13}\text{C}$ -INEPT spectra indicating disordered conformations at the N- and C- termini of the protein in these oligomers (Figure 5.5).





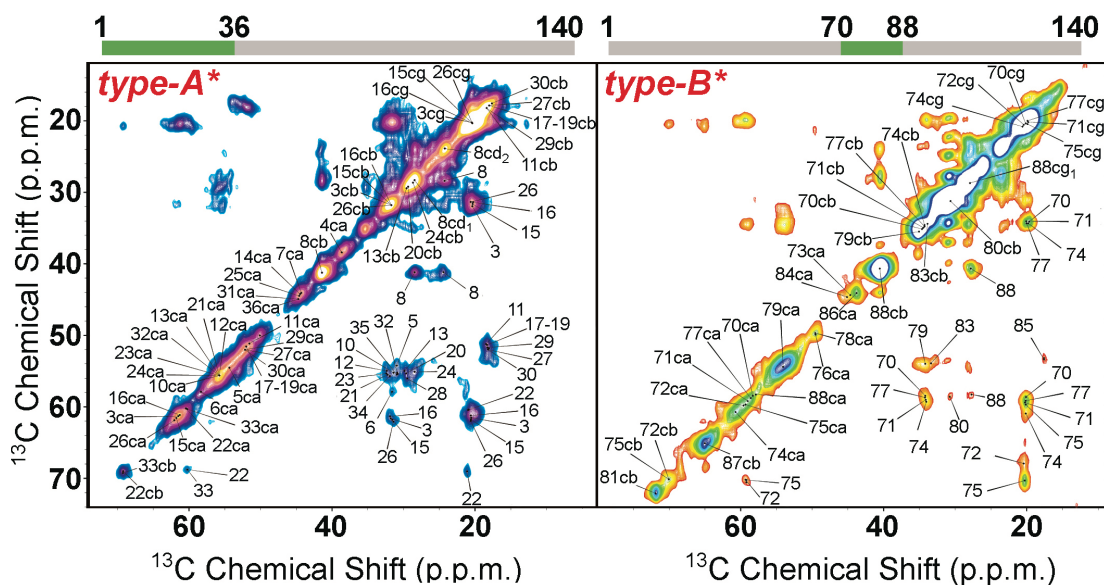


**Figure 5.7.**  $^{13}\text{C}$ - $^{13}\text{C}$  DARR spectrum of Type A\* and Type B\*  $\alpha\text{S}$  oligomers.  $^{13}\text{C}$ - $^{13}\text{C}$  DARR correlation spectrum of a sample of Type A\* (left panel) and Type B\* (right panel)  $\alpha\text{S}$  oligomers was recorded using a contact time of 1ms, mixing time of 50ms, at a temperature of 5 °C at a MAS rate of 12.5 kHz. The measurements were performed using a 14.09T NMR spectrometer (Varian) and 1.6mm MAS probe.

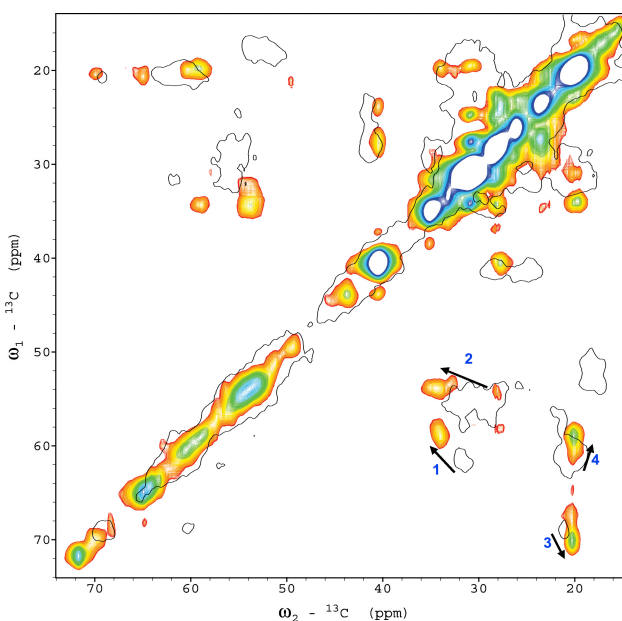


**Figure 5.8.** Overlay of  $^{13}\text{C}$ - $^{13}\text{C}$  DARR spectra of Type A\* and Type B\*  $\alpha\text{S}$  oligomers.  $^{13}\text{C}$ - $^{13}\text{C}$  DARR correlation spectrum of a sample of Type A\* has been drawn as in Figure 5.6 whereas for clarity of the overlay and Type B has been drawn on a single black contour line. Chemical shift “virtual moves” are indicated by arrows. In particular: mark 1 reports the Ca-Cb correlation of Val residues, mark 2 reports the Ca-Cb correlation of GLN/LYS residues, mark 3 reports the Ca-Cg correlation of THR residues and mark 4 reports the Ca-Cg correlation of Val residues. All the “virtual moves” from Type A\* to Type B\* indicate a difference between random-coil conformations and beta-sheet structures.

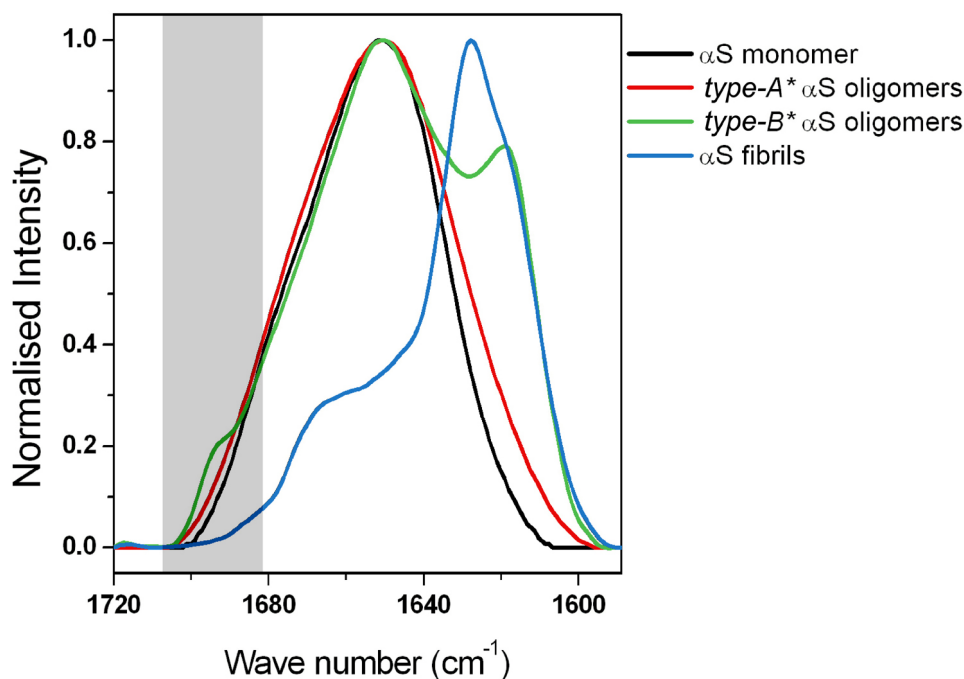


**Figure 5.9. FT-IR Type A\* and Type B\*  $\alpha$ S oligomers.** FT-IR spectra of Type A\* (red) and Type B\* (green)  $\alpha$ S oligomers studied in this investigation. The spectrum of the non-toxic Type A\* oligomers shows a single band centered at  $1654\text{ cm}^{-1}$  that overlaps clearly with the signal of the disordered  $\alpha$ S monomers (black). The spectrum of the Type B\*  $\alpha$ S oligomers (green) shows, in addition to the same band at  $1654\text{ cm}^{-1}$  that is indicative of disordered regions, the characteristic absorption band for antiparallel  $\beta$ -sheet structure (highlighted in grey background). This band is absent in the fibrillar form of  $\alpha$ S (cyan).

The fast relaxation of the ssNMR signals in MAS experiments of these oligomer samples prevented the multidimensional spectra to be measured in order to perform a canonical assignment of their  $^{13}\text{C}$ - $^{13}\text{C}$ -DARR in order to identify the core regions of the oligomers, however, we combined information from solution-state chemical exchange saturation transfer spectra (CEST, see Methods) with the known assignments of the fibrillar (54) and monomeric (114) states of  $\alpha$ S; this procedure led to the identification of 33 and 18 residues in the  $^{13}\text{C}$ - $^{13}\text{C}$ -DARR spectra of Type A\* and Type B\* oligomers, respectively. More specifically, in the case of the non-toxic *type-A\** species, CEST experiments showed a significant degree of saturation for the 40 N-terminal residues of the protein (Figure 5.10 a-c), which indicates a strong association of this region with the rigid core of the oligomers. By contrast, the lowest levels of saturation were observed for the C-terminal region and the segment between residues 70 and 90, indicating a minimal association of these regions with the rigid core of the non-toxic *Type A\**  $\alpha$ S oligomers. In

the case of the toxic *Type B\**  $\alpha$ S oligomers, CEST experiments showed a generally lower degree of saturation transfer throughout the sequence compared to the non-toxic *Type A\** oligomers, with no saturation associated with either the N- or C- terminal regions of the protein or with residues of three of the four major hydrophobic segments of the  $\alpha$ S sequence (residues 36-41, 47-56, 88-95, Fig. 5.10 d). This finding indicates that none of these regions is strongly associated with the core of the toxic *Type B\** oligomers, in contrast to the situation observed for the hydrophobic segment 70-79, for which significant saturation was detected in the CEST experiments (Fig. 5.10 d).

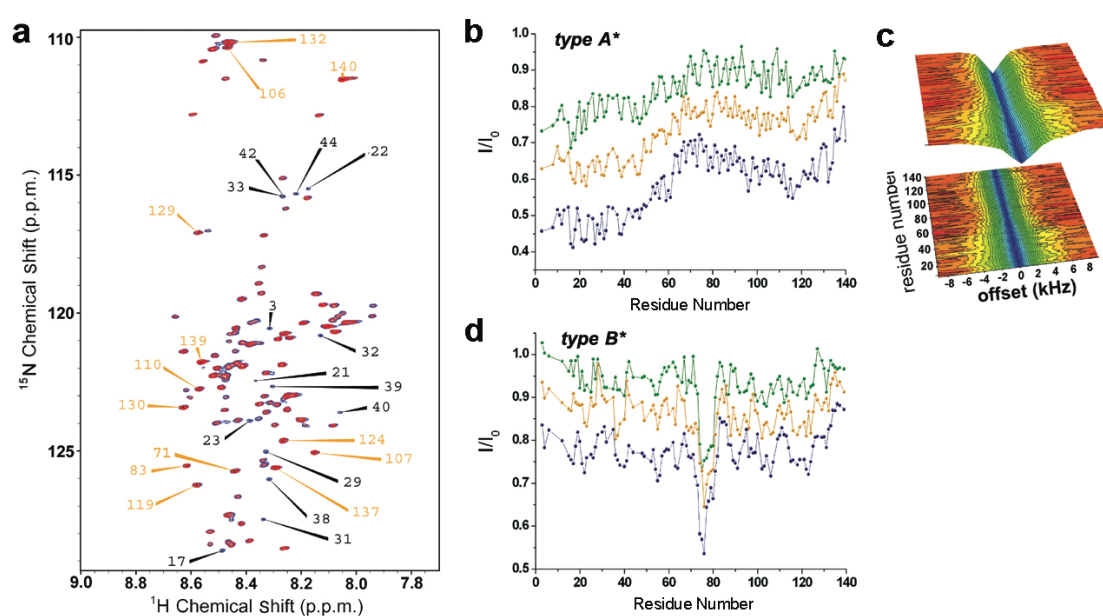


**Figure 5.10. Identification of core-associated and solvent exposed dynamical regions in  $\alpha$ S oligomers using CEST.** CEST experiments were recorded at a  $^1\text{H}$  frequency of 700MHz using a saturation RF band of 400 Hz placed at different offsets (-9, -8, -7, -6, -5, -4, -3, -1.5, 0, 1.5, 3, 4, 5, 6, 7, 8 and 9 kHz). (a) CEST study of the non-toxic type-A\*  $\alpha$ S oligomers measured at 10 °C. The spectrum measured with the saturation RF at an offset of -1.5 kHz (red) is overlaid onto the reference spectrum (blue). Labels identify peaks with very high (black) and very low (orange) level of saturation transfer. (b) CEST profiles of non-toxic type-A\*  $\alpha$ S oligomers measured at different saturation frequencies are shown as a function of the residue number. The plot reports the average values of CEST saturations measured using offsets of +1.5 kHz and -1.5 kHz (blue), +3.0 kHz and -3.0 kHz (orange), and +4.0 kHz and -4.0 kHz (green). (c) CEST surface for non-toxic type-A\*  $\alpha$ S oligomers. (d) CEST profiles of toxic type-B\*  $\alpha$ S oligomers measured at different saturation frequencies. Color code as in panel b.

#### ***5.4 The selective interaction with cellular membranes promote the toxicity of $\alpha$ S oligomers***

The interaction of protein oligomers with cellular membranes has been individuated as a key factor to distinguish between toxic and non-toxic species (202, 203). This interaction can result into lipid extraction, loss of membrane integrity and selective membrane permeability (203). We first analysed the binding affinity of *Type A\** and *Type B\**  $\alpha$ S oligomers for DOPE:DOPS:DOPC SUVs (as used in Chapter III) using fluorescence correlation spectroscopy (FCS). To this end, we produced oligomers of the two types by mutating  $\alpha$ S Alanine 90 with a Cysteine residue and subsequently, labelling this protein using maleimide-modified AF488. Oligomers produced with AF488  $\alpha$ S are therefore fluorescent and can be used in FCS. The advantage of using this approach (e.g. rather than DLS) is that this enables to specifically monitor the diffusion properties of the fluorescently labelled species, regardless of the presence of other species. In our application, we aimed at assessing the strength of interaction between the two types of oligomers and SUVs by monitoring their diffusion properties upon incubation. In principle an extremely strong binding would result in the oligomers adopting the same diffusion properties of the slower SUV species. The data (Figure 5.11) evidence that the diffusion properties of *Type A\** and *Type B\**  $\alpha$ S oligomers are similar, with residence time “ $\tau$ ” in the confocal volume of 0.86 ms and 1.15 ms, respectively. By incubating the oligomers with 0.5 mg/ml of SUVs, both oligomers showed higher residence times in the confocal volume (2.61 ms and 3.52 ms for *Type A\** and *Type B\**  $\alpha$ S oligomers, respectively). The changes in the diffusion properties were however stronger in the case of *Type B\**, indicating that these oligomers interact more tightly with the membrane surface than *Type A\**. Interestingly, by increasing the concentration of SUVs to 5.0 mg/ml, the residence time of *Type B\**  $\alpha$ S oligomers (6.93 ms) approached the limit of the residence time of the SUV (7.48 ms), which indicates that the interaction between *Type B\**  $\alpha$ S oligomers and the membrane is extremely tight such that these oligomers behave almost as an integral part of the SUVs. On the contrary, under the same conditions, *Type A\**  $\alpha$ S oligomers have a residence time of 4.58 ms, which indicates that *Type A\** have a non-negligible affinity for membranes but the membrane-interaction is weaker than that of *Type B\**  $\alpha$ S oligomers.

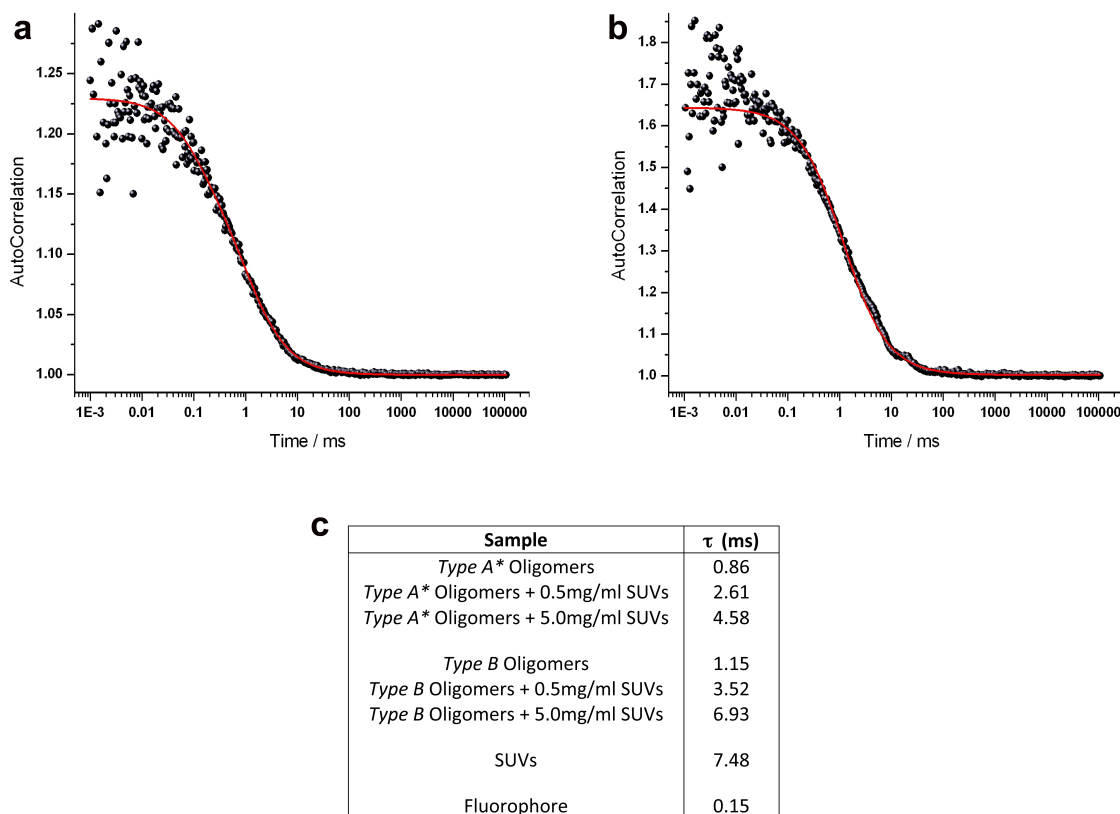


**Figure 5.11. Fluorescence correlation spectroscopy of Type A\* and Type B\*  $\alpha$ S oligomers at the surface of SUVs.** FCS was performed on Type A\* and Type B\*  $\alpha$ S-AF488 oligomers by exciting the fluorophores at 488nm (AF488) and by recording autocorrelation function of the fluorescence. **a)** Type A\*  $\alpha$ S-AF488. **b)** Type B\*  $\alpha$ S-AF488. **c)** Table reporting the residence time in all the analysed samples.

To gain a deeper understanding of this selective interaction we measured PREs between lipids and oligomers by doping the lipid bilayers with 2% of lipids containing paramagnetic centres (114). PREs are highly sensitive probes of macromolecular interactions and, by using lipids having paramagnetic centres at the hydrophilic heads or bottom hydrophobic tails of the lipids, we characterised the levels of insertion of the oligomers in the bilayers (see also reference 114). We first measured PRE using the spin label at the surface of the membrane, i.e. by doping the DOPE:DOPS:DOPC bilayer with 2% of 1,2-dimyristoyl-sn-glycero-3-phosphoethanolamine-N-DTPA (gadolinium salt, which carries an unpaired electron in the hydrophilic head of the lipid, Figure 5.12). In line with the FCS, this analysis showed that the spectra of both types of oligomers are affected by the paramagnetic groups, indicating that Type A\* and Type B\*  $\alpha$ S oligomers are both associated with the

surface of the membrane. Selective quenching was clear in both aliphatic and carbonyl regions in these experiments (Figure 5.12).

We then performed PRE experiments by doping the lipid bilayer with 2% of 1-palmitoyl-2-stearoyl-[16-doxy]-sn-glycero-3-phosphocholine, which carries an unpaired electron at the position of the carbon 16 of the lipid tail (Figure 5.13). In this case, however, we observed no selective quenching of the DARR resonances of *Type A\**  $\alpha$ S oligomers, indicating that these oligomers, as in the case of  $\alpha$ S monomers (114), remain mainly at the top of the membrane and do not experience any specific membrane insertion. A different scenario, however, was found in the case of *Type B\**  $\alpha$ S oligomers, which showed PRE effects with some specific resonance broadening (Figure 5.13), suggesting that the structured regions of *Type B\**  $\alpha$ S oligomers do insert up to a certain extent into the hydrophobic region of the membrane bilayer.

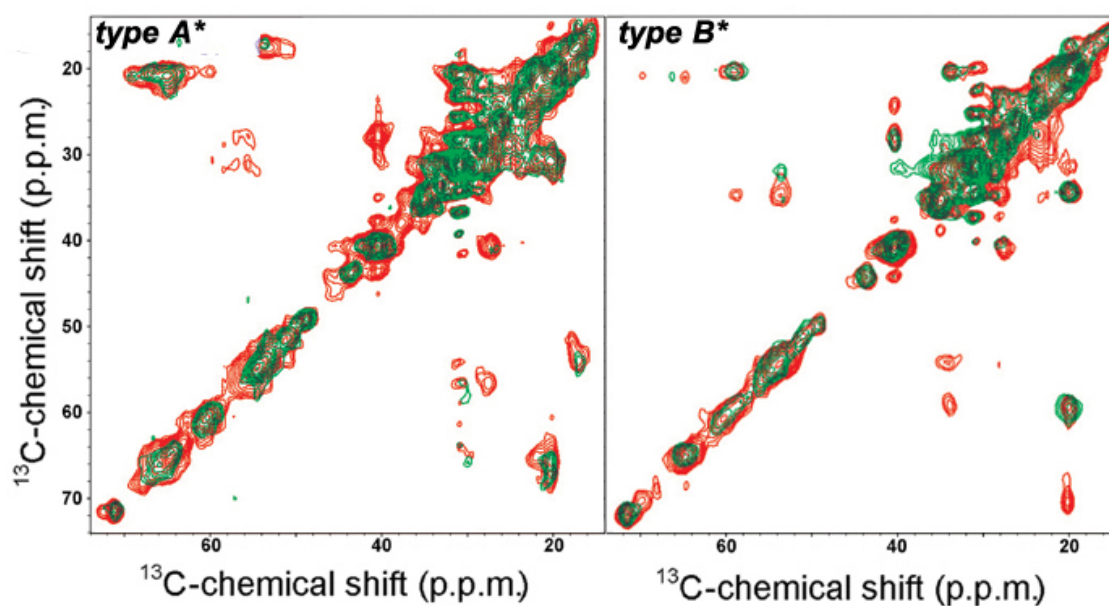


**Figure 5.12. PRE experiments of Type A\* and Type B\*  $\alpha$ S oligomers at the surface of SUVs.** Top and bottom panels for Type A\* and Type B\*  $\alpha$ S oligomers, as indicated. PRE were measured by incubating the two types of ligomers with DOPE:DOPS:DOPC SUVs doped with 2% of 1,2-dimyristoyl-sn-glycero-3-phosphoethanolamine-N-DTPA (gadolinium salt, which carries an unpaired electron in the hydrophilic head of the lipid). The  $^{13}\text{C}$ - $^{13}\text{C}$ -DARR spectra the membrane-bound oligomers were measured as described in figure 5.7 at spinning rate, mixing and contact times of 12.5 kHz, 50 ms and 1 ms, respectively, and in the presence (green) and absence (red) of paramagnetic labelled lipids. Cross-correlations between aliphatic and carbonyl groups (left side of the spectra) and aliphatic-aliphatic groups (right side of the spectra) are reported.

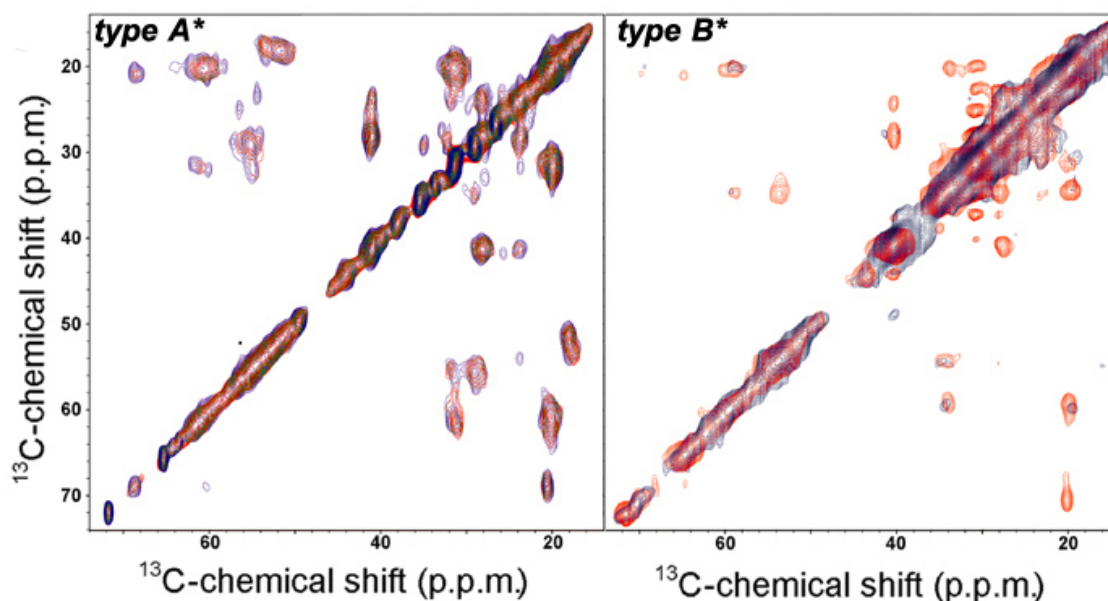


**Figure 5.13. PRE experiments of Type A\* and Type B\*  $\alpha$ S oligomers in the interior of lipid bilayers of SUVs.** Top and bottom panels for Type A\* and Type B\*  $\alpha$ S oligomers, as indicated. PRE were measured by incubating the two types of ligomers with DOPE:DOPS:DOPC SUVs doped with 2% of 1-palmitoyl-2-stearoyl-[16-doxyl]-sn-glycero-3-phosphocholine, which carries an unpaired electron at the position of the carbon 16 of the lipid tail. The  $^{13}\text{C}$ - $^{13}\text{C}$ -DARR spectra the membrane-bound oligomers were measured as described in figure 5.7 at spinning rate, mixing and contact times of 12.5 kHz, 50 ms and 1 ms, respectively, and in the presence (blue) and absence (red) of paramagnetic labelled lipids. Cross-correlations between aliphatic and carbonyl groups (left side of the spectra) and aliphatic-aliphatic groups (right side of the spectra) are reported.

In order to characterise further the structural nature of the membrane binding by the two types of  $\alpha$ S oligomers, we measured  $^{13}\text{C}$ - $^{13}\text{C}$ -DARR spectra at  $-19^\circ\text{C}$ , a condition that has been shown to enhance the signal-to-noise ratios of the resonances of the regions of  $\alpha$ S that are tightly bound to DOPE:DOPS:DOPC lipid bilayers (114). In the case of the toxic Type B\* species, this analysis revealed a set of well-defined resonances that are additional to, and distinct from, those observed in the  $^{13}\text{C}$ - $^{13}\text{C}$ -DARR spectra of the isolated oligomers (Figure. 5.14). These additional resonances match closely those of the N-terminal region of monomeric  $\alpha$ S bound to DOPE:DOPS:DOPC membranes (Figure 3.2 b), where the protein adopts an amphipathic  $\alpha$ -helical conformation (114), and indicate that the N-terminal region of the protein is strongly associated with the lipid bilayer in the membrane-bound state of the toxic Type B\* oligomers. In the case of the

non-toxic *Type A\** oligomers, however, these experiments revealed a different set of additional  $^{13}\text{C}$ - $^{13}\text{C}$ -DARR peaks (Figure 5.14), whose chemical shifts are characteristic of the  $^{13}\text{C}\alpha$ - $^{13}\text{C}\beta$  cross correlations of lysine residues. The low intensities and the broad linewidths of these resonances indicate the absence of a specific and well-defined region of the protein that is tightly bound to the membrane, and suggest that the binding of the non-toxic *Type A\** oligomers to the bilayer involves lysine-rich segments located randomly throughout the first 97 residues of the  $\alpha\text{S}$  sequence.

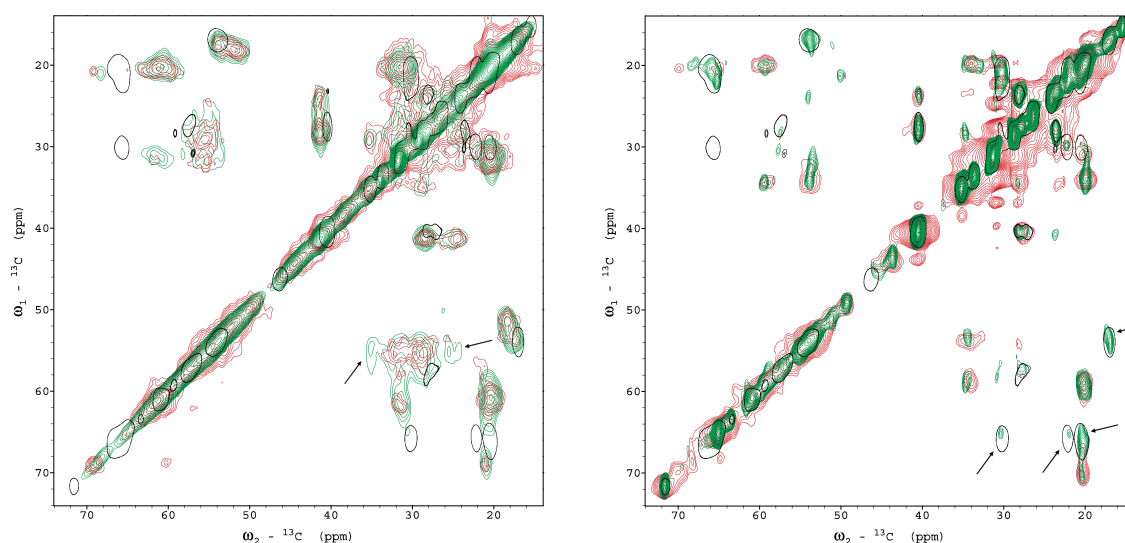


**Figure 5.14.  $^{13}\text{C}$ - $^{13}\text{C}$  DARR of *Type A\** and *Type B\**  $\alpha\text{S}$  oligomers at the surface of SUVs.** Left and right panels report the analyses of *Type A\** and *Type B\**  $\alpha\text{S}$  oligomers, respectively. Each oligomer was incubated with DOPE:DOPS:DOPC SUVs and spun down at 68000 rpm to create the pellet for filling the MAS rotor.  $^{13}\text{C}$ - $^{13}\text{C}$  DARR of oligomers in the absence (red) and presence (green) of lipids were measured at  $-19\text{ }^\circ\text{C}$  to enable the transition of the lipids in gel phase (145). Under these conditions, the  $^{13}\text{C}$ - $^{13}\text{C}$  DARR of monomers of  $\alpha\text{S}$  in the presence of SUVs detects peaks corresponding to the membrane-anchor region in an amphipathic helix conformation (Chapter III), which are reported here using black contour lines. Arrows in the left panel, *Type A\**, show resonances corresponding to Lys and Gln residues that are enhanced in the presence of lipids at  $-19\text{ }^\circ\text{C}$ . In the case of *Type B\**, right panel, the resonances that are enhanced in the presence of lipids at  $-19\text{ }^\circ\text{C}$  correspond to those of the membrane-anchor region, as in the case of the monomeric state of  $\alpha\text{S}$  bound to SUVs.

Overall, therefore, our study of the binding of the toxic *Type B\** and non-toxic *Type A\**  $\alpha\text{S}$  oligomers to the SUVs has revealed that the two types of oligomers have different modes

of binding to acidic membranes (Figure 5.15). The *Type A\**  $\alpha$ S species appear to interact only with the head groups of the lipid bilayers *via* multiple lysine-rich regions of the protein sequence (Figure 5.15). By contrast, the toxic *Type B\** oligomers are anchored onto the membrane surface by a highly specific region of the  $\alpha$ S sequence, the exposed N-terminal region that adopts an amphipathic helical conformation upon membrane binding (Figure 5.14). Moreover, the highly structured and rigid regions of the toxic *Type B\** oligomers insert to a significant degree into the interior of the bilayer (Figure 5.13).

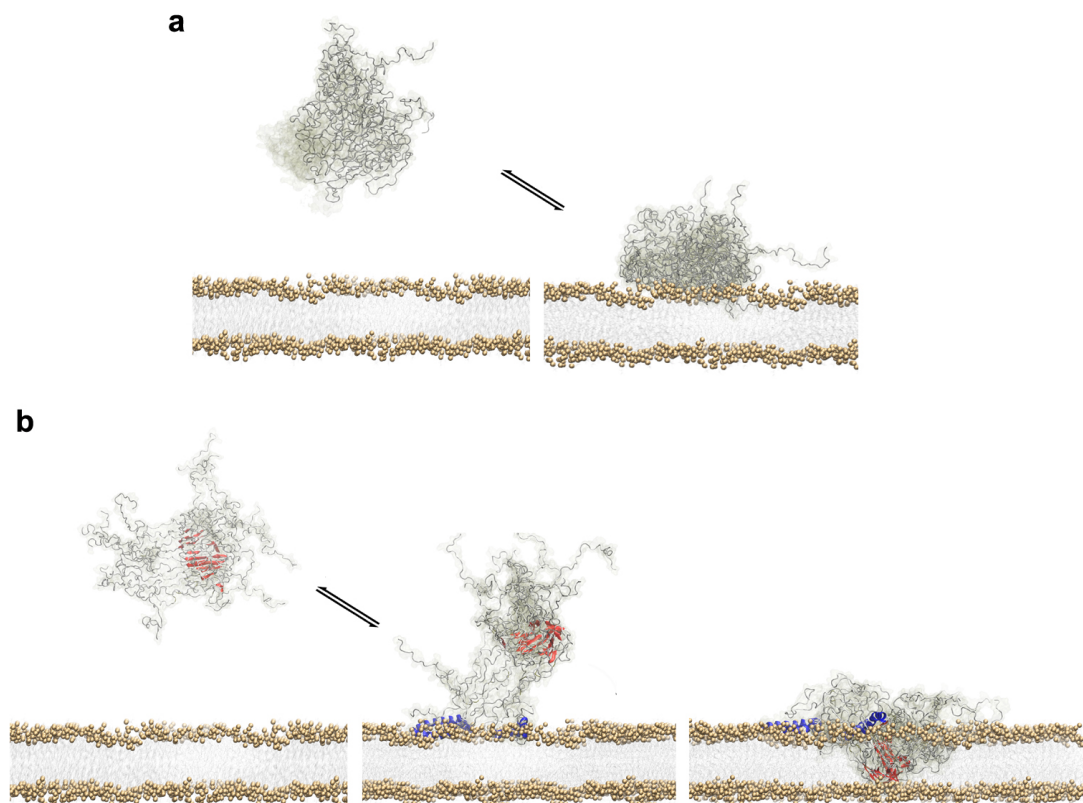


**Figure 5.15. Structural basis of membrane binding of  $\alpha$ S oligomers.** **a)** Non-toxic type-A\*  $\alpha$ S oligomers are represented in disordered conformations using grey ribbons. ssNMR experiments show that non-toxic Type A\*  $\alpha$ S oligomers bind to the surface of acidic lipid bilayers (PRE, Figure 5.12) *via* various lysine rich segments randomly exposed to the surface of the oligomer (membrane-bound  $^{13}\text{C}$ - $^{13}\text{C}$ -DARR, Figure 5.14) and without inserting into the core of the bilayer (PRE, Figure 5.13). **b)** Toxic Type B\*  $\alpha$ S oligomers feature both structured (red) and disordered (grey) regions and bind the surfaces of the lipid bilayers *via* the exposed N-terminal regions of  $\alpha$ S molecules in the oligomer, which fold into amphipathic  $\alpha$ -helices (blue) upon membrane binding (membrane-bound  $^{13}\text{C}$ - $^{13}\text{C}$ -DARR, Figure 5.14). In contrast to Type A\* rigid regions of Type B\* oligomers, which are rich in  $\beta$ -sheet structure, insert into the lipid bilayers (PRE experiments, Figure 5.13).

## 5.5 Discussion

The characterisation of transient toxic  $\alpha$ S oligomers that form under the pathological conditions leading to PD is a major challenge for current biochemistry. In this Chapter we have identified an approach to characterise structural properties and mechanisms of membrane interaction of two types of  $\alpha$ S oligomers exhibiting significantly different toxicity levels (Figure 5.4). The toxic  $\alpha$ S oligomers (*Type B\**) have been previously characterised at low resolution in the Dobson group (60, 204) for their toxicity and general properties of secondary structure, shape and size. Unfortunately the non-toxic *Type A* identified by Cremades et al (60) (*Type A*) cannot be isolated in significant quantities to enable biophysical characterisations. To circumvent this problem, in my thesis I explored the possibility of using oligomers formed by  $\alpha$ S in the presence of the natural molecule EGCG, designated as *Type A\**. We showed that *Type A\** oligomers have similar properties to those of the original *Type A* identified by Cremades *et al* (60), including consisting FRET efficiency (Figure 5.2), size distribution (Figure 5.3) and low toxicity (Figure 5.4). Having identified two types of  $\alpha$ S with similar low-resolution structural properties but very different neuronal toxicity, we aimed at higher resolution characterisation in order to achieve a structure-toxicity relationship through the analysis of *Type A\** and *Type B\** oligomers.

ssNMR experiments using cross polarisation and INEPT regimes suggested major differences in these two types of oligomers. In particular, non-toxic *Type A\** oligomers showed INEPT resonances from residues from the C-terminal negatively charged region and part of the NAC region, suggesting that these regions compose the outer part of the oligomers. Conversely, INEPT experiments of *Type B\** showed that the dynamical regions of the oligomers include both N- and C- terminal regions (Figure 5.6 c). Both oligomers are disordered in their dynamical regions, as indicated by chemical shifts from INEPT spectra (Figure 5.6). Using CP experiments, we obtained  $^{13}\text{C}$ - $^{13}\text{C}$ -DARR spectra that are sensibly different in the two types oligomers, with *Type A\** having rigid moieties that lack specific signatures of relevant secondary structure elements and *Type B\** having core regions that are rich in  $\beta$ -sheet structure (Figures 5.7 and 5.8). These data are in general agreement with FT-IR experiments (Figure 5.9), but provide a residue-specific characterisation of the protein conformations in the oligomers.

One of the interesting results of the ssNMR analysis is that *Type A\**  $\alpha$ S oligomers possess rigid regions that are entirely devoid of secondary structure (Figure 5.7). This is likely to be associated with the intrinsic affinity of EGCG for coil regions. In Figure 5.16 it is shown indeed that EGCG binds the most exposed and unstructured loops in human Lysozyme. This is consistent with the spectra of another folded protein, namely mAcP (Figure 5.17), for which EGCG binds its catalytic loop that in the apo form is highly dynamical and exposed to the solvent. When mAcP is unfolded by 6M of guanidinium hydrochloride, however, the binding of EGCG is extended to the whole protein sequence, indicating that this molecule has no sequence specificity but a conformational specificity toward random coil states. It is therefore likely that the effect of EGCG on  $\alpha$ S assembly into *Type A\** oligomers is to stabilise random conformations and prevent the protein from forming secondary structures. This indication could be useful in future strategies to design molecules that could redirect the aggregation of proteins toward non-toxic oligomers within the mechanisms leading to neurodegenerative diseases. It is however important to stress that finding small molecules that bind disordered proteins with high specificity is a very ambitious challenge.

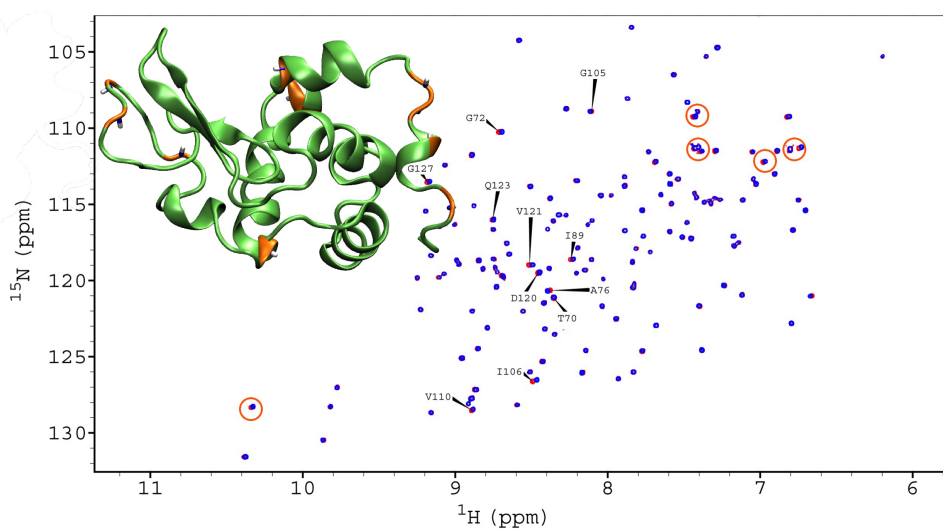


**Figure 5.16. Binding of EGCG to human Lysozyme.**  $^1\text{H}$ - $^{15}\text{N}$ -HSQC spectra of human Lysozyme isolated (red) and in the presence of 5 equivalents (blue) of EGCG. The spectra were measured at the proton resonance of 700MHz, by using a BRUKER avance III spectrometer with cryoprobe TXO. The experiments have been measured at 298K in 50mM phosphate buffer and pH 5.5. The structure of human lysozyme is shown using green ribbons by highlighting in orange the residues that have major chemical shift changes in the presence of EGCG.

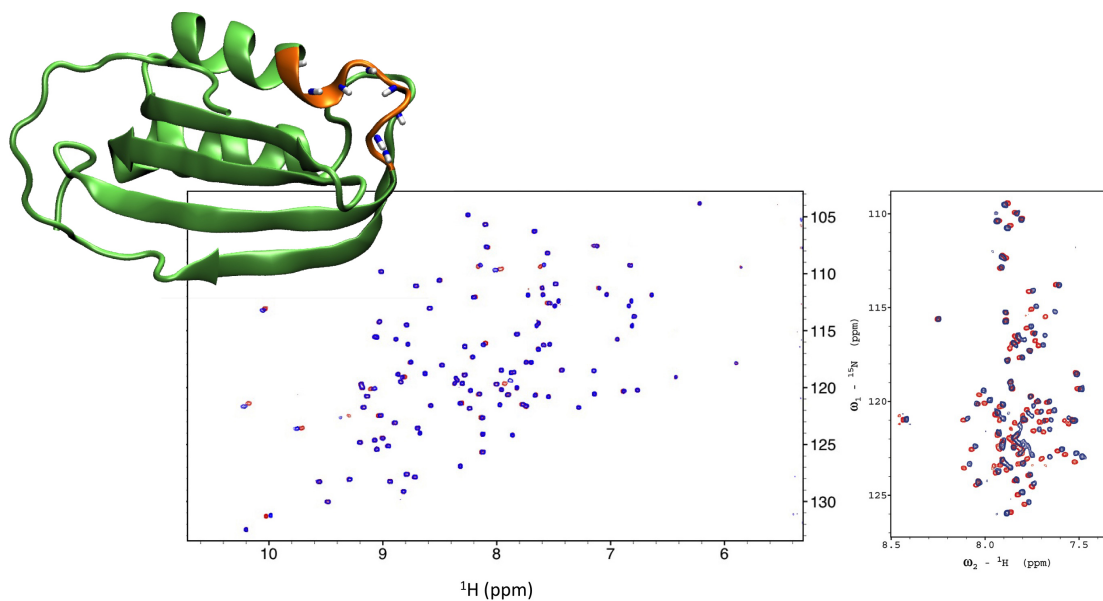


**Figure 5.17. Binding of EGCG to human mAcP.**  $^1\text{H}$ - $^{15}\text{N}$ -HSQC spectra of human mAcP isolated (red) and in the presence of 5 equivalents (blue) of EGCG. The spectra were measured at the proton resonance of 700MHz, by using a BRUKER avance III spectrometer with cryoprobe TXO. The experiments have been measured at 298K in 50mM acetate buffer and pH 5.5. The structure of human lysozyme is shown using green ribbons by highlighting in orange the residues that have major chemical shift changes in the presence of EGCG. Right panel reports the same experiments but in the presence of 6M guanidine hydrochloride.

In addition to the characterisation of the structural differences of the toxic and non-toxic  $\alpha\text{S}$  oligomers, this chapter provides key information on the nature of their interaction with lipid membranes. First, we could observe that both oligomers bind with the surface of DOPE:DOPC:DOPS SUVs (Figure 5.13). Thus even the non-toxic oligomers bind lipid membranes. This result should not surprise as  $\alpha\text{S}$  is a strongly lipophilic protein, therefore, even in the case of the formation of non-toxic oligomers, it is very unlikely that the protein would lose completely its affinity for membranes. However, while both oligomers bind the membranes, only *Type B\**  $\alpha\text{S}$  oligomers can bind the lipid bilayers with sufficient strength to initiate significant levels of insertion as indicated by PRE measurements with a paramagnetic label at the position of the carbon 16 of the lipid tail. It is worth to recall that in the case of the monomeric  $\alpha\text{S}$ , PRE measurements with this spin did not produce any significant broadening of the NMR resonances (Chapter III). This

evidence clearly shows that the nature of the membrane interaction is significantly changed when  $\alpha$ S aggregates into *Type B\** oligomers.

We could also characterise the different binding modes of the two types of oligomers. *Type A\**  $\alpha$ S oligomers interact with the membranes *via* electrostatic interactions from sparse lysine residues on the protein sequence (Figure 5.15) whereas *Type B\**  $\alpha$ S oligomers employ the specific N-terminal to bind the vesicles in a structured manner that involves the membrane-anchor region (Chapter III). By considering the cooperative effect generated by the amount of N-terminal regions exposed on a single *Type B\**  $\alpha$ S oligomer, these data show why the membrane affinity is extremely high in these oligomers. The specific binding through the N-terminus and the insertion of the structured NAC region in the lipid bilayer (Figure 5.15) provide an explanation for the observed membrane disruption properties of *Type B\**  $\alpha$ S oligomers, which is a property that is directly correlated to their ability to impair the viability of the cells and induce neuronal toxicity (Figure 5.4).

# Chapter VI

## *Discussion*

### **6.1 Insight into the functional role of $\alpha$ S**

Although it is now generally recognised that the formation of fibrillar aggregates by  $\alpha$ S is a hallmark of Parkinson's disease, much remains to be understood about the physiological role of this protein (4).  $\alpha$ S possesses an eclectic character and the ability to adopt different conformations resulting in a variety of cytosolic, membrane-bound and aggregated states. In aqueous solutions (15) as well as in cellular milieu (16),  $\alpha$ S has been shown to behave as an intrinsically disordered protein, although there has been evidence for and against the possible existence of more highly structured forms of soluble  $\alpha$ S in some environments and in complexes (26, 27). Considerable attention has also been focused on the membrane-associated state of  $\alpha$ S, which has been suggested to be of great significance in both physiological and pathological contexts. It is indeed evident that  $\alpha$ S exists *in vivo* in an equilibrium between cytosolic and membrane-bound states, with membrane partitioning being tightly regulated (3, 164).

A particularly intriguing issue in this context is the mechanism by which the affinity of  $\alpha$ S to lipid membranes is modulated. There is strong evidence that the population of the bound state is regulated by the intrinsic structural properties of  $\alpha$ S and on the composition and the physical properties of the membrane bilayer, such as curvature, charge, packing defects and surface hydrophobicity (20, 118, 119, 146, 165).

We explored this fundamental issue by probing the structure and conformational dynamics of  $\alpha$ S bound to membranes in its physiological, non-aggregated state. This membrane-bound state is effectively intractable to current X-ray crystallography techniques but the success of solution state NMR spectroscopy in describing the disordered soluble proteins (15, 16, 18-21, 118, 146, 166, 167) and of solid state NMR studies in defining the structural properties of the polymorphic forms of the aggregated state of  $\alpha$ S (57, 168-170) has prompted us to explore the use of a combination of these techniques to define the structures and dynamics of  $\alpha$ S bound in its non-aggregated state to lipid membranes.

Our approach could directly probe the interaction with lipid mixtures that mimic those of synaptic vesicles without requiring alterations of the protein sequence or any chemical modification. We have found that, in line with the metamorphic nature of  $\alpha$ S(171), three distinct regions of this protein (the N-terminal, central, and C-terminal segments) interact in very different ways with lipid bilayers as a result of their different structural and dynamical properties.

The N-terminal 25 residues, which we denote as the membrane anchor region, adopt a well-defined and highly motionally restricted  $\alpha$ -helical conformation that appears to be largely independent of lipid composition. We have characterised the molecular nature of the protein-lipid interactions that this region of  $\alpha$ S establishes with the surface of synaptic-like lipid vesicles. The finding that the resonances of this segment of  $\alpha$ S are detectable in cross polarisation spectra measured at the magic angle indicates that the N-terminal anchor of  $\alpha$ S associates with the lipid bilayer with significantly high affinity, despite being in rapid equilibrium between its bound and unbound states (exchange constant of *ca* 200 ms (19)). We have probed the local topology of this region of the protein with respect to the lipid bilayer by using both simulations and experiments of oriented ssNMR and PRE. These studies indicate that the membrane anchor region adopts a topology in its bound state that involves a partial insertion of the initial 12 residues in the lipid bilayer. This insertion is likely to contribute significantly to the overall ability of  $\alpha$ S to bind tightly to the vesicles, however, by remaining largely on the surface of the vesicles in an amphipathic helical conformation, the membrane-anchor region enables  $\alpha$ S to exist in rapid equilibrium between membrane-bound and membrane-detached states.

By contrast to the N-terminal membrane-anchor, the central segment of the protein (residues 26-97), which can be described as a membrane-sensor region, has intermediate dynamical properties. This region is indeed too flexible to be detected by cross-polarization experiments but too rigid to be seen by INEPT-type transfer experiments. It is legitimate to assume, based on EPR measurements (119, 121) and transferred NOE data (19), that this membrane-sensor region adopts  $\alpha$ -helical structure when transiently bound to a lipid membrane surface. The present results indicate that the NAC sequence, which has been shown to play a role in the mechanisms of  $\alpha$ S aggregation (4, 172-174),

being included in the membrane-sensor region is also likely to have functional relevance, specifically in defining the affinity of  $\alpha$ S for lipid membranes and therefore to modulate the partitioning between membrane-bound and membrane-free states in the synaptic termini. Finally, we have found from PRE experiments that the C-terminal domain (residues 99-140), which has been reported to be highly unstructured and extremely flexible, experiences weak and transient interactions with the membrane surface.

A number of studies support an emerging view that a key biological role of  $\alpha$ S is to mediate interactions and assembly of vesicles (177, 178). Vesicle clustering by  $\alpha$ S has been shown to be a vital step in many functional processes, including the ER-to-Golgi vesicle trafficking (71, 176) and SVs recycling within the mechanisms of neuronal communication (40). In the present PhD work we provided the details of the structural mechanism underlying the  $\alpha$ S-induced SUVs interactions and assembly by characterising the membrane binding properties of two mutational variants of  $\alpha$ S linked with familial Parkinson's disease. This analysis evidenced that two key regions of the protein, namely the N-terminal membrane-anchor (initial 25 residues) and the central region of the sequence (residues 65 to 97), have independent membrane binding properties and therefore are not only able to interact with a single SUV, but can also simultaneously bind to two different vesicles (Figure 4.6) thereby promoting their interaction and assembly as shown *in vitro* and *in vivo* (19, 177, 178). The resulting double-anchor mechanism explains the evidence that either the deletion of the hydrophobic residues in the NAC or the impairment of the membrane affinity at the N-terminal region reduces significantly the ability of  $\alpha$ S to induce vesicular clustering *in vivo* (178).

We tested this molecular mechanism by engineering a mutational variant of  $\alpha$ S, called  $\alpha$ S<sub>Sc</sub>, which was designed to enhance the probability of  $\alpha$ S to bind simultaneously two different vesicles. Our studies of the  $\alpha$ S<sub>Sc</sub> variant have provided strong evidence in support of the proposed mechanism by showing that enhanced exposure of the central region spanning residues 65 to 97 in the membrane-bound state of  $\alpha$ S promotes more strongly the interaction and assembly of the vesicles, as shown by the fusion of SUVs *in vitro* (Figure 4.13). It has previously been suggested that a broken  $\alpha$ -helix structural topology of  $\alpha$ S (118, 193), which is a conformation that  $\alpha$ S adopts upon binding to detergent micelles, could play a role in vesicle-vesicle interactions stimulated by  $\alpha$ S (80, 194). The present study, however, shows experimentally that the underlying mechanism

by which  $\alpha$ S mediates the interactions between lipid vesicles relies on the balance between ordered (membrane-bound) and disordered (membrane-detached) conformational states of the region spanning residues 65 to 97 of the protein. Perturbing this balance, as we have done rationally with  $\alpha$ S<sub>Sc</sub>, or upon alteration of the expression levels of  $\alpha$ S, can dramatically affect its ability to promote the physiological vesicle assembly *in vivo* leading to defects in the regulation of vesicle trafficking (40, 68-71, 176, 195, 196).

Other studies also suggest that  $\alpha$ S could act as a molecular chaperone for the formation of SNARE complexes, which appears to result from the direct interaction between  $\alpha$ S and synaptobrevin-2 at the surface of SVs (65, 177). Such an interaction was shown to be independent of the NAC region, suggesting that this region has no direct functional role in this particular process (197). The present data, however, show that the NAC region is not only involved in  $\alpha$ S aggregation, as extensive evidence has indicated (4, 35, 173), but also has a specific role in a key molecular mechanism associated with the normal function of  $\alpha$ S. This study provides evidence that the membrane affinity of the NAC region of  $\alpha$ S is finely tuned to ensure an optimal degree of local detachment from the membrane surface to enable binding to occur between different vesicles. The conformations that, in the membrane-bound state of  $\alpha$ S, feature an exposed region 65 to 97 are shown to be the active states for mediating vesicle interactions *via* the double-anchor mechanism.

## ***6.2 Molecular role of $\alpha$ S in Parkinson's Disease***

In the first part of this thesis, we have pointed out the possible role of the NAC region in the function of  $\alpha$ S. Indeed this region is an integral part of the sensor that determines the affinity of  $\alpha$ S for lipid binding (Chapter III) and also works as an “antenna” to promote vesicle-vesicle interactions (Chapter IV) in the context of synaptic vesicle clustering. Thus the intermediate level of binding of the NAC when  $\alpha$ S is bound to the surface of synaptic vesicles is not trivial and has a very specific functional role. We note, however, a possible aberrant behaviour associated with this functional mechanism, as by increasing the accessibility of the amyloidogenic NAC region, these states can also be vulnerable to self-association leading to  $\alpha$ S aggregation at membrane surfaces (40, 75, 198-200). Taken

together, these findings provide therefore a new mechanistic link between functional and pathological roles of  $\alpha$ S.

The aggregation of  $\alpha$ S *via* the NAC regions is compatible with the generation of *Type B\**  $\alpha$ S oligomers, whose properties were characterised in the Chapter V of this thesis. Using a combination of solution NMR and ssNMR, we found indeed that the major difference between toxic (*Type B\**) and non toxic (*Type A\**)  $\alpha$ S oligomers is in the regions of the protein composing the core and those that are exposed to the solvent. Moreover, we evidenced that the toxic oligomers have a well-defined core composed of the segment 70 to 88 (which is an integral part of the NAC). This segment includes the sequence VVTGVTAVAQ recently characterised in amyloid fibrillar conformation by the Eisenberg group (35). On the other hand, the non toxic *Type A\**  $\alpha$ S oligomers have core regions that lack specific secondary structure motifs and include the N-terminus of the protein.

Thus the accessibility of the N-terminus to the solvent is an important element to enhance the toxicity of *Type B\**  $\alpha$ S oligomers. Indeed we could show that, by making accessible the region of the membrane anchor, *Type B\**  $\alpha$ S oligomers are able to bind strongly lipid membranes with a specific mechanism that takes advantage of the cooperative effect based on the exposure of many copies of the N-terminal membrane-anchor at the surface of the assembly. On the other hand, *Type A\**  $\alpha$ S oligomers bind membranes in a weaker manner that is based on aspecific electrostatic interactions that do not require conformational rearrangements of the protein. As a result of this specificity, *Type B\**  $\alpha$ S oligomers are the only species able to show PRE effects when the paramagnetic label is positioned in the centre of the membrane (both *Type A\** and monomeric  $\alpha$ S do not reach this level of insertion and give no PRE effect with these labels), suggesting that its fibrillar core is able to insert in the lipid bilayer thereby disrupting the integrity of the membrane. Thus the data produced in this thesis provide a detailed structural mechanism by which toxic oligomeric species of  $\alpha$ S are able to alter the properties biological membranes and cause influx of molecules and ions thorough these membranes, a mechanism that has downstream effects on mitochondrial function, generation of ROS and other mechanisms generating cellular toxicity.

### **6.3 Challenges in $\alpha$ S research**

The research in  $\alpha$ S features a number of key open questions, including understanding its function and its role in the underlying mechanisms of Parkinson's disease (PD). One of the major challenges in this study is to characterise biomolecular processes that are heterogeneous and disordered in nature, as the plasticity of  $\alpha$ S drives its ability to generate biological activity under both physiological and pathological conditions. By combining solution-state and solid-state NMR techniques, my PhD work has contributed to study of some of the key structural mechanisms of membrane interaction by  $\alpha$ S. We could show the manner in which disorder to order transitions dominate the biological properties of  $\alpha$ S at the surface of lipid membranes. The conformational heterogeneity associated with these mechanisms, however, can be detrimental as it may favour conformations of  $\alpha$ S in which the amyloidogenic NAC region (4, 35, 173) is accessible to establish protein-protein interactions inducing aberrant aggregation into amyloids, as found in the case of the active state of  $\alpha$ S that promotes vesicle-vesicle interactions. We also observed that the N-terminal region plays key roles for both the membrane binding by the monomeric  $\alpha$ S and the mechanism by which its oligomers disrupt neuronal membranes thereby inducing neuronal toxicity. We therefore begin to uncover the bridge between physiological and pathological forms of  $\alpha$ S, showing these states are not extremely different in their nature. The connection between functional and pathological mechanisms in  $\alpha$ S holds important insights to set the key questions in Parkinson's research. Understanding this balance is a fundamental challenge that requires new multidisciplinary approaches to overcome intrinsic limitations in studying such a dynamical and metamorphic protein.

## References

1. Luk KC, *et al.* (2012) Pathological alpha-synuclein transmission initiates Parkinson-like neurodegeneration in nontransgenic mice. *Science* 338(6109):949-953.
2. Dobson CM (2003) Protein folding and misfolding. *Nature* 426(6968):884-890.
3. Uversky VN & Eliezer D (2009) Biophysics of Parkinson's disease: structure and aggregation of alpha-synuclein. *Current protein & peptide science* 10(5):483-499.
4. Chiti F & Dobson CM (2006) Protein misfolding, functional amyloid, and human disease. *Annual review of biochemistry* 75:333-366.
5. Luth ES, Stavrovskaya IG, Bartels T, Kristal BS, & Selkoe DJ (2014) Soluble, prefibrillar alpha-synuclein oligomers promote complex I-dependent, Ca<sup>2+</sup>-induced mitochondrial dysfunction. *The Journal of biological chemistry* 289(31):21490-21507.
6. Lashuel HA, Overk CR, Oueslati A, & Masliah E (2013) The many faces of alpha-synuclein: from structure and toxicity to therapeutic target. *Nature reviews. Neuroscience* 14(1):38-48.
7. Rutherford NJ, Moore BD, Golde TE, & Giasson BI (2014) Divergent effects of the H50Q and G51D SNCA mutations on the aggregation of alpha-synuclein. *Journal of neurochemistry* 131(6):859-867.
8. Lee SJ & Masliah E (2015) Neurodegeneration: Aggregates feel the strain. *Nature* 522(7556):296-297.
9. Sian-Hulsmann J, Monoranu C, Strobel S, & Riederer P (2015) Lewy bodies: A spectator or salient killer? *CNS & neurological disorders drug targets*.
10. Goedert M, Spillantini MG, Del Tredici K, & Braak H (2013) 100 years of Lewy pathology. *Nature reviews. Neurology* 9(1):13-24.
11. Bosco DA, *et al.* (2006) Elevated levels of oxidized cholesterol metabolites in Lewy body disease brains accelerate alpha-synuclein fibrilization. *Nature chemical biology* 2(5):249-253.
12. Ikenoue T, *et al.* (2014) Cold denaturation of alpha-synuclein amyloid fibrils. *Angewandte Chemie* 53(30):7799-7804.
13. Jucker M & Walker LC (2013) Self-propagation of pathogenic protein aggregates in neurodegenerative diseases. *Nature* 501(7465):45-51.
14. Paslawski W, Mysling S, Thomsen K, Jorgensen TJ, & Otzen DE (2014) Co-existence of two different alpha-synuclein oligomers with different core structures determined by hydrogen/deuterium exchange mass spectrometry. *Angewandte Chemie* 53(29):7560-7563.
15. Dedmon MM, Lindorff-Larsen K, Christodoulou J, Vendruscolo M, & Dobson CM (2005) Mapping long-range interactions in alpha-synuclein using spin-label NMR and ensemble molecular dynamics simulations. *Journal of the American Chemical Society* 127(2):476-477.
16. Waudby CA, *et al.* (2013) In-cell NMR characterization of the secondary structure populations of a disordered conformation of alpha-synuclein within E. coli cells. *PLoS one* 8(8):e72286.

17. Weinreb PH, Zhen W, Poon AW, Conway KA, & Lansbury PT, Jr. (1996) NACP, a protein implicated in Alzheimer's disease and learning, is natively unfolded. *Biochemistry* 35(43):13709-13715.
18. Maltsev AS, Ying J, & Bax A (2012) Impact of N-terminal acetylation of alpha-synuclein on its random coil and lipid binding properties. *Biochemistry* 51(25):5004-5013.
19. Bodner CR, Dobson CM, & Bax A (2009) Multiple tight phospholipid-binding modes of alpha-synuclein revealed by solution NMR spectroscopy. *Journal of molecular biology* 390(4):775-790.
20. Ulmer TS, Bax A, Cole NB, & Nussbaum RL (2005) Structure and dynamics of micelle-bound human alpha-synuclein. *The Journal of biological chemistry* 280(10):9595-9603.
21. Eliezer D, Kutluay E, Bussell R, Jr., & Browne G (2001) Conformational properties of alpha-synuclein in its free and lipid-associated states. *Journal of molecular biology* 307(4):1061-1073.
22. Lee JH, Li F, Grishaev A, & Bax A (2015) Quantitative residue-specific protein backbone torsion angle dynamics from concerted measurement of 3J couplings. *Journal of the American Chemical Society* 137(4):1432-1435.
23. Drescher M (2012) EPR in protein science : intrinsically disordered proteins. *Topics in current chemistry* 321:91-119.
24. Allison JR, Rivers RC, Christodoulou JC, Vendruscolo M, & Dobson CM (2014) A relationship between the transient structure in the monomeric state and the aggregation propensities of alpha-synuclein and beta-synuclein. *Biochemistry* 53(46):7170-7183.
25. Theillet FX, *et al.* (2016) Structural disorder of monomeric alpha-synuclein persists in mammalian cells. *Nature* 530(7588):45-50.
26. Bartels T, Choi JG, & Selkoe DJ (2011) alpha-Synuclein occurs physiologically as a helically folded tetramer that resists aggregation. *Nature* 477(7362):107-110.
27. Fauvet B, *et al.* (2012) alpha-Synuclein in central nervous system and from erythrocytes, mammalian cells, and Escherichia coli exists predominantly as disordered monomer. *The Journal of biological chemistry* 287(19):15345-15364.
28. Wang W, *et al.* (2011) A soluble alpha-synuclein construct forms a dynamic tetramer. *Proceedings of the National Academy of Sciences of the United States of America* 108(43):17797-17802.
29. Uversky VN (2008) Alpha-synuclein misfolding and neurodegenerative diseases. *Current protein & peptide science* 9(5):507-540.
30. Polymeropoulos MH, *et al.* (1997) Mutation in the alpha-synuclein gene identified in families with Parkinson's disease. *Science* 276(5321):2045-2047.
31. Singleton AB, *et al.* (2003) alpha-Synuclein locus triplication causes Parkinson's disease. *Science* 302(5646):841.
32. Feany MB & Bender WW (2000) A Drosophila model of Parkinson's disease. *Nature* 404(6776):394-398.
33. Haass C & Kahle PJ (2000) Parkinson's pathology in a fly. *Nature* 404(6776):341, 343.

34. Peelaerts W, *et al.* (2015) alpha-Synuclein strains cause distinct synucleinopathies after local and systemic administration. *Nature* 522(7556):340-344.
35. Rodriguez JA, *et al.* (2015) Structure of the toxic core of alpha-synuclein from invisible crystals. *Nature* 525(7570):486-490.
36. Perry G, *et al.* (2001) Biochemistry of neurodegeneration. *Science* 291(5504):595-597.
37. Willingham S, Outeiro TF, DeVit MJ, Lindquist SL, & Muchowski PJ (2003) Yeast genes that enhance the toxicity of a mutant huntingtin fragment or alpha-synuclein. *Science* 302(5651):1769-1772.
38. Yang Q, *et al.* (2009) Regulation of neuronal survival factor MEF2D by chaperone-mediated autophagy. *Science* 323(5910):124-127.
39. Burre J, *et al.* (2013) Properties of native brain alpha-synuclein. *Nature* 498(7453):E4-6; discussion E6-7.
40. Auluck PK, Caraveo G, & Lindquist S (2010) alpha-Synuclein: membrane interactions and toxicity in Parkinson's disease. *Annual review of cell and developmental biology* 26:211-233.
41. Singleton A, *et al.* (2004) Association between cardiac denervation and parkinsonism caused by alpha-synuclein gene triplication. *Brain : a journal of neurology* 127(Pt 4):768-772.
42. Spillantini MG, Crowther RA, Jakes R, Hasegawa M, & Goedert M (1998) alpha-Synuclein in filamentous inclusions of Lewy bodies from Parkinson's disease and dementia with lewy bodies. *Proceedings of the National Academy of Sciences of the United States of America* 95(11):6469-6473.
43. Masliah E, *et al.* (2000) Dopaminergic loss and inclusion body formation in alpha-synuclein mice: implications for neurodegenerative disorders. *Science* 287(5456):1265-1269.
44. Kuwahara T, *et al.* (2006) Familial Parkinson mutant alpha-synuclein causes dopamine neuron dysfunction in transgenic *Caenorhabditis elegans*. *The Journal of biological chemistry* 281(1):334-340.
45. Franssens V, *et al.* (2010) Yeast unfolds the road map toward alpha-synuclein-induced cell death. *Cell death and differentiation* 17(5):746-753.
46. Giasson BI, *et al.* (2003) Initiation and synergistic fibrillization of tau and alpha-synuclein. *Science* 300(5619):636-640.
47. Guo JL, *et al.* (2013) Distinct alpha-synuclein strains differentially promote tau inclusions in neurons. *Cell* 154(1):103-117.
48. Pornsuwan S, *et al.* (2013) Long-range distances in amyloid fibrils of alpha-synuclein from PELDOR spectroscopy. *Angewandte Chemie* 52(39):10290-10294.
49. Shivu B, *et al.* (2013) Distinct beta-sheet structure in protein aggregates determined by ATR-FTIR spectroscopy. *Biochemistry* 52(31):5176-5183.
50. Yasuda T, Nakata Y, & Mochizuki H (2013) alpha-Synuclein and neuronal cell death. *Molecular neurobiology* 47(2):466-483.
51. Zhao M, Cascio D, Sawaya MR, & Eisenberg D (2011) Structures of segments of alpha-synuclein fused to maltose-binding protein suggest intermediate states

- during amyloid formation. *Protein science : a publication of the Protein Society* 20(6):996-1004.
52. Serpell LC, Berriman J, Jakes R, Goedert M, & Crowther RA (2000) Fiber diffraction of synthetic alpha-synuclein filaments shows amyloid-like cross-beta conformation. *Proceedings of the National Academy of Sciences of the United States of America* 97(9):4897-4902.
  53. Sawaya MR, *et al.* (2007) Atomic structures of amyloid cross-beta spines reveal varied steric zippers. *Nature* 447(7143):453-457.
  54. Tuttle MD, *et al.* (2016) Solid-state NMR structure of a pathogenic fibril of full-length human alpha-synuclein. *Nature structural & molecular biology* 23(5):409-415.
  55. Orcelliet ML & Fernandez CO (2011) Structures behind the amyloid aggregation of alpha-synuclein: an NMR based approach. *Current protein & peptide science* 12(3):188-204.
  56. Vilar M, *et al.* (2008) The fold of alpha-synuclein fibrils. *Proceedings of the National Academy of Sciences of the United States of America* 105(25):8637-8642.
  57. Heise H, *et al.* (2005) Molecular-level secondary structure, polymorphism, and dynamics of full-length alpha-synuclein fibrils studied by solid-state NMR. *Proceedings of the National Academy of Sciences of the United States of America* 102(44):15871-15876.
  58. Buell AK, *et al.* (2014) Solution conditions determine the relative importance of nucleation and growth processes in alpha-synuclein aggregation. *Proceedings of the National Academy of Sciences of the United States of America* 111(21):7671-7676.
  59. Breydo L, Wu JW, & Uversky VN (2012) Alpha-synuclein misfolding and Parkinson's disease. *Biochimica et biophysica acta* 1822(2):261-285.
  60. Cremades N, *et al.* (2012) Direct observation of the interconversion of normal and toxic forms of alpha-synuclein. *Cell* 149(5):1048-1059.
  61. Goedert M & Cheng Y (2015) Parkinson's disease: Crystals of a toxic core. *Nature* 525(7570):458-459.
  62. Iwai A, *et al.* (1995) The precursor protein of non-A beta component of Alzheimer's disease amyloid is a presynaptic protein of the central nervous system. *Neuron* 14(2):467-475.
  63. Burre J (2015) The Synaptic Function of alpha-Synuclein. *Journal of Parkinson's disease* 5(4):699-713.
  64. Barbour R, *et al.* (2008) Red blood cells are the major source of alpha-synuclein in blood. *Neuro-degenerative diseases* 5(2):55-59.
  65. Burre J, *et al.* (2010) Alpha-synuclein promotes SNARE-complex assembly in vivo and in vitro. *Science* 329(5999):1663-1667.
  66. Chandra S, Gallardo G, Fernandez-Chacon R, Schluter OM, & Sudhof TC (2005) Alpha-synuclein cooperates with CSPalpha in preventing neurodegeneration. *Cell* 123(3):383-396.
  67. Pelkonen A & Yavich L (2011) Neuromuscular pathology in mice lacking alpha-synuclein. *Neuroscience letters* 487(3):350-353.

68. Abeliovich A, *et al.* (2000) Mice lacking alpha-synuclein display functional deficits in the nigrostriatal dopamine system. *Neuron* 25(1):239-252.
69. Cabin DE, *et al.* (2002) Synaptic vesicle depletion correlates with attenuated synaptic responses to prolonged repetitive stimulation in mice lacking alpha-synuclein. *The Journal of neuroscience : the official journal of the Society for Neuroscience* 22(20):8797-8807.
70. Nemani VM, *et al.* (2010) Increased expression of alpha-synuclein reduces neurotransmitter release by inhibiting synaptic vesicle recluster after endocytosis. *Neuron* 65(1):66-79.
71. Cooper AA, *et al.* (2006) Alpha-synuclein blocks ER-Golgi traffic and Rab1 rescues neuron loss in Parkinson's models. *Science* 313(5785):324-328.
72. Lee HJ & Lee SJ (2002) Characterization of cytoplasmic alpha-synuclein aggregates. Fibril formation is tightly linked to the inclusion-forming process in cells. *The Journal of biological chemistry* 277(50):48976-48983.
73. Bodner CR, Maltsev AS, Dobson CM, & Bax A (2010) Differential phospholipid binding of alpha-synuclein variants implicated in Parkinson's disease revealed by solution NMR spectroscopy. *Biochemistry* 49(5):862-871.
74. Perrin RJ, Woods WS, Clayton DF, & George JM (2000) Interaction of human alpha-Synuclein and Parkinson's disease variants with phospholipids. Structural analysis using site-directed mutagenesis. *The Journal of biological chemistry* 275(44):34393-34398.
75. Comellas G, Lemkau LR, Zhou DH, George JM, & Rienstra CM (2012) Structural intermediates during alpha-synuclein fibrillogenesis on phospholipid vesicles. *Journal of the American Chemical Society* 134(11):5090-5099.
76. Uversky VN, Lee HJ, Li J, Fink AL, & Lee SJ (2001) Stabilization of partially folded conformation during alpha-synuclein oligomerization in both purified and cytosolic preparations. *The Journal of biological chemistry* 276(47):43495-43498.
77. Goers J, *et al.* (2003) Nuclear localization of alpha-synuclein and its interaction with histones. *Biochemistry* 42(28):8465-8471.
78. Guerrero E, Vasudevaraju P, Hegde ML, Britton GB, & Rao KS (2013) Recent advances in alpha-synuclein functions, advanced glycation, and toxicity: implications for Parkinson's disease. *Molecular neurobiology* 47(2):525-536.
79. Martin LJ, *et al.* (2006) Parkinson's disease alpha-synuclein transgenic mice develop neuronal mitochondrial degeneration and cell death. *The Journal of neuroscience : the official journal of the Society for Neuroscience* 26(1):41-50.
80. Snead D & Eliezer D (2014) Alpha-synuclein function and dysfunction on cellular membranes. *Experimental neurobiology* 23(4):292-313.
81. Jo E, McLaurin J, Yip CM, St George-Hyslop P, & Fraser PE (2000) alpha-Synuclein membrane interactions and lipid specificity. *The Journal of biological chemistry* 275(44):34328-34334.
82. Hoyer W, *et al.* (2002) Dependence of alpha-synuclein aggregate morphology on solution conditions. *Journal of molecular biology* 322(2):383-393.

83. Dunker AK, Obradovic Z, Romero P, Garner EC, & Brown CJ (2000) Intrinsic protein disorder in complete genomes. *Genome Inform Ser Workshop Genome Inform* 11:161-171.
84. Krieger JM, *et al.* (2014) Conformational recognition of an intrinsically disordered protein. *Biophysical journal* 106(8):1771-1779.
85. Cornilescu G, Delaglio F, & Bax A (1999) Protein backbone angle restraints from searching a database for chemical shift and sequence homology. *Journal of biomolecular NMR* 13(3):289-302.
86. Camilloni C, Robustelli P, De Simone A, Cavalli A, & Vendruscolo M (2012) Characterization of the conformational equilibrium between the two major substates of RNase A using NMR chemical shifts. *Journal of the American Chemical Society* 134(9):3968-3971.
87. De Simone A, *et al.* (2013) Structures of the excited states of phospholamban and shifts in their populations upon phosphorylation. *Biochemistry* 52(38):6684-6694.
88. De Simone A, Richter B, Salvatella X, & Vendruscolo M (2009) Toward an accurate determination of free energy landscapes in solution states of proteins. *Journal of the American Chemical Society* 131(11):3810-3811.
89. Camilloni C, De Simone A, Vranken WF, & Vendruscolo M (2012) Determination of secondary structure populations in disordered states of proteins using nuclear magnetic resonance chemical shifts. *Biochemistry* 51(11):2224-2231.
90. Allison JR, Varnai P, Dobson CM, & Vendruscolo M (2009) Determination of the free energy landscape of alpha-synuclein using spin label nuclear magnetic resonance measurements. *Journal of the American Chemical Society* 131(51):18314-18326.
91. Vallurupalli P, Bouvignies G, & Kay LE (2012) Studying "invisible" excited protein states in slow exchange with a major state conformation. *Journal of the American Chemical Society* 134(19):8148-8161.
92. Dyson HJ & Wright PE (2002) Coupling of folding and binding for unstructured proteins. *Current opinion in structural biology* 12(1):54-60.
93. Dyson HJ & Wright PE (2002) Insights into the structure and dynamics of unfolded proteins from nuclear magnetic resonance. *Adv Protein Chem* 62:311-340.
94. Keeler J (2010) Understanding NMR Spectroscopy. *Wiley*.
95. Bermel W, *et al.* (2012) Speeding up sequence specific assignment of IDPs. *Journal of biomolecular NMR* 53(4):293-301.
96. Bermel W, *et al.* (2006) Protonless NMR experiments for sequence-specific assignment of backbone nuclei in unfolded proteins. *Journal of the American Chemical Society* 128(12):3918-3919.
97. Bermel W, *et al.* (2013) High-dimensionality <sup>13</sup>C direct-detected NMR experiments for the automatic assignment of intrinsically disordered proteins. *Journal of biomolecular NMR* 57(4):353-361.
98. Bertini I, Felli IC, Gonnelli L, Kumar MVV, & Pierattelli R (2011) <sup>13</sup>C direct-detection biomolecular NMR spectroscopy in living cells. *Angewandte Chemie* 50(10):2339-2341.

99. Breydo L, *et al.* (2014) The crowd you're in with: effects of different types of crowding agents on protein aggregation. *Biochimica et biophysica acta* 1844(2):346-357.
100. Felli IC, Gonnelli L, & Pierattelli R (2014) In-cell (1)(3)C NMR spectroscopy for the study of intrinsically disordered proteins. *Nature protocols* 9(9):2005-2016.
101. Gil S, *et al.* (2013) NMR spectroscopic studies of intrinsically disordered proteins at near-physiological conditions. *Angewandte Chemie* 52(45):11808-11812.
102. Hsu ST, Bertoni CW, & Dobson CM (2009) Use of protonless NMR spectroscopy to alleviate the loss of information resulting from exchange-broadening. *Journal of the American Chemical Society* 131(21):7222-7223.
103. Kuszewski J, *et al.* (2004) Completely automated, highly error-tolerant macromolecular structure determination from multidimensional nuclear overhauser enhancement spectra and chemical shift assignments. *Journal of the American Chemical Society* 126(20):6258-6273.
104. Wüthrich. (1986) NMR of Proteins and Nucleic Acids. *John Wiley & Sons*.
105. Cavalli A, Salvatella X, Dobson CM, & Vendruscolo M (2007) Protein structure determination from NMR chemical shifts. *Proceedings of the National Academy of Sciences of the United States of America* 104(23):9615-9620.
106. Shen Y, *et al.*, Baker D, & Bax A (2008) Consistent blind protein structure generation from NMR chemical shift data. *Proceedings of the National Academy of Sciences of the United States of America* 105(12):4685-4690.
107. De Simone A, Cavalli A, Hsu ST, Vranken W, & Vendruscolo M (2009) Accurate random coil chemical shifts from an analysis of loop regions in native states of proteins. *Journal of the American Chemical Society* 131(45):16332-16333.
108. Berjanskii MV & Wishart DS (2007) The RCI server: rapid and accurate calculation of protein flexibility using chemical shifts. *Nucleic acids research* 35(Web Server issue):W531-537.
109. Hess B, Kutzner C, van der Spoel D, & Lindahl E (2008) GROMACS 4: Algorithms for highly efficient, load-balanced, and scalable molecular simulation. *Journal of chemical theory and computation* 4(3):435-447.
110. De Simone A, *et al.* (2011) Experimental free energy surfaces reveal the mechanisms of maintenance of protein solubility. *Proceedings of the National Academy of Sciences of the United States of America* 108(52):21057-21062.
111. Kohlhoff KJ, Robustelli P, Cavalli A, Salvatella X, & Vendruscolo M (2009) Fast and accurate predictions of protein NMR chemical shifts from interatomic distances. *Journal of the American Chemical Society* 131(39):13894-13895.
112. Fawzi NL, Ying J, Ghirlando R, Torchia DA, & Clore GM (2011) Atomic-resolution dynamics on the surface of amyloid-beta protofibrils probed by solution NMR. *Nature* 480(7376):268-272.
113. Milojevic J, Esposito V, Das R, & Melacini G (2007) Understanding the molecular basis for the inhibition of the Alzheimer's A $\beta$ -peptide oligomerization by human serum albumin using saturation transfer difference and off-resonance relaxation NMR spectroscopy. *Journal of the American Chemical Society* 129(14):4282-4290.

114. Fusco G, *et al.* (2014) Direct observation of the three regions in alpha-synuclein that determine its membrane-bound behaviour. *Nature communications* 5:3827.
115. Su Y, Andreas L, & Griffin RG (2015) Magic angle spinning NMR of proteins: high-frequency dynamic nuclear polarization and  $^1\text{H}$  detection. *Annual review of biochemistry* 84:465-497.
116. Reif B (2012) Ultra-high resolution in MAS solid-state NMR of perdeuterated proteins: implications for structure and dynamics. *Journal of magnetic resonance* 216:1-12.
117. Taylor GF, Marius P, Ford C, & Williamson PT (2014) Solid-state NMR spectroscopy of biopolymers. *Wiley*.
118. Ulmer TS & Bax A (2005) Comparison of structure and dynamics of micelle-bound human alpha-synuclein and Parkinson disease variants. *The Journal of biological chemistry* 280(52):43179-43187.
119. Jao CC, Hegde BG, Chen J, Haworth IS, & Langen R (2008) Structure of membrane-bound alpha-synuclein from site-directed spin labeling and computational refinement. *Proceedings of the National Academy of Sciences of the United States of America* 105(50):19666-19671.
120. Lokappa SB & Ulmer TS (2011) Alpha-synuclein populates both elongated and broken helix states on small unilamellar vesicles. *The Journal of biological chemistry* 286(24):21450-21457.
121. Cheng CY, Varkey J, Ambroso MR, Langen R, & Han S (2013) Hydration dynamics as an intrinsic ruler for refining protein structure at lipid membrane interfaces. *Proceedings of the National Academy of Sciences of the United States of America* 110(42):16838-16843.
122. Fuxreiter M (2012) Fuzziness: linking regulation to protein dynamics. *Molecular bioSystems* 8(1):168-177.
123. Fuxreiter M & Tompa P (2012) Fuzzy complexes: a more stochastic view of protein function. *Advances in experimental medicine and biology* 725:1-14.
124. Tompa P & Fuxreiter M (2008) Fuzzy complexes: polymorphism and structural disorder in protein-protein interactions. *Trends in biochemical sciences* 33(1):2-8.
125. Takegoshi K & Terao T (1999)  $^{13}\text{C}$ - $^1\text{H}$  dipolar recoupling under very fast magic-angle spinning using virtual pulses. *Solid state nuclear magnetic resonance* 13(4):203-212.
126. Gor'kov PL, *et al.* (2007) Using low-E resonators to reduce RF heating in biological samples for static solid-state NMR up to 900 MHz. *Journal of magnetic resonance* 185(1):77-93.
127. Mote KR, *et al.* (2011) Multidimensional oriented solid-state NMR experiments enable the sequential assignment of uniformly  $^{15}\text{N}$  labeled integral membrane proteins in magnetically aligned lipid bilayers. *Journal of biomolecular NMR* 51(3):339-346.
128. Fung BM, Khitritin AK, & Ermolaev K (2000) An improved broadband decoupling sequence for liquid crystals and solids. *Journal of magnetic resonance* 142(1):97-101.

129. Lindorff-Larsen K, *et al.* (2010) Improved side-chain torsion potentials for the Amber ff99SB protein force field. *Proteins* 78(8):1950-1958.
130. Horn HW, *et al.* (2004) Development of an improved four-site water model for biomolecular simulations: TIP4P-Ew. *The Journal of chemical physics* 120(20):9665-9678.
131. Jambeck JP & Lyubartsev AP (2012) Derivation and systematic validation of a refined all-atom force field for phosphatidylcholine lipids. *The journal of physical chemistry. B* 116(10):3164-3179.
132. Hess B, Bekker H, Berendsen HW, & Fraaije JG (1997) LINCS: A linear constraint solver for molecular simulations. *J Comput Chem* 18:1463-1472.
133. Darden T, Perera L, Li L, & Pedersen L (1999) New tricks for modelers from the crystallography toolkit: the particle mesh Ewald algorithm and its use in nucleic acid simulations. *Structure* 7(3):R55-60.
134. Bussi G, Donadio D, & Parrinello M (2007) Canonical sampling through velocity rescaling. *The Journal of chemical physics* 126(1):014101.
135. Vostrikov VV, Mote KR, Verardi R, & Veglia G (2013) Structural dynamics and topology of phosphorylated phospholamban homopentamer reveal its role in the regulation of calcium transport. *Structure* 21(12):2119-2130.
136. Ramamoorthy A, Wei Y, & Lee D (2004) PISEMA solid state NMR Spectroscopy. In: *Advances in solid state NMR studies of materials and polymers.* . Elsevier Acad. Pr.:1-51.
137. Lee DK, Wildman KH, & Ramamoorthy A (2004) Solid-state NMR spectroscopy of aligned lipid bilayers at low temperatures. *Journal of the American Chemical Society* 126(8):2318-2319.
138. Cady SD, *et al.* (2010) Structure of the amantadine binding site of influenza M2 proton channels in lipid bilayers. *Nature* 463(7281):689-692.
139. Krepiy D, *et al.* (2009) Structure and hydration of membranes embedded with voltage-sensing domains. *Nature* 462(7272):473-479.
140. Wang S, *et al.* (2013) Solid-state NMR spectroscopy structure determination of a lipid-embedded heptahelical membrane protein. *Nature methods* 10(10):1007-1012.
141. Gustavsson M, *et al.* (2013) Allosteric regulation of SERCA by phosphorylation-mediated conformational shift of phospholamban. *Proceedings of the National Academy of Sciences of the United States of America* 110(43):17338-17343.
142. Lange A, *et al.* (2006) Toxin-induced conformational changes in a potassium channel revealed by solid-state NMR. *Nature* 440(7086):959-962.
143. Grobner G, *et al.* (2000) Observations of light-induced structural changes of retinal within rhodopsin. *Nature* 405(6788):810-813.
144. Traaseth NJ, *et al.* (2009) Structure and topology of monomeric phospholamban in lipid membranes determined by a hybrid solution and solid-state NMR approach. *Proceedings of the National Academy of Sciences of the United States of America* 106(25):10165-10170.
145. Nagle JF & Tristram-Nagle S (2000) Structure of lipid bilayers. *Biochimica et biophysica acta* 1469(3):159-195.

146. Rao JN, Jao CC, Hegde BG, Langen R, & Ulmer TS (2010) A combinatorial NMR and EPR approach for evaluating the structural ensemble of partially folded proteins. *Journal of the American Chemical Society* 132(25):8657-8668.
147. Morris GA & Freeman R (1979) Enhancement of Nuclear Magnetic-Resonance Signals by Polarization Transfer. *Journal of the American Chemical Society* 101(3):760-762.
148. Robustelli P, Kohlhoff K, Cavalli A, & Vendruscolo M (2010) Using NMR chemical shifts as structural restraints in molecular dynamics simulations of proteins. *Structure* 18(8):923-933.
149. Shen Y & Bax A (2010) SPARTA+: a modest improvement in empirical NMR chemical shift prediction by means of an artificial neural network. *Journal of biomolecular NMR* 48(1):13-22.
150. Maltsev AS, Chen J, Levine RL, & Bax A (2013) Site-specific interaction between alpha-synuclein and membranes probed by NMR-observed methionine oxidation rates. *Journal of the American Chemical Society* 135(8):2943-2946.
151. Wang C, Shah N, Thakur G, Zhou F, & Leblanc RM (2010) Alpha-synuclein in alpha-helical conformation at air-water interface: implication of conformation and orientation changes during its accumulation/aggregation. *Chemical communications* 46(36):6702-6704.
152. Kabsch W & Sander C (1983) Dictionary of protein secondary structure: pattern recognition of hydrogen-bonded and geometrical features. *Biopolymers* 22(12):2577-2637.
153. De Simone A, Mote KR, & Veglia G (2014) Structural dynamics and conformational equilibria of SERCA regulatory proteins in membranes by solid-state NMR restrained simulations. *Biophysical journal* 106(12):2566-2576.
154. Magzoub M, Eriksson LE, & Graslund A (2002) Conformational states of the cell-penetrating peptide penetratin when interacting with phospholipid vesicles: effects of surface charge and peptide concentration. *Biochimica et biophysica acta* 1563(1-2):53-63.
155. Zhang Y, *et al.* (2015) Computational design and experimental characterization of peptides intended for pH-dependent membrane insertion and pore formation. *ACS chemical biology* 10(4):1082-1093.
156. Ashworth Briggs EL, *et al.* (2015) Interaction between the NS4B amphipathic helix, AH2, and charged lipid headgroups alters membrane morphology and AH2 oligomeric state--Implications for the Hepatitis C virus life cycle. *Biochimica et biophysica acta* 1848(8):1671-1677.
157. Miao Y, *et al.* (2012) M2 proton channel structural validation from full-length protein samples in synthetic bilayers and E. coli membranes. *Angewandte Chemie* 51(33):8383-8386.
158. Pandey MK, *et al.* (2012) Determination of <sup>15</sup>N chemical shift anisotropy from a membrane-bound protein by NMR spectroscopy. *The journal of physical chemistry. B* 116(24):7181-7189.
159. Sharma M, *et al.* (2010) Insight into the mechanism of the influenza A proton channel from a structure in a lipid bilayer. *Science* 330(6003):509-512.

160. Can TV, *et al.* (2012) Magic angle spinning and oriented sample solid-state NMR structural restraints combine for influenza A M2 protein functional insights. *Journal of the American Chemical Society* 134(22):9022-9025.
161. Verardi R, Shi L, Traaseth NJ, Walsh N, & Veglia G (2011) Structural topology of phospholamban pentamer in lipid bilayers by a hybrid solution and solid-state NMR method. *Proceedings of the National Academy of Sciences of the United States of America* 108(22):9101-9106.
162. De Angelis AA & Opella SJ (2007) Bicelle samples for solid-state NMR of membrane proteins. *Nature protocols* 2(10):2332-2338.
163. Li C, *et al.* (2009) <sup>19</sup>F NMR studies of alpha-synuclein conformation and fibrillation. *Biochemistry* 48(36):8578-8584.
164. Lee HJ, Choi C, & Lee SJ (2002) Membrane-bound alpha-synuclein has a high aggregation propensity and the ability to seed the aggregation of the cytosolic form. *The Journal of biological chemistry* 277(1):671-678.
165. Ouberei MM, *et al.* (2013) alpha-Synuclein senses lipid packing defects and induces lateral expansion of lipids leading to membrane remodeling. *The Journal of biological chemistry* 288(29):20883-20895.
166. Kang L, Wu KP, Vendruscolo M, & Baum J (2011) The A53T mutation is key in defining the differences in the aggregation kinetics of human and mouse alpha-synuclein. *Journal of the American Chemical Society* 133(34):13465-13470.
167. Leftin A, Job C, Beyer K, & Brown MF (2013) Solid-state (1)(3)C NMR reveals annealing of raft-like membranes containing cholesterol by the intrinsically disordered protein alpha-Synuclein. *Journal of molecular biology* 425(16):2973-2987.
168. Gath J, *et al.* (2014) Yet another polymorph of alpha-synuclein: solid-state sequential assignments. *Biomolecular NMR assignments* 8(2):395-404.
169. Bousset L, *et al.* (2013) Structural and functional characterization of two alpha-synuclein strains. *Nature communications* 4:2575.
170. Gath J, *et al.* (2012) Solid-state NMR sequential assignments of alpha-synuclein. *Biomolecular NMR assignments* 6(1):51-55.
171. Uversky VN (2003) A protein-chameleon: conformational plasticity of alpha-synuclein, a disordered protein involved in neurodegenerative disorders. *Journal of biomolecular structure & dynamics* 21(2):211-234.
172. Ma QL, Chan P, Yoshii M, & Ueda K (2003) Alpha-synuclein aggregation and neurodegenerative diseases. *Journal of Alzheimer's disease : JAD* 5(2):139-148.
173. Cookson MR (2005) The biochemistry of Parkinson's disease. *Annual review of biochemistry* 74:29-52.
174. Karpinar DP, *et al.* (2009) Pre-fibrillar alpha-synuclein variants with impaired beta-structure increase neurotoxicity in Parkinson's disease models. *The EMBO journal* 28(20):3256-3268.
175. Wislet-Gendebien S, *et al.* (2006) Cytosolic proteins regulate alpha-synuclein dissociation from presynaptic membranes. *The Journal of biological chemistry* 281(43):32148-32155.

176. Gitler AD, *et al.* (2008) The Parkinson's disease protein alpha-synuclein disrupts cellular Rab homeostasis. *Proceedings of the National Academy of Sciences of the United States of America* 105(1):145-150.
177. Diao J, *et al.* (2013) Native alpha-synuclein induces clustering of synaptic-vesicle mimics via binding to phospholipids and synaptobrevin-2/VAMP2. *eLife* 2:e00592.
178. Soper JH, *et al.* (2008) Alpha-synuclein-induced aggregation of cytoplasmic vesicles in *Saccharomyces cerevisiae*. *Molecular biology of the cell* 19(3):1093-1103.
179. Kang L, *et al.* (2012) N-terminal acetylation of alpha-synuclein induces increased transient helical propensity and decreased aggregation rates in the intrinsically disordered monomer. *Protein science : a publication of the Protein Society* 21(7):911-917.
180. Fauvet B, *et al.* (2012) Characterization of semisynthetic and naturally Nalpha-acetylated alpha-synuclein in vitro and in intact cells: implications for aggregation and cellular properties of alpha-synuclein. *The Journal of biological chemistry* 287(34):28243-28262.
181. Bussell R, Jr. & Eliezer D (2004) Effects of Parkinson's disease-linked mutations on the structure of lipid-associated alpha-synuclein. *Biochemistry* 43(16):4810-4818.
182. Ahmed S, Holt M, Riedel D, & Jahn R (2013) Small-scale isolation of synaptic vesicles from mammalian brain. *Nature protocols* 8(5):998-1009.
183. Takamori S, *et al.* (2006) Molecular anatomy of a trafficking organelle. *Cell* 127(4):831-846.
184. Hell SW & Wichmann J (1994) Breaking the diffraction resolution limit by stimulated emission: stimulated-emission-depletion fluorescence microscopy. *Optics letters* 19(11):780-782.
185. Klar TA & Hell SW (1999) Subdiffraction resolution in far-field fluorescence microscopy. *Optics letters* 24(14):954-956.
186. Mahou P, Curry N, Pinotsi D, Kaminski Schierle GS, & Kaminski CF (2015) Stimulated emission depletion microscopy to study amyloid fibril formation. *Proc. SPIE*. 9331:9331OU.
187. Pinotsi D, *et al.* (2016) Nanoscopic insights into seeding mechanisms and toxicity of alpha-synuclein species in neurons. *Proceedings of the National Academy of Sciences of the United States of America*.
188. Kruger R, *et al.* (1998) Ala30Pro mutation in the gene encoding alpha-synuclein in Parkinson's disease. *Nature genetics* 18(2):106-108.
189. Zarranz JJ, *et al.* (2004) The new mutation, E46K, of alpha-synuclein causes Parkinson and Lewy body dementia. *Annals of neurology* 55(2):164-173.
190. Baker LA & Baldus M (2014) Characterization of membrane protein function by solid-state NMR spectroscopy. *Current opinion in structural biology* 27:48-55.
191. Sekhar A, Rosenzweig R, Bouvignies G, & Kay LE (2015) Mapping the conformation of a client protein through the Hsp70 functional cycle. *Proceedings of the National Academy of Sciences of the United States of America* 112(33):10395-10400.

192. De Simone A, *et al.* (2012) Intrinsic disorder modulates protein self-assembly and aggregation. *Proceedings of the National Academy of Sciences of the United States of America* 109(18):6951-6956.
193. Mazumder P, Suk JE, & Ulmer TS (2013) Insight into alpha-synuclein plasticity and misfolding from differential micelle binding. *The journal of physical chemistry. B* 117(39):11448-11459.
194. Dikiy I & Eliezer D (2012) Folding and misfolding of alpha-synuclein on membranes. *Biochimica et biophysica acta* 1818(4):1013-1018.
195. Outeiro TF & Lindquist S (2003) Yeast cells provide insight into alpha-synuclein biology and pathobiology. *Science* 302(5651):1772-1775.
196. Tardiff DF, Khurana V, Chung CY, & Lindquist S (2014) From yeast to patient neurons and back again: powerful new discovery platform. *Movement disorders : official journal of the Movement Disorder Society* 29(10):1231-1240.
197. Burre J, Sharma M, & Sudhof TC (2012) Systematic mutagenesis of alpha-synuclein reveals distinct sequence requirements for physiological and pathological activities. *The Journal of neuroscience : the official journal of the Society for Neuroscience* 32(43):15227-15242.
198. Grey M, Linse S, Nilsson H, Brundin P, & Sparr E (2011) Membrane interaction of alpha-synuclein in different aggregation states. *Journal of Parkinson's disease* 1(4):359-371.
199. Grey M, *et al.* (2015) Acceleration of alpha-synuclein aggregation by exosomes. *The Journal of biological chemistry* 290(5):2969-2982.
200. Galvagnion C, *et al.* (2015) Lipid vesicles trigger alpha-synuclein aggregation by stimulating primary nucleation. *Nature chemical biology* 11(3):229-234.
201. Bucciantini M, *et al.*, Dobson CM, & Stefani M (2002) Inherent toxicity of aggregates implies a common mechanism for protein misfolding diseases. *Nature* 416(6880):507-511.
202. Campioni S, *et al.*, & Chiti F (2010) A causative link between the structure of aberrant protein oligomers and their toxicity. *Nature chemical biology* 6(2):140-147.
203. Stefani M (2010) Biochemical and biophysical features of both oligomer/fibril and cell membrane in amyloid cytotoxicity. *The FEBS journal* 277(22):4602-4613.
204. Chen SW, *et al.* (2015) Structural characterization of toxic oligomers that are kinetically trapped during alpha-synuclein fibril formation. *Proceedings of the National Academy of Sciences of the United States of America* 112(16):E1994-2003.
205. Lendel C, *et al.*, & Hard T (2014) A hexameric peptide barrel as building block of amyloid-beta protofibrils. *Angewandte Chemie* 53(47):12756-12760.
206. Devine MJ, Gwinn K, Singleton A, & Hardy J (2011) Parkinson's disease and alpha-synuclein expression. *Movement disorders : official journal of the Movement Disorder Society* 26(12):2160-2168.
207. Angelova PR, *et al.* (2015) Lipid peroxidation is essential for alpha-synuclein-induced cell death. *Journal of neurochemistry* 133(4):582-589.
208. Deas E & *et al.* (2015) *Plos Medicine* under review.

209. Ehrnhoefer DE, *et al.* (2008) EGCG redirects amyloidogenic polypeptides into unstructured, off-pathway oligomers. *Nature structural & molecular biology* 15(6):558-566.
210. Laue TM, Shah BD, Ridgeway TM, & Pellettier SM (1992) Computer-aided interpretation of analytical sedimentation data for proteins. *Analytical Ultracentrifugation in Biochemistry and Polymer Science*:90-125.